Australian National University

Advancing Electrochemical Performance of Li–S Batteries: Strategies for Polysulfide Immobilization and Catalytic Enhancement

Huimin Gu

February 2025

A thesis submitted for the degree of Doctor of Philosophy of

The Australian National University

DECLARATION

I hereby declare that this dissertation presents the primary research outcomes of my independent work during my PhD program. To the best of my knowledge, it does not contain any material previously published or written by another person, nor does it include substantial portions of work accepted for any other degree or diploma at the Australian National University (ANU) or any other institution, except where proper acknowledgment and references are provided. Contributions from collaborators at ANU or elsewhere have been explicitly acknowledged. I also declare that the intellectual content of this thesis is my own work, except where assistance with project design, conception, style, presentation, or linguistic expression is acknowledged. This thesis comprises three manuscripts, in which I am the first or co-first author. Chapter Two has been published, while Chapters Three and Four are currently under submission.

Signed: Huimin Gu

Date: 25th February 2025

COPYRIGHT STATEMENT

AUTHENTICITY STATEMENT

I certify that the library deposit digital copy is a direct equivalent of the final, officially approved version of my thesis. If there are any minor variations in formatting, they are the result of the conversion to digital format.

Signed: Huimin Gu

Date: 25th February 2025

ABSTRACT

With the rising demand for efficient and cost-effective energy storage technology, Lithium–sulfur (Li–S) battery has emerged as a promising candidate for the next-generation of high-energy batteries. Despite their low operating voltages (ca. 2.1 V), Li–S batteries offer a theoretical energy density of up to 2600 Wh kg^{-1}, with the practical energy density for packaged cells reaching 400 to 600 Wh kg^{-1} (387 W h kg^{-1} for $LiCoO_2$/C battery, commercial lithium-ion batteries). Additionally, sulfur's natural abundance, low cost, and environmental benignity make it an appealing option for sustainable energy solutions.

However, the electrochemistry brings significant challenges that hinder the practical application of Li–S batteries. One major issue is the shuttle effect of soluble long-chain lithium polysulfides (LiPSs) (Li_2S_n, $4 \leq n \leq 8$), which migrate uncontrollably through the electrolyte, leading to rapid capacity fade, poor sulfur utilization, and severe corrosion of the lithium metal anode. Furthermore, the sluggish redox kinetics of LiPSs exacerbates these issues, reducing the overall electrochemical efficiency. Additionally, sulfur's intrinsically poor electrical conductivity ($\sim 5 \times 10^{-30}$ S cm^{-1}) and the large volume expansion (~80%) between S_8 and final reduction product Li_2S create mechanical instability in the cathode. These combined factors significantly impair the long-term cycling stability, Coulombic efficiency, and overall performance, thereby limiting their feasibility for the practical application in energy storage systems.

This thesis explores strategies to mitigate LiPSs shuttle effects by constructing

modified membranes designed to immobilize LiPSs through both physisorption and chemisorption mechanisms, alongside approaches to enhance sulfur redox reaction (SRR) by compositing electrocatalysts with sulfur cathodes to improve overall performance of Li–S battery. In investigating modified membrane for physically blocking LiPSs movement, we elaborated on the critical balance between LiPSs confinement and energy loss by quantifying the key role played by the modified membrane in lithium-ion permeability. For the electrocatalysis LiPSs conversion, we analyzed catalytic kinetics and efficiency by quantifying the precipitation of Li_2S_2/Li_2S.

In the first study, we investigated several commonly reported membrane materials (i.e., GO, rGO, $Co(OH)_2$, SnS_2, and MoS_2), along with holey-structured material with varying porous density (030HG and 050HG), as modified membranes for lithium-sulfur batteries. These micro-porous membranes effectively suppress the movement of polysulfides, but they also introduce varying levels of hindrance to Li^+ transport, creating a trade-off between Li^+ permeability and energy density. To quantify the impact of these membranes on Li^+ permeability, we measured overpotential, Li^+ diffusion coefficient (D_{Li^+}), Li^+ activation energy ($E_{a\text{-}Li^+}$), and Li^+ conductance (σ_{Li^+}). Tests using Li|Li symmetric cell revealed that certain membranes, such as GO, MoS_2, and rGO, exhibited overpotentials exceeding 250 mV at 1 C rate. Fabrication and testing of porous membrane with controlled mesoporosity (e.g., holey graphene membranes) and modeling confirmed that the overpotentials stem from physical obstruction of Li^+ transport. This highlights the need to balancing polysulfide blocking and minimal energy loss. For optimal battery performance, the effective hole area should be close

to commercial PP separators (~15.5%), i.e., small enough to mitigate the LiPSs shuttle effect and to prevent internal short circuiting but large enough to minimize increases in overpotential. Holey graphene membranes with 18.2% and 11.1% of surface holy area reduced the polysulfide diffusion by 62.5% and 113%, while only raising the overpotential for Li^+ transport by 33.3% and 60%, respectively.

The second study focused on developing functional holey membranes with high Li^+ mobility for enhanced sulfur catalysis. we tried to redefine the strategies for improving Li–S battery performance by highlighting the significant role of Li^+ transport in sulfur redox reactions (SRR), an often-overlooked aspect in membrane design. Traditional membrane design strategies focus on controlling the lithium polysulfides migration and catalyzing SRR. However, the critical influence of lithium-ion transport on SRR kinetics is frequently neglected. To address this gap, we introduced a novel holey graphene membrane embedded with Co_9S_8 (Co_9S_8/HG), with a porosity of 16.2%, to promote rapid lithium-ion diffusion and efficient polysulfides conversion. This design not only tackles the notorious shuttle effect of LiPSs, but also significantly enhances SRR kinetics, overcoming the limitations of conventional membrane designs that impede lithium-ion flow. The Co_9S_8/HG/PP membrane, as a result, achieved a notable discharge capacity of 671 mAh g^{-1} over 900 cycles at 0.2 C and exhibits robust rate performance, maintaining 784 mAh g^{-1} capacity when switching from 2 C to 0.2 C.

In the third study, we developed a holey-structured Co_3S_4-T400 as a model electrocatalyst to investigate how its porous architecture enhances SRR kinetics and facilitates Li_2S precipitation by promoting localized Li^+ transport in the cathode.

Transmission electron microscopy (TEM) characterization and statistical analysis revealed that the Co_3S_4-T400 nanosheets exhibit a porosity of 13.6% with a uniformly distributed pore structure. This suggests that Co_3S_4-T400 causes less polarization and localized Li^+ flow compared to its non-holey counterpart of Co_3S_4-T200. Electrochemical surface area (ECSA) measurements further demonstrated that Co_3S_4-T400 possesses an active surface area four times larger than that of Co_3S_4-T200, providing abundant catalytic sites for effectively encapsulating and converting lithium polysulfides (LiPSs). As a result, cells incorporating the Co_3S_4-T400 catalyst exhibited a smaller Tafel slope, a higher Li^+ diffusion coefficient (D_{Li^+}), and more uniform Li_2S deposition. These findings indicate that the holey structure of Co_3S_4-T400 significantly enhances Li^+ diffusivity, thereby accelerating SRR kinetics and regulating Li_2S precipitation. As a proof of concept, Li-S batteries utilizing S/Co_3S_4-T400/C demonstrated outstanding long-term cycling performance, retaining a specific capacity of 657 mAh g^{-1} with a low-capacity decay rate of 0.051% per cycle and a high average coulombic efficiency of 98.5% over 1000 cycles. These results highlighted the effectiveness of employing a porous catalyst to facilitate localized Li^+ diffusion, thereby enhancing SRR kinetics, controlling Li_2S precipitation, and improving the overall performance of Li-S batteries.

The three projects not only demonstrated the effectiveness of the research methods in advancing the performance of Li–S batteries, but also provided valuable insights for future research in sustainable energy storage fields. Moreover, these studies revealed several previously unexplored challenges that warrant further investigate in the future.

ACKNOWLEGEMENT

As I stand on this side of time and look back on the past few years of my Ph.D. journey, I find myself at a loss for words to fully express my gratitude to the supervisors, colleagues, school staff, and my families and friends who have tirelessly guided and supported me along the way. My Ph.D. experience has become an invaluable treasure in my life, shaping me in ways that extend far beyond academic knowledge. The growth I have achieved during these years will profoundly influence both my professional aspirations and my personal outlook on life.

First and foremost, I would like to express my sincere gratitude to my supervisors, Prof. Zongyou Yin, Prof. Antonio Tricoli, and Dr. Borui Liu. Without their invaluable guidance, unwavering support, constant encouragement, and professional mentorship, I would not have achieved the research outcomes presented in this thesis. Their supervision makes the journey towards the completion of my PhD degree unforgettable and deeply impactful. A special thanks to Dr. Borui Liu, who not only teaches me how to conduct research but also helps me develop critical thinking skills. Conducting research under Dr. Borui Liu's supervision is both challenging and rewarding, as his guidance inspired me to explored broader research areas, including lithium-ion batteries, solid-state electrolytes, and catalytic hydrogen production. Finally, I am also thankful to my panel members A/Prof. Alexey Glushenkov (now left ANU), Prof. Valeska Ting and A/Prof. Juan Felipe Torres for their valuable suggestions and support during various stages of my PhD program. I sincerely hope that my supervisors' groups continue to achieve

remarkable progress in the future.

I also want to thank the colleagues who have worked with me, including Dr. Thrinath Reddy Ramireddy, Kili Liu, Hang Yin, Qi Wang (University of Sydney), Kim Anh Nguyen (University of Sydney), Xuan Minh Chau Ta (University of Sydney), Dr. Sandra Saji, Zhehao Sun, Xuechen Jing, Yi-Lun Chen, Muhammad Usman, Dr. M.D. Nasir Uddin, and Dr. Mahdiar Taheri. Specially, I would like to thank Qi for collaborating with me on completing the third project. Thanks for his great help in characterizations, such as XPS, Raman, EELS, TEM and SEM. I sincerely wish everyone a very successful career in the future.

I would also like to thank Dr. Felipe Kremer, Dr. Frank Brink who helped me a lot in microscopic imaging in the Center of Advanced Microscopy (CAM) of ANU. I am also thankful for the financial support from the AGRTP Domestic Scholarships.

I also want to express my appreciation to the faculty and staff at the Research School of Chemistry, especially, Timothy Borough, Genmiao Zhang, Michael Hill, Daniel Barkus, Michael Stevens, and the admin team for providing me with the support and the resources to complete this research.

I want to express my gratitude to my dearest parents. I could not have reached to this point of life without their continuous love, support, encouragement, and patience. My words cannot fully express my love for my them, as they have always been my greatest source of strength and inspiration. Their belief in me has been the foundation of my perseverance and courage.

I am deeply grateful to my beloved daughter, Angela, and my little son, Guyan, for their constant companionship throughout this joinery. In particular, I want to express my love to my sweet, intelligent, beautiful, kind, thoughtful, and brave daughter Angela. Their presence has been a source of immeasurable joy and strength, uplifting me during the most challenging moments of this journey. I am endlessly proud of them and cherish the love and support they have given me.

Finally, I want to express my gratitude to myself—the determined and resilient version of me. Thank you for my hard work, for persevering through challenges, and for remaining steadfast despite the achievements of outstanding colleagues and moments of self-doubt. Pursuing a Ph.D. has been one of the greatest challenges of my life, but the growth I have experienced throughout this journey has profoundly shaped my perspective. This experience will undoubtedly remain a cherished asset for years to come.

LIST OF ABBREVIATIONS

Li	lithium
S	sulfur
Li–S	lithium–sulfur
LIBs	lithium-ion batteries
$LiCoO_2$	lithium cobalt oxide
$LiPFeO_4$	lithium iron phosphate
NMC	lithium nickel manganese cobalt oxide
NCA	lithium nickel cobalt aluminum oxide
$LiNO_3$	lithium nitrate
LiPSs	lithium polysulfides
Li_2S	lithium sulfide
Li_2S_x	lithium polysulfide
G	graphene
GO	graphene oxide
rGO	reduced graphene oxide
2D	two–dimensional
3D	three–dimensional

C	C rate, for describing the charge/discharge rates of batteries
CNT(s)	carbon nanotubes
CNF(s)	carbon nanofibers
MOF(s)	metal-organic framework(s)
ZIF	zeolitic imidazolate framework
Ea	activation energy
D_{Li^+}	lithium-ion diffusion coefficient
σ_{Li^+}	Li^+ conductance
SSA	specific surface area
TGA	thermogravimetric analysis
UV-vis	X-ray photoelectron spectroscopy
BET	Brunauer-Emmett-Teller
EDS	energy dispersive X-ray spectroscopy
EELS	electron energy loss spectroscopy
TEM	transmission electron microscopy
HRTEM	high-resolution transmission electron microscopy
SEM	scanning electron microscopy
STEM	scanning transmission electron microscopy
XPS	X-ray photoelectron spectroscopy

XRD	X-ray diffraction
ECSA	electrochemical surface area
CV	cyclic voltammetry
LSV	linear sweep voltammetry
DME	dimethyl ether
DOL	1,3-dioxolane
NMP	N-Methyl-2-pyrrolidone
LiTFSI	lithium bis(trifluoromethanesulfonyl)imide
SP	SuperP carbon black
$Co(OH)_2$	cobalt hydroxide
MoS_2	molybdenum disulfide
SnS_2	stannum disulfide
HCl	hydrochloric acid
Co_3S_4	cobalt sulfide
Co_9S_8	cobalt sulfide
H_2S	hydrogen sulfide
PP	polyethylene
PVDF	polyvinylidene fluoride
EG	ethylene glycol

$Co(AC)_2$	cobalt acetate
ASSLSBs	all-solid-state lithium sulfur batteries
ESSs	energy storage systems
C_{dl}	double-layer capacitance

TABLE OF CONTENT

LIST OF FIGURES

Chapter 1 Introduction

1.1 Background

Over the past two decades, rapid industrialization and the over-exploitation of fossil fuels have driven a global energy crisis, leading to rising temperatures and exacerbating environmental challenges. This situation has created an urgent need for countries around the world to prioritize the energy transition, reduce reliance on the fossil fuel, and strive for a carbon-neutral economy. Consequently, sustainable energy sources, such as solar, wind, and wave energy, have become promising alternatives. However, the intermittent and variable nature of these renewable sources requires integration with energy storage systems to maintain a stable and reliable energy supply.

Among various storage options, lithium-ion batteries (LIBs) are extensively utilized in energy storage applications, including portable electronic devices, electric vehicles (EVs) and hybrid electric vehicles due to the advantages of high energy density and long-term cycling stability. Despite these advantages, LIBs possess several limitations, including a relatively low energy-to-weight ratios (100-265 Wh kg^{-1}) and high production costs,[1-3] often exceeding $200 per kWh for battery packs.[4] To support the growth of EVs and energy storage systems (ESSs), the development of batteries with high energy densities and low production costs is of significant importance.

Li–S battery has been considered as a promising candidate for the next-generation energy storage application. Despite their lower operating voltages (ca. 2.1 V), Li–S

batteries offer a theoretical energy density of up to 2600 Wh kg^{-1}, with the practical energy density for packaged cells ranging from 400 to 600 Wh kg^{-1}.[5, 6] This is substantially higher than that of commercialized cathodes materials, such as $LiCoO_2$ (387 Wh kg^{-1}),[7] $LiFePO_4$ (90-160 Wh kg^{-1}),[8] NMC (150-220 Wh kg^{-1}),[9] and NCA (200-250 Wh kg^{-1}).[10] Furthermore, sulfur's natural abundance, low cost, and environmental friendliness make Li-S batteries as a strong contender for high-energy applications. However, the commercialization of Li-S batteries remains challenging, which is primarily related to the intrinsic properties of the sulfur cathode materials. (I) Electron insulating nature of sulfur/Li_2S and volume expansion, and elemental S_8 and solid Li_2S present extremely low ionic conductivities, (S_8: 10^{-20} - 10^{-25} S cm^{-1}, $5x10^{-30}$ S cm^{-1}; Li_2S: 10^{-6}-10^{-8} S cm^{-1}, 10^{-13}-10^{-14} S cm^{-1} respectively).[11, 12] This poor conductivity significantly impedes the charge transfer efficiency, necessitating the use of conductive additives or host to maintain the conductivity within the cathode. Additionally, the density differences between the elemental sulfur (2.03 g cm^{-3}) and the reduced product Li_2S (1.66 g cm^{-3}) leads to a volume expansion of approximately 80%,[13, 14] which can cause structural instability during cycling. (II) Shuttle effect of LiPSs. Shuttle effect arises from the formation, dissolution and accumulation during electrodes reactions,[15, 16] causing rapid capacity decay and poor cycling performance. Dissolved polysulfides penetrate the separator and migrate to the anode side, where they are reduced by Li metal, forming a passivation layer consisting mainly of Li_2S_2 and Li_2S, further deteriorate the battery performance.[17-19] (III) Sluggish sulfur reduction reaction kinetics. The conversion from high-order polysulfides to insoluble Li_2S_2/Li_2S represents the most

challenging step, leading to an accumulation of soluble LiPSs in the electrolyte and exacerbation of the shuttling issue. An electrocatalytic process could help accelerate SRR kinetics and reduce LiPSs accumulation. (IV) Dendrite formation on Li anode. Li dendrite formed as a result of uneven deposition of the solid-electrolyte-interface (SEI) during the charging/discharging cycles.[20-22] The shuttled soluble LiPSs can react with metallic Li, forming an insoluble and insulating layer of Li_2S_2/Li_2S on the anode surface. This layer retards the efficient Li^+ transport during prolonged cycling, resulting in poor Coulombic efficiency and potentially accelerating battery failure.[23, 24]

1.2 Electrochemistry mechanism of Li–S batteries

A Li–S battery consists of a sulfur cathode, a lithium metal anode, a separator facilitates lithium ions to transport between electrodes, and an ether-based electrolyte for lithium ions conduction.[17] (Figure 1-1a)

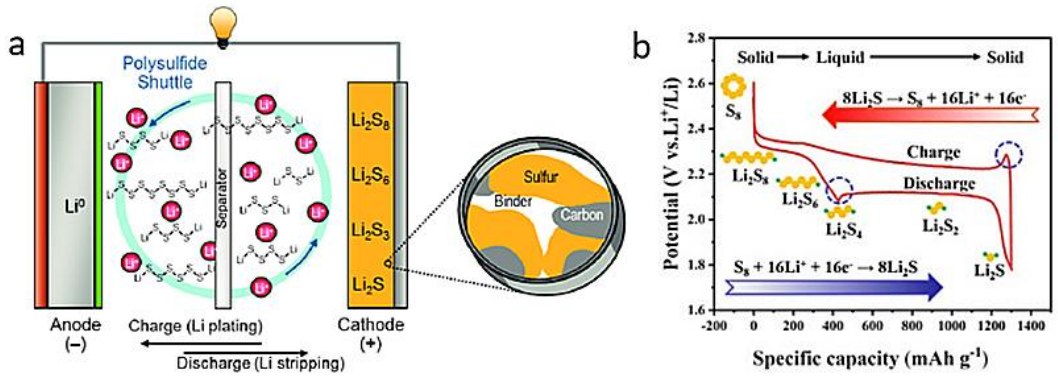

Figure 1-1. (a) Schematic configuration of Li–S battery and, (b) Charge-discharge profile of traditional Li–S battery.[25] Adapted from Zhang et al. (2020) with permission. Copyright 2020 Elsevier

As illustrated in Figure 1b, during discharge, the sulfur cathode undergoes multi-stage reduction reactions involve a sequential formation of LiPSs. Initially, S_8 ring molecules

react with lithium ions to form long-chain Li_2S_8, corresponding to the first plateau at approximately 2.4 V. Successive cleavage of S-S bonds produces a series of intermediate polysulfide (S_n^{2-}, 8≥n≥3), resulting in the slop section of the discharge curve around 2.4-2.1 V, contributing to about one-quarter of the theoretical capacity of sulfur (418.75 mAh g^{-1}). At approximately 2.1 V, a second plateau appears. Some literature suggests that this transition happens concurrently with the start of the formation of solid Li_2S_2 and Li_2S,[25, 26] accounting for the three-quarters (1256.25 mAh g^{-1}) of the total discharge capacity (Figure 1-1b). The final slop represents the conversion of Li_2S_2 to Li_2S, where the voltage rapidly drops as the cathode becomes largely covered by nonconductive Li_2S_2/Li_2S. This coating significantly increases the cell resistance and obstructs charge transfer pathways. The potential dip at the beginning of the second discharging plateau originates from the concentration polarization caused by the rising viscosity of electrolyte.[27] Similarly, an increase in potential is observed at initial charging. This because the ionically insulating nature of Li_2S_2/Li_2S requires extra driving force for oxidation to soluble LiPSs.[28] The following single charging plateau at 2.3-2.4 V corresponds to the oxidation of LiPSs to S_8.

The liquid–liquid conversion occurs between soluble LPSs involves the transformation of Li_2S_8 to Li_2S_4 during discharge and Li_2S_4 to Li_2S_8 during charge. These processes bridge the solid phases of elemental sulfur and Li_2S_2/Li_2S, playing a crucial role in Li–S redox chemistry. At such stage, soluble polysulfides readily shuttle across the separator.[29-31] When these polysulfides diffuse outside of the cathode region or are reduced by lithium metal to form insoluble Li_2S_2/Li_2S precipitated on anode side, they

are no longer available to participate in the reaction, leading to a permanent capacity loss.[16, 32] Also, the delayed phase conversions accelerate the LiPSs accumulation in the electrolyte and exacerbate the shuttle effect.[33, 34] In this viewpoint, accelerating the conversion rate amongst the dissolved polysulfides could reduce LiPSs buildup in the electrolyte, thereby enhancing the electrochemical performance of the battery.[35-37]

The electrochemical performance of Li–S batteries is significantly restricted by the challenges such as the insulating nature of sulfur, LiPSs shuttle movements and SRR sluggish kinetics, impacting both cycling stability and rate capability, thereby hindering the commercialization of Li–S batterie. To address these issues, tremendous research endeavors have been performed and the following strategies were proposed to be able to improve the electrochemical performance of Li-S batteries: 1. Suppressing shuttling movement of LiPSs species by physisorption or chemisorption via constructing porous hosts,[38-43] modifying the separator or introducing a functional interlayer,[44-48] and accelerating the LiPSs conversion kinetics;[49-53] 2. Developing solid-state electrolytes[5, 54-56] or additives for liquid electrolyte[57-62] to optimizing LiPSs solubility and facilitate LiPSs conversion reaction rate; 3. Protecting lithium anode from corrosion and dendrite growth.[63-66]

1.3 Suppressing shuttle effect of Polysulfides

1.3.1 Physical anchoring of LiPSs

Nazar's research group pioneered the research with a highly ordered mesoporous carbon (CMK-3)[67] to accommodate sulfur, achieving a reversible capacity of 1320 mAh

g^{-1} at 168mA g^{-1}. Since then, numerous research groups have reported using various carbon materials and derivatives as sulfur hosts and interlayer barriers to effectively mitigate the LiPSs shuttle effect. These carbon materials and carbon derivatives are widely investigated due to their hollow, layered structures with high specific surface area, excellent electrical conductivity, and dimensional stability. Notable examples include carbon nanotube/fibers,[68-71] mesoporous carbon,[72-75] graphene,[76-80] MXene,[81-84] and metal organic framework (MOF).[85-88]

On the cathode side, carbonaceous materials have been strategically engineered into various morphologies and dimensions to effectively encapsulate sulfur, thereby providing a physical barrier to suppress the shuttle effect of lithium polysulfides.[89-92] Gu et al. developed a microporous carbon-coated sulfur composite, R-S@MPS,[93] with three distinct types of pores that function synergistically to improve sulfur retention and mitigate shuttle effect. Therefore, it delivered a decay rate of 0.013% per cycle after 500 cycles at 1 C with a sulfur loading of 4 mg cm^{-2}. Chen's group presented graphene wrapped chromium-MOF ,GNS-MIL-101 (Cr)-sulfur composite with a large specific area and a conductive shell (0.1 S cm^{-1}), achieving 809 mAh g^{-1} at 0.8 C with a sulfur content of 58.8%.[94] This research demonstrated that the addition of graphene sacrificed the sulfur content to obtain a satisfactory cycle performance.

For Li–S battery, the modified separator is crucial for inhibiting the shuttle effect of LiPSs. In 2012, Manthiram pioneered the use of nonpolar carbon materials by integrating a microporous carbon (MPC) interlayer between cathode and separator for anchoring migrating LiPSs.[95] This carbon layer also functions as an additional current

collector, enhancing sulfur utilization by promoting electron transport and facilitating more efficient electrochemical reactions within the cathode side. Additionally, Manthiram group coated an ultralight-weight layer (0.17 mg cm^{-2}) of multiwall carbon nanotubes (MWCNTs) on the PP separator.[96] This MWCNT-coated membranes effectively trapped diffused polysulfides by physical adsorption them at microporous sits. As a result, the cycled MWCNT-coated separator exhibited a much lower surface area of 30.58 m^2 g^{-1} and pore volume of 0.06 cm^3 g^{-1}, achieved a capacity of 621 mAh g^{-1} after 300 cycles at 1 C with a fading rate of 0.14% per cycle.

Although physical barrier and absorption strategy can mitigate the shuttle effect, the weak affinity between nonpolar carbon materials and polar intermediates allows polysulfides to continuously dissolve into electrolyte, leading to a growing concentration of LiPSs, resulting in fast capacity decay and poor coulombic efficiency. Thus, numerous works focus on polarizing carbon materials to construct the “sulfiphilic” surface to absorb LiPSs by introducing heteroatom (e.g., N, O, S, and P)[97-99] and doping functional groups (e.g., phosphate, sulfonic, and amino groups).[100-102] However, due to the sluggish conversion kinetics of SRR, the confined LiPSs cannot be rapidly reduced to Li_2S_2/Li_2S, resulting accumulating of LiPSs and exacerbating the shuttle effect. Wu et al. utilized density functional theory (DFT)[103] to reveal a linear relationship between the chemisorption of LiPSs and specific capacity, establishing a direct connection between adsorption ability and battery performance.

1.3.2 Chemical adsorption and catalytic conversion of LiPSs

In Li–S batteries, achieving rapid sulfur reduction kinetics requires sulfur to be in

contact with the electrolyte, inevitably leading to the dissolution of LiPSs. Consequently, the most effective strategy to mitigate LiPSs shuttling is to accelerate the conversion of dissolved LiPSs to insoluble Li_2S_2 and Li_2S.[104-106] However, during the reverse reaction, oxidizing solid Li_2S_2/Li_2S back into soluble LiPSs requires significant activation energy.[106-108] This process is further impeded by the aggregation tendency of Li_2S_2/Li_2S, which not only slows oxidation reaction kinetics but also increases internal resistance due to the insulating nature of Li_2S_2/Li_2S. Therefore, enhancing the bidirectional conversion kinetics of LiPSs to and from Li_2S_2/Li_2S is essential to effectively suppress shuttling.

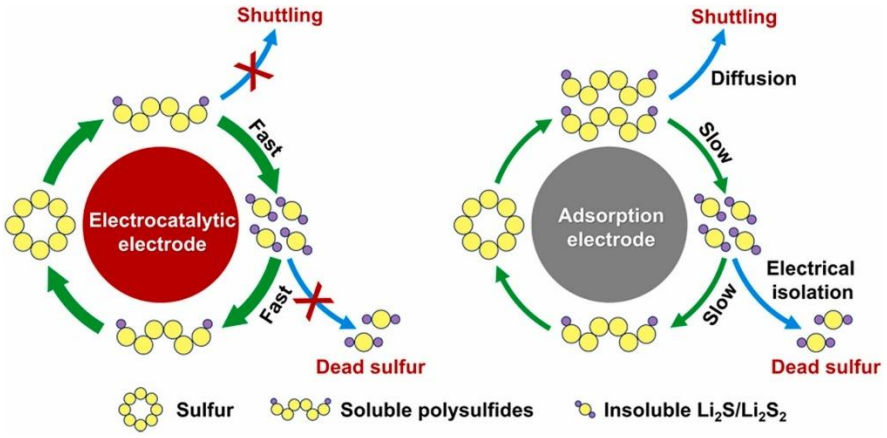

Figure 1-2. Schematic comparison of SRR kinetics with electrocatalysts and polar adsorbents in electrodes[109] Adapted from Yu et al. (2018) with permission. Copyright 2018 Elsevier

Electrocatalysts play a crucial role in this context, as they not only capture LiPSs but also accelerate redox reaction kinetics by facilitating efficient ion and electron transport. In contrast, while polar adsorbents can anchor LiPSs, they lack the ability to promote redox reactions, limiting their effectiveness in reducing shuttling (Figure 1-2). This emphasizes the importance of chemical interactions between electrocatalytic materials

and LiPSs to drive efficient catalytic conversion.[110-112]

Cui's group[113] conducted a computational study on the anchoring effect of various 2D layered materials (oxides, sulfides, and chlorides) on LiPSs across the full lithiation process in lithium-sulfur batteries. They discovered that the binding strength between sulfur (S) in LiPSs and metal atoms in the anchoring materials was a key factor influencing adsorption characteristics. This binding strength, aligning with the Sabatier principle,[114, 115] affects the Li–S bonds in LiPSs during the lithiation process. They highlighted those anchoring materials with moderate binding strength effectively capture LiPSs while allow for their complete reduction. In contrast, strong binding strength can induce the destruction of LiPSs which would hinder further redox reactions and reduce the battery's discharge capacity. This balance enables efficient LiPSs retention without obstructing the essential redox processes.

Recent studies have shown that certain polar materials, including metal oxides, metal sulfides, metal nitrides, and some metal-free compounds, have been developed for use in cathodes and separators due to the enhanced chemical interaction towards LiPSs. These materials not only exhibit strong affinity for LiPSs but also catalytically enhance their conversion kinetics.

1.4 Catalytic LiPSs

1.4.1 Metals host for sulfur

The Arava group was among the first to investigate the catalytic activity of Pt in enhancing the sulfur redox reaction.[116] They grafted Pt and Ni nanoparticles onto

graphene, forming Pt/graphene and Ni/graphene composites with a high surface area. Tafel plots and exchange current density values confirmed their catalytic effect during the charge/discharge process, showing that both Pt/graphene and Ni/graphene effectively promote the LiPSs conversion. He et al. demonstrated through[117] theoretical calculation that the Pt@Ni core–shell catalyst promotes Li_2S oxidation by lower the decomposition barrier (0.101eV) for insoluble Li_2S, resulting in an improvement in the specific capacity and cycle stability of Li–S batteries. Although noble metal catalysts exhibit excellent catalytic properties, their application is hindered by high costs and scarce availability. Transition metals are attractive alternatives due to their effective binding capabilities with polysulfide species. This binding ability is influenced by the alignment of metal's d-band center with the sulfur species' p-band center, making the selection of appropriate transition metals for LiPSs adsorption essential. Cobalt is one of the most extensively studied transition metals due to its strong catalytic effect and anchoring capabilities for LiPSs. Zhou et al. developed a composite consisting of cobalt and graphitic porous carbon Co@GC–PC as sulfur host,[118] achieving a capacity of 790 mAh g^{-1} after 220 cycles at 0.2 C, significantly outperforming carbon-based cathode. DFT calculations revealed a strong interaction between Li_2S and Co with an adsorption energy of 4.39 eV, and a lower decomposition barrier of Li_2S on Co (0.13 eV) compared to carbon materials (1.8 eV). This suggests that Co not only enhances Li_2S adsorption but also serves as an efficient catalyst for its oxidation back to LiPSs.

Metal catalysts combined with high surface area carbon materials can significantly enhance the SRR redox reaction kinetics and improve sulfur utilization due to their high

electronic conductivity. However, the high cost of noble metals and toxicity of heavy metals limit their practical applications. Furthermore, increasing active surface area and dispersion is essential to enhance the catalytic efficiency of metal catalysts.

1.4.2 Transition metal Oxides (TMOs) host for sulfur

In contrast to the previously discussed metal catalysts, low-cost transition metal oxides, such as Fe_3O_4,[119, 120] TiO_2,[121-123] V_2O_5,[124-126] and SnO_2,[127, 128] which contain O^{2-} anions, exhibit strong chemical absorption capability that effectively suppress LiPSs mobility.[129] Strong adsorption of LiPSs on polar surfaces is widely recognized as critical for enhancing performance of Li–S battery.

However, Cui and co-workers[130] demonstrated that, for nonconductive metal oxides to effectively facilitate lithium polysulfide conversion, LiPSs must diffuse efficiently from the oxide surface to a conductive matrix. They highlighted the importance of balancing adsorption and diffusion on polar surfaces. Among the oxides investigated, Al_2O_3 exhibited the strongest adsorption toward Li_2S with an adsorption energy of -7.12 eV, compared to La_2O_3 (-5.85 eV), MgO (-5.71 eV), and CeO_2 (-6.33 eV). Although Al_2O_3's strong binding favors adsorption, it restricts the surface diffusion of LiPSs. These binding energies illustrate the diverse capabilities of each oxide in adsorbing and retaining lithium polysulfides, which is crucial for optimizing Li–S battery performance. The study further emphasized that the oxides like MgO, CeO_2, and La_2O achieve a balance between strong adsorption and adequate diffusion, promoting efficient sulfur utilization and minimize capacity decay. To address the kinetic barrier to surface

diffusion, facilitating electron transfer to the adsorbed lithium polysulfides is essential. Linda Nazar et al. synthesized Ti_4O_7 nanocrystals[131] (electrical conductivity, ~2 x 10^3 S cm^{-1} at room temperature) to composite with S, achieving a low-capacity decay of 0.08% per cycle at 0.5 C after 250 cycles. This performance was attributed to the metallic conductivity of Ti_4O_7 and strong chemical interaction of Ti^{3+} with Li_2S_4, leading to a faster reduction kinetics and decreased shuttle effect.

Unlike previous strategies to anchor LiPSs by physical or chemical interaction, Nazar group proposed a mechanism of entrap LiPSs within cathode by forming a surface-bound polythionate species. They synthesized ultrathin MnO_2 nanosheet (NS) to mediate the polysulfide conversion in a two-sept redox process.[132] The MnO_2 NSs first reacted with LiPSs to form insoluble thiosulfate groups while Mn^{4+} is reduced to Mn^{2+}. The newly formed LiPSs then readily anchored to S-S bonds of the thiosulfate groups, leading to the formation of polythionate complexes and short-chain LiPSs. The low solubility of the polythionate complex considerably suppressed the polysulfides shuttle mobility. This conversion continues progressively throughout discharge until the complete transformation to Li_2S_2/Li_2S is achieved. XPS analysis confirmed this process by identifying the existence of thiosulfate (167.2 eV) and polythionate (168.2 eV). The resulting S/MnO_2 cathode, with a sulfur loading of 75wt.%, exhibited an impressive cycle stability, showing only 0.036% capacity fading per cycle over 2000 cycles at a high rate of 2 C. This highlights the crucial role of MnO_2 in effectively inhibiting polysulfides loss and significantly enhancing the electrochemical performance of sulfur cathodes. However, due to the poor conductivity of MnO_2, incorporating conductive

materials is essential to improve sulfur utilization and rate performance. In their follow-up work, Nazar et al. concluded that transition metal oxides with a redox potential window of 2.4–3.05 V, such as VO_2, could trigger this reaction mechanism by chemically anchoring polysulfides. This range allows these metals to oxidize polysulfides to thiosulfate and polythionate species, which can then form stable surface-bound intermediates.[133]

Transition metal oxides exhibit strong chemisorption for polysulfides due to their hydrophilic functional groups and the coexistence of lithium and oxygen bonds, which helps suppress the shuttle effect. However, this strong binding also leads to slow redox kinetics, especially in the reduction of long-chain polysulfides to shorter species like Li_2S, which limits efficient polysulfide conversion.[134] Additionally, the intrinsic poor electrical conductivity of most metal oxides impedes electron transport within cathode, thereby limiting the electrocatalytic efficiency and overall performance of the battery.

1.4.3 Transition metal Sulfides host for sulfur

Transition metal sulfides (TMSs) exhibit superior electrochemical performance and enhanced redox capability compared to transition metal oxides (TMOs). This advantage is attributed to TMSs' moderate chemical affinity with polysulfides, achieved through M-S bond formation with adsorption energies ranging from 1 to 3 eV (TMOs typically show adsorption energies between 2 and 4 eV[135]). The difference enables TMSs with effective interaction with LiPSs while avoiding overly binding that would inhibit redox reactions. Additionally, TMSs possess better electrical conductivity than

TMOs, facilitating redox kinetics.

Among TMSs, two-dimensional transition metal dichalcogenides (TMDs) such as XS_2 (where X = Mo, W, V, Ti, Zr) have demonstrated catalytic effectiveness a series studies. Arava's group investigated the electrocatalytic mechanism of TMDs with WS_2 and MoS_2 in facilitating LiPSs conversion,[136] finding that Li_2S_4 preferentially adsorbed at the edge sites of TMSs nanosheets where sulfur atoms are unsaturated. This adsorption at reactive edge sites underscores TMSs' catalytic potential. Lin et al. synthesized sulfur-deficient MoS_{2-x},[137] introducing numerous unsaturated sulfur sites on the basal plane. The increased presence of sulfur-deficient active sites enhances redox reaction kinetics by stabilizing intermediate species, thereby reducing capacity decay over extended cycling, achieving an impressive initial discharge capacity of 1159.9 mAh g^{-1} and retaining 628.2 mAh·g^{-1} after 600 cycles at 0.5 C.

The lithium-ion diffusion barrier is also crucial in promoting polysulfide redox reactions. Cui et al. used CI-NET calculation to simulate lithium-ion diffusion barriers on graphene and six TMSs (Ni_3S_2, SnS_2, FeS, CoS_2, VS_2 and TiS_2).[138] Finding that these TMSs, with diffusion barriers between 0.12 and 0.26 eV, exhibited lower diffusion barriers than graphene (0.3 eV), facilitating faster lithium-ion diffusion on sulfide materials. Liu group revealed that the low Li^+ diffusion energy barrier on the CoS_2 surface results from reduced electron density around the sulfur (S) atoms, enhancing Co–S covalent bonding and catalytic activity of CoS_2 by facilitating the conversion of lithium polysulfides (LiPSs).[139] The ZnS-SnS heterostructure developed by Sun group effectively facilitates Li^+ diffusion, playing a pivotal role in improving lithium polysulfide

(LiPSs) conversion kinetics. This heterostructure exhibits a lithium-ion diffusion energy barrier difference, with SnS at 0.37 eV and ZnS at 0.82 eV, enabling lithium ions to diffuse efficiently from the SnS surface to the ZnS surface via the heterointerface. The optimized heterostructure's interface between ZnS and SnS provides a continuous pathway for Li^+ migration, crucial for high-performance and long-term cycling in lithium-sulfur batteries. ZnS imparts strong catalytic activity, facilitating rapid redox reactions, while SnS contributes superior conductivity, collectively advancing sulfur electrochemistry and overall battery efficiency.[140]

In general, the conversion from Li_2S_4 to Li_2S is generally the rate-limiting step in sulfur reduction, requiring additional energy to proceed. Both transition metal oxides (TMOs) and transition metal sulfides (TMSs) can lower the decomposition barrier for Li_2S, enhancing redox activity between Li_2S and lithium polysulfides (LiPSs). However, TMSs are particularly effective for sulfur reduction due to their high electrical conductivity and catalytic activity, which resembles that of noble metals.[141]

1.4.4 Modified separator with Catalytic effect toward LiPSs

The aforementioned catalytic materials are not only used to host sulfur in the cathode but are also applied to modify the surface properties of conventional separators. These materials demonstrate bifunctional roles: first, the modified separators with ionic permselective properties physically block LiPSs through physisorption or chemisorption, preventing their diffusion and subsequent reaction with the Li metal anode. Second, they act as an additional current collector with the assistance of

carbonaceous materials, reactivating adsorbed sulfur species on their catalytic surfaces to participate in redox reactions, which enhances sulfur utilization and capacity.

Wang et al. applied a cobalt-embedded nitrogen-doped porous carbon nanosheet/graphene (Co-N_x@NPC/G)[142] coating to a commercial PP separator. The cobalt enhanced the polarity of the carbon material and catalyzed polysulfide conversion. The cell integrated with Co-N_x@NPC/G-coated separator achieved a high discharge capacity of 1042 mAh g^{-1} after 200 cycles at 0.5 C, with a low decay rate of 0.06% per cycle. Liu and co-workers used V_2O_5 to modify commercial PP[143] to trap polysulfide anions. A 5-mA h pouch cell of this design was charged/discharged over 300 cycles without noticeable degradation, maintaining a capacity of 800 mAh g^{-1}. Kang's group developed a V_2O_5-decorated carbon nanofiber (VCNF) membrane as an interlayer to mitigate the self-discharge by preventing the spontaneous reduction and dissolution of sulfur speciess,[142] achieving a capacity retention of 70.6% after 1000 cycles at 3 C.

1.5 Summary of this Thesis

Energy density is a key performance indicator for energy storage systems, particularly for lithium–sulfur (Li–S) chemistry, which is regarded as a promising candidate for next-generation energy storage technologies due to its high theoretical energy density. Among the key factors impacting energy density, lithium-ion diffusivity plays a pivotal role by directly governing the reaction kinetics, charge/discharge rates, and the

utilization efficiency of active materials. This dissertation presents a comprehensive investigation into the impact of lithium-ion transport on the electrochemical performance of Li–S batteries, comprising three interconnected research projects. Specifically, the work explores two major design strategies: (1) the integration of functionalized interlayers, and (2) the incorporation of conductive and catalytically active sulfur host materials within the cathode. These studies collectively elucidate how tailored material and interfacial engineering can modulate Li^+ transport pathways and sulfur redox kinetics, ultimately enhancing the cycling stability, rate performance, and long-term durability of Li–S batteries.

To date, around 2,300 research articles on membranes for lithium–sulfur (Li–S) batteries have been published, collectively accumulating approximately 90,000 citations, reflecting an accelerating research focus in this field. These research-targeted materials for membrane modifications encompass carbonaceous materials, MOFs, sulfide, nitride, carbide and COF (covalent organic frameworks). (Web of Science data Fig. 3). While these studies primarily focused on polysulfide confinement, relatively little attention has been given to understanding how the membrane or barrier structures impact the lithium-ion mobility and contribute to energy loss in Li–S batteries.

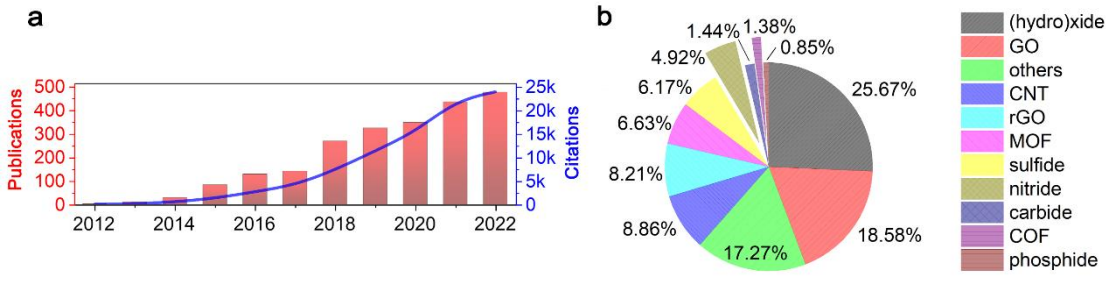

Figure 1-3 (a) Statistics of publications and citations related to polysulfide membranes for Li–S batteries between 2012 and 2022. (b) Materials for Li–S battery membranes

reported between 2012 and 2022.[143] Reproduced from Ref. 144 with permission from the Royal Society of Chemistry.

In the first project, we combined experimental investigation and modeling to assess the physical blockage towards the lithium-ion diffusion caused by the integration of five reported membranes, focusing on quantifying overpotential increases and theoretical loss in energy density. The membrane materials evaluated included graphene oxide (GO), reduced graphene oxide (rGO), cobalt hydroxide ($Co(OH)_2$), tin disulfide (SnS_2) and molybdenum disulfide (MoS_2). These micro-meso-porous materials were separately coated onto the commercial PP separators by vacuum filtration process with a uniform mass loading of 0.18 mg cm^{-2}. Scanning electron microscopy (SEM) characterization confirmed that the coating processes yield densely stacked structures without any noticeable uncovered areas. Overpotentials for Li^+ transport through these targeted membrane-modified separators were obtained from measurements using Li|PP|membrane|PP|Li symmetric cells. Results revealed that GO, the most favored separator modification material, exhibited an exceptionally high overpotential, which completely inhibited the transport of Li^+ in less than 8 mins at a moderate cycling rate of 0.5 C. At 1 C, membrane materials of SnS_2, rGO and MoS_2 produced overpotentials more than 250 mV, resulting in over 20% energy loss in the corresponding Li-S cells. Li^+ activation energy ($E_{a\text{-}Li^+}$) often considered as a criterion to evaluate Li^+ permeability of modified membranes. Our Nyquist plots revealed that this criterion cannot cover all the cases. Take commercial PP and GO membrane as examples, they showed similarly low $E_{a\text{-}Li^+}$ values of 0.095 eV and 0.064 eV, but with distinctively different obstruction effects towards Li^+ diffusion.

We further synthesized holey graphene nanosheets to study the blocking mechanism towards Li^+ transport. The holey graphene membranes were noted as 030HG (11.1%) and 050HG (18.6%) to depict the varying holey area percentage, sharing the similar average hole radius of 9 nm. We compared the Li^+ activation energy ($E_{a\text{-}Li^+}$), conductance (σ_{Li^+}) and Li^+ diffusion coefficient (D_{Li^+}) with membranes of 030HG, 050HG, and rGO. Membrane 050HG demonstrated smallest $E_{a\text{-}Li^+}$ and superior σ_{Li^+} and D_{Li^+} values, indicating the lowest physical obstruction to the lithium-ion transport. This mechanism was confirmed with the SEM characterization of the lithium foils disassembled after cycling. Membrane MoS_2 and GO effectively blocked Li^+ transport, leaving large areas with no lithium plating on lithium foil after cycling, while homogenously distributed on lithium foil coupled with 050HG and pristine PP separator. The COMSOL simulation was carried out with pristine PP, rGO/PP, 030HG/PP, and 050HG/PP. The results suggests that an optimal effective hole surface area (such as that of 050HG 13.5%), comparable to that of commercial PP separators (15.5%), is essential for efficient lithium-ion diffusion. We quantified the diffusion rates of 030HG, 050HG and rGO membranes using an H-cell setup followed with UV-vis measurements. Micro/mesoporous holey graphene membranes with 13.5% and 9.1% surface porosity reduced polysulfide diffusion by 62.5% and 113%, respectively, while only increasing the overpotential for Li^+ transport by 33.3% and 60%. These findings suggest that the structure engineering of modified membrane enables a balance between lithium-ion mobility and polysulfide confinement, thereby optimizing the battery performance and energy density.

In Li–S batteries, traditional membrane design strategies primarily focus on mitigating LiPSs migration and catalyzing the sulfur redox reactions (SRR), yet the critical role of lithium-ion transport in SRR kinetics is often overlooked. In our second study, we introduced a Co_9S_8-embedded holey graphene (Co_9S_8/HG) interlayer. Co_9S_8 exhibits a strong chemical binding energy of 4.03 eV with LiPSs species, resulting in the formation of Co–S and Li–S bonds that effectively trap LiPSs and suppress its diffusion. The Li^+ diffusion energy required on the Co_9S_8 surface is 0.31 eV,[137] nearly identical to that of pristine graphene (0.3 eV). Additionally, the holey graphene substrate provides migration channels for fast electrons and lithium-ions mobility during charging/discharging, therefore, the resulting holey structure allows for rapid Li^+ transport and demonstrates enhanced LiPSs conversion rates.

Transmission electron microscope (TEM) characterization confirmed that the Co_9S_8 nanoparticles (average size 22 nm) uniformly distributed on the holey graphene nanosheets. Statistical analysis showed a 17% porous area in Co_9S_8/HG composites, exceeding that of commercial PP separators (15.5%), indicating that the integration of Co_9S_8/HG/PP membrane will not result in excessive overpotential to inhibit Li^+ ion transport through the modified separator. BET measurements showed that the specific surface area of Co_9S_8/HG composite is 194.1 $m^2\ g^{-1}$, 67.5% higher than that of its non-hole counterpart Co_9S_8/G, enabling Co_9S_8/HG with abundant active sites for better encapsule capability towards LiPSs. Overpotential measurement, Li^+ activation energy ($E_{a\text{-}Li^+}$), conductance (σ_{Li^+}), and Li^+ diffusion coefficient (D_{Li^+}) was investigated to demonstrate that the holey structured Co_9S_8/HG effectively enhanced Li^+ mobility

kinetics. Cells with Co_9S_8/HG membranes demonstrate lower overpotential at all testing C rates, reduced Li^+ activation energy ($E_{a\text{-}Li^+}$), higher conductance (σ_{Li^+}) and Li^+ diffusion coefficient (D_{Li^+}) than that of cells integrating with Co_9S_8/G/PP separators.

Tafel plot, and Li_2S precipitation measurement was carried out to access the enhanced LiPSs conversion kinetics. Co_9S_8/HG membrane materials exhibit lower Tafel slop for both of the conversions at 2.3V (S_8 converted to long-chain Li_2S_n) and at around 2.05 V (long-chain Li_2S_n reduced to Li_2S_2/Li_2S), indicating enhanced electrochemical kinetics for SRR. The comparison of the current signals collected from Li_2S potentiostatic precipitation process (1.8 V) suggests that rapid Li^+ diffusion on the surface of membrane materials accelerate the Li_2S deposition, indicating that efficient Li^+ transport effectively promote the rate-determine step for the SRR. Battery performance, such as galvanostatic charging/discharging, long-term cycling and rates measures was conducted in coin cells integrated with Co_9S_8/HG/PP and Co_9S_8/G/PP separators. Cells with Co_9S_8/HG/PP separators exhibit a smaller polarization of 0.09 V compared with 0.14 V of Co_9S_8/G calculated by the voltage difference between the charge and discharge plateaus. At the onset dip of the 2.1 V plateau, the Co_9S_8/HG cell demonstrates a higher potential compared to the Co_9S_8/G cell, indicating a significant catalytic promotion in the conversion of long-chain LiPSs to Li_2S_2/Li_2S. Similarly, the lower initial charging voltage of 2.21 V further indicates that Co_9S_8/HG facilitates the oxidation of solid Li_2S_2/Li_2S to soluble polysulfides. Moreover, the catalytic activity of Co_9S_8/HG toward the sulfur redox reaction can be quantified by the ratio of Q1/Q2, where Q1 corresponds to the capacity produced at the discharge

plateau at ~2.3 V, and Q2 represents the capacity delivered at the plateau at ~2.1 V. The ratio for cells with Co_9S_8/HG is 2.13, which is higher than the theoretical value of 2.0, while the ratio for Co_9S_8/G (1.83), and pristine PP separator (1.81) are lower. This decreased ratio suggests that high-order polysulfides formed during the first stage are not fully reduced to low-order polysulfides in the subsequent stage, suggesting a severe shuttle effect in cells with pristine PP or Co_9S_8/G/PP separators. The cells with Co_9S_8/HG interlayers exhibit higher Q1 of (395.2 mAh g^{-1}) than that of Co_9S_8/G (328.5 mAh g^{-1}) and pristine PP (302.5 mAh g^{-1}), demonstrating that holey-structured Co_9S_8/HG, acting as an additional current collector, enhanced the utilization of sulfur cathode.

The cell with the Co_9S_8/HG/PP membrane also demonstrates superior discharge capacity at various current densities from 0.1 C to 2 C, which are 1182.4, 1056.1, 912.4, 696.5, and 538.1 mAh g^{-1}. Upon switching back to 0.2 C, a capacity of 792.1 mAh g^{-1} can be still recovered, indicating excellent stability and high reversibility. For the same C-rates, the discharge capacities are 853.7, 754.5, 660.2, 250.7 and 185.3 mAh g^{-1} for cells with Co_9S_8/G interlayer. More interestingly, at current densities of 1 C and 2 C, the discharge capacity for the cell with Co_9S_8/G interlayer are 250.7, and 185.3 mAh g^{-1}, respectively, which are lower than that of cells with pristine PP separator (472.8, and 229.2 mAh g^{-1}), suggesting that at high C rates, Co_9S_8/G interlayer exhibits a greater hindrance to Li^+ transport, resulting in severe polarization. These observations highlighted a crucial point: focusing solely on LiPSs entrapment and catalysis, without adequate consideration of lithium-ion transport, falls short of achieving optimal battery

performance.

To evaluate the durability of the Co_9S_8/HG electrocatalyst in supporting Li-S chemistry, cycling performance was conducted at current densities of 0.2 C and 0.5 C. The Co_9S_8/HG interlayer imparted a high initial capacity of 1096.5 mAh g^{-1} at 0.5 C, retaining 791.2 mAh g^{-1} after 200 cycles with a decay rate of 0.09% per cycle. This performance notably surpassed that of cells with Co_9S_8/G interlayer, which delivered an initial capacity of 864.1 mAh g^{-1} and a decay rate of 0.16% per cycle. In addition, the cells with Co_9S_8/HG interlayer delivered outstanding long-term cycling performance, maintaining a specific capacity of 671 mAh g^{-1} with a low-capacity decay of 0.044% per cycle and a high average coulombic efficiency of 98.1% over 900 cycles.

The sluggish conversion from Li_2S_4 to solid Li_2S is the rate-limiting step in the discharge process. Incorporating functional catalysts as sulfur hosts is a widely adopted strategy to enhance the electrochemical kinetics of the sulfur redox reactions (SRR). While significant efforts have been made to accelerate LiPSs conversion, the influence of sulfur host structures on Li^+ transport and their subsequent impact on SRR kinetics remain underexplored. In this study, we synthesized porous Co_3S_4 with distinct nanostructures and employed it as a model electrocatalyst to investigate the role of Li^+ diffusion in decreasing polarization, promoting SRR kinetics and regulating Li_2S precipitation. Experimental results revealed that the porosity of Co_3S_4-T400 nanosheet is 13.6% with a uniformly distribution of pours, indicating that the catalyst of Co_3S_4-T400 impose less residence towards Li^+ transport compared with that of non-holey Co_3S_4-T200. Electrochemical active surface area (ECSA) measurements showed that

the electrochemical active surface area of Co_3S_4-T400 is 4 times larger than that of non-hole material Co_3S_4-T200, providing abundant active sites in Co_3S_4-T400 to better encapsule and catalyze LiPSs. Cells with Co_3S_4-T400 catalyst host demonstrate smaller Tafel slope, higher Li^+ diffusion coefficient (D_{Li^+}), and more uniformly Li_2S deposition, suggesting that the holey structured Co_3S_4-T400 effectively facilitate Li^+ transport for enhanced SRR kinetics and controlled Li_2S precipitation. The Li-S batteries with S/Co_3S_4-T400/C exhibited outstanding long-term cycling performance, maintaining a specific capacity of 657 mAh g^{-1} with a low-capacity decay rate of 0.051% per cycle and a high average coulombic efficiency of 98.5% over 1000 cycles. These results suggest that facilitating localized Li^+ diffusion through a porous structured catalyst is an effective strategy to accelerate SRR kinetics and regulate Li_2S precipitation, thereby improving the overall performance of Li–S battery.

1.6 References

1. Bashir, T.; Ismail, S. A.; Song, Y.; Irfan, R. M.; Yang, S.; Zhou, S.; Zhao, J.; Gao, L., A review of the energy storage aspects of chemical elements for lithium-ion based batteries. *Energy Materials* **2021,** *1* (2), N/A-N/A.

2. Jayaprabakar, J.; Kumar, J. A.; Parthipan, J.; Karthikeyan, A.; Anish, M.; Joy, N., Review on hybrid electro chemical energy storage techniques for electrical vehicles: Technical insights on design, performance, energy management, operating issues & challenges. *Journal of Energy Storage* **2023,** *72*, 108689.

3. Abhijith, P.; Jishnu, N.; Balakrishnan, N. T.; Das, A.; Ahn, J.-H.; MJ, J. F.; Raghavan, P., Electrochemical Energy: The State-of-the-Art Energy Technologies. In *Polymer Electrolytes for Energy Storage Devices*, CRC Press: 2021; pp 1-34.

4. Nykvist, B.; Nilsson, M., Rapidly falling costs of battery packs for electric vehicles. *Nature climate change* **2015,** *5* (4), 329-332.

5. Yang, X.; Luo, J.; Sun, X., Towards high-performance solid-state Li–S batteries: from fundamental understanding to engineering design. *Chemical Society Reviews* **2020,** *49* (7), 2140-2195.

6. Zhu, Z.; Jiang, T.; Ali, M.; Meng, Y.; Jin, Y.; Cui, Y.; Chen, W., Rechargeable batteries for grid scale energy storage. *Chemical Reviews* **2022,** *122* (22), 16610-16751.

7. Yun, S.; Park, S. H.; Yeon, J. S.; Park, J.; Jana, M.; Suk, J.; Park, H. S., Materials and device constructions for aqueous lithium–sulfur batteries. *Advanced Functional Materials* **2018,** *28* (38), 1707593.

8. Wygant, B. R.; Merrill, L. C.; Harrison, K. L.; Talin, A. A.; Ashby, D. S.; Lambert, T. N., The role of electrolyte composition in enabling Li metal-iron fluoride full-cell batteries. *Advanced Science* **2022,** *9* (12), 2105803.

9. Roy, J. J.; Rarotra, S.; Krikstolaityte, V.; Zhuoran, K. W.; Cindy, Y. D. I.; Tan, X. Y.; Carboni, M.; Meyer, D.; Yan, Q.; Srinivasan, M., Green recycling methods to treat lithium-ion batteries E-waste: a circular approach to sustainability. *Advanced Materials*

2022, *34* (25), 2103346.

10. Choi, J. U.; Voronina, N.; Sun, Y. K.; Myung, S. T., Recent progress and perspective of advanced high-energy Co-less Ni-rich cathodes for Li-ion batteries: yesterday, today, and tomorrow. *Advanced Energy Materials* **2020,** *10* (42), 2002027.

11. Lin, Z.; Liang, C., Lithium–sulfur batteries: from liquid to solid cells. *Journal of Materials Chemistry A* **2015,** *3* (3), 936-958.

12. Lau, J.; DeBlock, R. H.; Butts, D. M.; Ashby, D. S.; Choi, C. S.; Dunn, B. S., Sulfide solid electrolytes for lithium battery applications. *Advanced Energy Materials* **2018,** *8* (27), 1800933.

13. Yang, G.; Shi, S.; Yang, J.; Ma, Y., Insight into the role of Li 2 S 2 in Li–S batteries: a first-principles study. *Journal of Materials Chemistry A* **2015,** *3* (16), 8865-8869.

14. Tan, L.; Li, X.; Wang, Z.; Guo, H.; Wang, J., Lightweight reduced graphene oxide@ MoS2 interlayer as polysulfide barrier for high-performance lithium–sulfur batteries. *ACS applied materials & interfaces* **2018,** *10* (4), 3707-3713.

15. Wang, Y.; Huang, X.; Zhang, S.; Hou, Y., Sulfur hosts against the shuttle effect. *Small Methods* **2018,** *2* (6), 1700345.

16. Huang, Y.; Lin, L.; Zhang, C.; Liu, L.; Li, Y.; Qiao, Z.; Lin, J.; Wei, Q.; Wang, L.; Xie, Q., Recent advances and strategies toward polysulfides shuttle inhibition for high-performance Li–S batteries. *Advanced Science* **2022,** *9* (12), 2106004.

17. Su, D.; Zhou, D.; Wang, C.; Wang, G., Toward high performance lithium–sulfur batteries based on Li2S cathodes and beyond: status, challenges, and perspectives. *Advanced Functional Materials* **2018,** *28* (38), 1800154.

18. Zheng, J.; Gu, M.; Wang, C.; Zuo, P.; Koech, P. K.; Zhang, J.-G.; Liu, J.; Xiao, J., Controlled nucleation and growth process of Li2S2/Li2S in lithium-sulfur batteries. *Journal of the Electrochemical Society* **2013,** *160* (11), A1992.

19. Cistjakov, W.; Hoppe, J.; Jung, J.; Röder, F.; Kim, H. T.; Krewer, U., Insight into the Impact of Electrolyte on Passivation of Lithium–Sulfur Cathodes. *Advanced Materials Interfaces* **2024**, 2400632.

20. Zhang, X.; Wang, A.; Liu, X.; Luo, J., Dendrites in lithium metal anodes:

suppression, regulation, and elimination. *Accounts of chemical research* **2019,** *52* (11), 3223-3232.

21. Cao, J.; Zhang, D.; Zhang, X.; Sawangphruk, M.; Qin, J.; Liu, R., A universal and facile approach to suppress dendrite formation for a Zn and Li metal anode. *Journal of Materials Chemistry A* **2020,** *8* (18), 9331-9344.

22. Song, B.; Su, L.; Liu, X.; Gao, W.; Wang, T.; Ma, Y.; Zhong, Y.; Cheng, X. B.; Zhu, Z.; He, J., An examination and prospect of stabilizing Li metal anode in lithium–sulfur batteries: a review of latest progress. *Electron* **2023,** *1* (2), e13.

23. Zhao, H.; Deng, N.; Yan, J.; Kang, W.; Ju, J.; Ruan, Y.; Wang, X.; Zhuang, X.; Li, Q.; Cheng, B., A review on anode for lithium-sulfur batteries: Progress and prospects. *Chemical Engineering Journal* **2018,** *347*, 343-365.

24. Deng, R.; Wang, M.; Yu, H.; Luo, S.; Li, J.; Chu, F.; Liu, B.; Wu, F., Recent advances and applications toward emerging lithium–sulfur batteries: working principles and opportunities. *Energy & Environmental Materials* **2022,** *5* (3), 777-799.

25. Barchasz, C.; Molton, F.; Duboc, C.; Leprêtre, J.-C.; Patoux, S.; Alloin, F., Lithium/sulfur cell discharge mechanism: an original approach for intermediate species identification. *Analytical chemistry* **2012,** *84* (9), 3973-3980.

26. Nelson, J.; Misra, S.; Yang, Y.; Jackson, A.; Liu, Y.; Wang, H.; Dai, H.; Andrews, J. C.; Cui, Y.; Toney, M. F., In operando X-ray diffraction and transmission X-ray microscopy of lithium sulfur batteries. *Journal of the American Chemical Society* **2012,** *134* (14), 6337-6343.

27. Yan, J.; Liu, X.; Li, B., Capacity fade analysis of sulfur cathodes in lithium–sulfur batteries. *Advanced Science* **2016,** *3* (12), 1600101.

28. Waluś, S.; Barchasz, C.; Bouchet, R.; Martin, J.-F.; Leprêtre, J.-C.; Alloin, F., Non-woven carbon paper as current collector for Li-ion/Li2S system: Understanding of the first charge mechanism. *Electrochimica Acta* **2015,** *180*, 178-186.

29. Li, G.; Wang, S.; Zhang, Y.; Li, M.; Chen, Z.; Lu, J., Revisiting the role of polysulfides in lithium–sulfur batteries. *Advanced Materials* **2018,** *30* (22), 1705590.

30. Zhao, X.; Cheruvally, G.; Kim, C.; Cho, K.-K.; Ahn, H.-J.; Kim, K.-W.; Ahn, J.-H.,

Lithium/sulfur secondary batteries: a review. *Journal of Electrochemical Science and Technology* **2016,** *7* (2), 97-114.

31. Yi, Y.; Hai, F.; Guo, J.; Tian, X.; Zheng, S.; Wu, Z.; Wang, T.; Li, M., Progress and prospect of practical lithium-sulfur batteries based on solid-phase conversion. *Batteries* **2022,** *9* (1), 27.

32. Liu, J.; Zhou, Y.; Yan, T.; Gao, X. P., Perspectives of High-Performance Li–S Battery Electrolytes. *Advanced Functional Materials* **2024,** *34* (4), 2309625.

33. Zhou, J.; Sun, A., Progress in the advancement of atomically dispersed catalysts for enhanced performance lithium-sulfur batteries. *Chemical Engineering Journal* **2024**, 150719.

34. Zhang, K.; Zhao, Z.; Chen, H.; Pan, Y.; Niu, B.; Long, D.; Zhang, Y., A Review of Advances in Heterostructured Catalysts for Li–S Batteries: Structural Design and Mechanism Analysis. *Small* **2025,** *21* (2), 2409674.

35. Xu, H.; Jiang, Q.; Shu, Z.; Hui, K. S.; Wang, S.; Zheng, Y.; Liu, X.; Xie, H.; Ip, W. F.; Zha, C., Fundamentally manipulating the electronic structure of polar bifunctional catalysts for lithium-sulfur batteries: heterojunction design versus doping engineering. *Advanced Science* **2024,** *11* (20), 2307995.

36. Liu, R.; Wei, Z.; Peng, L.; Zhang, L.; Zohar, A.; Schoeppner, R.; Wang, P.; Wan, C.; Zhu, D.; Liu, H., Establishing reaction networks in the 16-electron sulfur reduction reaction. *Nature* **2024,** *626* (7997), 98-104.

37. Han, Z.; Gao, R.; Jia, Y.; Zhang, M.; Lao, Z.; Chen, B.; Zhang, Q.; Li, C.; Lv, W.; Zhou, G., Catalytic effect in Li-S batteries: From band theory to practical application. *Materials Today* **2022,** *57*, 84-120.

38. Lin, Y.; Ticey, J.; Oleshko, V.; Zhu, Y.; Zhao, X.; Wang, C.; Cumings, J.; Qi, Y., Carbon-nanotube-encapsulated-sulfur cathodes for lithium–sulfur batteries: integrated computational design and experimental validation. *Nano Letters* **2021,** *22* (1), 441-447.

39. Kang, J.; Tian, X.; Yan, C.; Wei, L.; Gao, L.; Ju, J.; Zhao, Y.; Deng, N.; Cheng, B.; Kang, W., Customized structure design and functional mechanism analysis of carbon spheres for advanced lithium–sulfur batteries. *Small* **2022,** *18* (8), 2104469.

40. Nojabaee, M.; Sievert, B.; Schwan, M.; Schettler, J.; Warth, F.; Wagner, N.; Milow, B.; Friedrich, K. A., Ultramicroporous carbon aerogels encapsulating sulfur as the cathode for lithium–sulfur batteries. *Journal of Materials Chemistry A* **2021,** *9* (10), 6508-6519.

41. Rehman, S.; Gu, X.; Khan, K.; Mahmood, N.; Yang, W.; Huang, X.; Guo, S.; Hou, Y., 3D vertically aligned and interconnected porous carbon nanosheets as sulfur immobilizers for high performance lithium-sulfur batteries. *Advanced Energy Materials* **2016,** *6* (12), 1502518.

42. Qi, C.; Li, Z.; Wang, G.; Yuan, H.; Chen, C.; Jin, J.; Wen, Z., Microregion Welding Strategy Prevents the Formation of Inactive Sulfur Species for High-Performance Li–S Battery. *Advanced Energy Materials* **2021,** *11* (39), 2102024.

43. Hu, Y.; Chen, W.; Lei, T.; Jiao, Y.; Huang, J.; Hu, A.; Gong, C.; Yan, C.; Wang, X.; Xiong, J., Strategies toward high-loading lithium–sulfur battery. *Advanced Energy Materials* **2020,** *10* (17), 2000082.

44. Li, Y.; Li, X.; Hao, Y.; Kakimov, A.; Li, D.; Sun, Q.; Kou, L.; Tian, Z.; Shao, L.; Zhang, C., β-FeOOH interlayer with abundant oxygen vacancy toward boosting catalytic effect for lithium sulfur batteries. *Frontiers in Chemistry* **2020,** *8*, 309.

45. Wei, N.; Cai, J.; Wang, R.; Wang, M.; Lv, W.; Ci, H.; Sun, J.; Liu, Z., Elevated polysulfide regulation by an ultralight all-CVD-built ReS2@ N-Doped graphene heterostructure interlayer for lithium–sulfur batteries. *Nano Energy* **2019,** *66*, 104190.

46. Wang, F.; Qian, J.; Li, Y.; Yu, K.; Li, L.; Wu, F.; Chen, R., Co9S8 nanorods as an electrocatalyst to enhance polysulfide conversion and alleviate passivation in Li–S batteries under lean electrolyte conditions. *ACS applied materials & interfaces* **2020,** *12* (19), 21701-21708.

47. Pei, F.; Lin, L.; Fu, A.; Mo, S.; Ou, D.; Fang, X.; Zheng, N., A two-dimensional porous carbon-modified separator for high-energy-density Li-S batteries. *Joule* **2018,** *2* (2), 323-336.

48. Zeng, G.; Liu, Y.; Chen, D.; Zhen, C.; Han, Y.; He, W., Natural lepidolite enables fast polysulfide redox for high-rate lithium sulfur batteries. *Advanced Energy Materials*

2021, *11* (44), 2102058.

49. Feng, T.; Zhao, T.; Zhang, N.; Duan, Y.; Li, L.; Wu, F.; Chen, R., 2D amorphous Mo-doped CoB for bidirectional sulfur catalysis in lithium sulfur batteries. *Advanced Functional Materials* **2022,** *32* (30), 2202766.

50. Dong, Y.; Cai, D.; Li, T.; Yang, S.; Zhou, X.; Ge, Y.; Tang, H.; Nie, H.; Yang, Z., Sulfur reduction catalyst design inspired by elemental periodic expansion concept for lithium–sulfur batteries. *ACS nano* **2022,** *16* (4), 6414-6425.

51. Zhou, J.; Wu, T.; Pan, Y.; Zhu, J.; Chen, X.; Peng, C.; Shu, C.; Kong, L.; Tang, W.; Chou, S. L., Packing sulfur species by phosphorene-derived catalytic interface for electrolyte-lean lithium–sulfur batteries. *Advanced Functional Materials* **2022,** *32* (4), 2106966.

52. Qiu, S.; Liang, X.; Niu, S.; Chen, Q.; Wang, G.; Chen, M., Quantitative defect regulation of heterostructures for sulfur catalysis toward fast and long lifespan lithium-sulfur batteries. *Nano Research* **2022,** *15* (9), 7925-7932.

53. Lu, K.; Liu, Y.; Chen, J.; Zhang, Z.; Cheng, Y., Redox catalytic and quasi-solid sulfur conversion for high-capacity lean lithium sulfur batteries. *ACS nano* **2019,** *13* (12), 14540-14548.

54. Liang, J.; Sun, Q.; Zhao, Y.; Sun, Y.; Wang, C.; Li, W.; Li, M.; Wang, D.; Li, X.; Liu, Y., Stabilization of all-solid-state Li–S batteries with a polymer–ceramic sandwich electrolyte by atomic layer deposition. *Journal of Materials Chemistry A* **2018,** *6* (46), 23712-23719.

55. Tao, X.; Liu, Y.; Liu, W.; Zhou, G.; Zhao, J.; Lin, D.; Zu, C.; Sheng, O.; Zhang, W.; Lee, H.-W., Solid-state lithium–sulfur batteries operated at 37 C with composites of nanostructured Li7La3Zr2O12/carbon foam and polymer. *Nano letters* **2017,** *17* (5), 2967-2972.

56. Gao, X.; Zheng, X.; Tsao, Y.; Zhang, P.; Xiao, X.; Ye, Y.; Li, J.; Yang, Y.; Xu, R.; Bao, Z., All-solid-state lithium–sulfur batteries enhanced by redox mediators. *Journal of the American Chemical Society* **2021,** *143* (43), 18188-18195.

57. Elia, J.; Ungal, G.; Kao, C.; Ambrosini, A.; De Jesus-Rosario, N.; Larsen, L.;

Chiavacci, R.; Wang, T.; Kurian, C.; Titchen, K., Fasoracetam in adolescents with ADHD and glutamatergic gene network variants disrupting mGluR neurotransmitter signaling. *Nature communications* **2018,** *9* (1), 4.

58. Wang, Y.; Meng, Y.; Zhang, Z.; Guo, Y.; Xiao, D., Trifunctional electrolyte additive hexadecyltrioctylammonium iodide for lithium–sulfur batteries with extended cycle life. *ACS Applied Materials & Interfaces* **2021,** *13* (14), 16545-16557.

59. Wu, H.-L.; Shin, M.; Liu, Y.-M.; See, K. A.; Gewirth, A. A., Thiol-based electrolyte additives for high-performance lithium-sulfur batteries. *Nano Energy* **2017,** *32*, 50-58.

60. Sun, J.; Zhang, K.; Fu, Y.; Guo, W., Benzoselenol as an organic electrolyte additive in Li-S battery. *Nano Research* **2023,** *16* (3), 3814-3822.

61. Zhang, Q.; Li, F.; Huang, J. Q.; Li, H., Lithium–Sulfur Batteries: Co-Existence of Challenges and Opportunities. *Advanced Functional Materials* **2018,** *28* (38), 1804589.

62. Shen, Z.; Zhang, W.; Mao, S.; Li, S.; Wang, X.; Lu, Y., Tailored electrolytes enabling practical lithium–sulfur full batteries via interfacial protection. *ACS Energy Letters* **2021,** *6* (8), 2673-2681.

63. Ye, Y.; Wang, L.; Guan, L.; Wu, F.; Qian, J.; Zhao, T.; Zhang, X.; Xing, Y.; Shi, J.; Li, L., A modularly-assembled interlayer to entrap polysulfides and protect lithium metal anode for high areal capacity lithium–sulfur batteries. *Energy Storage Materials* **2017,** *9*, 126-133.

64. Wang, W.; Yue, X.; Meng, J.; Wang, J.; Wang, X.; Chen, H.; Shi, D.; Fu, J.; Zhou, Y.; Chen, J., Lithium phosphorus oxynitride as an efficient protective layer on lithium metal anodes for advanced lithium-sulfur batteries. *Energy storage materials* **2019,** *18*, 414-422.

65. Ren, Y.; Zeng, L.; Jiang, H.; Ruan, W.; Chen, Q.; Zhao, T., Rational design of spontaneous reactions for protecting porous lithium electrodes in lithium–sulfur batteries. *Nature Communications* **2019,** *10* (1), 3249.

66. Yan, C.; Zhang, X.-Q.; Huang, J.-Q.; Liu, Q.; Zhang, Q., Lithium-anode protection in lithium–sulfur batteries. *Trends in Chemistry* **2019,** *1* (7), 693-704.

67. Ji, X.; Lee, K. T.; Nazar, L. F., A highly ordered nanostructured carbon–sulphur

cathode for lithium–sulphur batteries. *Nature materials* **2009,** *8* (6), 500-506.

68. Ren, W.; Ma, W.; Zhang, S.; Tang, B., Nitrogen-doped carbon fiber foam enabled sulfur vapor deposited cathode for high performance lithium sulfur batteries. *Chemical Engineering Journal* **2018,** *341*, 441-449.

69. Mi, K.; Jiang, Y.; Feng, J.; Qian, Y.; Xiong, S., Hierarchical carbon nanotubes with a thick microporous wall and inner channel as efficient scaffolds for lithium–sulfur batteries. *Advanced Functional Materials* **2016,** *26* (10), 1571-1579.

70. Guo, J.; Xu, Y.; Wang, C., Sulfur-impregnated disordered carbon nanotubes cathode for lithium–sulfur batteries. *Nano letters* **2011,** *11* (10), 4288-4294.

71. Jin, F.; Xiao, S.; Lu, L.; Wang, Y., Efficient activation of high-loading sulfur by small CNTs confined inside a large CNT for high-capacity and high-rate lithium–sulfur batteries. *Nano letters* **2016,** *16* (1), 440-447.

72. Li, J.; Chen, C.; Chen, Y.; Li, Z.; Xie, W.; Zhang, X.; Shao, M.; Wei, M., Polysulfide confinement and highly efficient conversion on hierarchical mesoporous carbon nanosheets for Li–S batteries. *Advanced Energy Materials* **2019,** *9* (42), 1901935.

73. Oh, C.; Yoon, N.; Choi, J.; Choi, Y.; Ahn, S.; Lee, J. K., Enhanced Li–S battery performance based on solution-impregnation-assisted sulfur/mesoporous carbon cathodes and a carbon-coated separator. *Journal of Materials Chemistry A* **2017,** *5* (12), 5750-5760.

74. Balach, J.; Jaumann, T.; Klose, M.; Oswald, S.; Eckert, J. r.; Giebeler, L., Mesoporous carbon interlayers with tailored pore volume as polysulfide reservoir for high-energy lithium–sulfur batteries. *the Journal of Physical Chemistry C* **2015,** *119* (9), 4580-4587.

75. Li, Z.; Jiang, Y.; Yuan, L.; Yi, Z.; Wu, C.; Liu, Y.; Strasser, P.; Huang, Y., A highly ordered meso@ microporous carbon-supported sulfur@ smaller sulfur core–shell structured cathode for Li–S batteries. *ACS nano* **2014,** *8* (9), 9295-9303.

76. Deng, D. R.; Xue, F.; Bai, C.-D.; Lei, J.; Yuan, R.; Zheng, M. S.; Dong, Q. F., Enhanced adsorptions to polysulfides on graphene-supported BN nanosheets with

excellent Li–S battery performance in a wide temperature range. *ACS nano* **2018,** *12* (11), 11120-11129.

77. Zhang, C.; Lv, W.; Zhang, W.; Zheng, X.; Wu, M. B.; Wei, W.; Tao, Y.; Li, Z.; Yang, Q. H., Reduction of Graphene Oxide by Hydrogen Sulfide: A Promising Strategy for Pollutant Control and as an Electrode for Li-S Batteries. *Advanced Energy Materials* **2014,** *4* (7).

78. Tian, D.; Song, X.; Wang, M.; Wu, X.; Qiu, Y.; Guan, B.; Xu, X.; Fan, L.; Zhang, N.; Sun, K., MoN supported on graphene as a bifunctional interlayer for advanced Li-S batteries. *Advanced Energy Materials* **2019,** *9* (46), 1901940.

79. Li, H.; Tao, Y.; Zhang, C.; Liu, D.; Luo, J.; Fan, W.; Xu, Y.; Li, Y.; You, C.; Pan, Z. Z., Dense graphene monolith for high volumetric energy density Li–S batteries. *Advanced Energy Materials* **2018,** *8* (18), 1703438.

80. Tan, G.; Xu, R.; Xing, Z.; Yuan, Y.; Lu, J.; Wen, J.; Liu, C.; Ma, L.; Zhan, C.; Liu, Q., Burning lithium in CS2 for high-performing compact Li2S–graphene nanocapsules for Li–S batteries. *Nature Energy* **2017,** *2* (7), 1-10.

81. Li, X.; Guan, Q.; Zhuang, Z.; Zhang, Y.; Lin, Y.; Wang, J.; Shen, C.; Lin, H.; Wang, Y.; Zhan, L., Ordered mesoporous carbon grafted MXene catalytic heterostructure as Li-ion kinetic pump toward high-efficient sulfur/sulfide conversions for Li–S battery. *ACS nano* **2023,** *17* (2), 1653-1662.

82. Tang, H.; Li, W.; Pan, L.; Tu, K.; Du, F.; Qiu, T.; Yang, J.; Cullen, C. P.; McEvoy, N.; Zhang, C., A robust, freestanding MXene-sulfur conductive paper for long-lifetime Li–S batteries. *Advanced Functional Materials* **2019,** *29* (30), 1901907.

83. Zhao, Q.; Zhu, Q.; Liu, Y.; Xu, B., Status and prospects of MXene-based lithium–sulfur batteries. *Advanced Functional Materials* **2021,** *31* (21), 2100457.

84. Dong, Y.; Zheng, S.; Qin, J.; Zhao, X.; Shi, H.; Wang, X.; Chen, J.; Wu, Z.-S., All-MXene-based integrated electrode constructed by Ti3C2 nanoribbon framework host and nanosheet interlayer for high-energy-density Li–S batteries. *ACS nano* **2018,** *12* (3), 2381-2388.

85. Jiang, G.; Zheng, N.; Chen, X.; Ding, G.; Li, Y.; Sun, F.; Li, Y., In-situ decoration

of MOF-derived carbon on nitrogen-doped ultrathin MXene nanosheets to multifunctionalize separators for stable Li-S batteries. *Chemical Engineering Journal* **2019,** *373*, 1309-1318.

86. He, Y.; Chang, Z.; Wu, S.; Qiao, Y.; Bai, S.; Jiang, K.; He, P.; Zhou, H., Simultaneously inhibiting lithium dendrites growth and polysulfides shuttle by a flexible MOF-based membrane in Li–S batteries. *Advanced Energy Materials* **2018,** *8* (34), 1802130.

87. Song, C.-L.; Li, G.-H.; Yang, Y.; Hong, X.-J.; Huang, S.; Zheng, Q.-F.; Si, L.-P.; Zhang, M.; Cai, Y.-P., 3D catalytic MOF-based nanocomposite as separator coatings for high-performance Li-S battery. *Chemical Engineering Journal* **2020,** *381*, 122701.

88. Li, W.; Qian, J.; Zhao, T.; Ye, Y.; Xing, Y.; Huang, Y.; Wei, L.; Zhang, N.; Chen, N.; Li, L., Boosting high-rate Li–S batteries by an MOF-derived catalytic electrode with a layer-by-layer structure. *Advanced Science* **2019,** *6* (16), 1802362.

89. Tian, H.; Liang, J.; Liu, J., Nanoengineering carbon spheres as nanoreactors for sustainable energy applications. *Advanced Materials* **2019,** *31* (50), 1903886.

90. Bandosz, T. J.; Ren, T.-Z., Porous carbon modified with sulfur in energy related applications. *Carbon* **2017,** *118*, 561-577.

91. Sun, Q.; He, B.; Zhang, X.-Q.; Lu, A.-H., Engineering of hollow core–shell interlinked carbon spheres for highly stable lithium–sulfur batteries. *ACS nano* **2015,** *9* (8), 8504-8513.

92. Liu, S.; Zhao, T.; Tan, X.; Guo, L.; Wu, J.; Kang, X.; Wang, H.; Sun, L.; Chu, W., 3D pomegranate-like structures of porous carbon microspheres self-assembled by hollow thin-walled highly-graphitized nanoballs as sulfur immobilizers for Li–S batteries. *Nano Energy* **2019,** *63*, 103894.

93. Wang, Q.; Yang, M.; Wang, Z. B.; Li, C.; Gu, D. M., Functional Differentiation of Three Pores for Effective Sulfur Confinement in Li–S Battery. *Small* **2018,** *14* (11), 1703279.

94. Zhao, Z.; Wang, S.; Liang, R.; Li, Z.; Shi, Z.; Chen, G., Graphene-wrapped chromium-MOF (MIL-101)/sulfur composite for performance improvement of high-rate

rechargeable Li–S batteries. *Journal of materials chemistry A* **2014,** *2* (33), 13509-13512.

95. Su, Y.-S.; Manthiram, A., Lithium–sulphur batteries with a microporous carbon paper as a bifunctional interlayer. *Nature communications* **2012,** *3* (1), 1166.

96. Chung, S.-H.; Manthiram, A., High-performance Li–S batteries with an ultra-lightweight MWCNT-coated separator. *The journal of physical chemistry letters* **2014,** *5* (11), 1978-1983.

97. Manthiram, A.; Yu, X.; Wang, S., Lithium battery chemistries enabled by solid-state electrolytes. *Nature Reviews Materials* **2017,** *2* (4), 1-16.

98. Lv, W.; Li, Z.; Deng, Y.; Yang, Q.-H.; Kang, F., Graphene-based materials for electrochemical energy storage devices: opportunities and challenges. *Energy Storage Materials* **2016,** *2*, 107-138.

99. Hou, T. Z.; Chen, X.; Peng, H. J.; Huang, J. Q.; Li, B. Q.; Zhang, Q.; Li, B., Design principles for heteroatom-doped nanocarbon to achieve strong anchoring of polysulfides for lithium–sulfur batteries. *Small* **2016,** *12* (24), 3283-3291.

100. Wang, Z.; Dong, Y.; Li, H.; Zhao, Z.; Bin Wu, H.; Hao, C.; Liu, S.; Qiu, J.; Lou, X. W., Enhancing lithium–sulphur battery performance by strongly binding the discharge products on amino-functionalized reduced graphene oxide. *Nature communications* **2014,** *5* (1), 5002.

101. Zhang, M.; Chen, W.; Xue, L.; Jiao, Y.; Lei, T.; Chu, J.; Huang, J.; Gong, C.; Yan, C.; Yan, Y., Adsorption-catalysis design in the lithium-sulfur battery. *Advanced Energy Materials* **2020,** *10* (2), 1903008.

102. Cui, Y.; Zhang, Q.; Wu, J.; Liang, X.; Baker, A. P.; Qu, D.; Zhang, H.; Zhang, H.; Zhang, X., Developing porous carbon with dihydrogen phosphate groups as sulfur host for high performance lithium sulfur batteries. *Journal of Power Sources* **2018,** *378*, 40-47.

103. He, Q.; Xiao, W.; Wu, M.; Zhao, Y., First-Principles Calculations for Lithium-Sulfur Batteries. In *Computational Design of Battery Materials*, Springer: 2024; pp 211-240.

104. You, D.; Yang, W.; Liang, Y.; Yang, C.; Yu, Y.; Zhu, Z.; Li, X.; Zhang, Y.; Zhang, Y., Regulation of Li2S Deposition and Dissolution to Achieve an Efficient Bidirectional Lithium–Sulfur Battery. *Advanced Functional Materials*, 2421900.

105. Jin, Z.; Lin, T.; Jia, H.; Liu, B.; Zhang, Q.; Li, L.; Zhang, L.; Su, Z.-m.; Wang, C., Expediting the conversion of Li2S2 to Li2S enables high-performance Li–S batteries. *ACS nano* **2021,** *15* (4), 7318-7327.

106. Wu, Z.; Liu, M.; He, W.; Guo, T.; Tong, W.; Kan, E.; Ouyang, X.; Qiao, F.; Wang, J.; Sun, X., Unveiling the autocatalytic growth of Li2S crystals at the solid-liquid interface in lithium-sulfur batteries. *Nature Communications* **2024,** *15* (1), 9535.

107. Cheng, K.; Huang, X.; Li, Y.; Zhao, J.; Sun, L.; Xu, Y.; Cao, Z.; Chen, Y., Atom-Level 2D Catalysts Accelerating Deposition/Dissolution Kinetics in Lithium–Sulfur Batteries. *Advanced Functional Materials* **2025,** *35* (1), 2410742.

108. Liu, M.; Wu, Z.; Liu, S.; Guo, T.; Chen, P.; Cao, X.; Pan, S.; Zhou, T.; Pompizii, L.; Najafov, M., Accelerated Reversible Conversion of Li2S2 to Li2S by Spidroin Regulated Li+ Flux for High-performance Li-Sulfur Batteries. *Angewandte Chemie International Edition* **2025,** *64* (2), e202417624.

109. Yu, M.; Zhou, S.; Wang, Z.; Wang, Y.; Zhang, N.; Wang, S.; Zhao, J.; Qiu, J., Accelerating polysulfide redox conversion on bifunctional electrocatalytic electrode for stable Li-S batteries. *Energy Storage Materials* **2019,** *20*, 98-107.

110. Deng, S.; Guo, T.; Heier, J.; Zhang, C., Unraveling Polysulfide's Adsorption and Electrocatalytic Conversion on Metal Oxides for Li-S Batteries. *Advanced Science* **2023,** *10* (5), 2204930.

111. Mahankali, K.; Gottumukkala, S. V.; Masurkar, N.; Thangavel, N. K.; Jayan, R.; Sawas, A.; Nagarajan, S.; Islam, M. M.; Arava, L. M. R., Unveiling the electrocatalytic activity of 1T′-MoSe2 on lithium-polysulfide conversion reactions. *ACS Applied Materials & Interfaces* **2022,** *14* (21), 24486-24496.

112. Tao, X.; Yang, Z.; Yan, R.; Cheng, M.; Ma, T.; Cao, S.; Bai, M.; Ran, F.; Cheng, C.; Yang, W., Engineering MOFs-Derived Nanoarchitectures with Efficient Polysulfides Catalytic Sites for Advanced Li–S Batteries. *Advanced Materials*

Technologies **2023,** *8* (2), 2200238.

113. Zhang, Q.; Wang, Y.; Seh, Z. W.; Fu, Z.; Zhang, R.; Cui, Y., Understanding the anchoring effect of two-dimensional layered materials for lithium–sulfur batteries. *Nano letters* **2015,** *15* (6), 3780-3786.

114. Medford, A. J.; Vojvodic, A.; Hummelshøj, J. S.; Voss, J.; Abild-Pedersen, F.; Studt, F.; Bligaard, T.; Nilsson, A.; Nørskov, J. K., From the Sabatier principle to a predictive theory of transition-metal heterogeneous catalysis. *Journal of Catalysis* **2015,** *328*, 36-42.

115. Toulhoat, H.; Raybaud, P.; Kasztelan, S.; Kresse, G.; Hafner, J., Transition metals to sulfur binding energies relationship to catalytic activities in HDS: back to Sabatier with first principle calculations. *Catalysis Today* **1999,** *50* (3-4), 629-636.

116. Al Salem, H.; Babu, G.; V. Rao, C.; Arava, L. M. R., Electrocatalytic polysulfide traps for controlling redox shuttle process of Li–S batteries. *Journal of the American Chemical Society* **2015,** *137* (36), 11542-11545.

117. Liu, Y.; Kou, W.; Li, X.; Huang, C.; Shui, R.; He, G., Constructing patch-Ni-shelled Pt@ Ni nanoparticles within confined nanoreactors for catalytic oxidation of insoluble polysulfides in Li-S batteries. *Small* **2019,** *15* (34), 1902431.

118. Lu, Y.-Q.; Wu, Y.-J.; Sheng, T.; Peng, X.-X.; Gao, Z.-G.; Zhang, S.-J.; Deng, L.; Nie, R.; Świątowska, J.; Li, J.-T., Novel sulfur host composed of cobalt and porous graphitic carbon derived from MOFs for the high-performance Li–S battery. *ACS applied materials & interfaces* **2018,** *10* (16), 13499-13508.

119. Adi, A.; Taniguchi, I., Porous-crystalline C/Fe3O4 microspheres with highly accessible adsorptive/catalytic and conductive interfaces to manipulate polysulfide shuttling in Li-S batteries. *Electrochimica Acta* **2022,** *435*, 141385.

120. Xu, Z.; Wang, Z.; Wang, M.; Cui, H.; Liu, Y.; Wei, H.; Li, J., Large-scale synthesis of Fe9S10/Fe3O4@ C heterostructure as integrated trapping-catalyzing interlayer for highly efficient lithium-sulfur batteries. *Chemical Engineering Journal* **2021,** *422*, 130049.

121. Jiao, L.; Zhang, C.; Geng, C.; Wu, S.; Li, H.; Lv, W.; Tao, Y.; Chen, Z.;

Zhou, G.; Li, J., Capture and catalytic conversion of polysulfides by in situ built TiO2-MXene heterostructures for lithium–sulfur batteries. *Advanced Energy Materials* **2019,** *9* (19), 1900219.

122. Ma, L.; Zhang, Y.; Zhang, S.; Wang, L.; Zhang, C.; Chen, Y.; Wu, Q.; Chen, L.; Zhou, L.; Wei, W., Integrating energy band alignment and oxygen vacancies engineering of TiO2 anatase/rutile homojunction for kinetics-enhanced Li–S batteries. *Advanced Functional Materials* **2023,** *33* (48), 2305788.

123. Jiang, F.; Zeng, L.; Li, S.; Liu, G.; Wang, S.; Gong, J., Propane Dehydrogenation over Pt/TiO2–Al2O3 Catalysts. *ACS catalysis* **2015,** *5* (1), 438-447.

124. Liu, F.-J.; Luo, W.-L.; Zhang, Z.; Yu, J.; Cai, J.-X.; Yang, Z.-Y., Cation-doped V2O5 microsphere as a bidirectional catalyst to activate sulfur redox reactions for lithium-sulfur batteries. *Chemical Engineering Journal* **2023,** *456*, 140948.

125. Gao, X.-T.; Zhu, X.-D.; Gu, L.-L.; Wang, C.; Sun, K.-N.; Hou, Y.-L., Efficient polysulfides anchoring for Li-S batteries: combined physical adsorption and chemical conversion in V2O5 hollow spheres wrapped in nitrogen-doped graphene network. *Chemical Engineering Journal* **2019,** *378*, 122189.

126. Chen, K.; Zhang, G.; Xiao, L.; Li, P.; Li, W.; Xu, Q.; Xu, J., Polyaniline Encapsulated Amorphous V2O5 Nanowire-Modified Multi-Functional Separators for Lithium–Sulfur Batteries. *Small Methods* **2021,** *5* (3), 2001056.

127. Li, J.; Hou, X.; Mao, Y.; Lai, C.; Yuan, X., Enhanced performance of aprotic electrolyte Li–O2 batteries with SnS2–SnO2/C heterostructure as efficient cathode catalyst. *Energy & Fuels* **2020,** *34* (11), 14995-15003.

128. Yao, W.; Xu, J.; Cao, Y.; Meng, Y.; Wu, Z.; Zhan, L.; Wang, Y.; Zhang, Y.; Manke, I.; Chen, N., Dynamic intercalation–conversion site supported ultrathin 2D mesoporous SnO2/SnSe2 hybrid as bifunctional polysulfide immobilizer and lithium regulator for lithium–sulfur chemistry. *ACS nano* **2022,** *16* (7), 10783-10797.

129. Wang, Y.; Zhang, R.; Chen, J.; Wu, H.; Lu, S.; Wang, K.; Li, H.; Harris, C. J.; Xi, K.; Kumar, R. V., Enhancing catalytic activity of titanium oxide in lithium–sulfur batteries by band engineering. *Advanced Energy Materials* **2019,** *9* (24), 1900953.

130. Tao, X.; Wang, J.; Liu, C.; Wang, H.; Yao, H.; Zheng, G.; Seh, Z. W.; Cai, Q.; Li, W.; Zhou, G., Balancing surface adsorption and diffusion of lithium-polysulfides on nonconductive oxides for lithium–sulfur battery design. *Nature communications* **2016,** *7* (1), 11203.

131. Pang, Q.; Kundu, D.; Cuisinier, M.; Nazar, L., Surface-enhanced redox chemistry of polysulphides on a metallic and polar host for lithium-sulphur batteries. *Nature communications* **2014,** *5* (1), 4759.

132. Liang, X.; Hart, C.; Pang, Q.; Garsuch, A.; Weiss, T.; Nazar, L. F., A highly efficient polysulfide mediator for lithium–sulfur batteries. *Nature communications* **2015,** *6* (1), 5682.

133. Liang, X.; Kwok, C. Y.; Lodi-Marzano, F.; Pang, Q.; Cuisinier, M.; Huang, H.; Hart, C. J.; Houtarde, D.; Kaup, K.; Sommer, H., Tuning transition metal oxide–sulfur interactions for long life lithium sulfur batteries: the “Goldilocks” principle. *Advanced Energy Materials* **2016,** *6* (6), 1501636.

134. Liang, Q.; Wang, S.; Yao, Y.; Dong, P.; Song, H., Transition metal compounds family for Li–S batteries: the DFT-guide for suppressing polysulfides shuttle. *Advanced Functional Materials* **2023,** *33* (32), 2300825.

135. Babu, G.; Masurkar, N.; Al Salem, H.; Arava, L. M. R., Transition metal dichalcogenide atomic layers for lithium polysulfides electrocatalysis. *Journal of the American Chemical Society* **2017,** *139* (1), 171-178.

136. Lin, H.; Yang, L.; Jiang, X.; Li, G.; Zhang, T.; Yao, Q.; Zheng, G. W.; Lee, J. Y., Electrocatalysis of polysulfide conversion by sulfur-deficient MoS 2 nanoflakes for lithium–sulfur batteries. *Energy & Environmental Science* **2017,** *10* (6), 1476-1486.

137. Zhou, G.; Tian, H.; Jin, Y.; Tao, X.; Liu, B.; Zhang, R.; Seh, Z. W.; Zhuo, D.; Liu, Y.; Sun, J., Catalytic oxidation of Li2S on the surface of metal sulfides for Li−S batteries. *Proceedings of the National Academy of Sciences* **2017,** *114* (5), 840-845.

138. Yao, W.; Zheng, W.; Xu, J.; Tian, C.; Han, K.; Sun, W.; Xiao, S., ZnS-SnS@ NC heterostructure as robust lithiophilicity and sulfiphilicity mediator toward high-rate and long-life lithium–sulfur batteries. *ACS nano* **2021,** *15* (4), 7114-7130.

139. Li, K.; Li, T.; Wang, Z.; Shi, K.; Sun, Y.; Li, J.; Ren, J.; Lu, A.; Li, X.; Liu, Q., Regional Electron Delocalization Regulation Internalizes the Reduced-Order-Transformation of Polysulfides. *Advanced Functional Materials* **2024,** *34* (51), 2410517.

140. Cheng, Z.; Pan, H.; Chen, J.; Meng, X.; Wang, R., Separator modified by cobalt-embedded carbon nanosheets enabling chemisorption and catalytic effects of polysulfides for high-energy-density lithium-sulfur batteries. *Advanced Energy Materials* **2019,** *9* (32), 1901609.

141. Li, W.; Hicks-Garner, J.; Wang, J.; Liu, J.; Gross, A. F.; Sherman, E.; Graetz, J.; Vajo, J. J.; Liu, P., V2O5 polysulfide anion barrier for long-lived Li–S batteries. *Chemistry of Materials* **2014,** *26* (11), 3403-3410.

142. Liu, M.; Li, Q.; Qin, X.; Liang, G.; Han, W.; Zhou, D.; He, Y. B.; Li, B.; Kang, F., Suppressing self-discharge and shuttle effect of lithium–sulfur batteries with V2O5-decorated carbon nanofiber interlayer. *Small* **2017,** *13* (12), 1602539.

143. Liu, B.; Gu, H.; Torres, J. F.; Yin, Z.; Tricoli, A., Balancing polysulfide containment and energy loss in lithium–sulfur batteries. *Energy & Environmental Science* **2024,** *17* (3), 1073-1082.

Chapter 2 Research on Balancing Energy loss and Polysulfide Confinement in Li–S batteries

2.1 Prologue

This chapter is derived from the journal article authored with Dr. Borui Liu, myself, Assoc. Prof. Juan F. Torres, Prof. Zongyou Yin and Prof. Antonio Tricoli, titled “Balancing polysulfide containment and energy loss in lithium-sulfur batteries” published in Energy & Environmental Science on 04 January 2024. It includes a literature review, experimental methods, material characterization and data analysis and a detailed discussion related to the subjects.

Dr. Borui Liu and myself share the co-first authorship to this work. Dr. Borui, one of the co-supervisors in my PhD supervisory panel, I and Prof. Antonio Tricoli jointly designed this project. I conducted all the experiment measurements, collected, analyzed and interpreted the data. Dr Borui Liu and myself wrote this paper. Dr. Borui Liu and Assoc. Prof. Juan F. Torres contributed to the simulation section. Prof. Zongyou Yin and Prof. Antonio Tricoli reviewed this paper.

2.2 Abstract

The integration of micro- and mesoporous membranes in lithium–sulfur (Li–S) batteries provides a promising approach to mitigating capacity losses caused by the shuttling of soluble polysulfide species. However, these membranes also impede lithium-ion

transport, which can reduce the cell's overall energy density. This study presents a detailed investigation on the energy loss in Li–S batteries, examining how the composition and pore size of various membrane candidates affect performance. The overpotential experiments revealed that commonly employed membranes, such as MoS_2 and graphene oxide, exhibit significantly higher overpotentials (over 350 mV at 0.5 C) compared to commercial PP separators, leading to a notable energy density loss (~80%) in Li–S cells. Through comparative modeling and characterization of both pristine and holey (mesoporous) graphene membranes, the study reveals key insights into the mechanisms driving overpotential accumulation, highlighting the critical role of membrane structure in lithium-ion permeability. These findings underscore the challenges but also open avenues for designing advanced membranes—such as holey graphene (HG) membranes—that achieve an optimal balance between non-metal species containment (e.g., polysulfides) and efficient metal-cation transport (e.g., lithium ions). The results not only address specific challenges in Li–S battery systems but also offer a framework for balancing non-metal species confinement with metal-ion transport across a range of emerging rechargeable battery systems, including metal–sulfur and metal–halogen batteries.

2.3 Background and Motivation of this research

Lithium–sulfur (Li–S) batteries are a promising next-generation battery technology, offering a high theoretical energy density of 2600 Wh kg^{-1}, along with the advantages of sulfur's abundance, low cost, and environmental benignity.[1, 2] However, the practical

application of Li–S batteries several issues pose significant challenges for, including the low electrical conductivity of sulfur (5×10^{-30} S cm^{-1}), a significant volume variation (ca. 80%) during charging-discharging processes, and sluggish kinetics of the sulfur redox reactions (SRR) at high C-rates.[3, 4] Amongst these challenges, the shuttling of soluble polysulfides (Li_2S_x, $4 < x \leq 8$) to the lithium anode is the most significant barrier to practical applications.[5]

Over the past decade, researchers have explored a multitude of approaches to mitigate the polysulfide shuttle effect in Li–S batteries including spatial confinement through core-shell[6] and hollow[7] structures, physisorption with materials like mesoporous carbon[8, 9] and metal-organic frameworks[10], chemisorption using metal compounds[11-13], and blocking methods involving functional micro/meso-porous membranes[14], film-like electrodes[15-20], and solid-state electrolytes[21]. Among these, membrane modification stands out due to its cost-effectiveness, ease of integration, and congruence with battery manufacturing processes (Figure 2-1). Though not directly involved in the sulfur redox reactions, the membrane in Li–S batteries play a crucial role in determining their performance. By governing cell kinetics, it has a pronounced impact on cycling stability, energy, and power density, as well as safety.

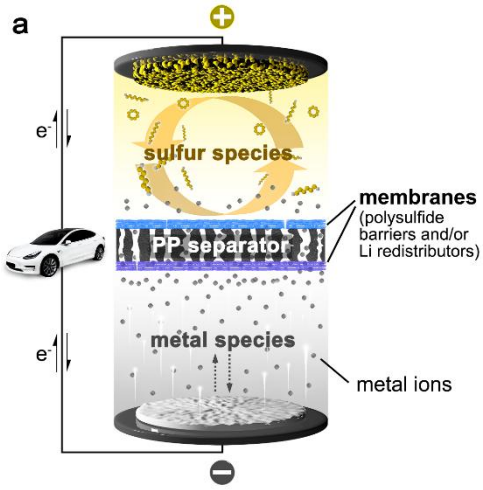

Figure 2-1. Schematic of Li–S batteries with a built-in polysulfide-barrier membrane

In this study, we investigate the impact of some commonly used membrane materials in the literature on the Li^+ transport in Li|Li symmetric and Li–S cells, focusing on the quantification of increments in overpotentials and reductions in energy density. Combined experimental and modeling investigations reveal that incorporation of polysulfide barrier materials, such as graphene and MoS_2, significantly increases the resistance to Li^+ transport during the charging and discharging cycles. This results in a substantial overpotential of over 350 mV at charging/discharging rates between 0.5 and 1 C. This is five times higher than the overpotential with commercial polypropylene (PP) separators and results in a loss of more than 80% of the Li–S cell energy density. GO membranes, instead, result in an even higher overpotential of more 3000 mV at 0.5 C and a loss of 100% of the cell capacity. These findings provide a first quantitative estimation of the energy cost over polysulfide species containment with a membrane-modified separator, providing guidelines for the design of practical Li–S battery systems.

2.4 Results and Discussion

2.4.1 Overpotential impact on Li–S system as a model

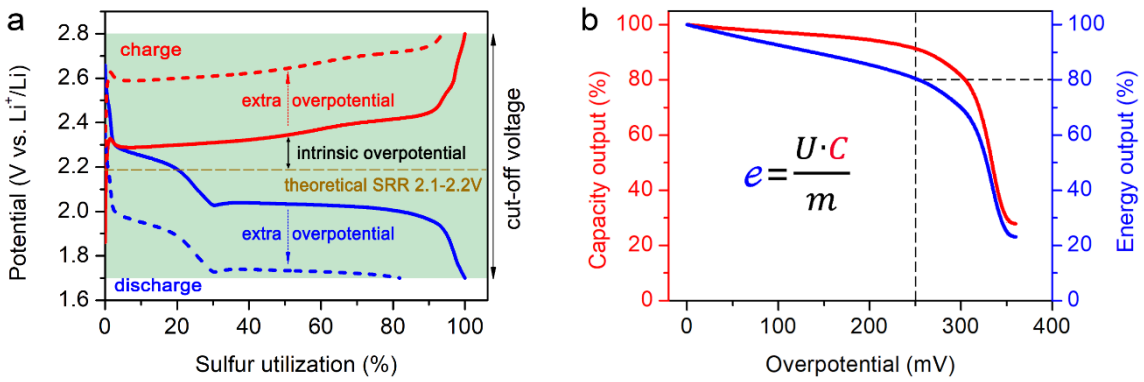

Figure 2-2. Correlation between overpotential and energy density loss in a model Li–S coin cell. (a) Conceptual illustration of the impact of overpotential, as induced by functional membranes, on the charging (red curve) and discharging (blue curve) plateaus of Li–S batteries. Green region: a typical cut-off voltage range of 1.7–2.8 V vs. Li/Li$^+$. The shift of charging/discharging plateaus indicated by the broken lines does not refer to a specific overpotential and is of qualitative nature. (b) Energy density as a function of overpotential, showing a significantly faster reduction when the overpotential exceeds 250 mV. Dashed line: a reduction of ~20% in energy density at an overpotential of 250 mV. In the equation, e is gravimetric energy density (J g^{-1}) of the cell, U is the approximate discharge plateau voltage (V) of the cell, C is the discharge capacity (Ah) of the cell, and m is the mass (g) of the active materials.

Figure 2-2 illustrates the relationship between overpotential and energy density loss in a model Li–S coin cell battery (see Experimental Methods). Figure 2-2a shows the charging and discharging plateaus of a Li–S cell during cycling. This indicates an upward shift for charging and downward shift for discharging, along with an increasing overpotential (the wide potential difference between the red and blue lines). These measurements are in line with the increase in overpotential deviating from the reversible SRR potential (2.1–2.2 V vs. Li/Li$^+$). As a result, the charging voltage increases, increasing the energy cost and reducing the capacity (C) and open circuit

voltage (U) of the cell, and the reduction in the energy density (e) of the Li–S cell is proportional to the product of U and C (Figure 2-2b). Furthermore, it is worth noting that the energy density (e) drops faster than the capacity (C), making it crucial to determine the overpotential induced by the membranes for developing practical high-energy Li–S batteries.

2.4.2 Morphological and electrochemical characterizations of membranes

The morphology and composition of the membranes are the key factors determining its electrochemical performance. To quantifying the underlying structural-functional correlations, here, we have performed a comparative analysis of five representative membrane structures composed of commonly used high-performance materials for polysulfide containment in Li–S batteries,[22] namely GO, rGO, cobalt hydroxide ($Co(OH)_2$), tin disulfide (SnS_2), and molybdenum disulfide (MoS_2).

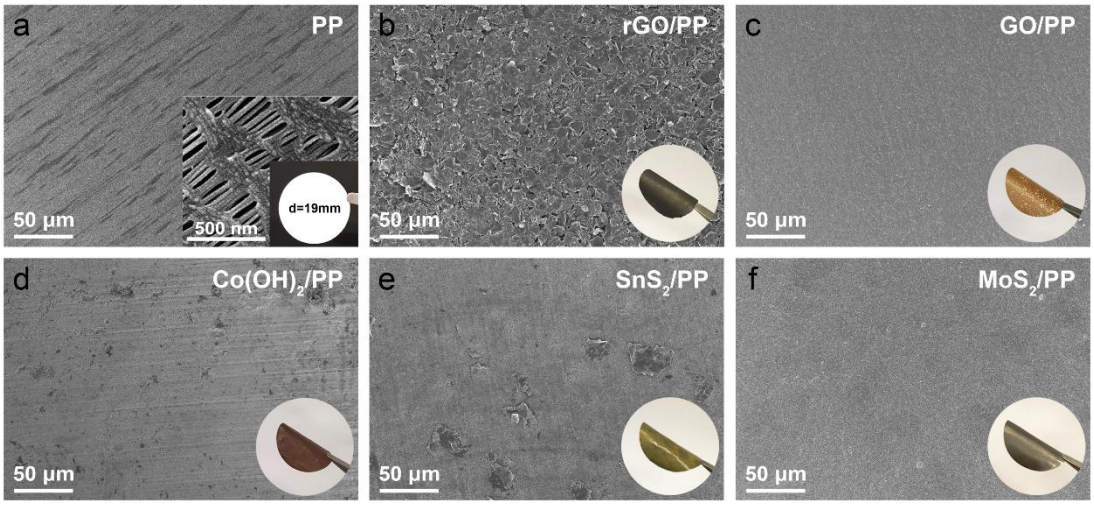

Figure 2-3. SEM characterization of membrane-modified separators, with a membrane material loading of ca. 0.18 mg cm^{-2}. Insets show corresponding photos.

The membranes were fabricated using ultrasonic dispersion of either in-house synthesized or purchased raw materials, followed by vacuum filtration on commercial PP separators to yield densely stacked structures. The membranes had a uniform single-sided loading of 0.18 mg cm^{-2}, optimized to achieve a uniform coverage of the commercial PP separator surface (Figure 2-3 and Figure S1-S5). The material loading of these membranes is in line with reported literature values (typically < 1.5 mg cm^{-2}).[23-32]

The commercial PP separator (Figure 2-3a) exhibits a flat white surface with non-uniformly distributed strip-like pore arrays measuring approximately 100 nm in length. This morphology is instrumental in accounting for the shuttle movement of long-chain polysulfides (~0.8 nm).[10, 33] By contrast, the micro/meso-porous coating layer of rGO, GO, $Co(OH)_2$, SnS_2, and MoS_2 (Figure 2-3b–f), applied over the commercial PP separator, is composed of compactly stacked membrane lamellae without any noticeable uncovered area on a large scale. Photos (Figure 2-3b–f insets) show these membranes revealing their intrinsic material colors. The compositions of the membranes were further confirmed by X-ray diffractions (Figure S6). The thickness of the bare and membrane-modified separators (Figure S7) was measured using a thickness gauge, resulting in a membrane thickness in the range of 1.6–8.4 μm that is consistent with those obtained from the cross-sectional SEM images (Figure S8).

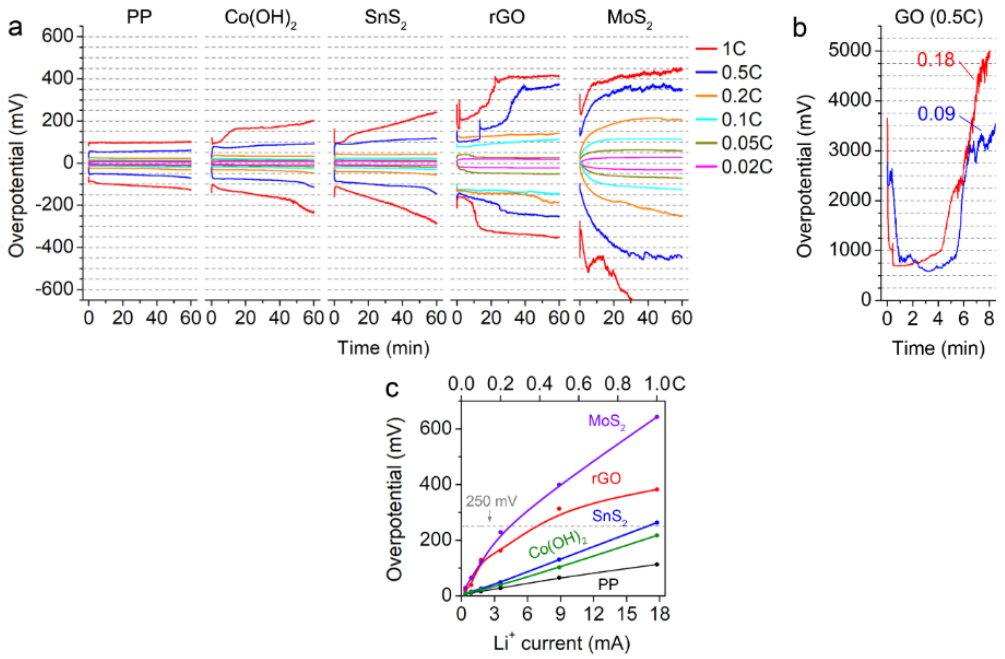

Figure 2-4. Overpotential measurements of PP separator and membrane-modified separators. (a) Overpotentials of Li|Li symmetric cells with built-in separators, consisting of a "Li|PP|membrane|PP|Li" structure, under various C-rates, calculated based on sulfur loadings of 6 mg cm^{-2} in Li–S cells. (b) Overpotentials of a Li|Li symmetric cell with a GO-modified separator with two different GO loadings (0.18 and 0.09 mg cm^{-2}) under 0.5C calculated based on sulfur loading of 6 mg cm^{-2} in Li–S cells. (c) Overpotentials of membrane-modified separators under various C-rates.

The induced overpotential for Li^+ transport through these membrane-modified separators was quantitatively analyzed and compared to that of a bare PP separator. Li|Li symmetric cells, consisting of a "Li|PP|membrane|PP|Li" structure, were utilized and cycled at various current densities, which are calculated based on the nominal C-rates of Li–S cells with an identical cathode sulfur loading of 6 mg cm^{-2}. It is worth noting that the overpotential of Li^+ transport must be low (e.g., < 250mV) to achieve a promising energy density in the full Li–S cell as the additional overpotential induced by the sluggish SRR reactions will further worsen the cell performance. Galvanostatic charging/discharging measurements were carried out at current densities corresponding to a charge/discharge rate from 0.02 C to 1 C for a duration of 60 min

(Figure 2-4). To prevent contact with the lithium electrodes and lithiation of the coating materials, the micro/meso-scale porous coating layer (i.e., the membrane) was sandwiched between two PP separators, while the control was made of two bare PP separators without the membrane. This facilitates comparison between the membrane-modified separator and the bare PP separator, enabling assessment of the micro/meso-porous membrane's effects on the Li^+ transport (detailed in the Experimental Methods).

Figure 2-4a, b shows that the commercial PP separator has the lowest overpotentials at all employed C-rates, whereas the separators modified with $Co(OH)_2$, SnS_2, rGO, MoS_2, and GO coatings resulted in gradually increasing overpotentials from the benchmark case with commercial PP separator. Notably, the GO-modified separators, which have a promising polysulfide blocking performance,[17, 34-36] exhibited an overpotential of 3000 mV in less than 8 min at a moderate rate of 0.5 C, with both a loading of 0.18 mg cm^{-2} (fully covering PP) and 0.09 mg cm^{-2} (partially covering PP) (Figure 2-4b). Such a high overpotential would stop the transport of lithium ions in a full Li–S cells, rendering them inoperable. We tentatively attribute this large overpotential to the functional groups on GO that promote the restacking of the GO lamellae, resulting in a highly compact and seamless film that presents a significant obstacle to the transport of lithium ions. We observed that decreasing the GO loading to ca. 0.09 mg cm^{-2} hardly covers the entire surface of the PP separator (SEM image not included), leaving perforations permeable to both lithium ions and polysulfides. Overpotential measurements (Figure 2-4c) also revealed that most of the membrane

materials, including SnS_2, rGO, and MoS_2, produced overpotentials of more than 250 mV at 1 C, resulting in a loss of over 20% of the energy density in the corresponding Li–S cell.

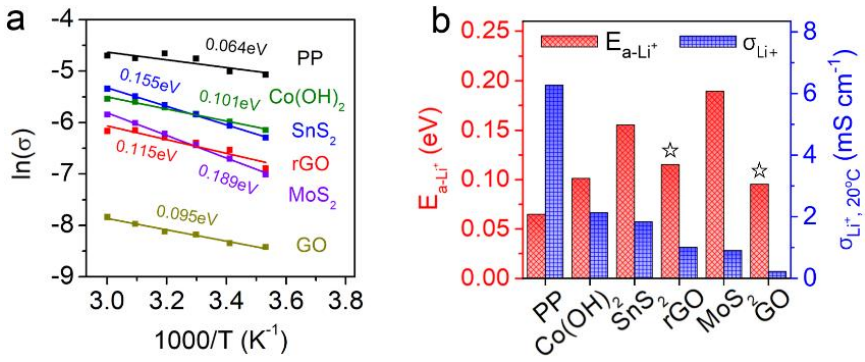

Figure 2-5. Li^+ conductance, Li^+ activation energy ($E_{a\text{-}Li^+}$) of different membrane-modified separators. (a) Arrhenius plots of Li^+ conductance of different membrane-modified separators. (b) Li^+ activation energy ($E_{a\text{-}Li^+}$) and Li^+ conductance at 20℃ (σ_{Li^+}) of different membrane-modified separators.

To investigate the underlying mechanisms inducing these significant overpotentials, detailed microscopic analysis was performed to examine the surface morphology of the membranes. The SEM images reveal that the rGO membrane morphology (Figure S1 and S8b) consists of large flakes (~10 μm), while the GO (Figure S2 and S8c) and MoS_2 membranes (Figure S5 and S8f) formed into dense films during the filtration and drying processes. These dense films act as physically impermeable barriers to lithium ions[37-40], thereby limiting lithium ions diffusion mainly through narrow gaps and cracks in the films. This results in a notable overpotential at high currents. In contrast, the commercial PP separator (Figure 2-3a, inset), $Co(OH)_2$ membrane (Figure S3), and SnS_2 membrane (Figure S4) exhibit a significant number of perforations that facilitate the passage of lithium ions. However, this feature also creates a conducive environment for polysulfide shuttling.

Moreover, the Li^+ activation energy ($E_{a\text{-}Li}{}^+$) and Li^+ conductance ($\sigma_{Li}{}^+$) (Figure 2-5) of the bare PP separator and membrane-modified separators were obtained from Nyquist plots by electrochemical impedance spectroscopy using stainless steel (SS)|SS symmetric cells, consisting of a "SS|PP|membrane|PP|SS" structure, (Figure S9, see Experimental Methods). The sequence of $\sigma_{Li}{}^+$ from high to low is as follows (Figure 2-5a): PP (0.394 S cm^{-1}), $Co(OH)_2$ (0.148 S cm^{-1}), SnS_2 (0.136 S cm^{-1}), rGO (0.086 S cm^{-1}), MoS_2 (0.072 S cm^{-1}), and GO (0.014 S cm^{-1}), which is consistent with the order of overpotential in Figure 2-4c. However, the order of $E_{a\text{-}Li}{}^+$ from low to high is only partially consistent with the order of $\sigma_{Li}{}^+$, as shown in Figure 2-5b, except for the rGO and GO membranes (labeled with asterisks). Previous studies have often used $E_{a\text{-}Li}{}^+$ as a criterion to evaluate the Li^+ permeability of separators.[20, 32, 41-43] However, our data suggest that $E_{a\text{-}Li}{}^+$ is unreliable when used to compare different separators. This is tentatively attributed to the hindered diffusion of lithium ions normal to the separator plane, caused by the presence of impermeable graphene nanosheets, which significantly restricts their mobility. Consequently, even under elevated temperatures of up to 60ºC, membranes exhibiting extremely high inhibitory effects (e.g., GO) on Li^+ transport are unlikely to yield substantial improvements. This hypothesis finds support in the plots of ln(σ) vs. 1000/T, showing flat lines with near-zero slopes in the extreme cases where the membrane either strongly obstructs (e.g., GO, Figure 2-4b, 2-5a) or allows nearly effortless passage of Li^+ (e.g., PP, Figure 2-5a), resulting in similarly low $E_{a\text{-}Li}{}^+$ values of 0.095 eV and 0.064 eV, respectively. However, the low $E_{a\text{-}Li}{}^+$ for the

GO-modified separator is an artifact of the Arrhenius model[20, 44-46] due to the near-zero Li^+ flux through the GO membrane in this temperature range (i.e., from 10 to 60°C).

2.4.3 Mechanism of membrane hindering Li^+ transport

To quantify the observed physical hindrance of the Li^+ transport by the above membrane materials, we synthesized two additional types of membranes using holey graphene (HG) nanosheets with varying hole densities (Figure 2-6), namely 030HG, and 050HG.

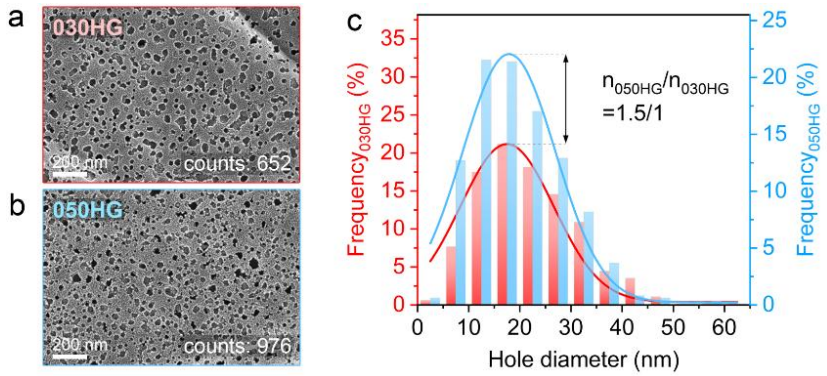

Figure 2-6. SEM images of HG nanosheets with varying hole densities. (a) 030HG and (b) 050HG. (c) Statistical analysis on the hole size (diameter) distribution for both 030HG and 050HG nanosheets.

The 030HG (Figure 2-6a) and 050HG nanosheets (Figure 2-6b) were synthesized based on a modified method from our previous publication.[10] In brief, metal oxide nanoparticles are employed to etch graphene nanosheets at elevated temperatures, resulting in the formation of holes in the rGO nanosheets. The synthesis process and the intermediate products, including the cobalt precursor on graphene nanosheets (Co-pre/G), cobalt nanoparticles on graphene nanosheets (CoNP/G), cobalt oxide-cobalt metal nanoparticles on graphene nanosheets (Co_3O_4-CoNP/G), and cobalt nanoparticles on holey graphene nanosheets (CoNP/HG) are confirmed by a set of

complementary analysis including XRD (Figure S10) and SEM (Figure S11–S14). Statistically (Figure 2-6c), the 030HG and 050HG membranes have a quite similar average hole radius of 9 nm, and a hole density of 656 and 438 holes μm^{-2}, respectively. This results in a hole area percentage of 18.6% and 11.1% on the 050HG and 030HG membranes, respectively.

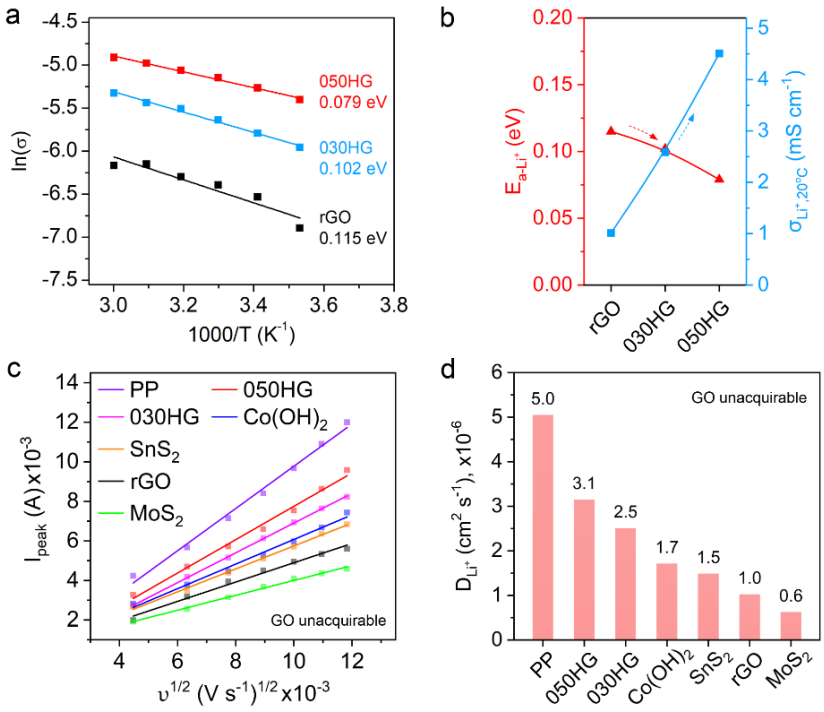

Figure 2-7. Li^+ diffusion through rGO/PP and HG/PP separators. (a) Arrhenius plots for 050HG/PP, 030HG/PP, and rGO/PP separators. (b) Comparison of $E_{a\text{-}Li^+}$ and σ_{Li^+}. (c) Peak currents, I_{peak}, as a function of the square root of scan rates, $\upsilon^{1/2}$, derived from LSV results of Li|SS cells, consisting of a "Li|PP|membrane|PP|SS" structure, with PP and membrane-modified separators. (d) Diffusion coefficient of lithium ions, D_{Li^+}, in the Li|SS cells with PP and membrane-modified separators. Data for the GO/PP separator could not be acquired due to excessively high overpotential generated by the GO membrane.

Arrhenius plots were generated for the rGO/PP, holey 030HG/PP, and 050HG/PP separators (Figure 2-7a). The results show that the $E_{a\text{-}Li^+}$ increased and the σ_{Li^+} decreased in the order of 050HG/PP, 030HG/PP, and rGO/PP, indicating that the lower

physical obstruction to the lithium-ion transport leads to a lower $E_{a\text{-}Li^+}$ and a higher σ_{Li^+} (Figure 2-7b). Additionally, the Li^+ diffusion coefficients (D_{Li^+}) of the PP separator and modified separators were obtained from linear sweep voltammetry (LSV) tests performed with Li|SS cells (CR2032) consisting of a "Li|PP|membrane|PP|SS" structure (Figure S15, see Experimental Methods). In brief, a fixed-capacity 1 mAh Li-electroplating is performed on the SS electrode, followed by electrostripping the lithium from the SS plate using LSV to obtain peak currents at different scan rates. Figure 7c, and 7d shows that the D_{Li^+} for all Li|SS cells using modified separators are smaller than that of the commercial PP separator. This is consistent with the σ_{Li^+} results of the modified separators obtained previously (Figure 2-5 and 2-7b). Moreover, a comparison between $E_{a\text{-}Li^+}$ (0.064 eV) and σ_{Li^+} (0.394 S cm^{-1}) of the commercial PP separator (Figure 2-5) and the experimental results obtained for the modified separators (Figure 2-5 and 2-7a, b) indicates that the hindrance of Li^+ transport cannot be completely avoided even with mesoporous materials such as the 030HG and 050HG. Consequently, our data suggests that the less physical obstruction of lithium ions by the membrane, the lower the $E_{a\text{-}Li^+}$ and the higher the σ_{Li^+} of the separator, and vice versa.

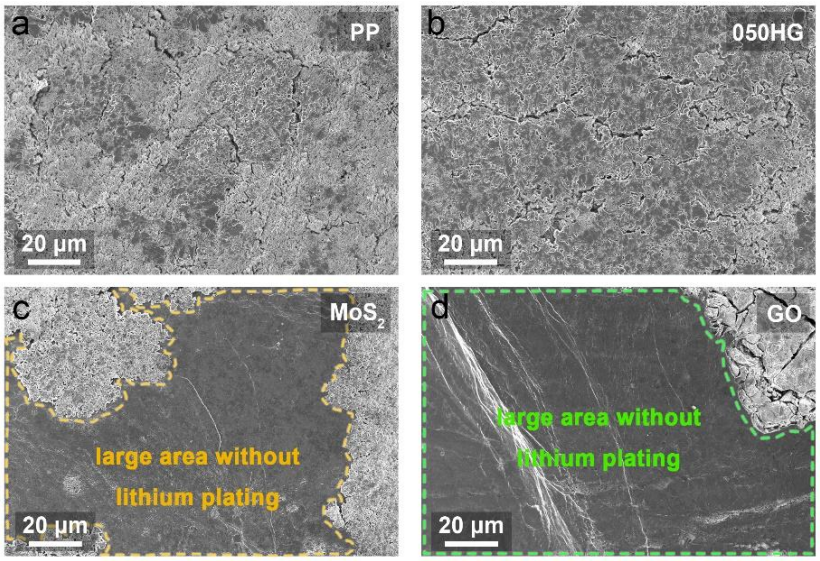

Figure 2-8. Surface morphology of Li foil after cycling with different separators. (a) commercial PP, (b) 050HG/PP, (c) MoS_2/PP, and (d) GO/PP. The area within the dashed boundary in the image of (c) and (d) indicates a region on the Li foil surface lacking lithium deposition.

Further evidence of Li^+ transport hindrance in these membranes is sought by disassembling the Li|Li (i.e., Li|PP|membrane|PP|Li) cells after cycling. The surface morphology of the lithium foils was examined under SEM (Figure 2-8). The findings indicate that the Li foils in the cells using membranes with relatively lower overpotentials, such as the commercial PP separator (Figure 2-8a), 050HG (Figure 2-8b), $Co(OH)_2$ (Figure S17), SnS_2 (Figure S18), and rGO (Figure S19), are all covered with Li deposits, while for those using membranes with very large overpotentials there exist extensive areas without Li plating. In contrast, for membranes with very large overpotentials, such as MoS_2 (Figure 2-8c) and GO (Figure 2-8d), extensive smooth surfaces are present indicating an unutilized section of the lithium foils. This observation implies that dense membranes significantly impeded Li^+ transport, leading to considerable inhomogeneity in Li^+ distribution and deposition on the electrodes.

To obtain further insight on the membrane morphology impact on the internal dynamics of the cells, simulations of Li^+ mass transfer were carried out across four types of separators: commercial PP, rGO/PP, 030HG/PP, and 050HG/PP (Figure 2-9). The physics-controlled mesh was set to extremely fine and controlled by the COMSOL's physical field alone to ensure accuracy. The simulation duration was set to 60 s with a time step of 0.1 s. A 2D cut point was set at 0.5 μm below the PP separator, and a 2D cut line perpendicular to the separator traversed the entire cell for data observation and collection purposes (Figure S21). Geometrical parameters of the membranes and PP separator required for the modeling were obtained by statistical analysis of SEM images (Figure S22). For commercial PP separator, the statistical analysis revealed that the total hole area accounts for 15.48% of its surface area. For the membranes of rGO, 030HG, and 050HG, the average gap area between graphene nanosheets on their surfaces was approximately 0.09366 μm^{-2}, with an average gap size of ~380 nm. Regarding the 030HG and 050HG membranes, the population density of nano-holes on holey graphene nanosheets was 438.05 holes μm^{-2} and 655.73 holes μm^{-2}, respectively.

No table of figures entries found.

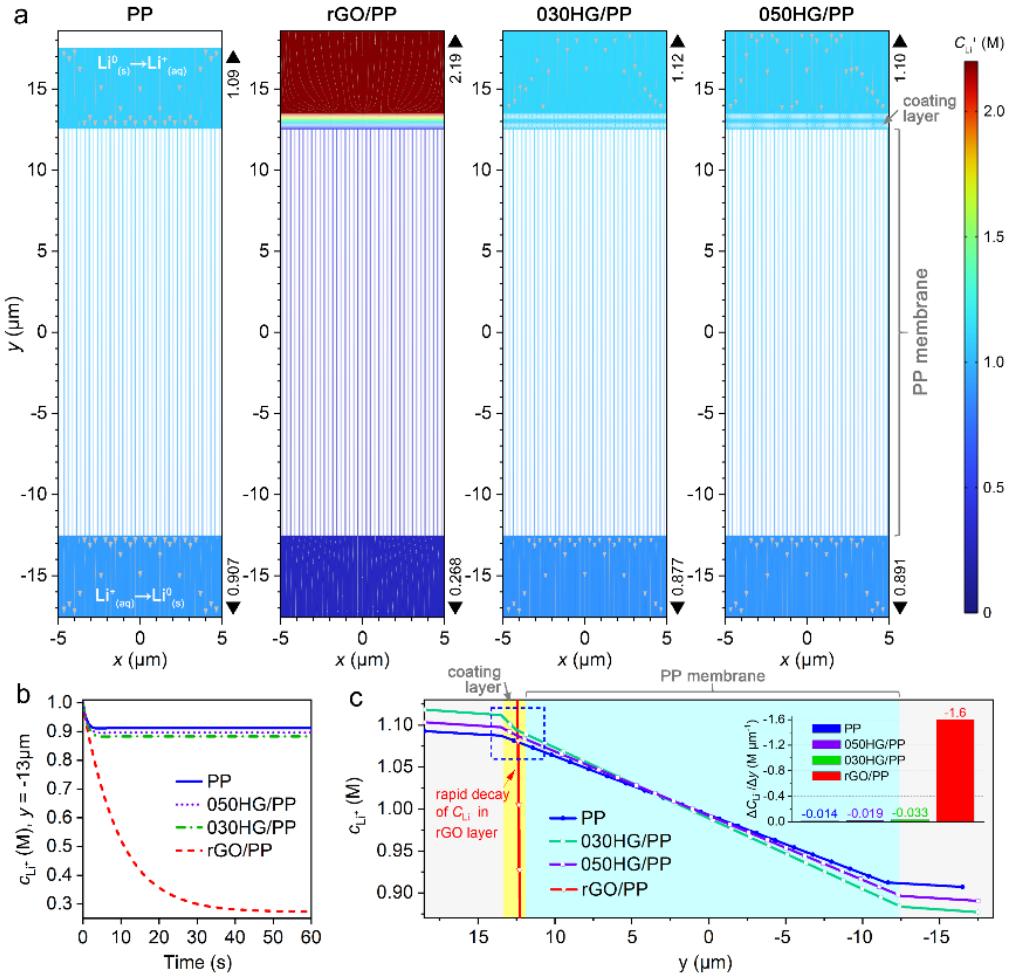

Figure 2-9. Li^+ transport modeling results through various separators in Li|Li symmetric cells (i.e., "Li|PP|Li" and "Li|membrane|PP|Li" structures). (a) Topographic maps of C_{Li}^+ within Li|Li symmetric cells using bare PP, rGO/PP, 030HG/PP, and 050HG/PP separators, where all the membrane layers have a thickness of 1 μm. Numerical values indicated by the black arrows represent the minimum and maximum C_{Li}^+. (b) Temporal evolution of C_{Li}^+ examined at a control point 0.5 μm below the PP separator. (c) Variation in C_{Li}^+ along y, on the normal direction of the separators, indicating their effect on spatial C_{Li}^+ distribution. The inset plots the lithium-ion concentration gradients across various membranes. Yellow region: membrane layer. Blue region: PP separator.

Figure 2-9a presents the Li^+ concentration (C_{Li}^+) distribution in cells with different separators, captured at the final simulation time of t = 60 s, for which a quasi-steady state had been reached (Figure 2-9b). Among them, the cell with the rGO/PP separator displays the highest polarization, suggesting substantial Li^+ mass flux impedance by the rGO layer. Analysis of the cross-sectional C_{Li}^+ profiles (at y = −13 μm) reveals that

the rGO/PP separator reduces the Li^+ mass flux by ca. 3.4 times more than the bare PP and HG/PP separators. It is evident that the holey nanostructure within the HG membranes significantly alleviates this impedance. Figure 9c displays the C_{Li^+} spatial distribution after 60 s of cycling, revealing a significant decrease in C_{Li^+} at the membrane interface (see inset). The curves show the simulated variation of C_{Li^+} along the thickness (y direction) of the membrane layers (yellow region) and PP separator (blue region). The value of $\Delta C_{Li^+}/\Delta y$ is found to increase in the order of PP, 050HG/PP, 030HG/PP, and rGO/PP, consistent with experimental results (Figure 2-7a, b). The simulation results demonstrate that using compact membranes made of Li^+-impermeable materials in batteries increases the Li^+ diffusion path in the direction normal to the battery separator surface (y-axis). Such a configuration results in significant cell polarization and amplifies the overpotential. In relation to this, calculations highlight the significance of effective hole areas on the membrane for lithium-ion transport. Specifically, the 030HG membrane has 9.1% of its surface area as effective holes, whereas the 050HG membrane comprises 13.5%, which is nearly approaching the 15.5% of a commercial PP separator (Figure S22). This suggests that an optimal effective hole surface area close to that of commercial PP separators is crucial for efficient lithium-ion transport for building practical batteries.

2.4.4 Validation of Li^+ hinderance by membranes in H-cells

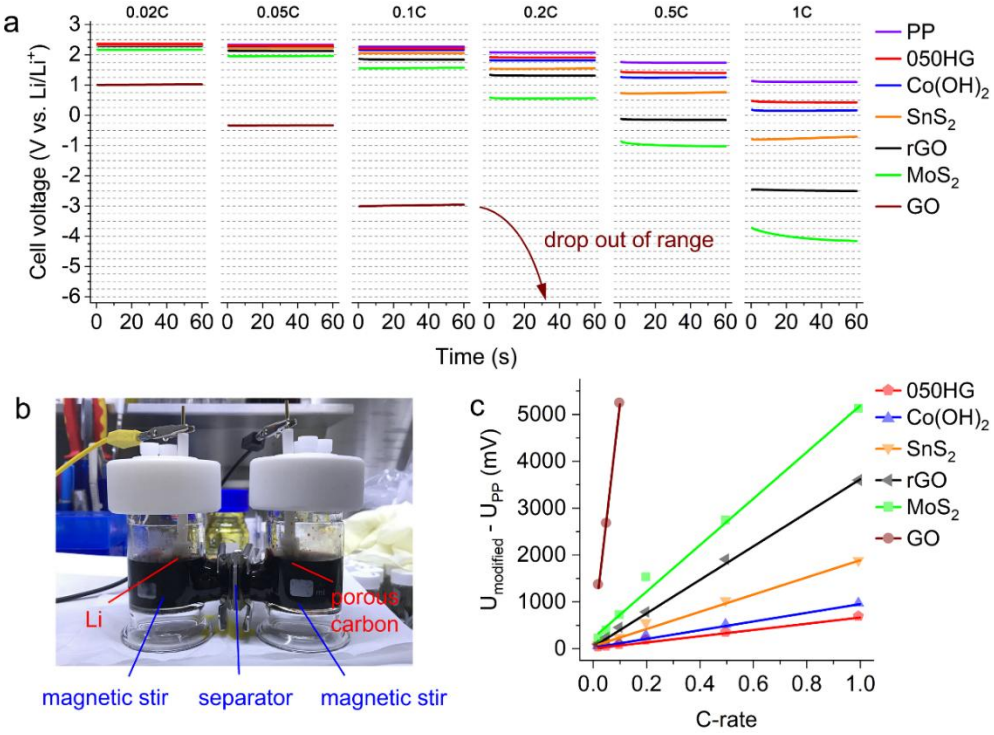

Figure 2-10. Overpotential measurements of PP and modified separators in Li–S H-cell**.** (a) Overpotential test results obtained with different separators in an H-cell. (b) H-cell configuration. (c) Difference in overpotential between the modified and PP separators at various C-rates.

Overpotential assessments were conducted to evaluate the effects of membrane-modified separators (coated with GO, MoS_2, rGO, SnS_2, $Co(OH)_2$, and 050HG) on the full Li–S cells (Figure 2-10). Figure 10a illustrates the overpotential test results obtained with different separators in an H-cell (Figure 2-10b, see also Experimental Methods). The H-cell comprises a Li metal foil as the anode, a porous carbon-coated Al foil as the cathode current collector, a separator tightly sealed in between, and a total of 70 mL 2M Li_2S_8 catholyte. Continuous magnetic stirring is applied on both sides of the H-cell to minimize diffusion impedance in the electrolyte during the measurements. The test currents were calculated based on the same C-rates

employed in the previous coin cell tests (Figure 2-4). The discharge plateau voltage of the GO/PP separator cell drops below 1 V at 0.02 C and exceeds the lower limit of the test voltage at 0.2 C, indicating a significant hindrance to Li^+ transfer. The MoS_2/PP separator shows slightly better performance than the GO/PP separator, with a discharge plateau below 1 V at 0.2 C, corresponding to the cutoff of the Li–S cell and a complete loss of its energy density. Other separators, such as rGO/PP, SnS_2/PP, and $Co(OH)_2$/PP, demonstrate varying degrees of overpotentials and energy density decrease. Notably, the overpotential of the cell using a 050HG/PP separator with a holey structure is only slightly higher than that of the commercial PP separator, but significantly lower than that of the other separators. These observations support the conclusion that the Li^+ permeability of the membranes has a critical impact on the overpotential and energy density of the Li–S batteries. Figure 2-10c summarizes the overpotential differences between all modified separators and the commercial PP separator at various C-rates. It was confirmed that modified separators always hinder the Li^+ diffusion. Additionally, it is worth noting that the overpotential differences measured with the H-cell are generally higher than those in the coin cells (Figure 2-4c), and this pattern remains consistent after repeated testing. We speculate that this may be because the diameter of the separator (~18–19 mm) in the coin cell is slightly smaller than that of the metal cell case (~19–20 mm), which causes a portion of the lithium ions to pass through the gap at the edge of the separators to the other side under high current, thereby partially mitigating the overpotential. However, in the H-

cell, the separator edge is tightly sealed by the O-rings, so lithium ions can only pass through the membrane layer, resulting in a larger overpotential.

Given the reasonable Li^+ transport performance of the 050HG/PP and 030HG/PP separators, which decrease Li-ion transport (σ_{Li^+}) by only 33.3% and 60%, respectively, with respect to the bare PP separator, their capability to hinder the polysulfide transport was further investigated in an H-cell configuration. One side of the H-cell was filled with a 37.5 mM concentrated solution of polysulfide in a DOL/DME (1:1, v/v) solvent and the other side, separated by the separator, was filled with a clean solution of the solvent (Figure S16, see Experimental Methods). Notably, when compared to the bare PP separator, the 050HG/PP and 030HG/PP separators decreased the polysulfide diffusion by 62.5% and 131%, respectively. These results indicate that by engineering the membrane structure, a balance between polysulfide containment and lithium-ion transport can be achieved, thereby optimizing the battery's performance and energy density.

2.5 Conclusions

The integration of micro/meso-porous membranes in multi-ion battery systems, although effective in suppressing the shuttling of separator-crossing species (e.g., polysulfides in metal-sulfur batteries), has its downsides. Notably, there is a compromise in metal-ion permeability and subsequent energy density. This study sheds light on these effects, using Li–S batteries as a representative model, by assessing the challenges of lithium-ion transport through a range of micro- and meso-

porous membranes. Our experimental findings indicate that Li–S batteries using a commercial PP separator undergo a minimum energy density reduction of 20% when overpotentials exceed 250 mV. The introduction of a microporous membrane as polysulfide barrier into the PP separator significantly increases this energy loss. Li|Li symmetric cell tests unveil those certain types of membranes (including GO, MoS_2, and rGO) display overpotentials surpassing 250 mV at 1 C rate. This issue becomes more pronounced when these membranes are tested within H-cells. Fabrication and testing of porous membrane with an induced level of mesoporosity (e.g., holey graphene membranes) and modeling confirm that the overpotentials stem from physical obstruction of Li^+ transport, revealing the need to compromise between soluble polysulfide blocking and energy loss. The implications are that for the construction of efficient batteries, the optimal effective hole area percentage should be close to the underlying separators (~15.5% in the case of commercial PP separators), i.e., small enough to mitigate the species shuttle effect and to prevent internal short-circuiting but large enough to avoid detrimental increments in overpotential. We also observe that micro/mesoporous holey graphene membranes with 13.5% and 9.1% of surface holes can decrease the polysulfide diffusion by 62.5% and 113%, while increasing the overpotential for Li^+ transport by only 33.3% and 60%, respectively. These insights chart a path for the design of multi-scale porous membranes for emerging rechargeable batteries, including metal–sulfur (e.g., Li–S, Na–S, Mg–S, Al–S) and metal–halogen systems (e.g., Li–I_2, Zn–Br), as well as other ion-selective electrochemical applications.

2.6 References

1. Zhou, G.; Chen, H.; Cui, Y., Formulating energy density for designing practical lithium–sulfur batteries. *Nature Energy* **2022,** *7* (4), 312-319.

2. Yang, X.; Li, X.; Adair, K.; Zhang, H.; Sun, X., Structural design of lithium–sulfur batteries: from fundamental research to practical application. *Electrochemical Energy Reviews* **2018,** *1*, 239-293.

3. Peng, L.; Wei, Z.; Wan, C.; Li, J.; Chen, Z.; Zhu, D.; Baumann, D.; Liu, H.; Allen, C. S.; Xu, X.; Kirkland, A. I.; Shakir, I.; Almutairi, Z.; Tolbert, S.; Dunn, B.; Huang, Y.; Sautet, P.; Duan, X., A fundamental look at electrocatalytic sulfur reduction reaction. *Nature Catalysis* **2020,** *3* (9), 762-770.

4. Raza, H.; Bai, S.; Cheng, J.; Majumder, S.; Zhu, H.; Liu, Q.; Zheng, G.; Li, X.; Chen, G., Li-S Batteries: Challenges, Achievements and Opportunities. *Electrochemical Energy Reviews* **2023,** *6* (1), 29.

5. Liu, B.; Taheri, M.; Torres, J. F.; Fusco, Z.; Lu, T.; Liu, Y.; Tsuzuki, T.; Yu, G.; Tricoli, A., Janus Conductive/Insulating Microporous Ion-Sieving Membranes for Stable Li–S Batteries. *ACS Nano* **2020,** *14* (10), 13852-13864.

6. Li, C.; Ge, W.; Qi, S.; Zhu, L.; Huang, R.; Zhao, M.; Qian, Y.; Xu, L., Manipulating Electrocatalytic Polysulfide Redox Kinetics by 1D Core–Shell Like Composite for Lithium–Sulfur Batteries. *Advanced Energy Materials* **2022,** *12* (16), 2103915.

7. Bai, Y.; Nguyen, T. T.; Chu, R.; Kim, N. H.; Lee, J. H., Core-shell hollow nanostructures as highly efficient polysulfide conversion and adsorption cathode for shuttle-free lithium-sulfur batteries. *Chemical Engineering Journal* **2023,** *454*, 140338.

8. Wang, L.; Li, X.; Zhang, Y.; Mao, W.; Li, Y.; Chu, P. K.; Kızılaslan, A.; Zheng, Z.; Huo, K., Subnanometer MoP clusters confined in mesoporous carbon (CMK-3) as superior electrocatalytic sulfur hosts for high-performance lithium-sulfur batteries. *Chemical Engineering Journal* **2022,** *446*, 137050.

9. Tu, S.; Chen, Z.; Zhang, B.; Wang, X.; Zhan, R.; Li, C.; Sun, Y., Realizing High Utilization of High-Mass-Loading Sulfur Cathode via Electrode Nanopore Regulation.

Nano Letters **2022,** *22* (14), 5982-5989.

10. Liu, B.; Torres, J. F.; Taheri, M.; Xiong, P.; Lu, T.; Zhu, J.; Liu, Y.; Yu, G.; Tricoli, A., Dual-Ion Flux Management for Stable High Areal Capacity Lithium–Sulfur Batteries. *Advanced Energy Materials* **2022,** *12* (10), 2103444.

11. Lieu, W. Y.; Fang, D.; Li, Y.; Li, X. L.; Lin, C.; Thakur, A.; Wyatt, B. C.; Sun, S.; Ghosh, T.; Anasori, B.; Ng, M.-F.; Yang, H. Y.; Seh, Z. W., Spherical Templating of CoSe2 Nanoparticle-Decorated MXenes for Lithium–Sulfur Batteries. *Nano Letters* **2022,** *22* (21), 8679-8687.

12. Zheng, Z.-J.; Ye, H.; Guo, Z.-P., Recent progress on pristine metal/covalent-organic frameworks and their composites for lithium–sulfur batteries. *Energy & Environmental Science* **2021,** *14* (4), 1835-1853.

13. Tian, X.; Cheng, Y.; Zhou, Y.; Zhang, B.; Wang, G., Long-cycling and high-loading lithium-sulfur battery enabled by free-standing three-dimensional porous NiCo2O4 nanosheets. *Applied Energy* **2023,** *334*, 120694.

14. Lei, T.; Chen, W.; Lv, W.; Huang, J.; Zhu, J.; Chu, J.; Yan, C.; Wu, C.; Yan, Y.; He, W.; Xiong, J.; Li, Y.; Yan, C.; Goodenough, J. B.; Duan, X., Inhibiting Polysulfide Shuttling with a Graphene Composite Separator for Highly Robust Lithium-Sulfur Batteries. *Joule* **2018,** *2* (10), 2091-2104.

15. Xiao, R.; Yang, S.; Yu, T.; Hu, T.; Zhang, X.; Xu, R.; Wang, Y.; Guo, X.; Sun, Z.; Li, F., A Janus Separator for Inhibiting Shuttle Effect and Lithium Dendrite in Lithium−Sulfur Batteries. *Batteries & Supercaps* **2022,** *5* (4), e202100389.

16. Chang, Z.; Yang, H.; Pan, A.; He, P.; Zhou, H., An improved 9 micron thick separator for a 350 Wh/kg lithium metal rechargeable pouch cell. *Nature Communications* **2022,** *13* (1), 6788.

17. Bai, S.; Liu, X.; Zhu, K.; Wu, S.; Zhou, H., Metal–organic framework-based separator for lithium–sulfur batteries. *Nature Energy* **2016,** *1* (7), 16094.

18. Shin, H. J.; Park, S.-W.; Park, S.; Kim, D.-W., Polymer Electrolyte/Sulfur Double-Shelled Anisotropic Reduced Graphene Oxide Lamellar Scaffold Enables Stable and High-Loading Cathode for Quasi-Solid-State Lithium-Sulfur Batteries. *Advanced*

Science **2023,** *10* (6), 2205424.

19. Chu, Z.; Gao, X.; Wang, C.; Wang, T.; Wang, G., Metal–organic frameworks as separators and electrolytes for lithium–sulfur batteries. *Journal of Materials Chemistry A* **2021,** *9* (12), 7301-7316.

20. Shen, L.; Wu, H. B.; Liu, F.; Brosmer, J. L.; Shen, G.; Wang, X.; Zink, J. I.; Xiao, Q.; Cai, M.; Wang, G.; Lu, Y.; Dunn, B., Creating Lithium-Ion Electrolytes with Biomimetic Ionic Channels in Metal–Organic Frameworks. *Advanced Materials* **2018,** *30* (23), 1707476.

21. Hu, B.; Xu, J.; Fan, Z.; Xu, C.; Han, S.; Zhang, J.; Ma, L.; Ding, B.; Zhuang, Z.; Kang, Q.; Zhang, X., Covalent Organic Framework Based Lithium–Sulfur Batteries: Materials, Interfaces, and Solid-State Electrolytes. *Advanced Energy Materials* **2023,** *13* (10), 2203540.

22. Zhang, X.; Ma, B.; Huang, S.; Han, D., Review on Multi-Functional Separator for Li-S Batteries. **2023**.

23. Zhang, J.; Hu, J.; Li, X.; Yang, L.; Yang, L.; Lin, J.; Huang, J.; Xu, G., High-performance MoS2 quantum dots/graphene functionalized separator and its failure analysis under high sulfur loading. *Chemical Engineering Journal* **2023,** *456*, 140972.

24. Ren, L.; Liu, J.; Zhao, Y.; Wang, Y.; Lu, X.; Zhou, M.; Zhang, G.; Liu, W.; Xu, H.; Sun, X., Regulating Electronic Structure of Fe–N4 Single Atomic Catalyst via Neighboring Sulfur Doping for High Performance Lithium–Sulfur Batteries. *Advanced Functional Materials* **2023,** *33* (12), 2210509.

25. Lei, J.; Fan, X.-X.; Liu, T.; Xu, P.; Hou, Q.; Li, K.; Yuan, R.-M.; Zheng, M.-S.; Dong, Q.-F.; Chen, J.-J., Single-dispersed polyoxometalate clusters embedded on multilayer graphene as a bifunctional electrocatalyst for efficient Li-S batteries. *Nature Communications* **2022,** *13* (1), 202.

26. Wang, M.; Emre, A. E.; Kim, J.-Y.; Huang, Y.; Liu, L.; Cecen, V.; Huang, Y.; Kotov, N. A., Multifactorial engineering of biomimetic membranes for batteries with multiple high-performance parameters. *Nature Communications* **2022,** *13* (1), 278.

27. Pan, H.; Tan, Z.; Zhou, H.; Jiang, L.; Huang, Z.; Feng, Q.; Zhou, Q.; Ma, S.;

Kuang, Y., Fe3C-N-doped carbon modified separator for high performance lithium-sulfur batteries. *Journal of Energy Chemistry* **2019,** *39*, 101-108.

28. Wang, N.; Chen, B.; Qin, K.; Liu, E.; Shi, C.; He, C.; Zhao, N., Rational design of Co9S8/CoO heterostructures with well-defined interfaces for lithium sulfur batteries: A study of synergistic adsorption-electrocatalysis function. *Nano Energy* **2019,** *60*, 332-339.

29. Wang, C.; Wu, K.; Cui, J.; Fang, X.; Li, J.; Zheng, N., Robust Room-Temperature Sodium-Sulfur Batteries Enabled by a Sandwich-Structured MXene@C/Polyolefin/MXene@C Dual-functional Separator. *Small* **2022,** *18* (43), 2106983.

30. Ghasemiestahbanati, E.; Shehzad, A.; Konstas, K.; Setter, C. J.; O'Dell, L. A.; Shaibani, M.; Majumder, M.; Hill, M. R., Exceptional lithium diffusion through porous aromatic framework (PAF) interlayers delivers high capacity and long-life lithium–sulfur batteries. *Journal of Materials Chemistry A* **2022,** *10* (2), 902-911.

31. Zeng, G.; Liu, Y.; Chen, D.; Zhen, C.; Han, Y.; He, W., Natural Lepidolite Enables Fast Polysulfide Redox for High-Rate Lithium Sulfur Batteries. *Advanced Energy Materials* **2021,** *11* (44), 2102058.

32. Yu, B.; Fan, Y.; Mateti, S.; Kim, D.; Zhao, C.; Lu, S.; Liu, X.; Rong, Q.; Tao, T.; Tanwar, K. K.; Tan, X.; Smith, S. C.; Chen, Y. I., An Ultra-Long-Life Flexible Lithium–Sulfur Battery with Lithium Cloth Anode and Polysulfone-Functionalized Separator. *ACS Nano* **2021,** *15* (1), 1358-1369.

33. Bo, R.; Taheri, M.; Liu, B.; Ricco, R.; Chen, H.; Amenitsch, H.; Fusco, Z.; Tsuzuki, T.; Yu, G.; Ameloot, R.; Falcaro, P.; Tricoli, A., Hierarchical Metal-Organic Framework Films with Controllable Meso/Macroporosity. *Advanced Science* **2020,** *7* (24), 2002368.

34. Liu, P.; Qu, L.; Tian, X.; Yi, Y.; Xia, J.; Wang, T.; Nan, J.; Yang, P.; Wang, T.; Fang, B.; Li, M.; Yang, B., Ti3C2Tx/Graphene Oxide Free-Standing Membranes as Modified Separators for Lithium–Sulfur Batteries with Enhanced Rate Performance. *ACS Applied Energy Materials* **2020,** *3* (3), 2708-2718.

35. Wei, Z.; Ren, Y.; Sokolowski, J.; Zhu, X.; Wu, G., Mechanistic understanding of the role separators playing in advanced lithium-sulfur batteries. *InfoMat* **2020,** *2* (3), 483-508.

36. Zhang, Y.; Miao, L.; Ning, J.; Xiao, Z.; Hao, L.; Wang, B.; Zhi, L., A graphene-oxide-based thin coating on the separator: an efficient barrier towards high-stable lithium–sulfur batteries. *2D Materials* **2015,** *2* (2), 024013.

37. Xin, Y.; Huang, A.; Hu, Q.; Shi, H.; Wang, M.; Xiao, Z.; Zheng, X.; Di, Z.; Chu, P. K., Barrier Reduction of Lithium Ion Tunneling through Graphene with Hybrid Defects: First-Principles Calculations. *Advanced Theory and Simulations* **2018,** *1* (2), 1700009.

38. Griffin, E.; Mogg, L.; Hao, G.-P.; Kalon, G.; Bacaksiz, C.; Lopez-Polin, G.; Zhou, T. Y.; Guarochico, V.; Cai, J.; Neumann, C.; Winter, A.; Mohn, M.; Lee, J. H.; Lin, J.; Kaiser, U.; Grigorieva, I. V.; Suenaga, K.; Özyilmaz, B.; Cheng, H.-M.; Ren, W.; Turchanin, A.; Peeters, F. M.; Geim, A. K.; Lozada-Hidalgo, M., Proton and Li-Ion Permeation through Graphene with Eight-Atom-Ring Defects. *ACS Nano* **2020,** *14* (6), 7280-7286.

39. Ju, Z.; King, S. T.; Xu, X.; Zhang, X.; Raigama, K. U.; Takeuchi, K. J.; Marschilok, A. C.; Wang, L.; Takeuchi, E. S.; Yu, G., Vertically assembled nanosheet networks for high-density thick battery electrodes. *Proceedings of the National Academy of Sciences* **2022,** *119* (40), e2212777119.

40. Foroozan, T.; Soto, F. A.; Yurkiv, V.; Sharifi-Asl, S.; Deivanayagam, R.; Huang, Z.; Rojaee, R.; Mashayek, F.; Balbuena, P. B.; Shahbazian-Yassar, R., Synergistic Effect of Graphene Oxide for Impeding the Dendritic Plating of Li. *Advanced Functional Materials* **2018,** *28* (15), 1705917.

41. Xue, K.; Zhao, Y.; Lee, P.-K.; Yu, D. Y. W., Sn foil as the cathode for a reversible 2.8 V Sn-Li battery. *Journal of Materials Chemistry A* **2023,** *11* (3), 1482-1490.

42. Gou, J.; Liu, W.; Tang, A., A novel method to prepare a highly porous separator based on nanocellulose with multi-scale pore structures and its application for rechargeable lithium ion batteries. *J. Membr. Sci.* **2021,** *639*, 119750.

43. Gong, Y.; Wang, Y.; Fang, Z.; Zhao, S.; He, Y.-s.; Zhang, W.; Mu, J.; Zhang,

L.; Ma, Z.-F., Constructing a catalytic reservoir using cobalt nanoparticles-MoS2@nitrogen doped carbon nanotubes on the separator to immobilize polysulfides and accelerate their conversion for lithium-sulfur batteries. *Chemical Engineering Journal* **2022,** *446*, 136943.

44. Weng, S.; Zhang, X.; Yang, G.; Zhang, S.; Ma, B.; Liu, Q.; Liu, Y.; Peng, C.; Chen, H.; Yu, H.; Fan, X.; Cheng, T.; Chen, L.; Li, Y.; Wang, Z.; Wang, X., Temperature-dependent interphase formation and Li+ transport in lithium metal batteries. *Nature Communications* **2023,** *14* (1), 4474.

45. Hu, S.; Lozada-Hidalgo, M.; Wang, F. C.; Mishchenko, A.; Schedin, F.; Nair, R. R.; Hill, E. W.; Boukhvalov, D. W.; Katsnelson, M. I.; Dryfe, R. A. W.; Grigorieva, I. V.; Wu, H. A.; Geim, A. K., Proton transport through one-atom-thick crystals. *Nature* **2014,** *516* (7530), 227-230.

46. Bukola, S.; Creager, S. E., A charge-transfer resistance model and Arrhenius activation analysis for hydrogen ion transmission across single-layer graphene. *Electrochimica Acta* **2019,** *296*, 1-7.

2.7 Supporting Information

2.7.1 Material synthesis

Synthesis of GO and rGO: Graphene oxide (GO) and reduced graphene oxide (rGO) were synthesized according to a previously reported method.[1] First, natural graphite was chemically oxidized using a modified Hummers' method to obtain GO. To prepare rGO, 30 mg of GO powder was ultrasonically dispersed in 50 mL of anhydrous ethylene glycol (EG, 99.8%) for at least 1 hour. The dispersion was then vigorously stirred at 180°C for 3 hours in a reflux reactor. The final rGO nanosheets were purified in ethanol and DI water and dried by lyophilization.

Synthesis of HG: Nanoscale holes were created on graphene nanosheets using solid-state etching by oxidative nanoparticles. For instance, to synthesize 030HG nanosheets, 60 mg of as-prepared GO powder and 74.7 mg (0.30 mmol) $(CH_3COO)_2Co{\cdot}4H_2O$ (≥98.0%) were added in 100 mL of anhydrous ethylene glycol (EG, 99.8%) and ultrasonicated for at least 1 hour. The mixture was vigorously stirred at 180°C for 3 hours in a reflux reactor to form a thin layer of cobalt compound precursor on graphene nanosheets (Co-pre/G, Figure S11). The Co-precursor/G nanosheets were purified in ethanol and DI water and dried by lyophilization. Subsequently, the Co-pre/G nanosheets were annealed at 800°C for 1 hour in N_2 flow to form Co metallic nanoparticles on graphene nanosheets (CoNP/G, Figure S12). The CoNP/G nanosheets were further annealed at 200°C for 2 hours in air to form partially oxidized Co_3O_4-Co nanoparticles on graphene nanosheets (Co_3O_4-CoNP/G). Next, the

Co_3O_4-CoNP/G nanosheets were re-annealed at 800°C for 1 hour in N_2 flow, during which the Co_3O_4 in-situ etched nanoscale holes on the graphene to form CoNPs/HG (Figure S13) nanosheets. The final 030HG nanosheets (Figure S14) were obtained by soaking the Co_3O_4/HG nanosheets in 8.0M HCl solution at 60°C overnight. To synthesize the 050HG nanosheets, $(CH_3COO)_2Co{\cdot}4H_2O$ was increased to 124.5 mg (0.50 mmol) in the above process, while keeping other parameters unchanged.

Synthesis of $Co(OH)_2$: $Co(NO_3)_2{\cdot}6H_2O$ (291 mg, 1 mmol, ≥98%) was dissolved in 100 mL of a mixture of methanol/DI H_2O (1:1, v/v) to form solution A. Ammonium hydroxide solution (NH_4OH, 28.0-30.0% NH_3 basis, 150 μL) was diluted in 50 mL of a mixture of methanol/DI H_2O (1:1, v/v) to form solution B. Solutions A and B were kept at 4°C in an ice-water bath, and then solution B was added dropwise into solution A under magnetic stirring at 1000 rpm. The reaction was maintained at 4°C for 30 minutes until a homogeneous greenish $Co(OH)_2$ colloidal solution formed. The resulting $Co(OH)_2$ powder was purified and collected by centrifugation in DI water multiple times and then dried by lyophilization.

Synthesis of SnS_2: First, 351 mg $SnCl_4$ (1 mmol, ≥98%) and 150 mg ethanethioamide (2 mmol, ≥99.0%) were thoroughly mixed in 100 mL ethanol. The reaction was kept under magnetic stirring for 30 min at 4°C in an ice-water bath. Then, the solution was ultrasonicated for 30 min until a homogeneous brownish SnS_2 colloidal solution was formed. The resulting SnS_2 powder was purified and collected by centrifugation in ethanol and DI H_2O multiple times, and then dried by lyophilization.

Fabrication of modified membranes

Here, the membrane is defined as the micro/meso-porous coating layer, while the "membrane-modified separator" or "modified separator" is defined as the structure comprising of the micro/meso-porous coating layer applied over the commercial PP separator (1x membrane + 1x PP). The membrane-modified separators were fabricated using a simple filtration process. A commercial PP separator (Celgard 2400, thickness 25 μm) was selected as the base material for coating the membranes, and it served as the filter paper during the fabrication process. The following materials were chosen for constructing membranes: rGO, GO, $Co(OH)_2$, SnS_2, MoS_2, 030HG, and 050HG. To prepare the coating dispersions, 10 mg of rGO, 030HG, or 050HG was added to 50 mL of anhydrous 1-Methyl-2-pyrrolidone (NMP, 99.5%), while 10 mg of GO, $Co(OH)_2$, SnS_2, or 10 mL of MoS_2 suspension (consisting of LiOH-stabilized few-layer MoS_2 nanosheets dispersed in ethanol/H_2O, with C_{MoS2} = 1 mg mL^{-1} and d_{MoS2} = 0.02-1 μm, Sigma) was added to 50 mL of DI water. The resulting mixtures were ultrasonicated for 12 hours to achieve a homogeneous dispersion.

To ensure a uniform membrane coating in all modified separators, the dispersions were slowly added to a 500 mL open bottle (d = 84 mm) of a filtering flask. The filtering flask was left undisturbed until the filtration process was complete. After filtration, the modified separators were dried at 50°C overnight before use. The mass of membranes coated on PP separators was approximately 0.18 mg cm^{-2}. For comparison, a thinner version of the GO membrane was also fabricated, with a loading of approximately 0.09 mg cm^{-2}.

2.7.2 Material characterization

The SEM analysis was performed using a Zeiss UltraPlus analytical FESEM at 3 kV. XRD measurements were conducted using a Bruker system (D2 Phaser) equipped with Cu Kα radiation, with an average wavelength of 1.54059 Å. The thicknesses of the membranes were determined using a Starrett 3732 digital thickness gauge with a resolution of 0.001 mm, and the differences in thickness between a bare PP separator and the modified separators were illustrated in Figure S7.

2.7.3 Derivation of capacity output and energy output vs overpotential

To conceptually illustrate the impact of overpotential, as induced by the membranes, on the charging/discharging plateaus of Li–S batteries, charging/discharging profiles of a model Li–S coin cell battery are needed as the theoretical reference. The model Li–S coin cell battery consists of a lithium metal anode, a sulfur cathode, and a 40 μL electrolyte containing 1M LiTFSI and 0.2 M $LiNO_3$ in DOL/DME (1:1, v/v), along with a layer of commercial polypropylene (PP) separator. The sulfur cathode features a sulfur mass loading of 0.1 mg cm^{-2}, including 5wt% LA133 binder and 20wt% carbon black. Experimental testing was conducted at 0.1C, and the charge-discharge data from the third cycle were utilized. The red and blue solid lines in Figure 2-2a represent the maximum values of specific capacity, denoting 100% sulfur utilization.

To derive the discharge capacity output and energy output curves in Figure 2-2b, the discharge curve of the model cell from Figure 2-2a were used as a reference. As the

overpotential gradually increases, the discharge plateau shifts downwards (as indicated by the qualitative shift of the blue dashed line in Figure 2-2a). This allows us to determine the discharge plateau voltage (approximately the average voltage) and capacity for each overpotential. The corresponding energy output can be calculated using the formula in Figure 2-2b.

2.7.4 Li^+ diffusion efficiency measurements

(1) Resistance of Li^+ transport through modified membranes

Li|Li symmetric cells (CR2032), consisting of a "Li|PP|membrane|PP|Li" structure, were used to investigate the overpotential of lithium-ion transfer through both the commercial PP separators (control cell) and various membrane-modified separators. The electrolyte consisted of a standard solution containing 1 M LiTFSI in DOL/DME (1:1, v/v). To prevent contact of the membranes with the lithium electrodes and unwanted lithiation reactions, the membranes were all sandwiched between two PP separators, while the control cell composed of only two bare PP separators.

(2) Li^+ diffusion coefficient

Li|SS cells (CR2032), consisting of a "Li|PP|membrane|PP|SS" structure, were used to measure the Li^+ diffusion coefficient (D_{Li^+}, $cm^2\ s^{-1}$) of different membrane-modified separators. Each cell was injected with 60 μL of electrolyte (1 M LiTFSI in DOL/DME, 1:1 v/v) to adequately meet the Li^+ conduction requirements. Firstly, a fixed amount of 1 mAh Li-electroplating was performed on the SS plate using the Li|SS half cells. Then, the electroplated Li was electrostripped off from the SS plate at different scan rates

using linear sweep voltammetry (LSV) method to obtain peak currents at different scan rates. It is worth noting that the D_{Li}^{+} measured here are the overall results of the half cells, which are dynamically affected by various factors during the electrochemical testing process, including the lithium foil condition, electrolyte condition, lithium deposition and stripping processes, solid-electrolyte interface formation, and membranes. Therefore, we would like to point out that it is inappropriate to solely consider D_{Li}^{+} as an inherent characteristic of the membrane or the separator itself, even though some studies did so. However, this test can be used to determine the effects of different membrane-modified separators on the diffusion of lithium ions in the batteries.

The LSV measurements were performed with seven sweeping rates, i.e., 0.02, 0.04, 0.06, 0.08, 0.10, 0.12, and 0.14 mV s^{-1}, as shown in Figure S15. The D_{Li+} was derived using the Randles–Sevcik equation as described below according to literature[2]:

$$I_P = 2.69 \times 10^5 \text{ C mol}^{-1} \text{ V}^{-1/2} \cdot n^{3/2} \cdot A \cdot D_{Li}^{1/2} \cdot v^{1/2} \cdot C_{Li}$$

where I_p indicates the peak current (A), n is the number of electrons in the reaction (n=1 for Li electroplating/stripping processes), A is the electrode area (cm^2), v is the scanning rate (V s^{-1}), and C_{Li} is the Li^+ concentration in the electrolyte (0.001 mol cm^{-3}). Note that the constant with a value of 2.69×10^5 has units of C mol^{-1} $V^{-1/2}$. The linear relationship between the I_p and the square root of $v^{1/2}$ can be derived from CV measurements.

(3) Overpotential measurements in H-cell configuration

The entire testing process was carried out in an Argon-filled glovebox (H_2O < 0.1 ppm, O_2 < 0.1 ppm). The H-cell consists of two symmetrical containers that can be locked together in the middle using a spring clip. Prior to the test, the separators to be tested (either PP or modified separators) was sandwiched between two O-ring foot pads and locked in the middle of the H-cell. Next, 35 mL of 1.0 M Li_2S_8 catholyte, which contained 1.0 M lithium bis(trifluoromethanesulfonyl)imide (LiTFSI, 99.95%, Sigma Aldrich) and a 1:1 volume ratio of DOL/DME, was added to both sides of the H-cell. The Li_2S_8 catholyte was obtained by mixing Li_2S and S powder at a molar ratio of 1:7 and heating and stirring the mixture in a 1:1 volume ratio of DOL/DME for 12 hours, followed by dissolving LiTFSI to make it 1.0 M. The anode of the H-cell was a lithium foil (d=15 mm) held in place with a platinum metal clamp, and the cathode was an aluminum foil coated with porous carbon (d=15 mm). A magnetic stirrer (1000 rpm) was placed on each side of the H-cell to reduce the impact of concentration polarization. The top covers of the H-cell were sealed with a Teflon tape to prevent evaporation of the catholyte. After each test, the H-cell was washed and dried, and a fresh catholyte was refilled for the next separator measurement.

The two electrodes of the H-cell were connected to the CHI660 tester outside the glovebox via feed-through cables. Galvanostatic discharge was used to record the discharge reaction points of the positive electrode, with each current being tested for 60 s. Since different membranes have different obstacles to Li^+ transport, membranes with a higher Li^+ impedance will cause a larger overpotential and shift the discharge plateau of the cathode to a lower voltage. By comparing the discharge potentials of the

H-cell with modified separators and PP separator, the difference in overpotential at a certain current or C-rate can be calculated.

The testing current densities were calculated based on the assumed C-rates corresponding to a sulfur loading of 6mg cm^{-2} on the cathode of a Li–S battery. For example, in this study, C-rates of 0.02, 0.05, 0.1, 0.2, 0.5, and 1.0C during the discharge processes equal to 0.355 mA, 0.888 mA, 1.776 mA, 3.552 mA, 8.88 mA, and 17.76 mA.

2.7.5 Li_2S_6 permeation tests through different separators

Polysulfide permeation tests were conducted using an H-cell, comprising two identical glass containers. These containers can be hermetically sealed at the top and connected at the center via a clamp, encompassing an aperture of 15 mm. In a standard procedure, a separator (diameter approximately 28 mm) was positioned to entirely cover this aperture. After sealing, the membrane underwent a meticulous inspection to detect any potential cracks or unblocked openings. Subsequently, 25 mL of a 37.5 mM Li_2S_6 in DOL/DME (1:1 v/v) solvent was introduced into one side of the H-cell, and an equivalent volume of a blank solvent without any Li_2S_6 was added to the opposite side. The assembly was then placed on a level surface. Quantitative assessments of polysulfide diffusion through four separators—commercial PP, 050HG/PP, 030HG/PP, and rGO/PP, each with an equal mass of membrane materials—were performed. These evaluations involved polysulfide permeation tests and UV-vis analysis (Figure S16). The permeation process was continuously

monitored by extracting 300 μL samples from the solution on the lower concentration side of the H-cell at 15-min intervals, repeating this process five times. To ensure that the absorbance readings fell within the accurate range (typically below 2) of the UV-vis spectrophotometer, the permeate solutions were diluted tenfold, and the final results were recalibrated by multiplying by a factor of 10. All solutions were handled in an argon-filled glovebox, and hermetically sealed before removal from the glovebox for UV-vis measurements.

2.7.6 Nyquist plots and Li^+ activation energies

Li^+ activation energies ($E_{a\text{-}Li^+}$) of commercial PP and modified separators were determined by Nyquist plots from the electrochemical impedance of stainless steel (SS)|SS symmetric cells, consisting of a "SS|PP|membrane|PP|SS" structure, featuring various membranes at multiple temperatures (i.e., 10, 20, 30, 40, 50, 60°C).

The SS|SS symmetric cells were assembled in an Ar-filled glovebox. The membranes were sandwiched between two PP separators for electrical insulation from the SS plates. Each cell was injected with 60 μL of electrolyte (1M LiTFSI in DOL/DME, 1:1 v/v) to adequately meet the ionic conduction requirements. Electrochemical impedance spectroscopy (EIS) was conducted within the frequency range of 1 MHz to 0.1 Hz. Before initiating the EIS tests, each cell was placed in a constant-temperature chamber via feed-through cables at finely controlled temperatures for at least 60 min to ensure good temperature uniformity within the cell, after which testing commenced, as exemplified in Figure S20. The value of $E_{a\text{-}Li^+}$ of each separator was derived from the

slope of the fitted line in the Arrhenius plot.

2.7.7 Modeling of Li^+ transfer through membranes

The Li^+ mass transport simulation was performed using the Mass Transport Module of COMSOL Multiphysics 6.1. The mass transport model employed in this study was developed by optimizing and refining the frameworks established in our previous investigations.[1, 3, 4] The additional mass transfer mechanisms encompassed convection and mass transfer in porous media, where the concentration was treated as a linear function with electric field migration neglected.

Specifically, the mass transport model consisted of a Li|PP|Li or Li|PP|membrane|Li cell configuration, which aimed to simulate the temporal evolution of C_{Li^+} between two electrodes within the cell under ideal unidirectional current transmission conditions. In this model, the cell current density was set at 5.92 mA cm^{-2}, equivalent to the current density observed in a Li–S battery with a low sulfur loading of 2 mg cm^{-2} cycled at 1C rate. The employed electrolyte was a commercially available electrolyte, consisting of 1M $LiPF_6$ in a 1:1 ratio of EC: DEC. The electrolyte was considered non-solid, and its initial concentration in the model was set to 1.0 M, while temperature and pressure were set to the standard values provided by the software. Although COMSOL currently lacks a ready model for 1M LiTFSI in a 1:1 ratio of DOL: DME electrolyte specific to Li–S batteries, we opted to use the available electrolyte model as a reasonable approximation. The activity coefficient for Li^+ in the electrolyte (f_C) was adopted from published literature, with a value of 0.60.[5] The average value of the lithium ion diffusion

coefficient (D_C) was determined as 6×10^{-10} m^2 s^{-1} and assumed to be isotropic based on literature.[5-7] The remaining physical properties of the electrolyte were set to default values within the software environment to ensure a consistent foundation for simulation parameters.

In this study, to improve simulation efficiency, a uniform thickness of 1 μm was assigned to the modification layer, while the PP separator remained at 25 μm. The upper and lower boundaries in the model corresponded to the stripping and deposition reactions of Li metal foils, with reaction rates of +6.14 mol m^{-2} s^{-1} and −6.14 mol m^{-2} s^{-1}, respectively, corresponding to the specified current density. Furthermore, no flux was present at the boundaries and within the model units of the PP separator and modification layers. In the modeling, graphene building blocks were set to have a thickness of 13 nm with an average vertical gap of 20 nm, so holes with a diameter greater than or equal to 13 nm were considered as effective Li^+ transport channels. Thus, the former has an effective hole ratio of 82.1%, and the latter has an effective hole ratio of 72.8%.

Additionally, it is worth noting that in previous simulation studies, researchers often failed to construct a reasonable model that recreates the hole size and structure. For instance, directly using the average hole size of 40–50 μm in the PP separator as the 2D dimension in modeling is incorrect, as it significantly overestimates (potentially by at least 5-6× as observed) the projected area ratio of Li^+ channels on the membrane cross-section. This leads to overly optimistic estimations in simulation results. This issue remains unresolved even when placing the 2D model into a polar coordinate

system. Therefore, in this study, we redesigned the equivalent area corresponding to the holes within the membranes to ensure that the proportion of available Li^+ channels on the membrane cross-section aligns with the actual projection area of holes in the PP separator and HG membranes.

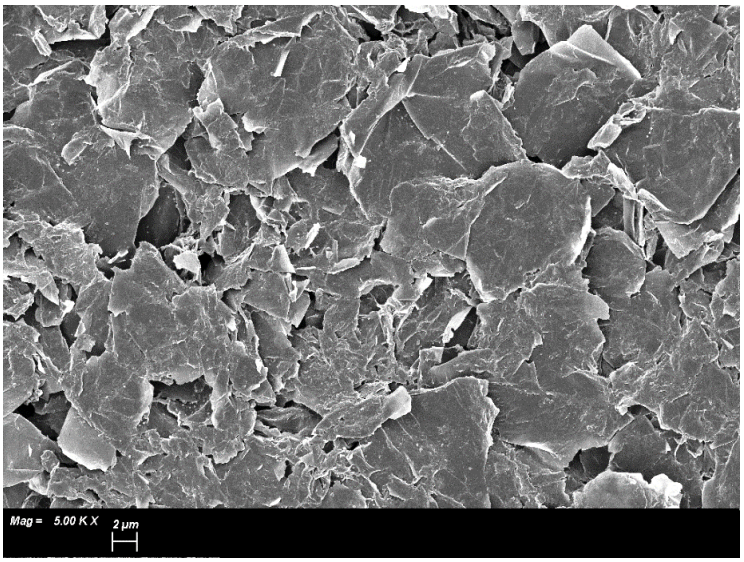

Figure S1. Top-view SEM image of rGO/PP separator. Pinholes and cracks were clearly observed across the surface of rGO/PP separator.

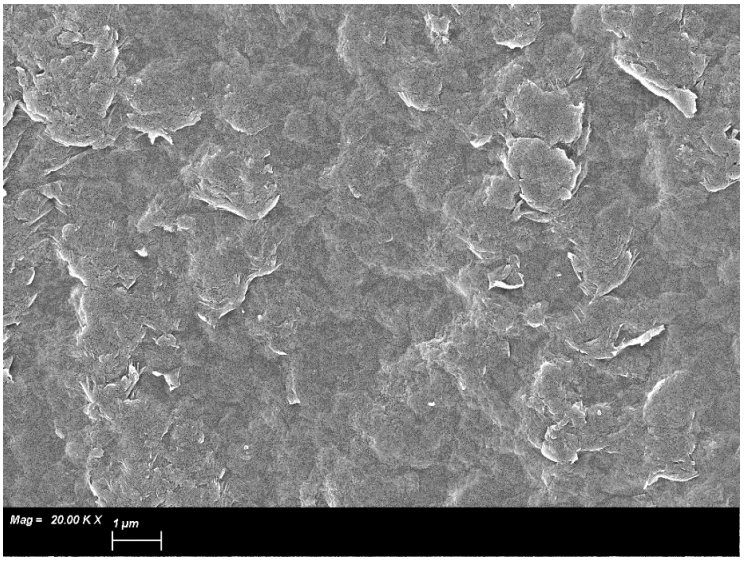

Figure S2. Top-view SEM image of GO/PP separator. No apparent pinholes or cracks were observed across the surface of GO/PP separator.

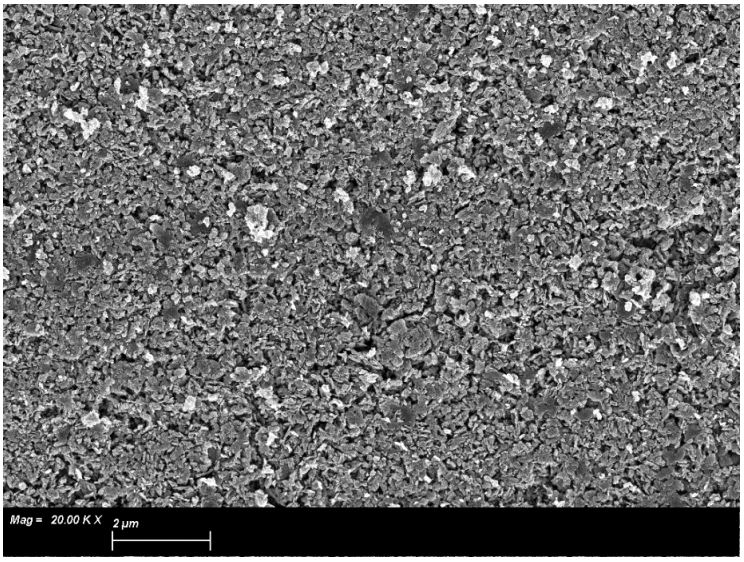

Figure S3. Top-view SEM image of $Co(OH)_2$/PP separator. Pinholes were clearly observed across the surface of $Co(OH)_2$/PP separator.

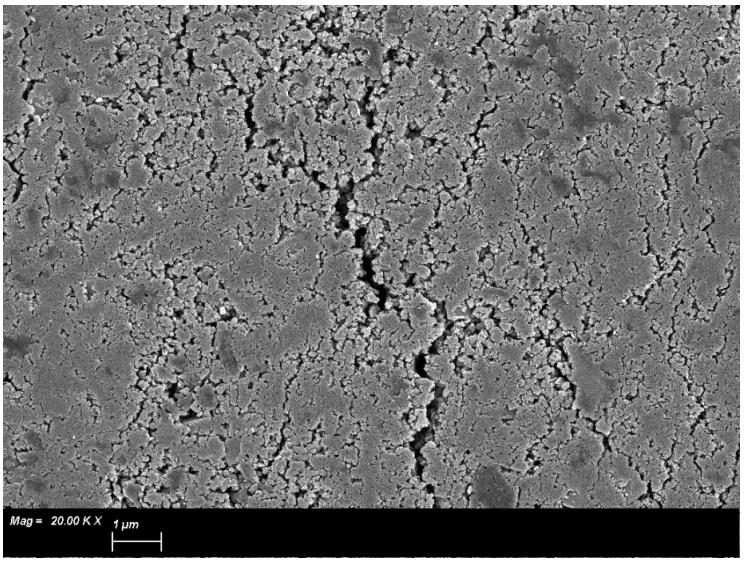

Figure S4. Top-view SEM image of SnS_2/PP separator. Obvious pinholes and cracks were observed across the surface of SnS_2/PP separator.

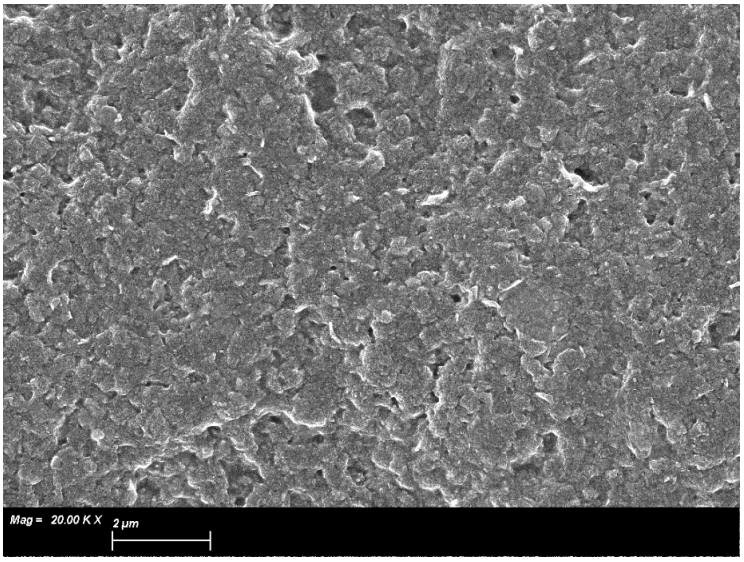

Figure S5. Top-view SEM image of MoS_2/PP separator. No apparent uncovered areas or cracks were observed across the surface of MoS_2/PP separator. Note that the darker regions are not holes, but shading caused by raised areas on the surface of the MoS_2 membrane.

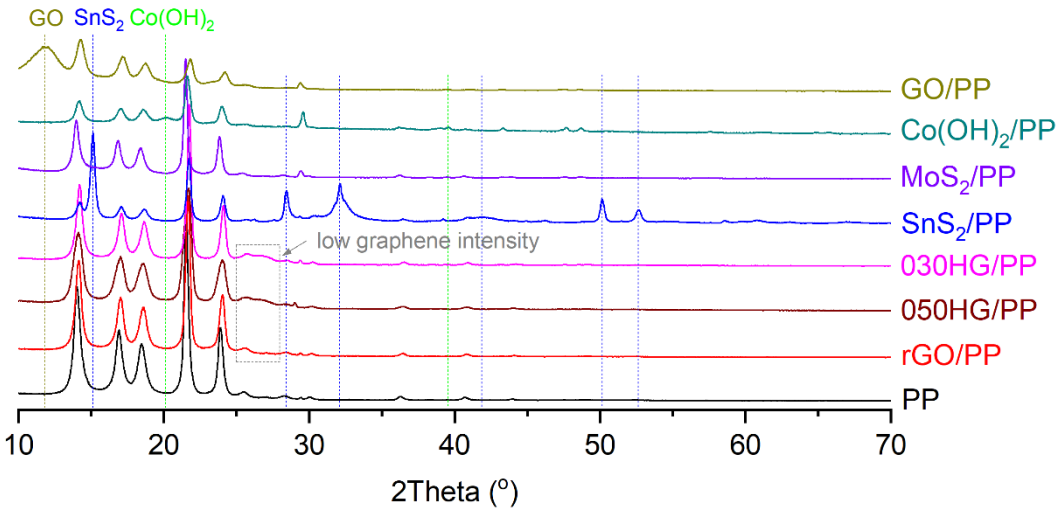

Figure S6. XRD results of commercial PP separator and various modified separators. The coating masses of all membranes are ~0.18 mg cm^{-2}.

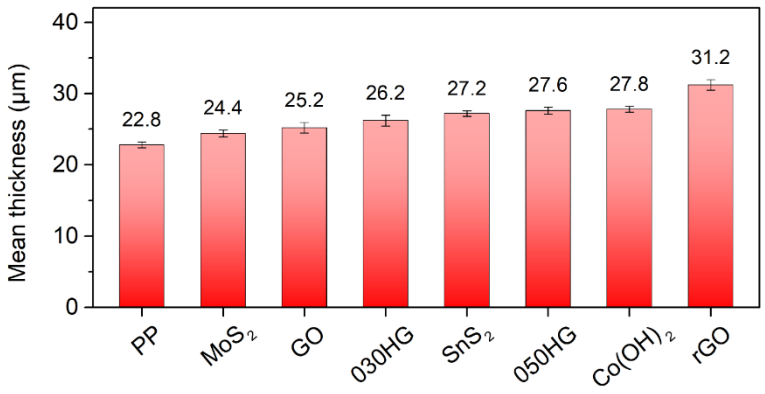

Figure S7. Measured thicknesses of commercial PP separator and various modified separators. Modified separators all have the same ~0.18 mg cm^{-2} loading of membrane materials.

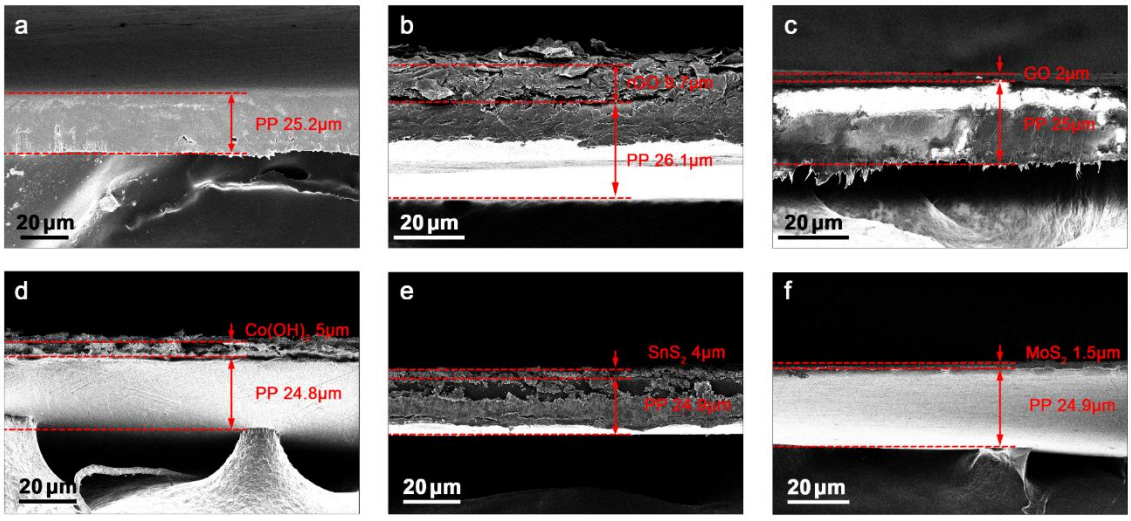

Figure S8. Cross-section SEM images of commercial PP and modified separators. Due to the extremely poor conductivity of PP separator itself, even after Pt coating, the uneven distribution of electronic conductivity in the separator results in overexposed areas in some SEM images.

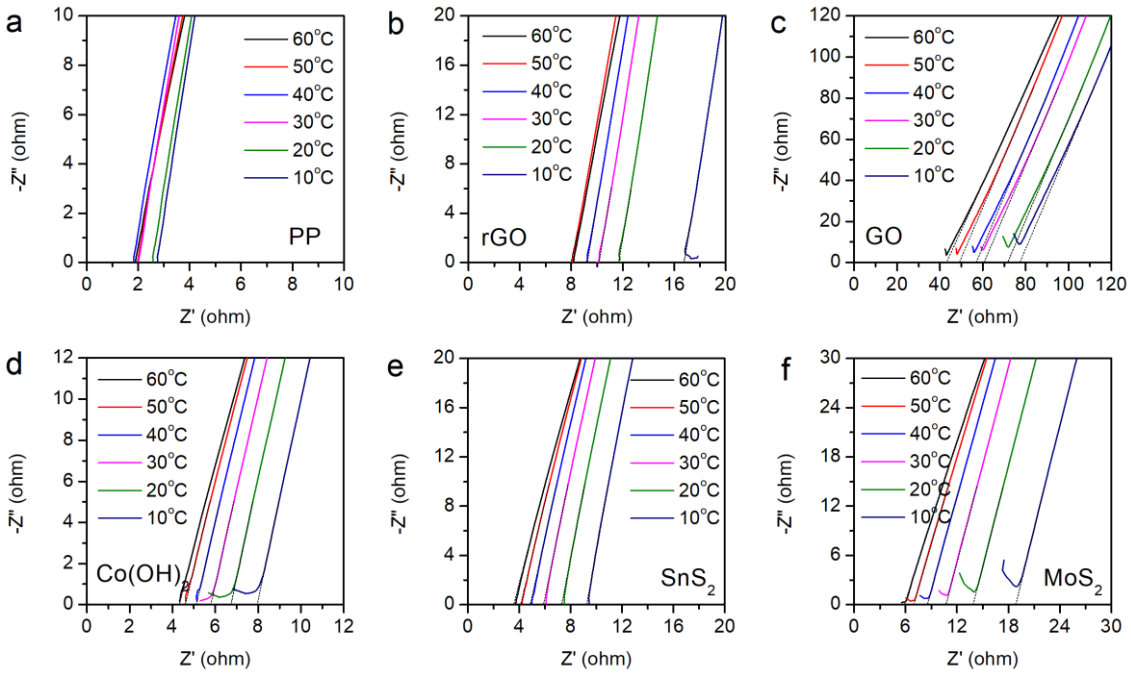

Figure S9. Electrochemical impedance spectroscopy (EIS) measurements performed at different temperatures for various separators.

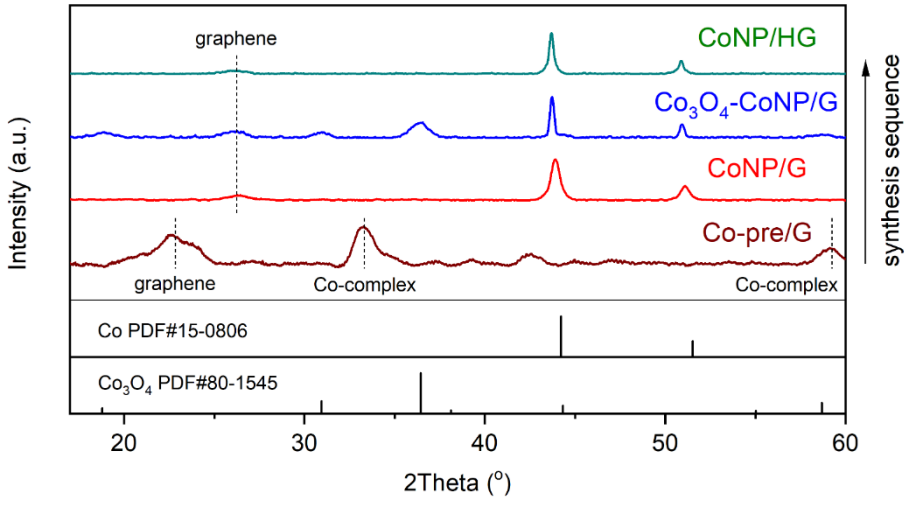

Figure S10. Synthesis sequence of HG before acid-treatment. The CoNP/HG obtained from the last step will be acid-treated using 8M hydrochloric acid solution at 60°C for at least 12 h to achieve the pure HG nanosheets.

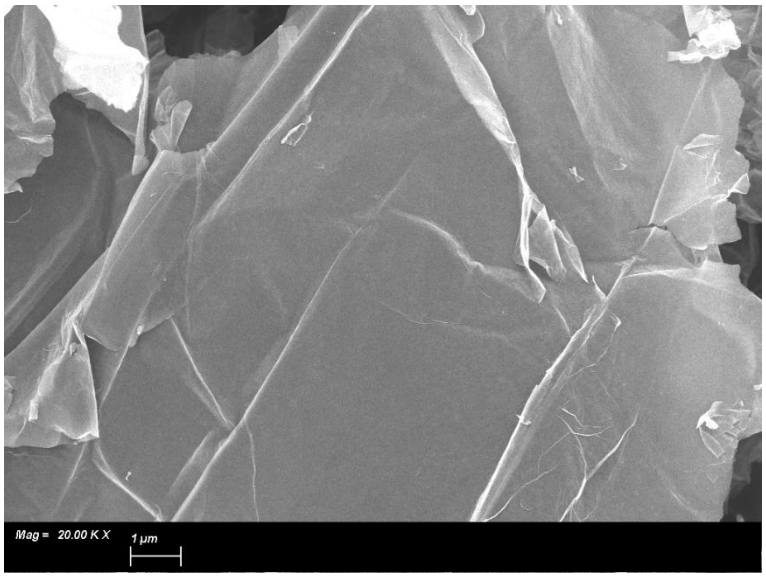

Figure S11. SEM image of Co-pre/G nanosheets.

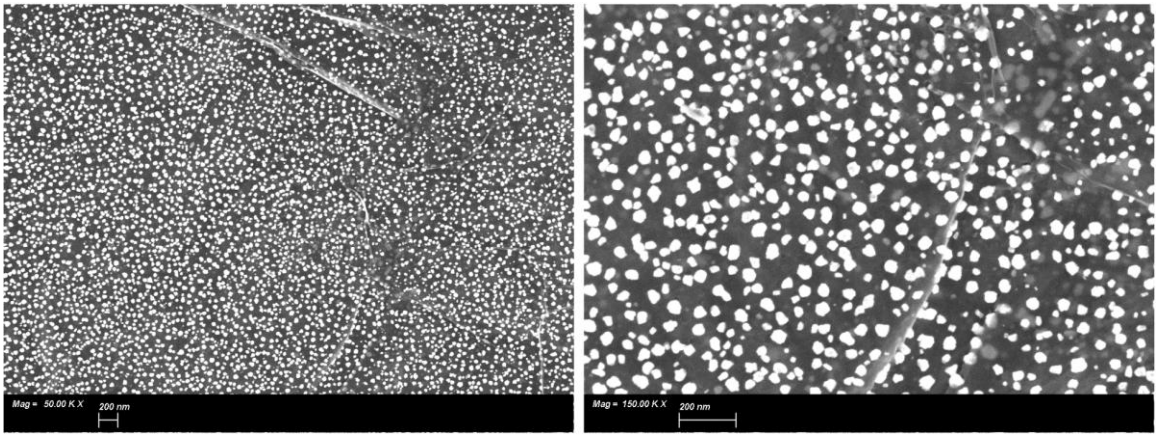

Figure S12. SEM image of CoNP/G nanosheets after annealed at 800°C in N_2. Note that at this stage of synthesis, the holes on graphene are not formed compared with Figure S13.

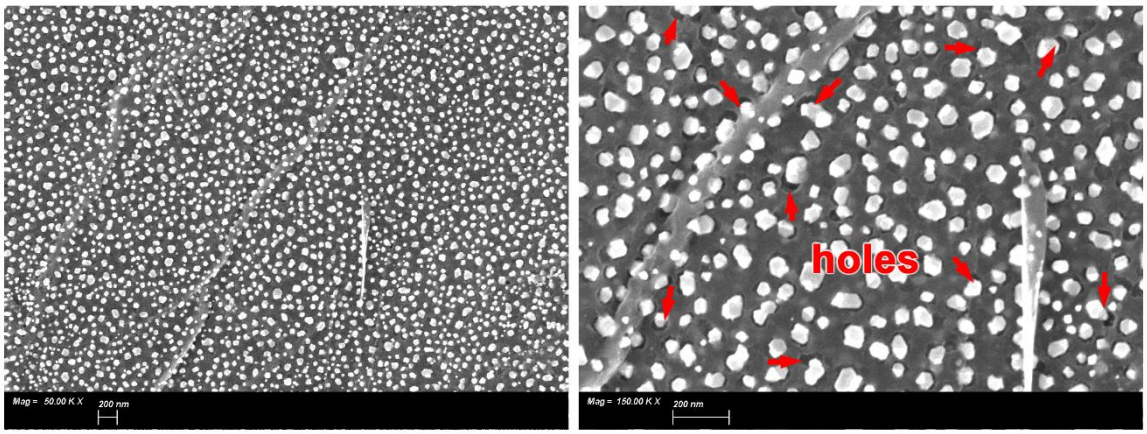

Figure S13. SEM images of CoNP/HG nanosheets after further annealing of the partially oxidized Co_3O_4-CoNP/G nanosheets at 800°C in N_2. Note that the holes on graphene (red arrows) began to reveal underneath the nanoparticles compared with Figure S12. This confirms that the holes are created by in-situ oxidation of graphene by the partially oxidized intermediate product Co_3O_4-Co nanoparticles, while the Co_3O_4 domains are carbothermically reduced to metallic Co at the same time.

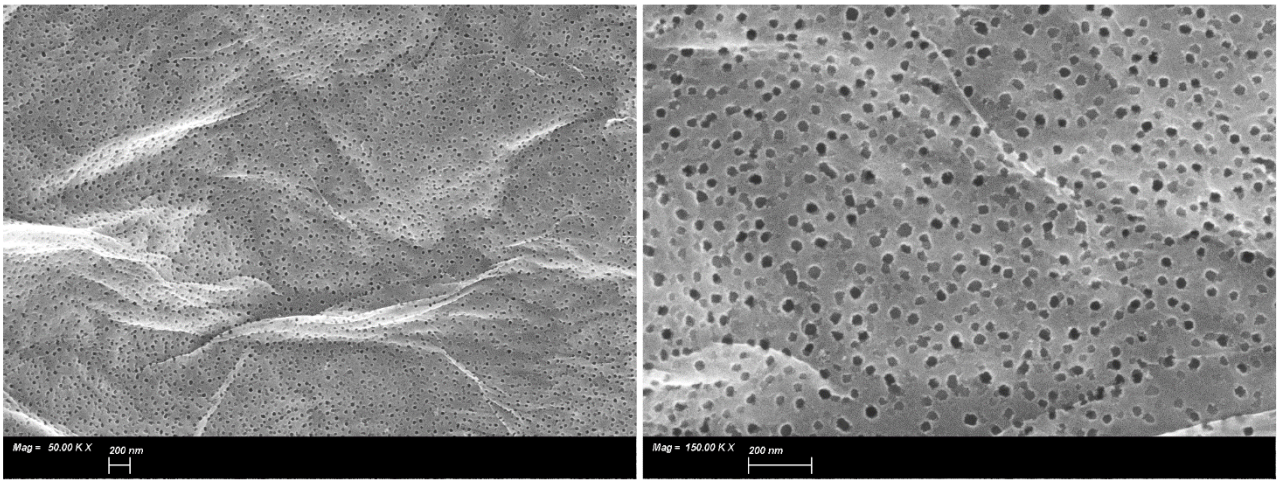

Figure S14. SEM images of 030HG nanosheets after acid-leaching.

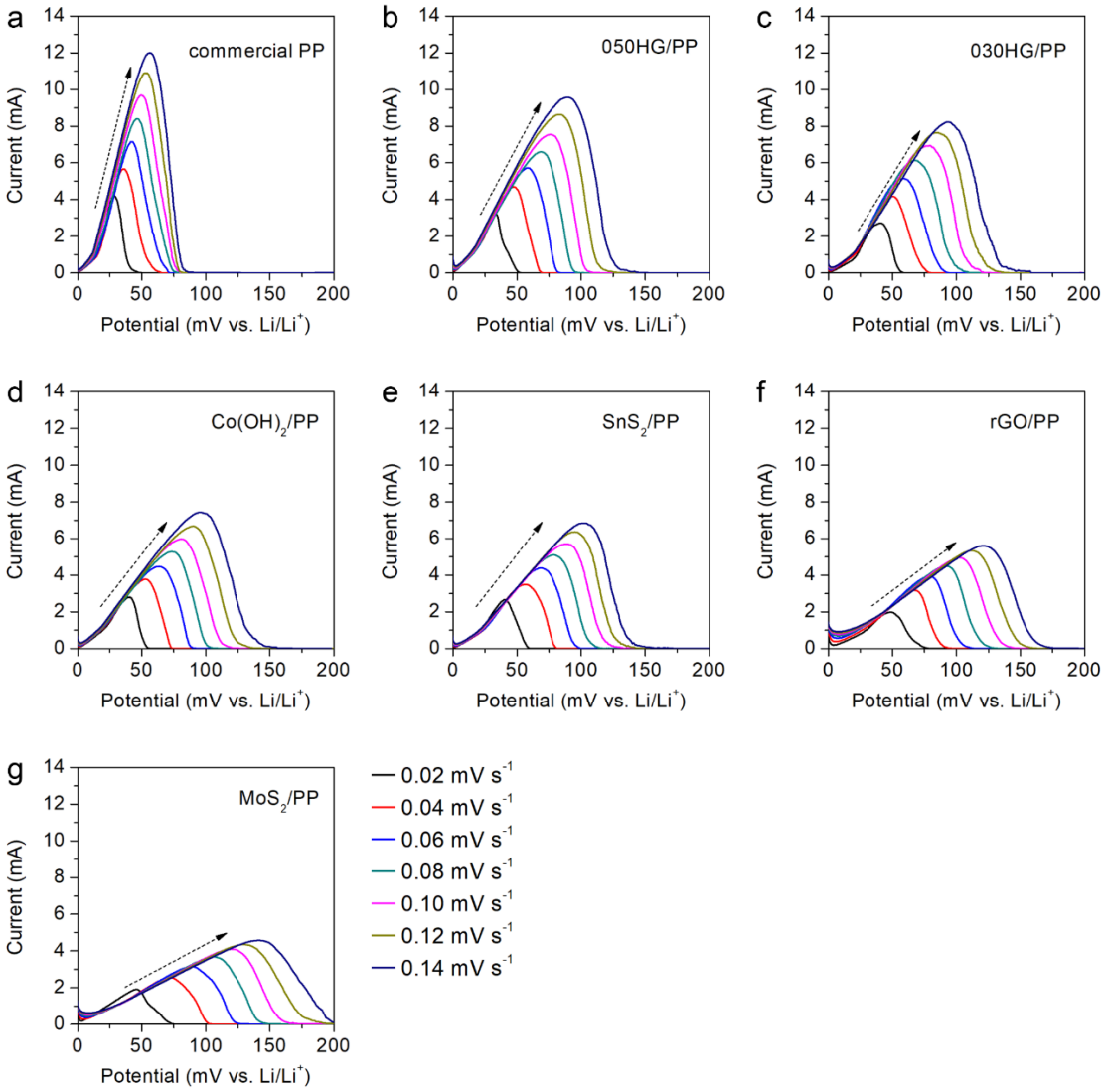

Figure S15. Linear sweep voltammetry (LSV) measurements performed at different sweeping rates for various separators.

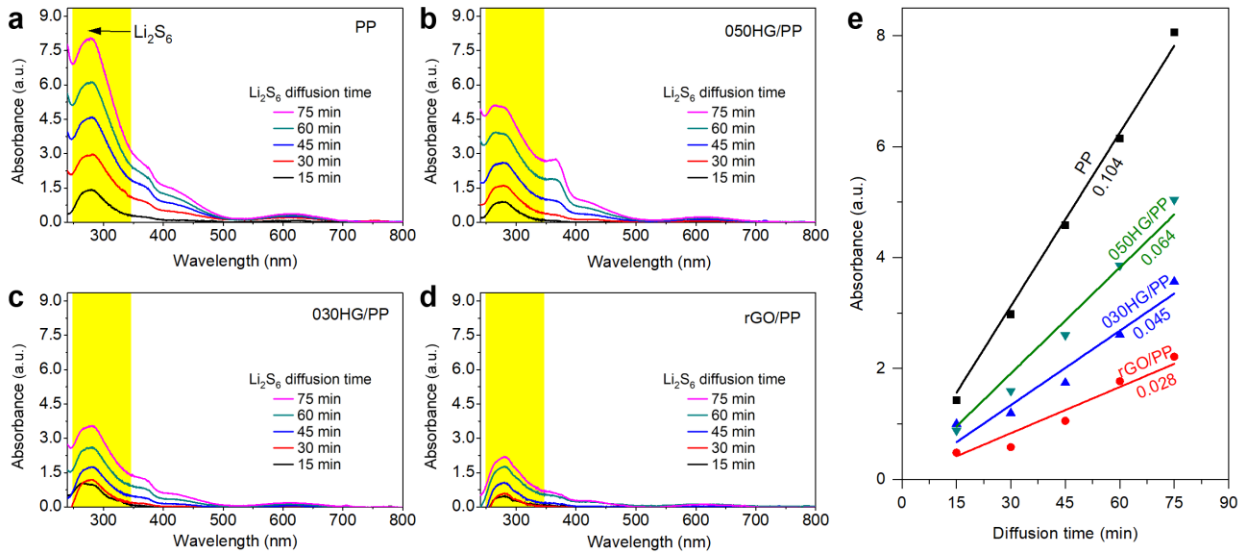

Figure S16. Soluble polysulfide (Li_2S_6) diffusion characterization through different separators in a H-cell. UV-vis absorbance of the clean solution during Li_2S_6 diffusion through the bare and membrane-modified separators: (a) PP, (b) 050HG/PP, (c) 030HG/PP, and (d) rGO/PP with the yellow highlighted area showing the wavelength absorption region of the polysulfides. (e) UV-vis absorbance peak values of Li_2S_6 at 280 nm as a function of the diffusion times for different separators. A larger slope of the fitted line indicates a higher Li_2S_6 diffusion rate through the membrane-modified and bare separators.

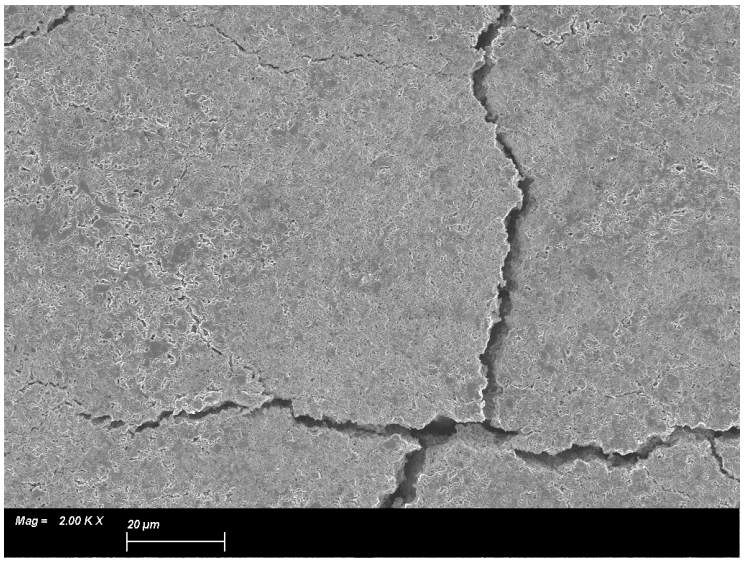

Figure S17. Surface morphology of Li foil after cycling with $Co(OH)_2$/PP separator. The surface of the lithium metal foil is covered with filaments, indicating that the Li^+ transport capability of the membrane in the battery is sufficient to fully utilize the lithium surface.

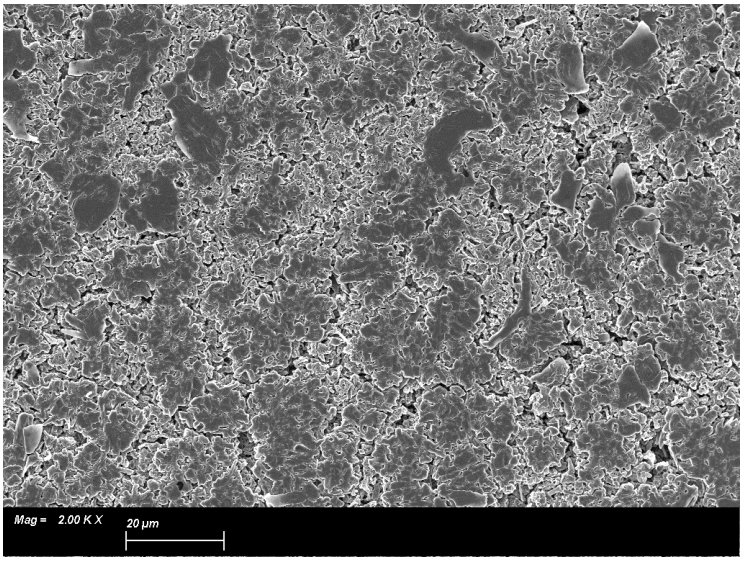

Figure S18. Surface morphology of Li foil after cycling with SnS_2/PP separator. The surface of the lithium metal foil is covered with filaments, indicating that the Li^+ transport capability of the membrane in the battery is sufficient to fully utilize the lithium surface.

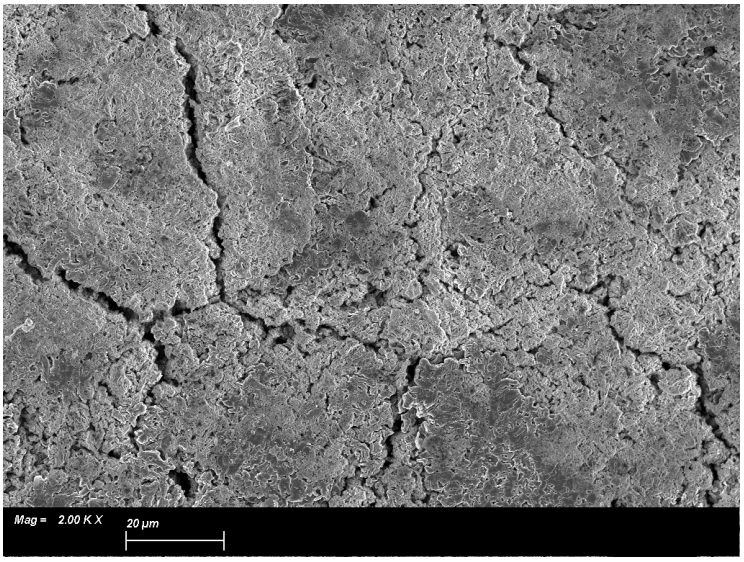

Figure S19. Surface morphology of Li foil after cycling with rGO/PP separator. The surface of the lithium metal foil is covered with filaments, indicating that the Li^+ transport capability of the membrane in the battery is sufficient to fully utilize the lithium surface.

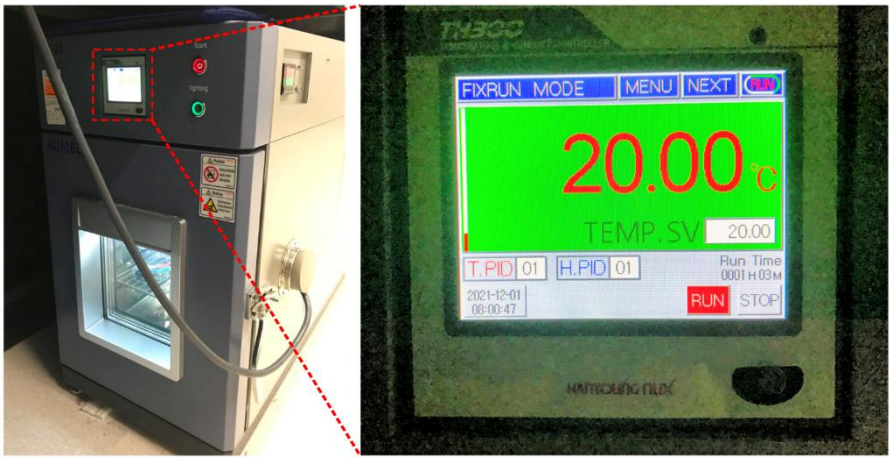

Figure S20. Constant-temperature chamber for temperature-dependent EIS tests.

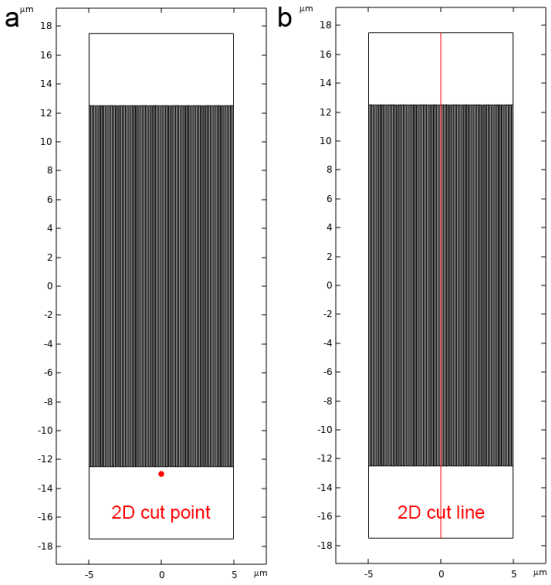

Figure S21. Data observation (control points) and collection method in modeling: (a) 2D cut point positioned 0.5 μm below the PP separator. (b) 2D cut line traversing the entire cell.

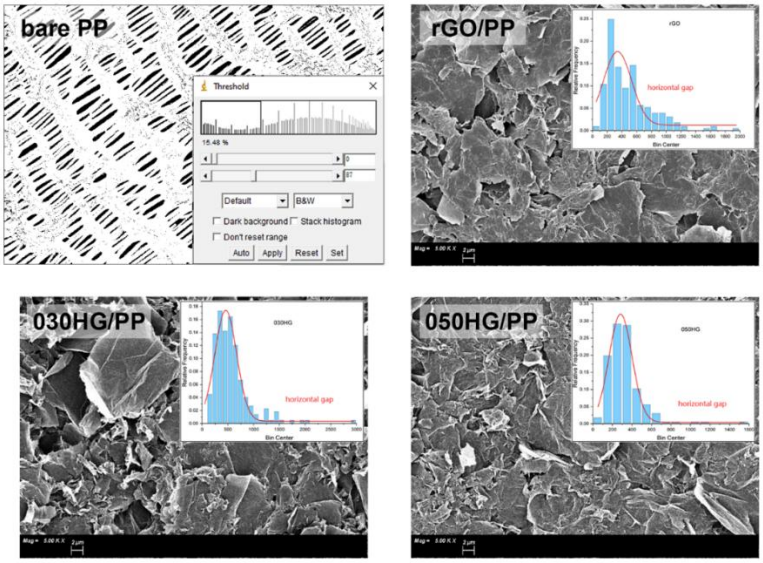

Figure S22. Statistical analysis of the pore area percentage of commercial PP separators and gap number and size between graphene nanosheets in the three types of modified separators.

2.8 SI References

1. Liu, B.; Torres, J. F.; Taheri, M.; Xiong, P.; Lu, T.; Zhu, J.; Liu, Y.; Yu, G.; Tricoli, A., Dual-Ion Flux Management for Stable High Areal Capacity Lithium–Sulfur Batteries. *Advanced Energy Materials* **2022,** *12* (10), 2103444.

2. Zhou, G.; Tian, H.; Jin, Y.; Tao, X.; Liu, B.; Zhang, R.; Seh, Z. W.; Zhuo, D.; Liu, Y.; Sun, J.; Zhao, J.; Zu, C.; Wu, D. S.; Zhang, Q.; Cui, Y., Catalytic oxidation of Li₂S on the surface of metal sulfides for Li−S batteries. *Proceedings of the National Academy of Sciences* **2017,** *114* (5), 840-845.

3. Liu, B.; Taheri, M.; Torres, J. F.; Fusco, Z.; Lu, T.; Liu, Y.; Tsuzuki, T.; Yu, G.; Tricoli, A., Janus Conductive/Insulating Microporous Ion-Sieving Membranes for Stable Li–S Batteries. *ACS Nano* **2020,** *14* (10), 13852-13864.

4. Torres, J. F.; Komiya, A.; Henry, D.; Maruyama, S., Measurement of Soret and Fickian diffusion coefficients by orthogonal phase-shifting interferometry and its application to protein aqueous solutions. *The Journal of Chemical Physics* **2013,** *139* (7), 074203.

5. Logan, E. R.; Gering, K. L.; Ma, X.; Dahn, J., Electrolyte Development for High-Performance Li-Ion Cells: Additives, Solvents, and Agreement with a Generalized Molecular Model. *The Electrochemical Society Interface* **2019,** *28* (2), 49.

6. Valøen, L. O.; Reimers, J. N., Transport Properties of LiPF6-Based Li-Ion Battery Electrolytes. *Journal of The Electrochemical Society* **2005,** *152* (5), A882.

7. Nishida, T.; Nishikawa, K.; Fukunaka, Y., Diffusivity Measurement of LiPF6, LiTFSI, LiBF4 in PC. *ECS Transactions* **2008,** *6* (18), 1.

Chapter 3 Holey Membranes with High Li^+ Mobility for Fast Sulfur Catalysis

3.1 Prologue

This chapter focus on the surface modification of separator with functionally designed membrane materials featuring tailored morphologies to enhance sulfur redox reaction (SRR) kinetics in lithium-sulfur (Li–S) batteries by facilitating Li^+ diffusion. The manuscript detailing this work is currently under review with my supervisors.

I designed this project, conducted the experiments, performed the material characterization, collected, analyzed and interpreted the data. Qi Wang from University of Sydney performed the XPS characterization, while Dr. Borui Liu contributed to the simulation part. I authored the manuscript, which was reviewed by Qi Wang, Prof. Zongyou Yin and Prof. Antonio Tricoli.

3.2 Abstract

Conventional strategies for designing membranes in Li–S batteries have mainly focused on mitigating the shuttle effect by entrapping polysulfides and promoting the sulfur redox reactions (SRRs) via catalyst integration. However, the negative impact of membrane morphology on Li^+ transport, which often hinders SRR, is frequently overlooked. This study introduces a Co_9S_8-grafted holey graphene (Co_9S_8/HG) electrocatalyst as a representative multifunctional membrane, highlighting the essential role of Li^+ transport in optimizing SRR processes. TEM and statistical analysis

reveal that the Co_9S_8/HG composite features a porosity of ~16.2%, higher than commercial PP separators (15.5%), ensuring minimal resistance to Li^+ migration. Experimental findings, supported by computational simulations, demonstrate that Co_9S_8/HG presents an improved SRR kinetics and Li_2S precipitation, suggesting that the holey-structured membrane provides abundant pathways for efficient Li^+ transport and thereby accelerating the rate-determining step during discharge. The resultant Li–S cells deliver superior rate performance compared to the non-porous counterpart (Co_9S_8/G) and exhibit exceptional cycling stability, maintaining a discharge capacity of 671 mAh g^{-1} over 900 cycles with a low decay rate of 0.044% per cycle. This work underscores the importance of balancing polysulfide retention with enhanced Li^+ transport, offering insights for rational design of advanced membranes in Li–S batteries and related systems.

3.3 Introduction

Lithium–sulfur (Li–S) batteries, with a high theoretical energy density of 2500 Wh kg^{-1}, represent a promising frontier in energy storage technology. The abundance and environmental friendliness of sulfur also add to their appeal as a future energy solution.[1, 2] Despite these advantages, the practical application of Li–S batteries is hindered by a number of persistent challenges, predominantly involving the shuttling effect, sluggish reaction kinetics of LiPSs, and a high electronic resistivity in the Li_2S precipitation.[3] This phenomenon, involving the dissolution-migration of LiPSs intermediates (Li_2S_n, $4 \leq n \leq 8$) and possible detachment of Li_2S from conductive

support, leads to rapid capacity fade, reduced sulfur utilization, and compromised Coulombic efficiency, hampering their practical application. [4-6]

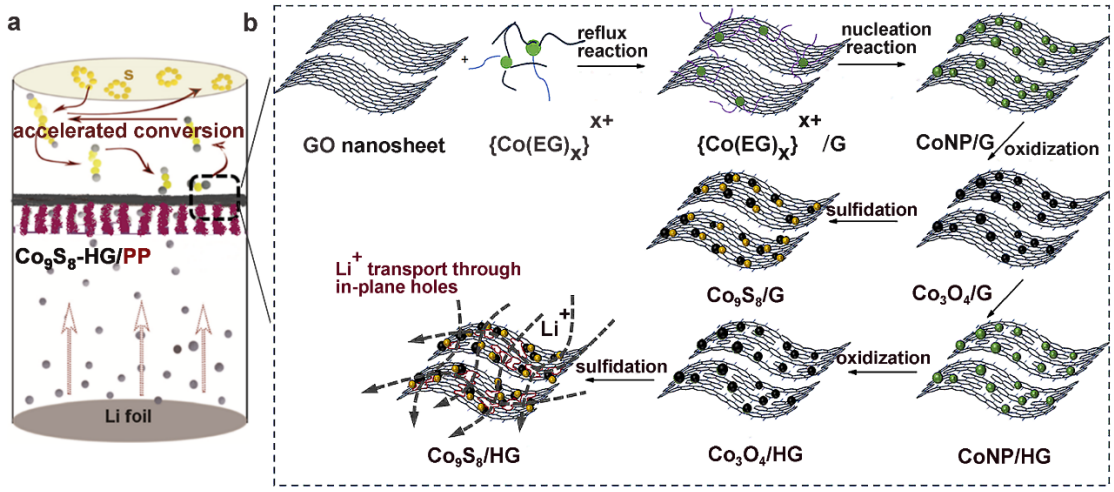

Figure 3-1. (a) Li–S batteries with built-in Co_9S_8/HG membrane. (b) Schematic of the synthesis process of Co_9S_8/HG nanosheets and Li^+ transport through the in-plane holes

Conventional approaches to suppress the LiPSs shuttle movement focus on optimizing sulfur hosts,[7-10] modifying membranes,[11-14] developing multifunctional binders,[15, 16] and solid-state electrolytes.[17-19] Among these approaches, the design of a multifunctional polysulfide-blocking membrane positioned between the separator and cathode is regarded as a straightforward and efficient strategy.[20-22] Two-dimensional (2D) materials such as graphene oxide (GO),[23-25] reduced graphene oxide (rGO),[26-28] transition metal dichalcogenides,[27] and functional polymers[29, 30] have garnered significant attention due to their structural diversity, the presence of abundant polar, lipophilic, or negative charged functional groups. These materials temporarily immobilize polysulfides through Li bond formation or by inducing electrostatic interactions. However, this chemisorption strategy does not fundamentally address the

shuttle effect. During charging and discharging, sulfur compounds undergo hysteretic transformations in the SRR processes, causing polysulfide accumulation. This accumulation intensifies the shuttle effect and reduces sulfur cathode utilization.[31-35] To address this, the integration of SRR electrocatalysts, such as metal oxides,[36, 37] nitrides,[32] and sulfides,[38, 39] onto membranes based on carbonaceous scaffold has been explored to enhance the conversion kinetics of contained LiPSs.[40-44] (Figure 3-1a). The carbon scaffold acts as a secondary electron collector,[45] capable of physically accommodating the soluble polysulfides while providing sufficient electronic conductivity for the electrochemical reactions. Despite these advancements, current solutions often overlook the symbiotic interaction between sulfur species and lithium cations in sulfur conversion reactions. This limitation is particularly evident in membrane designs that primarily focus on managing LiPSs migration and promoting SRR catalysis, while the crucial role of Li^+ transport in SRR kinetics has not been adequately studied. High Li^+ diffusivity enables Li^+ to rapidly reach active catalytic sites, thereby facilitating fast engagement in LiPSs redox reactions. Meanwhile, the Li_2S precipitation process is directly influenced by the efficiency of Li^+ and electron transport.[46] Enhanced Li^+ mobility and efficient electron pathways facilitate uniform and stable Li_2S deposition.

In this work, we introduced a Co_9S_8-embedded holey graphene (Co_9S_8/HG) membrane as a representative electrocatalyst, emphasizing its role in enhancing SRR kinetics and Li_2S precipitation through mediating Li^+ transport in a holey-structured modified membrane. Co_9S_8 exhibits a strong chemical binding energy of 4.03 eV with LiPS

species, forming stable Co–S and Li–S bonds that effectively trap LiPSs and suppress its diffusion.[47] Additionally, the Li^+ diffusion energy required on the surface of Co_9S_8 is 0.31 eV, nearly identical to that of pristine graphene (0.3 eV),[48] suggesting an enhanced conductivity with the Co_9S_8/HG membrane. The holey graphene substrate offers efficient migration channels for fast electron and Li^+ transfer,[49] thereby accelerating LiPSs conversion kinetics and decreasing the reaction resistance for Li_2S deposition process. This unique combination of strong chemical binding, effective LiPSs trapping, and optimized Li^+ transport pathways enable the Co_9S_8/HG membrane to accelerate SRR kinetics and improve battery stability.

3.4 Results and discussion

3.4.1 Morphology and composition Characterization

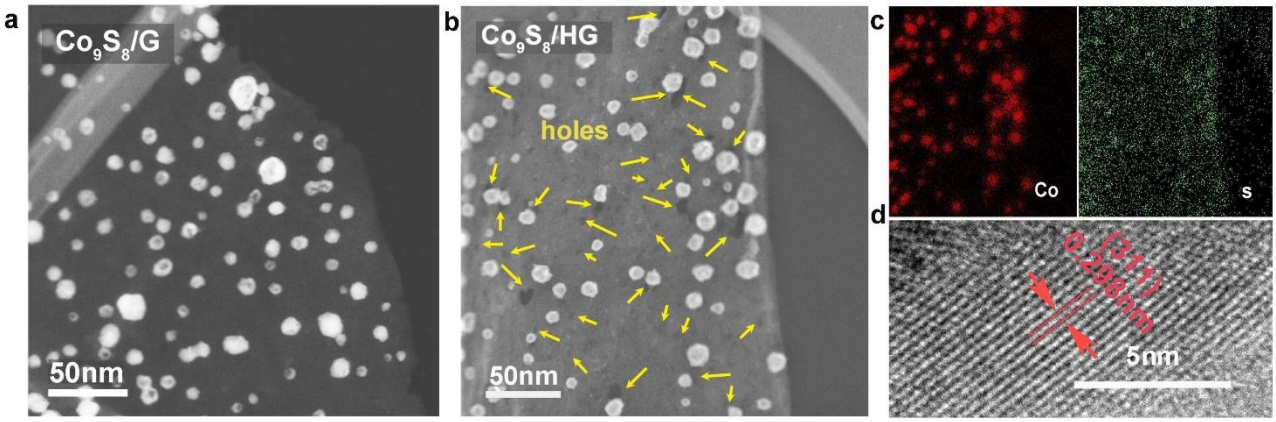

Figure 3-2. Morphology and composition characterization of Co_9S_8/HG and Co_9S_8/G nanosheets**.** TEM images of (a) Co_9S_8/G and (b) Co_9S_8/HG nanosheets. (c) EDS mapping of Co_9S_8/HG. (d) High-resolution TEM (HRTEM) image of Co_9S_8/HG.

Two membrane materials, namely the traditional Co_9S_8/G (non-hole structure) and the new Co_9S_8/HG (holey structure), are synthesized to illustrate the crucial role of rapid Li^+ diffusion in enhancing the kinetics of SRR processes. The synthesis procedures of

Co_9S_8/G and Co_9S_8/HG nanosheets are shown in Figure 3-1b (SI: Experimental Method). Specifically, GO flakes and cobalt acetate were subjected to a solvothermal reaction, yielding a uniform dispersion of cobalt precursor on rGO nanosheets, termed the Co-pre/G composite (Figure S1). Subsequent annealing of the Co-pre/G composite at 800°C under an N_2 atmosphere resulted in the formation of well-distributed cobalt nanoparticles on rGO nanosheets (CoNP/G, Figure S2). These CoNPs were then converted to cobalt oxides (Co_3O_4) through a mild thermal oxidation process in air. The resulting Co_3O_4/G underwent a gas-phase sulfidation reaction to form the non-hole Co_9S_8/G composite (Figure 2a). To fabricate the holey-structured Co_9S_8/HG composite, we repeated the above annealing procedures with Co_3O_4/G, employing a thermal etching technique to create nanoholes on the graphene basal plane, thus obtaining CoNPs on holey graphene (CoNP/HG, Figure S3) and Co_3O_4 on holey graphene (Co_3O_4/HG, Figure S4), respectively. The final transformation involved sulfurizing Co_3O_4/HG to synthesize the Co_9S_8/HG composite (Figure 2b).

The morphology and structure of the as-prepared samples were characterized using TEM and scanning electron microscopy (SEM). Figure 3-2a and Figure 3-2b show that Co_9S_8 nanoparticles are uniformly dispersed on graphene nanosheet while in Figure 3-2b visible nanoholes can be observed on the surface of Co_9S_8/HG lamellae. The EDS mapping of Co_9S_8/HG (Figure 3-2c) shows the elemental compositions of Co and S, confirming the successful gas-phase conversion of Co_3O_4 to Co_9S_8. HRTEM analysis confirms the crystalline phase of Co_9S_8, with the lattice fringe spacing of 0.298 nm corresponds to the (311) planes of Co_9S_8 (Figure 3-2d).

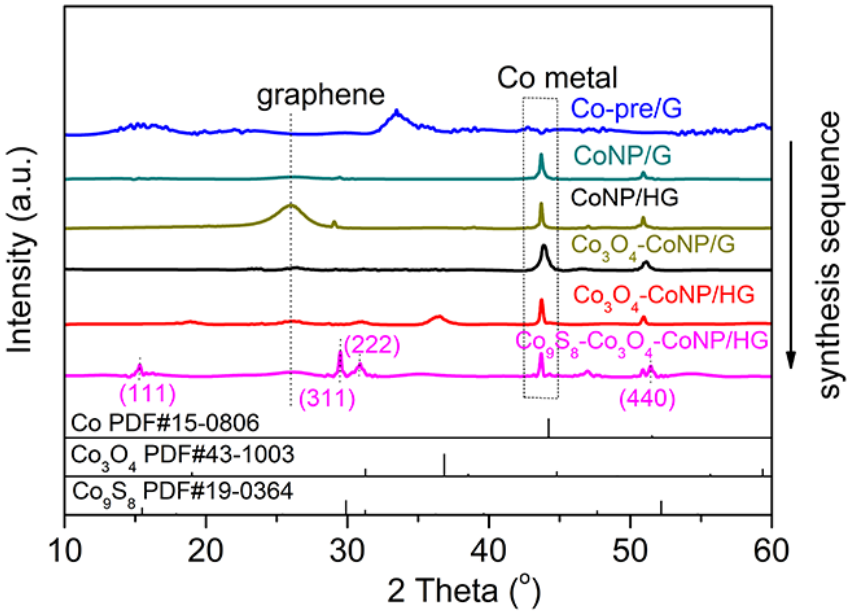

Figure 3-3. X-ray diffraction (XRD) results of the synthesized intermediates and final product.

The intermediate materials from Co-precursor to the generation of Co_9S_8 were examined by XRD (Figure 3-3). The four diffraction peaks at 15.5°, 29.9°, 31.2°, and 52.0° match the (111), (311), (222) and (440) peaks of cubic Co_9S_8 (PDF#19-0364). The main peak of metallic Co at 44.2° exist throughout the whole synthesis process. The reason is attributed to the core-shell structure formed during the synthesis.

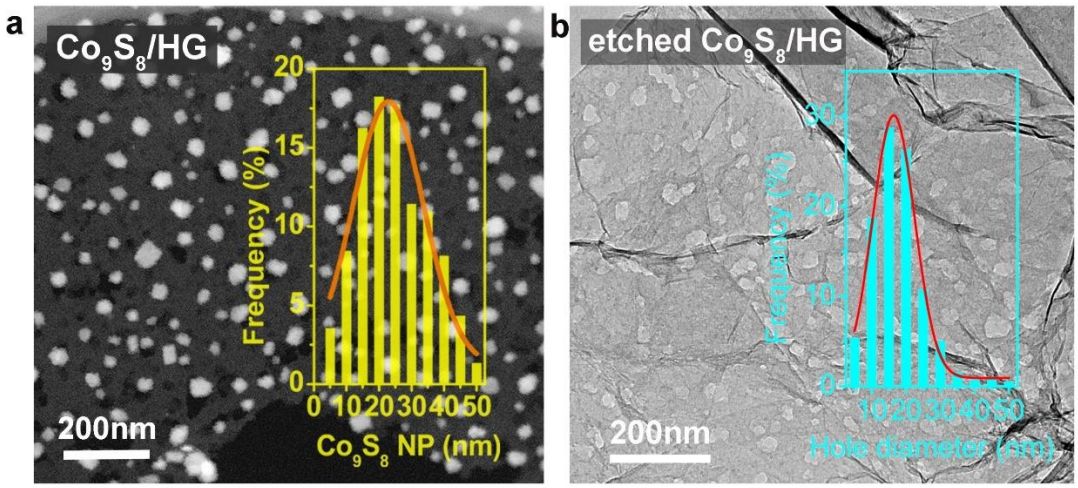

Figure 3-4. Statistical analysis of synthesized membranes. (a) Co_9S_8 nanoparticle size distribution, (b) hole size distribution of etched Co_9S_8/HG.

Figure 3-4a shows the size distribution of Co_9S_8 nanoparticles on the Co_9S_8/HG nanosheets, with an average size of ~22 nm, slightly larger than that of the Co_3O_4 nanoparticles (~15 nm, Figure S4). Figure 3-4a also reveals that the Co_9S_8 catalyst nanoparticles on graphene are situated adjacent to the engineered nanoholes, facilitating the rapid capture and conversion of sulfur species entrapped by the membrane pores into insoluble Li_2S_2/Li_2S phases, thereby enhancing the cyclic performance of the battery.

To quantify the size distribution of holes on the Co_9S_8/HG composite, hydrochloric acid was employed to remove Co_3O_4 nanoparticles from the Co_3O_4/HG nanosheets (the precursor of Co_9S_8/HG), thereby fully exposing the holes (Figure 3-4b). Statistical analysis indicates that the average hole diameter is ~18 nm with a population density of 306 holes μm^{-2}, which roughly aligns with that (366 NPs μm^{-2}) of the etchant 'Co_3O_4 NPs' (Figure S4). Furthermore, the holey area on the Co_9S_8/HG composite accounts for ~16.2% of the total graphene nanosheet surface, suppressing the pore area fraction on commercial PP membrane (~15.5%). Hence, these nanoholes can enable the swift passage of Li^+ across the membrane, effectively engaging them in electrocatalytic reactions with the captured LiPSs.

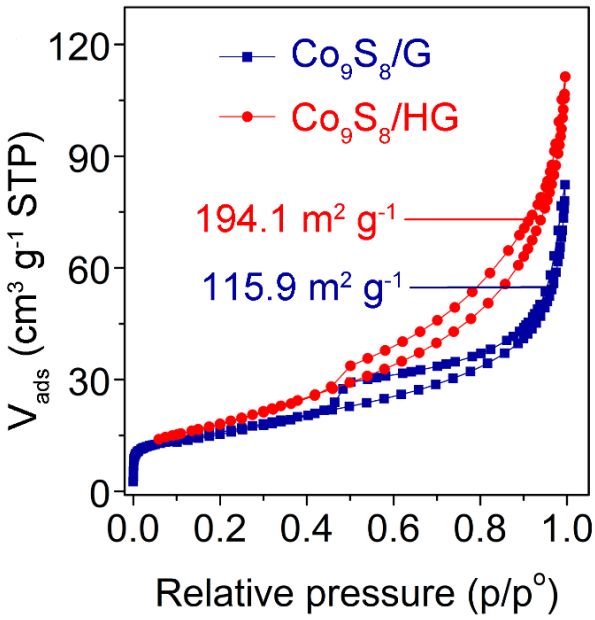

Figure 3-5. Brunauer-Emmett-Teller (BET) nitrogen adsorption-desorption analysis.

The specific surface areas (SSA) measured by the BET method for the prepared Co_9S_8/HG is 194.1 $m^2\ g^{-1}$, 67.5% higher than that of its non-hole counterpart Co_9S_8/G (Figure 3-5). The large SSA exposes a greater number of Co_9S_8 nanoparticles, enhancing the adsorption of LiPSs, accelerating their conversion, and promoting the deposition of Li_2S.

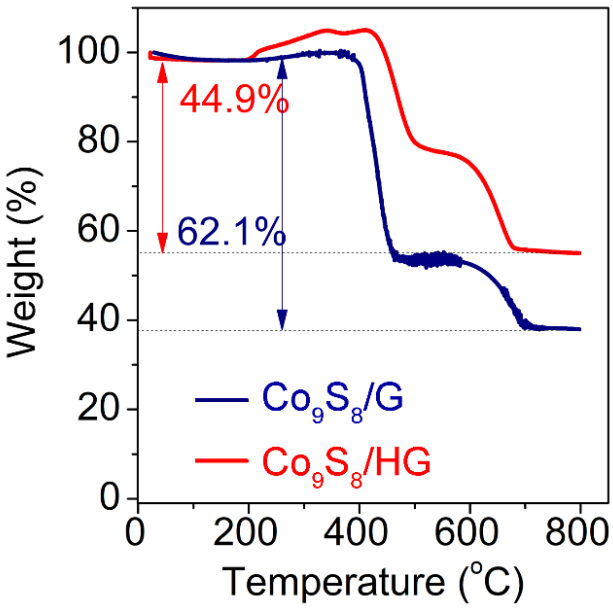

Figure 3-6. Thermalgravimetric analysis (TGA) results showing the weight ratio of Co_9S_8 to graphene.

TGA results (Figure 3-6) reveal that the Co_9S_8/HG composite contains 17.2% less graphene, which is attributed to the loss of carbon during formation of the holey structure process.

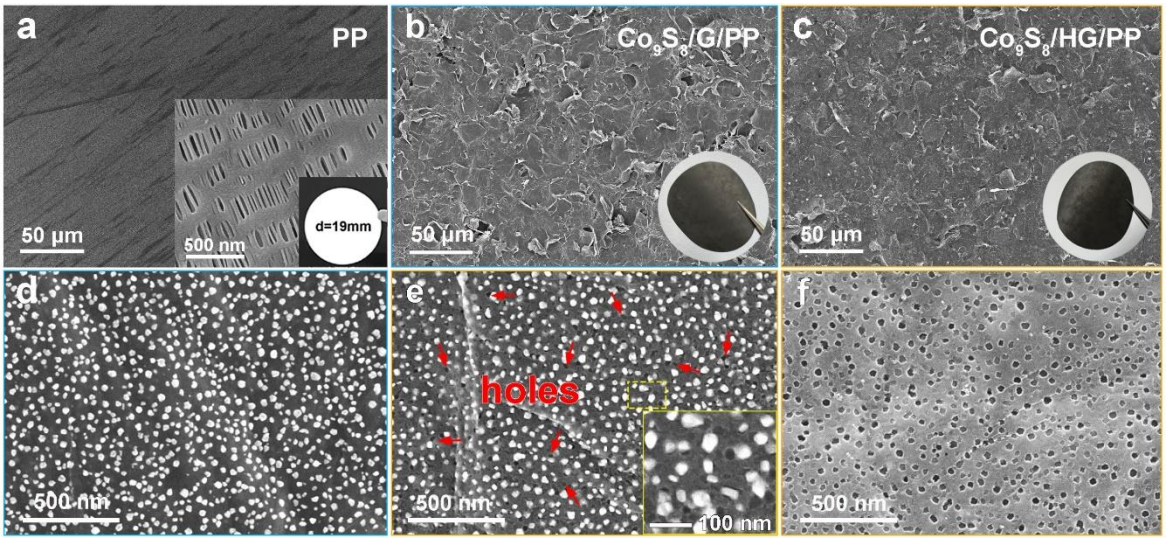

Figure3-7. SEM characterization of modified membranes**.** (a) commercial PP, (b) Co_9S_8/G/PP, and (c) Co_9S_8/HG/PP separators. The material loadings of Co_9S_8/G and Co_9S_8/HG are approximately 0.18 mg cm^{-2}. Insets: digital images of the separators showing their macroscopic appearance. SEM images showing the surface morphology

of (d) Co_9S_8/G and (e) Co_9S_8/HG membranes, and (f) Co_9S_8/HG membrane with Co_9S_8 nanoparticles removed.

The modified separators were prepared by ultrasonically dispersing synthesized Co_9S_8/HG, or Co_9S_8/G onto a commercial PP substrate (Celgard 2400), achieving a mass loading of 0.18 mg cm^{-2}, denoted as Co_9S_8/G/PP and Co_9S_8/HG/PP separators, respectively (SI: Experimental Method). The surface morphologies of these modified separators were analyzed by SEM (Figure 3-7), with insets displaying their macroscopic appearance. The commercial PP separator (Figure 3-7a) exhibits a flat surface with unevenly distributed strip-like pore arrays (~100 nm in length). In contrast, the roll-pressed Co_9S_8/G/PP (Figure 3-7b, d) and Co_9S_8/HG/PP separators (Figure 3-7c, e) are covered with tightly stacked 2D lamellae, leaving no visible uncovered areas. This compact morphology effectively inhibits the shuttle effect of soluble polysulfides.[49] The Co_9S_8/HG/PP separator further features pore-forming modifications (Figure 3-7f), enabling lithium-ion diffusion through densely stacked graphene layers. This unique structure reduces membrane resistance, enhances ion conductance, lowers overpotential, and ultimately improves the rate performance and energy density of Li–S batteries.

3.4.2 Li^+ diffusion resistance measurement

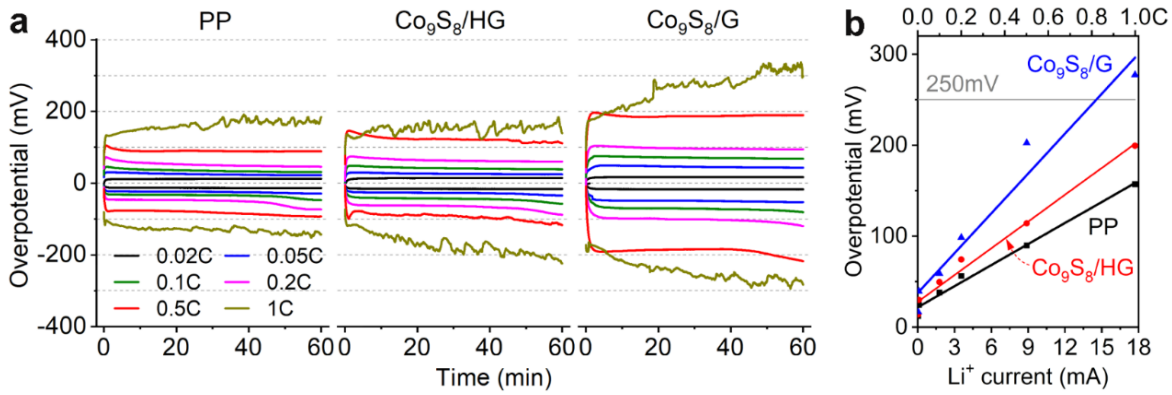

Figure 3-8. Overpotentials of Li^+ transport through different modified separators at various C-rates (assuming a sulfur loading of 6 mg cm^{-2} in Li–S cells).

To elucidate the impact of nano-perforations on modulating the Li^+ permeability in membranes, the charge/discharge overpotential, $E_{a\text{-}Li^+}$ and D_{Li^+} were investigated using two distinct cell configurations integrating separators made of PP, Co_9S_8/HG/PP, and Co_9S_8/G/PP (referred to as PP, Co_9S_8/HG, and Co_9S_8/G in the figure labels, respectively).

The overpotential associated with Li^+ transport was first measured in Li|Li symmetric coin cells with 1 M LiTFSI electrolyte, devised to eliminate the influence of SRR kinetics. To ensure that the observed effects originated from the modified layers alone, Co_9S_8/HG and Co_9S_8/G were sandwiched between two PP sheets, preventing any lithiation or side reactions involving Co_9S_8 (SI: Experimental Method). Galvanostatic charging/discharging assessments were performed at various nominal C-rates consistent with those of Li–S cells, each maintaining a sulfur loading of 6 mg cm^{-2}. As shown in Figure 3-8a, b, the overpotentials for Co_9S_8/HG/PP and Co_9S_8/G/PP separators are compared with that of the PP separator across current rates from 0.02

C to 1 C. Results reveal that while the modified coating layers increased diffusion impedance for Li^+ transport, the Co_9S_8/HG/PP separator exhibited a significantly lower overpotential (reduced by 31.8% and 32.8% at 0.5 C and 1 C, respectively) compared to the Co_9S_8/G/PP separator. This improvement is attributed to the holey structure of Co_9S_8/HG membrane, which provides cross-plane ion channels, reducing Li^+ diffusion distance through interlayer spaces and in-plane pathways. In contrast, the non-hole Co_9S_8/G/PP separator exhibits a high overpotential of approximately 290 mV at 1 C (Figure 3-8b), indicating a significant barrier to Li^+ transport. The findings highlight the advantage of introducing nano-perforations into the modified separator, which effectively mitigates the overpotential associated with non-porous structures and improves Li^+ transport dynamics.

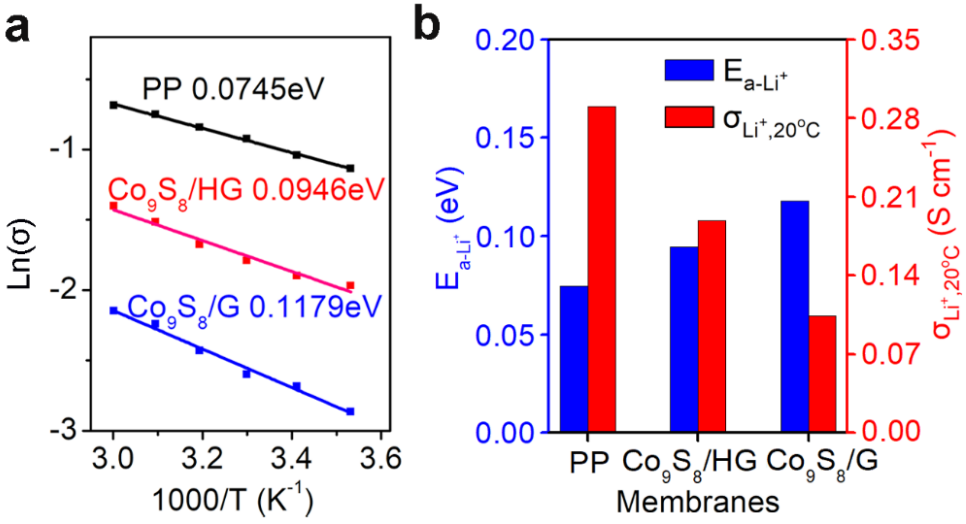

Figure 3-9. Li^+ activation energy ($E_{a\text{-}Li}{}^+$) and Li^+ conductance ($\sigma_{Li}{}^+$) of different modified membranes

Moreover, the $E_{a\text{-}Li}{}^+$ and $\sigma_{Li}{}^+$ of Li^+ transport through the modified separators (Figure 3-9) were investigated at room temperature (20℃) using Nyquist plots from electrochemical impedance spectroscopy (EIS) with stainless steel (SS)|SS symmetric

cells (Figure S6, SI: Experimental Method). The σ_{Li^+} values, in descending order, are (Figure 3-9b): PP (0.175 S cm^{-1}) > Co_9S_8/HG/PP (0.109 S cm^{-1}) > Co_9S_8/G/PP (0.068 S cm^{-1}). Correspondingly, $E_{a\text{-}Li^+}$ increased in the same order, indicating that physical obstruction in the membranes reduces Li^+ conductance by increasing $E_{a\text{-}Li^+}$.

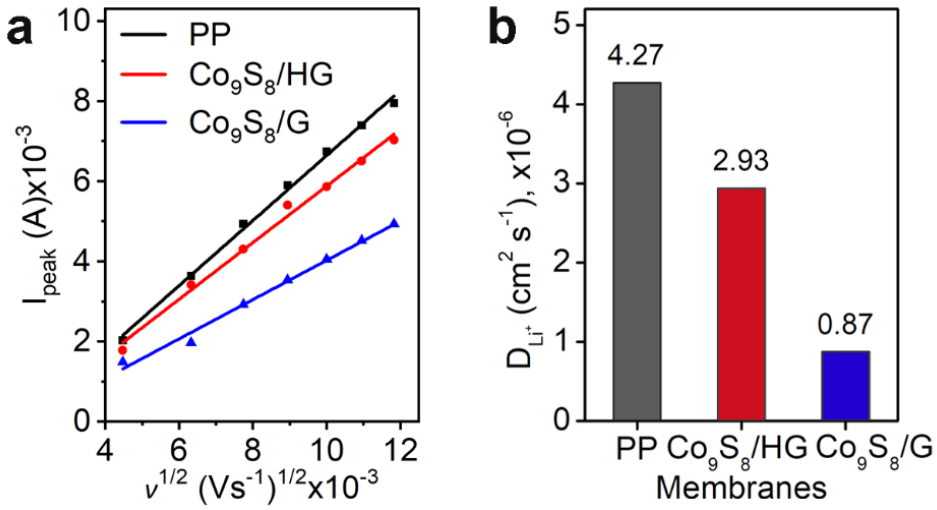

Figure 3-10. Li^+ diffusion coefficient (D_{Li^+}) analysis**.** (a) Linear relationship between peak current (I_{peak}) and the square root of scan rates ($u^{1/2}$) from linear sweep voltammetry (LSV) results. (b) Li^+ diffusion coefficient (D_{Li^+}) of Li|SS half cells with different separators.

The D_{Li^+} for PP, Co_9S_8/HG/PP, and Co_9S_8/G/PP separators were derived from LSV measurements in Li|SS half cells (Figure S7, SI: Experimental Method). Briefly, a fixed capacity of 1 mAh lithium is galvanostatic electroplated onto the SS plate, followed by electrostripping to obtain peak currents at varying scan rates. The results (Figure 3-10) show that the Co_9S_8/HG/PP separator (D_{Li^+} = 2.93 cm^2 s^{-1}) exhibits a significantly higher D_{Li^+} than Co_9S_8/G/PP (D_{Li^+} = 0.87 cm^2 s^{-1}), consistent with the σ_{Li^+} trend. These findings demonstrate that the holey-structured Co_9S_8/HG membrane facilitates efficient

Li^+ migration transport between cathode and anode. Enhanced Li^+ conductance serves as a key factor enabling rapid charge-discharge cycles in Li–S batteries.

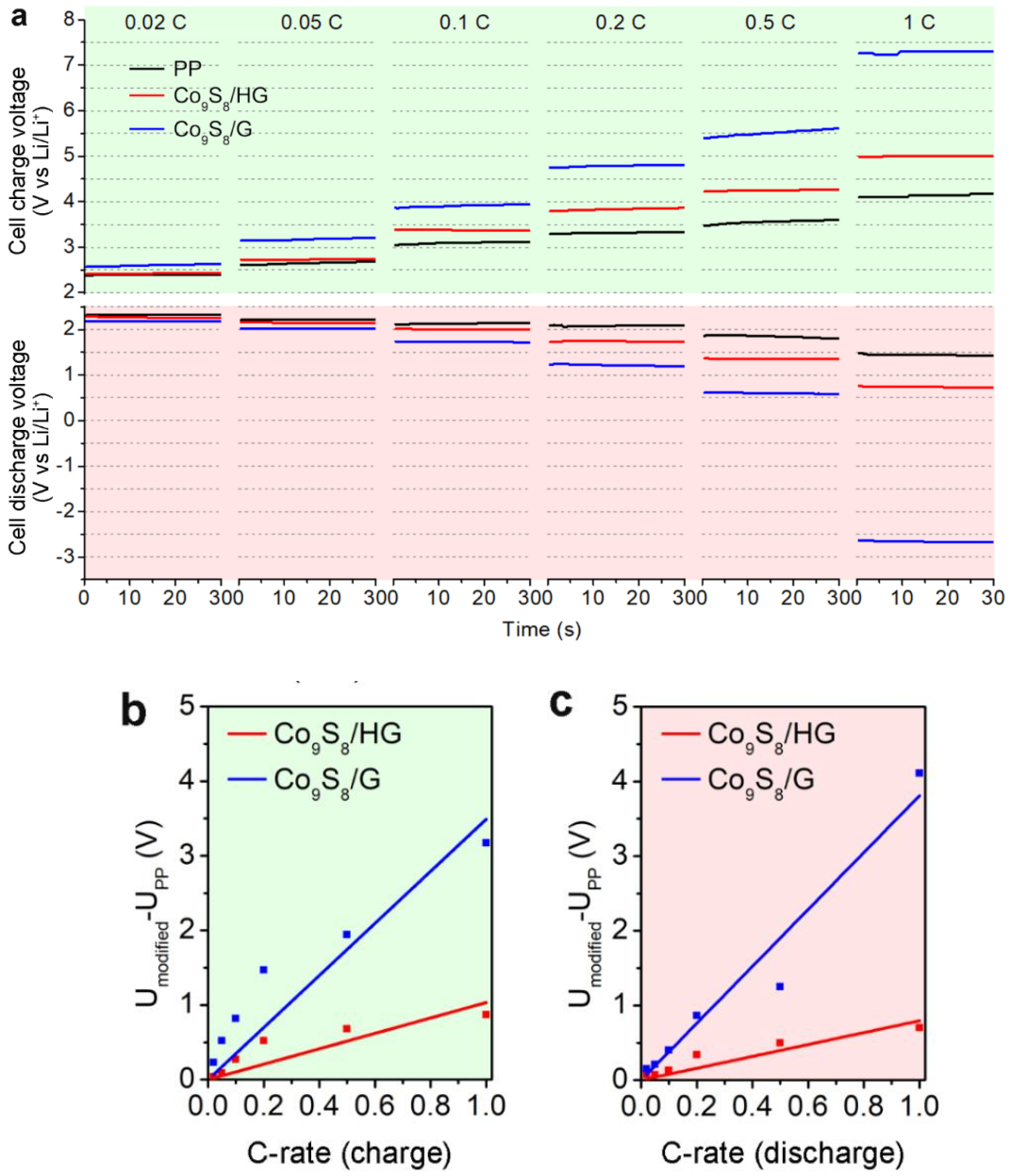

Figure 3-11. (a) Overpotential measurement in H-cell configuration with 0.2 M Li_2S_6 catholyte using different separators. Modified separators show higher overpotentials than the PP separator during (b) charging and (c) discharging across different C-rates.

To extend the evaluation of Li^+ transport properties, the impact of membranes on lithium-ion overpotentials was further examined using an H-cell configuration (Figure

S8) to address the cathode activation and diffusion impedance challenges. This setup consists of a lithium foil anode, a porous carbon-coated aluminum foil cathode current collector, a tightly sealed separator, and 40 mL of 0.2 M Li_2S_6 catholyte on each side, with continuous magnetic stirring to minimize diffusion impedance. The charging and discharging plateau voltages recorded from 30s-tests of the H-cell at different C-rates using the modified separators are compared to the commercial PP separator as a control (Figure 3-11a). The holey-structured Co_9S_8/HG/PP separator demonstrates a moderate increase in overpotential (e.g., 0.87 V and 0.70 V at 1 C for charge and discharge, respectively) compared to the commercial PP separator, but performed significantly better than the conventional non-hole Co_9S_8/G/PP separator, which exhibits substantially higher overpotentials (e.g., 3.17 V and 4.11 V for charge and discharge, respectively, vs. PP separator Figure 3-11b, c). These observations align with previous studies, which suggest that increased overpotentials can lead to notable energy density losses in batteries.[50] However, the holey-structured Co_9S_8/HG/PP separator mitigates overpotential by facilitating efficient Li^+ transport during charging and discharging processes, ensuring a sufficient Li^+ supply to the SRR catalysts, thereby maximizing their catalytic performance. This enhancement highlights the advantages of the holey-structured membranes in practical Li–S systems by rationally balancing the polysulfide blockage and the facilitation of rapid Li^+ transport to achieve efficient SRR catalysis.

3.4.3 Simulation Calculation of Li^+ transport through modified separator

To gain a deeper understanding of the mechanism behind the observed phenomena, simulations were conducted using COMSOL Multiphysics software to investigate lithium-ion diffusion through various separators: bare PP, Co_9S_8/G/PP, and Co_9S_8/HG/PP (Figure 3-12).

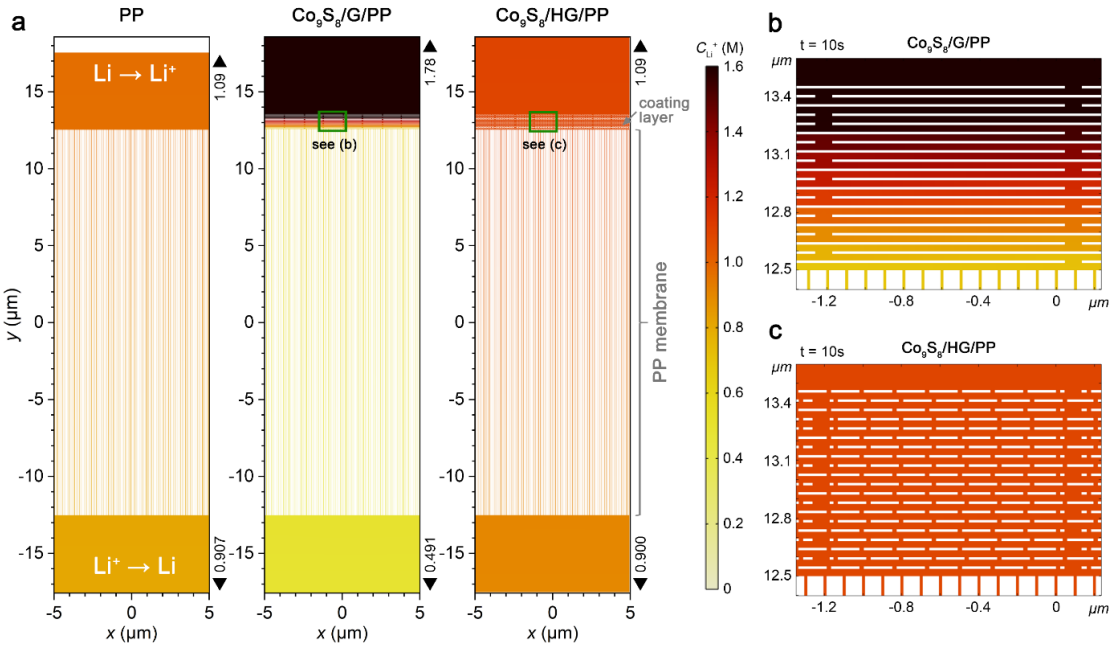

Figure 3-12. Simulation calculation of resistance towards Li^+ transport by incorporating Co_9S_8/G/PP, and Co_9S_8/HG/PP separators**.** (a) Topographic maps of lithium-ion concentration ($C_{Li}{}^+$) in Li|separator|Li symmetric cells using bare PP, Co_9S_8/G/PP, and Co_9S_8/HG/PP separators at t = 60 s, with a modification layer thickness of 1 μm. Numerical values indicated by the black arrows represent the minimum and maximum $C_{Li}{}^+$. Enlarged schematic models of (b) Co_9S_8/G/PP and (c) Co_9S_8/HG/PP separators, respectively, with corresponding concentration maps showing $C_{Li}{}^+$ gradients at t = 10 s.

These simulations modeled the lithium-ion concentration profiles in Li|Li symmetric cells (SI: Experimental Method). The electrolyte concentration and viscosity were aligned with actual experimental conditions and determined by the software's standard

values. Key parameters for the graphene-based membranes, including nanosheet dimensions and hole distributions, are derived from SEM characterization (Figure S9). For the Co_9S_8/HG/PP and Co_9S_8/G/PP separators, the average gap area between nanosheets in the membrane surfaces is approximately 0.116 μm^{-2}, with gap sizes of ~90 nm. For the Co_9S_8/HG nanosheets, the nano-hole density reaches 306 holes μm^{-2}. In the simulation, graphene building blocks were modeled with a thickness of 13 nm with an average vertical gap of 20 nm, so holes with a diameter ≥13 nm were identified as effective Li^+ transport channels, leading to an effective hole ratio of 74.4% for Co_9S_8/HG nanosheets, corresponding to 12.7% of the total membrane surface area. This is significantly larger than the holey area percentage of its non-porous counterpart (Co_9S_8/G membrane), which is only 2.53%, and closer to the pore area percentage of the PP membrane (15.5%). These findings indicate that the holey-structured Co_9S_8/HG membrane can provide more Li^+ transport pathways, thereby facilitating the SRR catalytic processes.

Figure 3-12a presents the C_{Li^+} distribution in cells with different separators, captured at t = 60 s during cycling. The depth of color in the topographic maps reflects the C_{Li^+} level, with a larger color difference between the anode and cathode indicating more severe concentration polarization. The results reveal that the non-hole Co_9S_8/G/PP separator (Figure 3-12b) exhibits significantly higher polarization compared to the commercial PP separator. In contrast, the holey nanostructured Co_9S_8/HG/PP separator (Figure 3-12c) demonstrates only a marginally higher polarization than the PP separator, with comparable C_{Li^+} levels in both separators - approximately twice as

high as that through the conventional non-hole Co_9S_8/G/PP separator (Figure S10). These findings indicate that the conventional separator significantly impeded the Li^+ mass flux, creating a pronounced concentration gradient due to the mismatch between ion transport across the membrane and electrochemical reaction rates at the electrodes. This is evident from the deeper color contrast in Figure 3-12b. Conversely, the holey-structured Co_9S_8/HG/PP separator effectively mitigated C_{Li^+} polarization by facilitating ion transport through its in-plane holes, reducing diffusion path lengths. As a result, it lowers internal overpotential and enhances battery performance.

3.4.4 Electrochemical performance measurements

The electrocatalytic kinetics of Co_9S_8/HG and Co_9S_8/G were investigated to highlight the advantages of the holey-structured material in enhancing SRR catalytic efficiency.

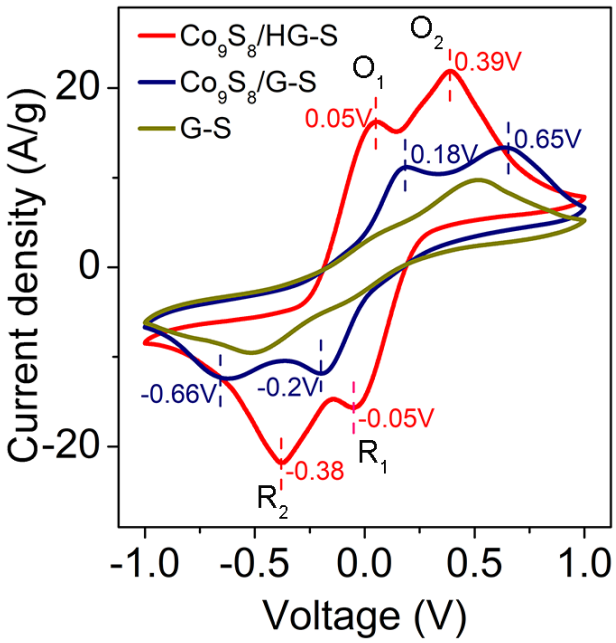

Figure 3-13. Cyclic voltammetry (CV) curves of symmetric cells at a scan rate of 3 mV s^{-1}.

To evaluate SRR behavior, CV measurements were conducted in symmetric cells assembled with a 1 M Li_2S_6 catholyte and electrodes prepared by loading samples on carbon-coated aluminum foils. As shown in Figure 3-13, cells with Co_9S_8/HG and Co_9S_8/G exhibit two pairs of redox peaks, while no distinct peaks are observed in symmetric cells with rGO. Notably, cells integrated with Co_9S_8/HG harvest a higher current response and smaller peak voltage separation (defined as E_{R1} - E_{O1} and E_{R2} - E_{O2}; 0.10 V and 0.77 V) compared to Co_9S_8/G (0.38 V and 1.31 V), indicating improved LiPSs conversion efficiency and enhanced electrochemical reversibility.

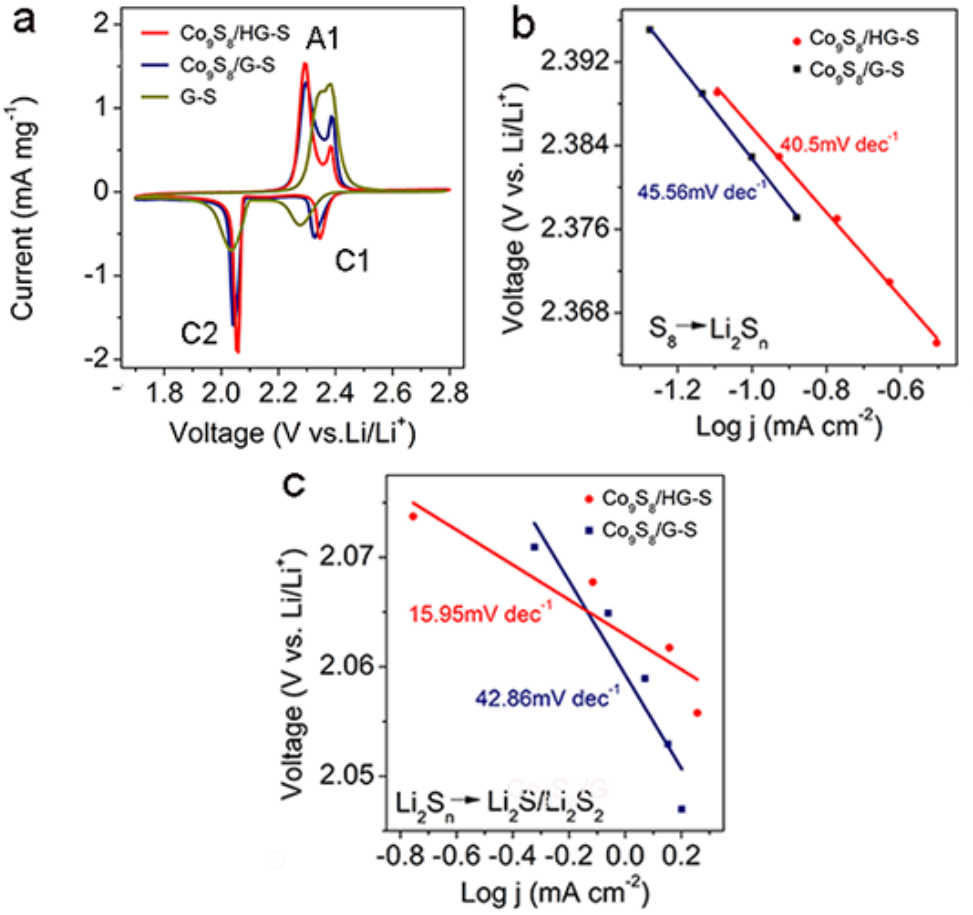

Figure 3-14. Tafel slope analysis**.** (a) CV profiles of Co_9S_8/HG-S, Co_9S_8/G-S, and G-S cathodes at 0.04 mV s^{-1}, highlighting their SRR catalytic performance. Tafel plots: (b) C1, conversion of S_8 to long-chain Li_2S_n ($4 \le n \le 8$); (c) C2, conversion of long-chain Li_2S_n ($4 \le n \le 8$) to Li_2S_2/Li_2S.

Tafel slopes, derived from CV curves, provide critical insights into the SRR reaction kinetics and catalytic activity of the materials.[51, 52] The cathodes consist of sulfur composites with synthesized materials (8 wt.%), denoted as Co_9S_8/HG-S, Co_9S_8/G-S, and rGO-S. As shown in Figure 3-14a, two pairs of redox peaks are observed for Co_9S_8/HG-S and Co_9S_8/G-S. The cathodic peaks represent the sequential reduction of sulfur species during a discharging process: peak C1 (Co_9S_8/HG-S: 2.35 V; Co_9S_8/G-S: 2.33 V; G-S: 2.27 V) corresponds to the formation of long-chain soluble lithium polysulfides (Li_2S_n, $4 \leq n < 8$), while peak C2 (Co_9S_8/HG-S: 2.06 V; Co_9S_8/G-S: 2.04 V; G-S: 2.03 V) reflects further reduction to short-chain Li_2S_2/Li_2S. The Co_9S_8/HG-S electrode exhibits a forward shift in reduction peak voltage and a backward shift in oxidation peak voltage, indicating decreased overpotential and reduced voltage polarization, thus significantly enhancing the electrochemical activity for LiPSs conversion. Figures 3-14b, c further reveals superior catalytic kinetics for Co_9S_8/HG, with a smaller Tafel slope of 40.5 mV dec^{-1} for the conversion of S_8 to long-chain Li_2S_n, compared to 45.56 mV dec^{-1} for Co_9S_8/G. For the Li_2S_n to Li_2S_2/Li_2S conversion, Co_9S_8/HG achieves a significantly lower Tafel slope of 15.95 mV dec^{-1} compared to Co_9S_8/G (42.86 mV dec^{-1}), indicating a pronounced improvement in the SRR catalytic activity. Notably, Co_9S_8/HG also exhibits superior catalytic performance in the oxidation of Li_2S back to long-chain Li_2S_n (Figure S11), with a Tafel slope of 41.42 mV dec^{-1} compared to 53.18 mV dec^{-1} for Co_9S_8/G. Considering the insulating nature of Li_2S and the crucial role of its oxidation in achieving a reversible capacity, facilitating charge transfer is essential for prolonged cycle life. This enhancement is attributed to the

porous HG substrate, which promotes Li^+ diffusivity and reduces electron transfer resistance, enabling rapid interaction with LiPSs encapsulated by the membrane. These structural advantages significantly boost the catalytic efficiency of LiPSs redox conversions.

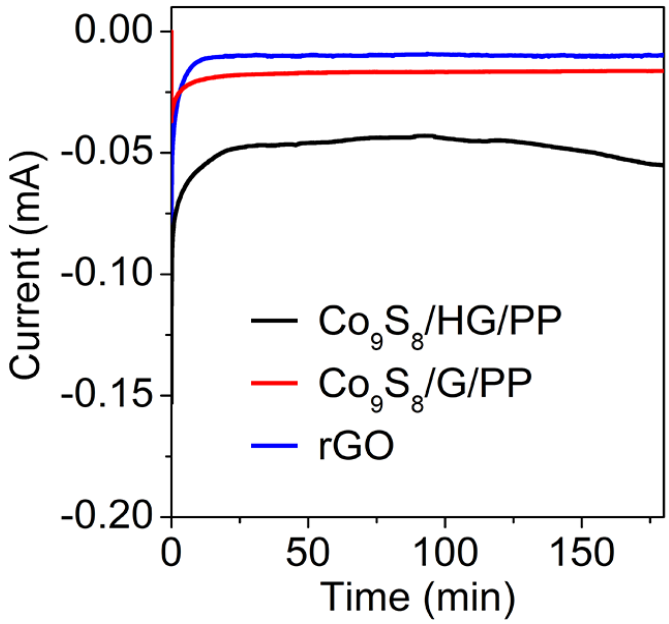

Figure 3-15. Potentiostatic discharge analysis at 2.02 V vs. Li/Li^+, showing catalytic differences in discharge behavior.

To evaluate the ability of the holey-structured Co_9S_8/HG to enhance Li_2S_2/Li_2S precipitation, potentiostatic discharge measurements were conducted at 2.01 V using an H-cell setup with Co_9S_8/HG, Co_9S_8/G, or rGO loaded onto carbon paper for comparison (SI: Experimental Method, Figure S12). The cell with Co_9S_8/HG exhibits a higher current response compared to Co_9S_8/G and rGO, indicating its superior capability to promote the conversion from LiPSs to Li_2S_2/Li_2S (Figure 3-15). This improvement arises from the structural advantages of holey graphene: its larger SSA (194.1 $m^2\ g^{-1}$) enables efficient physical adsorption of polysulfides (SI: Experimental Method, Figure S13), while its pore-rich structure, compared to PP, provides abundant

channels for rapid Li^+ and electron transport. These features, coupled with the catalytic activity of Co_9S_8, facilitate the participation of Li^+ and electrons in the Li_2S deposition process.

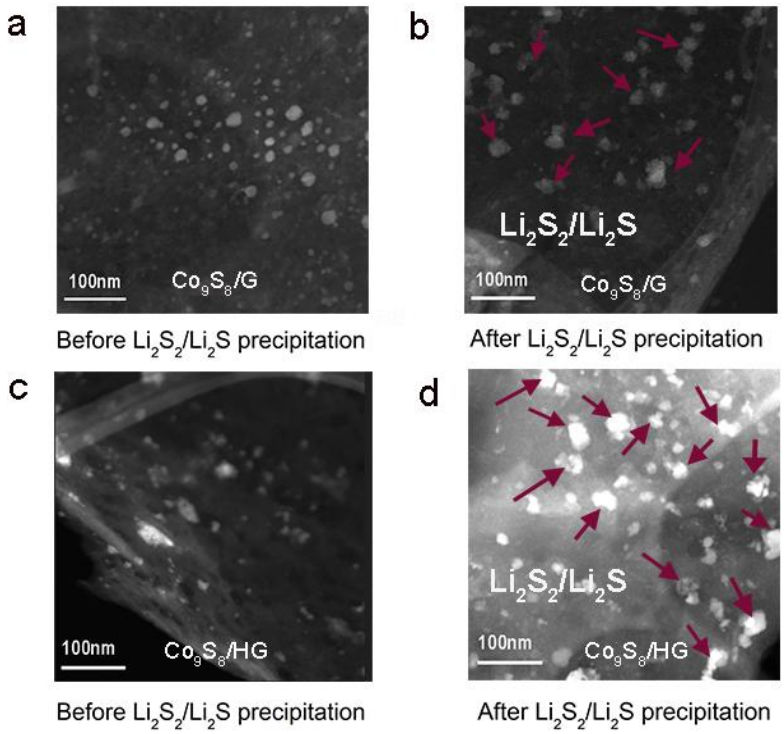

Figure 3-16. TEM characterization after potentiostatic discharging. (a, b) Co_9S_8/G and (c, d) Co_9S_8/HG before and after Li_2S_2/Li_2S precipitation.

To further investigate the deposition behavior and catalytic performance of Co_9S_8/HG, X-ray photoelectron spectroscopy and TEM analysis were conducted. The membranes, after being soaked in a DOM/DME mixture (1:1 by volume) and dried under an argon atmosphere, were characterized to confirm the reduction of polysulfides and the formation of Li_2S deposits. The S2p spectrum of Co_9S_8/HG after deposition shows a significant increase at 161.8 eV, confirming the effective reduction of polysulfides to insoluble Li_2S_2/Li_2S. In contrast, Co_9S_8/G displays no notable change at this binding energy before and after the deposition, suggesting weaker polysulfide conversion

ability (Figure S14). TEM images (Figure 3-16) further support this, revealing an increased Li_2S_2/Li_2S precipitation on the holey structured Co_9S_8/HG membrane. This highlights the enhanced electrocatalytic kinetics of Co_9S_8/HG in facilitating the conversion of polysulfides to Li_2S_2/Li_2S products.

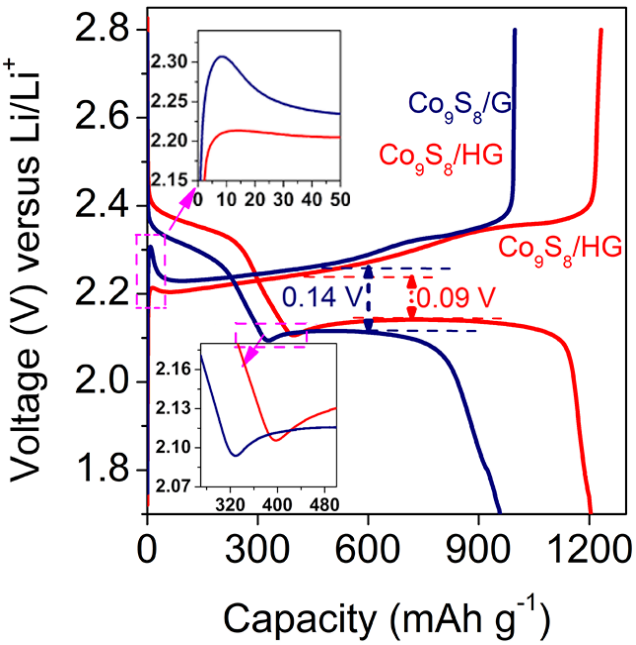

Figure 3-17. Galvanostatic charge/discharge profiles at 0.1 C during the first cycle, showing voltage plateaus indicative of polysulfide conversion (sulfur loading ~2.5 mg cm^{-2}).

To evaluate the electrochemical performance of the modified separators in Li–S batteries, 2032-type coin cells were assembled with a sulfur loading of ~ 2.0 mg cm^{-2}. Figure 17 compares the galvanostatic charge-discharge voltage profiles at 0.1 C for cells with Co_9S_8/HG and Co_9S_8/G membranes. The holey-structured Co_9S_8/HG membrane exhibits a smaller polarization of 0.09 V, compared to 0.14 V for Co_9S_8/G, as calculated from the voltage difference between the charge and discharge plateaus. Notably, at the onset dip of the 2.1 V plateau (Figure 3-17, inset), the Co_9S_8/HG cell maintains a higher potential, indicating an enhanced catalytic activity for the conversion

of long-chain Li_2S_n to Li_2S_2/Li_2S. Similarly, its lower initial charging voltage of 2.21 V suggests improved oxidation kinetics for Li_2S_2/Li_2S to soluble polysulfides. The catalytic activity of Co_9S_8/HG is further quantified by the Q_1/Q_2 ratio (Figure S15), where Q_1 corresponds to the capacity of the first discharge plateau (~2.3 V) and Q_2 represents the second plateau (~2.1 V). For cells with Co_9S_8/HG, the ratio reaches 2.13, exceeding the theoretical value of 2.0, indicating nearly complete reduction of high-order polysulfides. In contrast, lower Q_1/Q_2 ratios for pristine PP separator (1.81) and Co_9S_8/G (1.83), suggest incomplete reduction, likely due to a severe shuttle effect. Additionally, the Co_9S_8/HG membrane achieves a higher Q_1 value (395.2 mAh g^{-1}) compared to Co_9S_8/G (328.5 mAh g^{-1}) and pristine PP (302.5 mAh g^{-1}), demonstrating that the holey-structured Co_9S_8/HG effectively enhances sulfur utilization by acting as an auxiliary current collector.

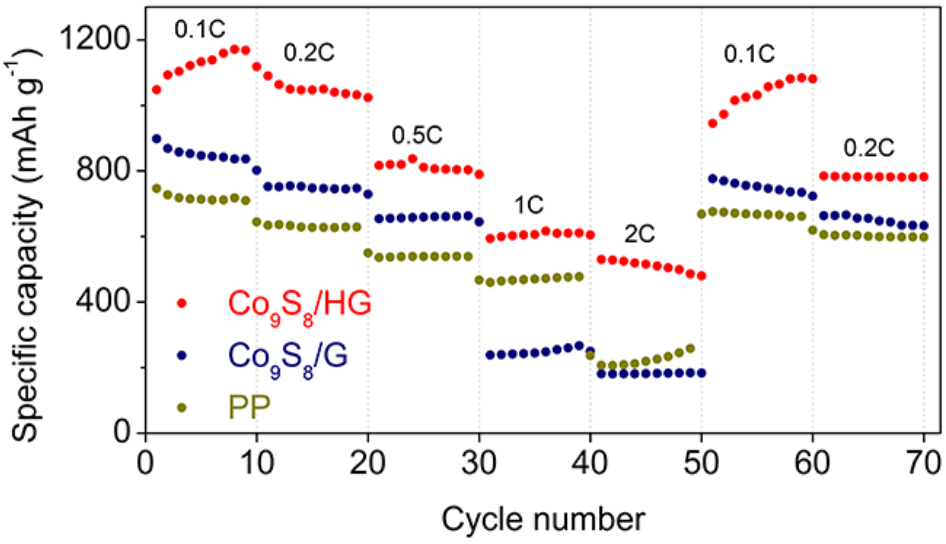

Figure 3-18. Rate performance comparison (sulfur loading ~2.3 mg cm^{-2})

Beyond reducing polarization and enhancing sulfur utilization, the Co_9S_8/HG membrane also exhibits impressive rate performance across a wide range of current

densities. The cell with the Co_9S_8/HG membrane demonstrates superior discharge capacity at various current densities from 0.1 C to 2 C, achieving 1182.4, 1056.1, 912.4, 696.5, and 538.1 mAh g^{-1}, respectively (Figure 3-18). When the current density is switched back to 0.2 C, a capacity of 792.1 mAh g^{-1} is recovered, indicating remarkable stability and high reversibility. In contrast, cells with Co_9S_8/G membrane deliver lower capacities at the same C-rates: 853.7, 754.5, 660.2, 250.7, and 185.3 mAh g^{-1}. Notably, at higher current densities of 1 C and 2 C, the Co_9S_8/G membrane results in discharge capacities of only 250.7 and 185.3 mAh g^{-1}, which are even lower than those of cells with a pristine PP separator (472.8 and 229.2 mAh g^{-1}). This suggests that at high C-rates, the Co_9S_8/G membrane imposes significant resistance to Li^+ transport, leading to a reduced capacity. These findings highlight a critical insight: focusing solely on LiPSs entrapment and catalysis, without addressing lithium-ion transport, is insufficient to achieve optimal battery performance.

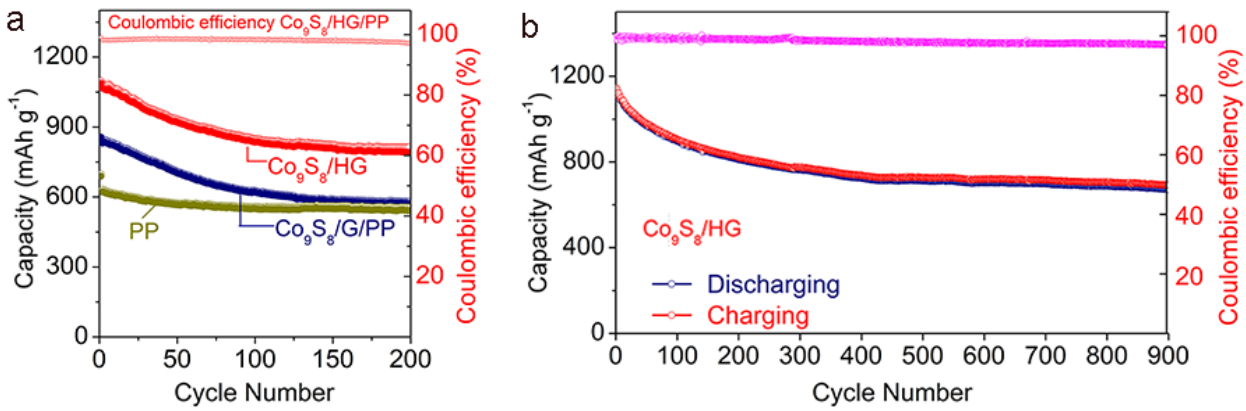

Figure 3-19. Cycling stability tests**.** (a) At 0.5 C, Co_9S_8/HG/PP demonstrated significantly lower capacity fading over 200 cycles compared to Co_9S_8/G/PP and pristine PP separator. (b) Long-term cycling test of cells with Co_9S_8/HG/PP separators at 0.2 C over 900 cycles (sulfur loading: > 2.0 mg cm^{-2}).

To assess the durability of the Co_9S_8/HG electrocatalyst membrane in Li–S batteries, cycling performance was evaluated at 0.5 C and 0.2 C, respectively (Figure 3-19). At 0.5 C, the Co_9S_8/HG membrane achieves an initial capacity of 1096.5 mAh g^{-1}, retaining 791.2 mAh g^{-1} after 200 cycles with a low decay rate of 0.09% per cycle, outperforming the Co_9S_8/G membrane, which shows an initial capacity of 864.1 mAh g^{-1} and a higher decay rate of 0.16% per cycle. At 0.2 C, the Co_9S_8/HG membrane delivers remarkable long-term cycling stability, maintaining a specific capacity of 671 mAh g^{-1} over 900 cycles with a capacity decay of just 0.044% per cycle and an average Coulombic efficiency of 98.1%. These improvements are attributed to the holey graphene substrate, which provides efficient Li^+ and electron migration pathways, enabling rapid Li^+ transport during cycling and accelerating lithium polysulfide conversion kinetics. Collectively, these findings highlight the significant potential of holey-structured, electrocatalyst-equipped membranes for improving the energy density and cycling stability of Li–S batteries, paving the way for their practical applications.

3.5 Conclusions

In this work, we introduced a Co_9S_8-embeded holey graphene (Co_9S_8/HG) electrocatalyst as a representative membrane, demonstrating the critical role of efficient Li^+ transport in enhancing the catalytic kinetics of sulfur redox reactions. The unique structure of Co_9S_8/HG, with a 16.2% porous area, effectively balances polysulfide containment and lithium-ion diffusion, avoiding additional overpotential

while maintaining rapid Li^+ transport kinetics. Experimental and computational analysis confirmed that the holey graphene substrate provides abundant migration channels, facilitating rapid Li^+ diffusion, accelerating LiPSs conversion kinetics, and reducing reaction resistance during Li_2S precipitation. As a result, Li-S batteries integrating with Co_9S_8/HG membrane present a lower Tafel slope and a higher Li_2S deposition discharging current, indicate that efficient Li^+ transport effectively promote the reaction kinetics of rate-limiting step for the SRR. Li–S cells with Co_9S_8/HG membrane exhibit superior rate performance at C-rates above 1 C compared to those with the non-porous Co_9S_8/G membrane. Additionally, the Co_9S_8/HG membrane demonstrates remarkable cycling stability, retaining a discharge capacity of 791.2 mAh g^{-1} at 0.5 C after 200 cycles (decay rate: 0.09% per cycle) and 671 mAh g^{-1} at 0.2 C over 900 cycles (decay rate: 0.044% per cycle). These findings underscore the importance of a balanced approach to separator modification in Li–S batteries, addressing both sulfur containment and lithium-ion diffusion. This study establishes a new paradigm for the design of multifunctional membranes, paving the way for high-performance, long-lasting Li–S batteries.

3.6 References

1. Peng, L.; Wei, Z.; Wan, C.; Li, J.; Chen, Z.; Zhu, D.; Baumann, D.; Liu, H.; Allen, C. S.; Xu, X., A fundamental look at electrocatalytic sulfur reduction reaction. *Nature Catalysis* **2020,** *3* (9), 762-770.

2. Sharma, R.; Kumar, H.; Kumar, G.; Sharma, S.; Aneja, R.; Sharma, A. K.; Kumar, R.; Kumar, P., Progress and challenges in electrochemical energy storage devices: Fabrication, electrode material, and economic aspects. *Chemical engineering journal* **2023,** *468*, 143706.

3. Fan, F. Y.; Carter, W. C.; Chiang, Y.-M., Mechanism and Kinetics of Li2S Precipitation in Lithium-Sulfur Batteries. *Advanced Materials (Deerfield Beach, Fla.)* **2015,** *27* (35), 5203-5209.

4. Wang, Y. X.; Lai, W. H.; Chou, S. L.; Liu, H. K.; Dou, S. X., Remedies for polysulfide dissolution in room-temperature sodium–sulfur batteries. *Advanced Materials* **2020,** *32* (18), 1903952.

5. Liu, B.; Taheri, M.; Torres, J. F.; Fusco, Z.; Lu, T.; Liu, Y.; Tsuzuki, T.; Yu, G.; Tricoli, A., Janus conductive/insulating microporous ion-sieving membranes for stable Li–S batteries. *ACS nano* **2020,** *14* (10), 13852-13864.

6. Nguyen, V. P.; Kim, J.-H.; Lee, S.-M., Strategies of boosting synergistic adsorption-catalysis effect for high-performance lithium–sulfur batteries. *Materials Today Energy* **2023,** *38*, 101451.

7. Pang, Q.; Liang, X.; Kwok, C. Y.; Nazar, L. F., Advances in lithium–sulfur batteries based on multifunctional cathodes and electrolytes. *Nature Energy* **2016,** *1* (9), 1-11.

8. Zhang, J.; Huang, H.; Bae, J.; Chung, S. H.; Zhang, W.; Manthiram, A.; Yu, G., Nanostructured host materials for trapping sulfur in rechargeable Li–S batteries: structure design and interfacial chemistry. *Small Methods* **2018,** *2* (1), 1700279.

9. Zhou, L.; Danilov, D. L.; Eichel, R. A.; Notten, P. H., Host materials anchoring polysulfides in Li–S batteries reviewed. *Advanced Energy Materials* **2021,** *11* (15), 2001304.

10. Tsao, Y.; Gong, H.; Chen, S.; Chen, G.; Liu, Y.; Gao, T. Z.; Cui, Y.; Bao, Z., A nickel-decorated carbon flower/sulfur cathode for lean-electrolyte lithium–sulfur batteries. *Advanced Energy Materials* **2021,** *11* (36), 2101449.

11. Chung, S. H.; Manthiram, A., Bifunctional separator with a light-weight carbon-coating for dynamically and statically stable lithium-sulfur batteries. *Advanced Functional Materials* **2014,** *24* (33), 5299-5306.

12. Yu, X.; Wu, H.; Koo, J. H.; Manthiram, A., Tailoring the pore size of a polypropylene separator with a polymer having intrinsic nanoporosity for suppressing the polysulfide shuttle in lithium–sulfur batteries. *Advanced Energy Materials* **2020,** *10* (1), 1902872.

13. Lei, T.; Chen, W.; Lv, W.; Huang, J.; Zhu, J.; Chu, J.; Yan, C.; Wu, C.; Yan, Y.; He, W., Inhibiting polysulfide shuttling with a graphene composite separator for highly robust lithium-sulfur batteries. *Joule* **2018,** *2* (10), 2091-2104.

14. Liu, R.; Han, Z.; Han, J.; Peng, L.; Gu, S.; Shao, J.; Lv, W., A permselective protection layer assembled by two-dimensional organic vermiculite produces a highly stable lithium metal anode for lithium-sulfur batteries. *Materials Today Energy* **2023,** *38*, 101452.

15. Kim, S.; Cho, M.; Lee, Y., Multifunctional chitosan–RGO network binder for enhancing the cycle stability of Li–S batteries. *Advanced Functional Materials* **2020,** *30* (10), 1907680.

16. Yuan, H.; Huang, J. Q.; Peng, H. J.; Titirici, M. M.; Xiang, R.; Chen, R.; Liu, Q.; Zhang, Q., A review of functional binders in lithium–sulfur batteries. *Advanced Energy Materials* **2018,** *8* (31), 1802107.

17. Gao, Z.; Sun, H.; Fu, L.; Ye, F.; Zhang, Y.; Luo, W.; Huang, Y., Promises, challenges, and recent progress of inorganic solid-state electrolytes for all-solid-state lithium batteries. *Advanced materials* **2018,** *30* (17), 1705702.

18. Yang, X.; Luo, J.; Sun, X., Towards high-performance solid-state Li–S batteries: from fundamental understanding to engineering design. *Chemical Society Reviews* **2020,** *49* (7), 2140-2195.

19. Fang, R.; Xu, H.; Xu, B.; Li, X.; Li, Y.; Goodenough, J. B., Reaction mechanism

optimization of solid-state Li–S batteries with a PEO-based electrolyte. *Advanced Functional Materials* **2021,** *31* (2), 2001812.

20. Tian, D.; Song, X.; Wang, M.; Wu, X.; Qiu, Y.; Guan, B.; Xu, X.; Fan, L.; Zhang, N.; Sun, K., MoN supported on graphene as a bifunctional interlayer for advanced Li-S batteries. *Advanced Energy Materials* **2019,** *9* (46), 1901940.

21. Wang, S.; Li, X.; Zhang, Y.; Zheng, W.; Dai, Y.; He, G., Highly efficient polysulfide trapping and ion transferring within a hierarchical porous membrane interlayer for high-energy lithium–sulfur batteries. *ACS Applied Energy Materials* **2020,** *3* (5), 5050-5057.

22. Kim, M. S.; Ma, L.; Choudhury, S.; Archer, L. A., Multifunctional Separator Coatings for High-Performance Lithium-Sulfur Batteries. *Advanced Materials Interfaces* **2016,** *3* (22).

23. Bai, S.; Liu, X.; Zhu, K.; Wu, S.; Zhou, H., Metal–organic framework-based separator for lithium–sulfur batteries. *Nature Energy* **2016,** *1* (7), 1-6.

24. Joshi, R.; Carbone, P.; Wang, F.-C.; Kravets, V. G.; Su, Y.; Grigorieva, I. V.; Wu, H.; Geim, A. K.; Nair, R. R., Precise and ultrafast molecular sieving through graphene oxide membranes. *science* **2014,** *343* (6172), 752-754.

25. Lee, D. K.; Kim, S. J.; Kim, Y. J.; Choi, H.; Kim, D. W.; Jeon, H. J.; Ahn, C. W.; Lee, J. W.; Jung, H. T., Graphene oxide/carbon nanotube bilayer flexible membrane for high-performance Li–S batteries with superior physical and electrochemical properties. *Advanced Materials Interfaces* **2019,** *6* (7), 1801992.

26. Ghazi, Z. A.; He, X.; Khattak, A. M.; Khan, N. A.; Liang, B.; Iqbal, A.; Wang, J.; Sin, H.; Li, L.; Tang, Z., MoS2/celgard separator as efficient polysulfide barrier for long-life lithium–sulfur batteries. *Advanced Materials* **2017,** *29* (21), 1606817.

27. Jiao, L.; Zhang, C.; Geng, C.; Wu, S.; Li, H.; Lv, W.; Tao, Y.; Chen, Z.; Zhou, G.; Li, J., Capture and catalytic conversion of polysulfides by in situ built TiO2-MXene heterostructures for lithium–sulfur batteries. *Advanced Energy Materials* **2019,** *9* (19), 1900219.

28. Jiang, Y.; Liang, P.; Tang, M.; Sun, S.; Min, H.; Han, J.; Shen, X.; Yang, H.; Chao, D.; Wang, J., A high-throughput screening permeability separator with high

catalytic conversion kinetics for Li–S batteries. *Journal of Materials Chemistry A* **2022,** *10* (41), 22080-22092.

29. Yang, Y.; Wang, W.; Li, L.; Li, B.; Zhang, J., Stable cycling of Li–S batteries by simultaneously suppressing Li-dendrite growth and polysulfide shuttling enabled by a bioinspired separator. *Journal of Materials Chemistry A* **2020,** *8* (7), 3692-3700.

30. Li, Z.; Jiao, S.; Yu, D.; Zhang, Q.; Liu, K.; Han, J.; Guo, Z.; Liu, J.; Wang, L., Cationic-polymer-functionalized separator as a high-efficiency polysulfide shuttle barrier for long-life Li–S battery. *ACS Applied Energy Materials* **2021,** *4* (3), 2914-2921.

31. Wu, Q.; Yao, Z.; Zhou, X.; Xu, J.; Cao, F.; Li, C., Built-in catalysis in confined nanoreactors for high-loading Li–S batteries. *ACS nano* **2020,** *14* (3), 3365-3377.

32. Li, R.; Peng, H.; Wu, Q.; Zhou, X.; He, J.; Shen, H.; Yang, M.; Li, C., Sandwich-like catalyst–carbon–catalyst trilayer structure as a compact 2D host for highly stable lithium–sulfur batteries. *Angewandte Chemie International Edition* **2020,** *59* (29), 12129-12138.

33. Wang, C.; Song, H.; Yu, C.; Ullah, Z.; Guan, Z.; Chu, R.; Zhang, Y.; Zhao, L.; Li, Q.; Liu, L., Iron single-atom catalyst anchored on nitrogen-rich MOF-derived carbon nanocage to accelerate polysulfide redox conversion for lithium sulfur batteries. *Journal of Materials Chemistry A* **2020,** *8* (6), 3421-3430.

34. Safari, M.; Kwok, C. Y.; Nazar, L. F., Transport properties of polysulfide species in lithium–sulfur battery electrolytes: coupling of experiment and theory. *ACS central science* **2016,** *2* (8), 560-568.

35. Wang, D.; Ma, K.; Hao, J.; Zhang, W.; Shi, H.; Wang, C.; Xiong, Z.; Bai, Z.; Chen, F.-R.; Guo, J., Engineering single-atom catalysts as multifunctional polysulfide and lithium regulators toward kinetically accelerated and durable lithium-sulfur batteries. *Chemical Engineering Journal* **2023,** *466*, 143182.

36. Lu, Y.; Qin, J. L.; Shen, T.; Yu, Y. F.; Chen, K.; Hu, Y. Z.; Liang, J. N.; Gong, M. X.; Zhang, J. J.; Wang, D. L., Hypercrosslinked polymerization enabled N-doped carbon confined Fe2O3 facilitating Li polysulfides interface conversion for Li–S batteries. *Advanced Energy Materials* **2021,** *11* (42), 2101780.

37. Wu, W.; Pu, J.; Wang, J.; Shen, Z.; Tang, H.; Deng, Z.; Tao, X.; Pan, F.; Zhang, H., Biomimetic bipolar microcapsules derived from Staphylococcus aureus for enhanced properties of lithium–sulfur battery cathodes. *Advanced Energy Materials* **2018,** *8* (12), 1702373.

38. Luo, L.; Li, J.; Yaghoobnejad Asl, H.; Manthiram, A., In-situ assembled VS4 as a polysulfide mediator for high-loading lithium–sulfur batteries. *ACS Energy Letters* **2020,** *5* (4), 1177-1185.

39. Wang, J.; Yi, S.; Liu, J.; Sun, S.; Liu, Y.; Yang, D.; Xi, K.; Gao, G.; Abdelkader, A.; Yan, W., Suppressing the shuttle effect and dendrite growth in lithium–sulfur batteries. *Acs Nano* **2020,** *14* (8), 9819-9831.

40. Gao, W.; Wang, Z.; Peng, C.; Kang, S.; Cui, L., Accelerating the redox kinetics by catalytic activation of “dead sulfur” in lithium–sulfur batteries. *Journal of Materials Chemistry A* **2021,** *9* (23), 13442-13458.

41. Zhou, F.; Wang, R.; He, S.; Liu, X.; Liu, S.; Shao, H.; Liu, X.; Xiao, Z.; Liu, J., Defect-Rich Hierarchical Porous Mn-Doped CoP Hollow Microspheres Accelerate Polysulfide Conversion. *Advanced Functional Materials* **2023,** *33* (8), 2211124.

42. Qiao, Z.; Zhang, Y.; Meng, Z.; Xie, Q.; Lin, L.; Zheng, H.; Sa, B.; Lin, J.; Wang, L.; Peng, D. L., Anchoring polysulfides and accelerating redox reaction enabled by Fe-based compounds in lithium–sulfur batteries. *Advanced Functional Materials* **2021,** *31* (21), 2100970.

43. Pang, Q.; Kwok, C. Y.; Kundu, D.; Liang, X.; Nazar, L. F., Lightweight metallic MgB2 mediates polysulfide redox and promises high-energy-density lithium-sulfur batteries. *Joule* **2019,** *3* (1), 136-148.

44. Luo, L.; Chung, S. H.; Yaghoobnejad Asl, H.; Manthiram, A., Long-life lithium–sulfur batteries with a bifunctional cathode substrate configured with boron carbide nanowires. *Advanced Materials* **2018,** *30* (39), 1804149.

45. Su, Y.-S.; Manthiram, A., Lithium–sulphur batteries with a microporous carbon paper as a bifunctional interlayer. *Nature communications* **2012,** *3* (1), 1166.

46. Zhou, S.; Shi, J.; Liu, S.; Li, G.; Pei, F.; Chen, Y.; Deng, J.; Zheng, Q.; Li, J.;

Zhao, C., Visualizing interfacial collective reaction behaviour of Li–S batteries. *Nature* **2023,** *621* (7977), 75-81.

47. Zhou, G.; Tian, H.; Jin, Y.; Tao, X.; Liu, B.; Zhang, R.; Seh, Z. W.; Zhuo, D.; Liu, Y.; Sun, J., Catalytic oxidation of Li2S on the surface of metal sulfides for Li− S batteries. *Proceedings of the National Academy of Sciences* **2017,** *114* (5), 840-845.

48. Liu, B.; Gu, H.; Torres, J. F.; Yin, Z.; Tricoli, A., Balancing polysulfide containment and energy loss in lithium–sulfur batteries. *Energy & Environmental Science* **2024,** *17* (3), 1073-1082.

49. Son, D.; Lim, W.-G.; Lee, J., A short review of the recent developments in functional separators for lithium-sulfur batteries. *Korean Journal of Chemical Engineering* **2023,** *40* (3), 473-487.

50. Zhao, M.; Peng, H. J.; Zhang, Z. W.; Li, B. Q.; Chen, X.; Xie, J.; Chen, X.; Wei, J. Y.; Zhang, Q.; Huang, J. Q., Activating inert metallic compounds for high‐rate lithium–sulfur batteries through in situ etching of extrinsic metal. *Angewandte Chemie International Edition* **2019,** *58* (12), 3779-3783.

51. Cai, J.; Sun, Z.; Cai, W.; Wei, N.; Fan, Y.; Liu, Z.; Zhang, Q.; Sun, J., A robust ternary heterostructured electrocatalyst with conformal graphene chainmail for expediting Bi-directional sulfur redox in Li–S batteries. *Advanced Functional Materials* **2021,** *31* (23), 2100586.

52. Park, M.-S.; Yu, J.-S.; Kim, K. J.; Jeong, G.; Kim, J.-H.; Jo, Y.-N.; Hwang, U.; Kang, S.; Woo, T.; Kim, Y.-J., One-step synthesis of a sulfur-impregnated graphene cathode for lithium–sulfur batteries. *Physical Chemistry Chemical Physics* **2012,** *14* (19), 6796-6804.

3.7 Supporting Information

3.7.1 Material synthesis

Synthesis of GO, rGO, and Co-pre/G

Graphene oxide (GO) was produced from natural graphite using a modified Hummers' method.[1] To create Disperse 30 mg of GO in 60 mL of anhydrous ethylene glycol (EG, ≥99%, Merck Australia) and subjecting it to ultrasonication for an hour. Subsequently, a solution of 40 mmol cobalt acetate (≥98.0%, Merck Australia) in 20 mL EG was gradually mixed into the GO suspension and stirred for an hour. The mixture was then heated to 185°C at a rate of 2°C per minute, maintained at this temperature for two hours, and allowed to cool to room temperature. The product was purified using ethanol and DI water, followed by lyophilization for 24 hours to get Co-precursor (Co-pre/rGO, Figure S1). The same process was repeated for the preparation of reduced graphene oxide (rGO), without adding cobalt acetate.

Synthesis of Co_9S_8/G and Co_9S_8/HG

Synthesis of Co_9S_8/G nanosheets: The process begins with the calcination of pre-prepared Co-pre/G powder at 800°C in nitrogen for 1 hour in tube furnace, forming cobalt metallic nanoparticles on graphene nanosheets (CoNP/G, Figure S2). These nanosheets are then annealed in air at 200°C for 2 hours to get core-shell nanoparticle of Co_3O_4-Co on graphene (Co_3O_4-CoNP/G). The final step involves reacting Co_3O_4-CoNP/G with H_2S gas at 350°C for 1 hour to produce Co_9S_8/G.

Synthesis of Co_9S_8/HG nanosheets: In contrast, the Co_9S_8/HG variant involves an additional annealing of Co_3O_4-CoNP/G nanosheets at 800°C for 1 hour in nitrogen, facilitating in-situ etching on graphene and creating nanoscale holes, forming CoNP/HG (Figure S3). These nanosheets undergo further annealing in air at 200°C for 2 hours, leading to the formation of core-shell structured Co_3O_4-Co nanoparticles on holey graphene (Co_3O_4-CoNP/HG Figure S4). The final product Co_9S_8/HG is obtained by reacting Co_3O_4/HG with H_2S gas at 350°C for 1 hour.

Synthesis of HG

Holey graphene (HG) nanosheets, as illustrated in Figures 3-2f and 3-3f, were produced by immersing Co_3O_4/HG nanosheets in an 8.0 M hydrochloric acid solution at 60°C within a securely sealed container for overnight. After this, the resulting material was washed thrice using a mixture of ethanol and deionized water, until the pH level stabilized at 7. The purified product was then subjected to a lyophilization process for 24 hours.

Preparation of electrolyte and Li_2S_4, Li_2S_6 catholyte

The electrolyte, comprising 1M lithium bis(trifluoromethanesulfonyl) imide (LiTFSI, 99.95%, Merck Australia) and 0.2 M lithium nitrate (99.99%, Merck Australia) in a 1:1 volumetric mixture of 1,2-dimethoxyethane (DME, anhydrous, Merck Australia) and 1,3-dioxolane (DOL, anhydrous, Merck Australia), was marked as the blank electrolyte, which served as the base for preparing Li_2S_6 catholyte. The Li_2S_4/Li_2S_6 catholyte were

produced by reacting Li_2S (99.98%, Merck Australia) and sulfur powder (99.98%, Merck Australia) in molar ratios of 1:3/1:5 in the blank electrolyte.

3.7.2 Modified separator fabrications

Fabrication Co_9S_8/HG/PP and Co_9S_8/G/PP separators

The modified membranes were fabricated through a filtration method using a commercial polypropylene (PP) membrane (Celgard 2400, 25 μm thickness) as a substrate. 10 mg each of reduced graphene oxide (rGO), Co_9S_8/G, and Co_9S_8/HG were dispersed in 50 mL of anhydrous 1-Methyl-2-pyrrolidone (NMP, 99.5%, Merck Australia) through 1 hour of ultrasonication. These dispersions were then gradually filtrated to get the resultant coatings (loading mass 0.18 mg cm^{-2}), Co_9S_8/HG/PP and Co_9S_8/G/PP, were dried at 50°C for overnight. The thickness of Co_9S_8/HG/PP and Co_9S_8/G/PP separators were measured with Cross-section SEM (Figure S5).

Fabrication Co_9S_8/HG/carbon paper, Co_9S_8/G/carbon paper and rGO/carbon paper

Co_9S_8/G, Co_9S_8/HG or rGO, Super P and PVDF were mixed (weight ratio is 85:10:5) to prepare slurry, after mixed by THINKY ARE250 mixer, the slurry was coated onto carbon paper and dried in the vacuum oven under the temperature of 50°C for further measurements.

3.7.3 Material characterizations

The SEM characterization was performed using a Zeiss UltraPlus analytical FESEM at 3 kV. TEM characterization and EDX mapping were conducted on a JEOL 2100F FEGTEM (200 kV). XRD measurements were conducted using a Bruker system (D2 Phaser) equipped with Cu Kα radiation, with an average wavelength of 1.54059 Å. N_2-adsorption isotherms measurements were conducted using a TristarII BET analyzer (Micromeritics, USA). Thermogravimetric (TG) analysis was conducted on a NETZSCH STA 449 F3 Jupiter analyzer. Ultraviolet-visible (UV-Vis) diffuse reflectance spectroscopy (DRS) was carried out on a PDA UV/Vis Lambda 465 Spectrophotometer (PerkinElmer).

3.7.4 Electrochemical performance measurements approach

(1) Nyquist plots and Li^+ activation energies

Li^+ activation energies ($E_{a\text{-}Li^+}$) of commercial PP, Co_9S_8/HG/PP and Co_9S_8/G/PP separators were measured by Nyquist plots achieved from the electrochemical impedance with SS|SS symmetric cells at multiple temperatures (i.e., 10, 20, 30, 40, 50, 60°C). Before each test, the coin cell was placed in the constant-temperature chamber for 1 hour to ensure good temperature uniformity. The SS|SS coin cells were fabricated in an Argon-filled glovebox. The Co_9S_8/HG and Co_9S_8/G modification layers were sandwiched between two layers of commercial PP membranes for electrical insulation from the SS plates. Each cell was injected with 64 μL of electrolyte (1 M LiTFSI in DOL/DME, 1:1 v/v) to adequately meet the ionic conduction requirements.

Electrochemical impedance spectroscopy (EIS) was conducted within the frequency range of 1 MHz to 0.1 Hz. The value of $E_{a\text{-}Li^+}$ of each membrane was derived from the slope of the fitted line in the Arrhenius plot (Figure S6).

(2) Li^+ diffusion coefficient

A lithium|stainless steel (Li|SS) half-cell configuration was employed. The cell was filled with 64 μL of 1 M LiTFSI electrolyte solution, mixed in equal volumes of DOL and DME. This setup was instrumental in determining the diffusion coefficient of lithium ions (D_{Li^+}). The procedure began with electroplating 1 mAh of lithium onto SS substrates. Subsequent electrostripping was performed at various scan rates, utilizing linear sweep voltammetry (LSV) as the method. This methodology, centered on Li|SS coin cells, was designed to reduce external variable effects while thoroughly considering the influence of aspects such as the condition of the lithium foil and electrolyte, alongside the processes of deposition, stripping, and the formation of a solid-electrolyte interface.

The LSV measurements were performed with seven sweeping rates, i.e., 0.02, 0.04, 0.06, 0.08, 0.10, 0.12, and 0.14 mV s^{-1}, as shown in Figure S7. The D_{Li+} was derived using the Randles–Sevcik equation as described below according to literature[2]:

$$I_P = 2.69 \times 10^5\ C\ mol^{-1}\ V^{-1/2} \cdot n^{3/2} \cdot A \cdot D_{Li}^{1/2} \cdot v^{1/2} \cdot C_{Li}$$

where I_p indicates the peak current (A), n is the number of electrons in the reaction (n=1 for Li electroplating/stripping processes), A is the electrode area (cm^2), v is the scanning rate (V s^{-1}), and C_{Li} is the Li^+ concentration in the electrolyte (0.001 mol cm^{-3}).

Note that the constant with a value of 2.69×10^5 has units of C mol^{-1} $V^{-1/2}$. The linear relationship between the I_p and the square root of v can be derived from CV measurements. Please note that to prevent materials in the modification layer, such as graphene or metal compounds, from reacting with lithium, the modification layer in the cells tested with LSV was sandwiched between two layers of electrically insulating PP membrane. Therefore, each cell contained two PP membranes, and the D_{Li}^+ measured for each membrane is approximated to the situation where there is only one PP membrane present. This approximation does not affect the trend and conclusions drawn from the lateral comparison of D_{Li}^+ across the three types of separators: PP, Co_9S_8/HG/PP, and Co_9S_8/G/PP.

(3) H-cell measurements

The overpotential measurements with H-cell (Figure S8) were carried out in an argon-filled glovebox (H_2O < 0.1 ppm, O_2 < 0.1 ppm). The H-cell consists of two containers locked together in the middle with a spring clip. The testing membrane was sandwiched between two O-ring foot pads. 35 mL of 0.2 M Li_2S_6 catholyte was added to each side of the H-cell. The anode of the H-cell was a lithium foil (d=15 mm) held with a stainless-steel clamp, and the cathode was porous carbon (Ketjenblack EC-600JD, d=15 mm) coated aluminum foil. A magnetic stirrer (1000 rpm) was placed on each side of the H-cell to reduce the impact of concentration polarization. The H-cell was sealed with a Teflon tape to prevent evaporation of the catholyte. After each test, the H-cell was washed and dried, and a fresh catholyte was refilled for the next measurement.

The H-cell device was connected to the CHI-660 potentiostat via feed-through cables. Galvanostatic charging and discharging processes were used to record the SRR potential of the cathode, with each current being tested for 60 seconds. Since different membranes have different resistance towards Li^+ transport, membranes with a higher Li^+ impedance will cause a larger overpotential and shift the charge and discharge plateaus of the cathode to a higher and lower voltage, respectively. By comparing the charge and discharge potentials of the cells using modified membranes with the PP membrane, the differences in overpotential at a certain current or C-rate can be calculated.

The testing current densities were calculated based on the assumed C-rates corresponding to a sulfur loading of 6mg cm^{-2} on the cathode of a Li–S battery. For example, in this study, C-rates of 0.02, 0.05, 0.1, 0.2, 0.5, and 1.0 C during the discharge processes equal to 0.355, 0.888, 1.776, 3.552, 8.88, and 17.76 mA.

(4) Modeling Li^+ mass transfer through membranes

The Li^+ mass transport simulation was performed using the Mass Transport Module of COMSOL Multiphysics 6.1. The mass transport model employed in this study was developed by optimizing and refining the frameworks established in previous investigations.[1, 3] This model extends previous frameworks by incorporating convection and mass transfer in porous media, with linear concentration treatment and excluding electric field migration.

The simulation focused on a symmetric Li|membrane|Li cell, designed to track the

temporal evolution of C_{Li^+} across electrodes under steady unidirectional current (Figure S10). The current density was set to 5.92 mA cm^{-2}, akin to a Li–S battery with a sulfur loading of 2 mg cm^{-2} at 1C rate. The chosen electrolyte was 1 M $LiPF_6$ (EC:DEC volume ratio 1:1), treated as non-solid at standard temperature and pressure settings. Although a specific model for 1 M LiTFSI in DOL:DME (suitable for Li–S batteries) was not available in COMSOL, the employed electrolyte model served as an acceptable approximation. The Li^+ activity coefficient (f_C) used was 0.60, and the lithium-ion diffusion coefficient (D_{Li^+}) was averaged at 6×10^{-10} m^2 s^{-1}, assumed isotropic.[4-6] Other electrolyte properties were set to the software's default values. In the simulation, a uniform 1 μm thickness was assigned to the modification layer, while the PP membrane was maintained at 25 μm. This is because the thicknesses of the two membranes are comparable with a similar material loading. The model's boundaries were aligned with the Li metal foils' stripping and deposition reactions, with reaction rates of ±6.14 mol m^{-2} s^{-1}, matching the set current density. There was no flux at the boundaries or within the PP membrane and modification layers. An extremely fine, physics-controlled mesh from COMSOL was utilized for accuracy, with a simulation duration of 60 seconds and a time step of 0.1 seconds. Parameters for the membrane were derived from SEM image analysis (Figure S9). and a randomization was applied to the distribution of holes in HG nanosheets. The model's boundary conditions, representing the interfaces of the two electrodes of the Li|Li symmetric cell with the electrolyte, were defined by the production and consumption rates of lithium ions at these interfaces, as determined by the charge/discharge current density of a Li–S battery with a sulfur loading of 6 mg

cm^{-2} at a charge/discharge rate of 1 C.

(5) Potentiostatic discharging measurements

The setup for this measurement is shown in Figure S12. The potentiostatic discharging process was measured with H-cell in the argon-filled glovebox (H_2O < 0.1 ppm, O_2 < 0.1 ppm). The H-cell consists of two identical containers that can be locked together with a spring clip. 35 mL of 1 M Li_2S_4 catholyte was added to right side container, while adding 35 mL blank LiTFSI electrolyte to the left. In the left side, lithium foil (d=15 mm) was held with a stainless-steel clamp serves as anode, Co_9S_8/HG/carbon cloth/PP, Co_9S_8/G/carbon cloth/PP or rGO/carbon cloth/PP were sandwiched in the neck. The Li_2S_4 passes through the necking area to the left side to form a circuit by reacting with Li^+. The carbon cloth serves as the current collector. The H-cell assembly was connected to the potentiostat located outside the glovebox using feed-through cables. The applied potential range is from 2.01 V to 1.7 V. Since porous-structured Co_9S_8/HG facilitates LiPSs transmitting rates and Li^+ diffusivity than that of non-porous structured material, additionally, the porous structured material possesses a large specific surface area, which enhances the catalytic performance of Co_9S_8 in polysulfide conversion reactions.

By comparing the current responses collected through discharging process, the catalytic effectivity can be confirmed. The morphology and formation of the surface area of the membranes after potentiostatic precipitation were studied with TEM and XPS to further confirm the redox reaction product (Figure 3-14).

(6) Polysulfide adsorption for holey and non-hole membranes

The preparation of a 1 mM Li_2S_6 solution in a DOL/DME solvent with a 1:1 v/v was conducted. Li_2S and sulfur powder were dispersed in a DOL/DME solvent mixture (1:1 v/v) at a molar ratio of 1:5. This mixture was placed in a tightly sealed container and heated above 60°C overnight inside the glovebox to ensure the dissolution of all solid substances, resulting in a homogeneous yellow solution. 8 mL of the Li_2S_6 solution was allocated into three glass vials. Each vial received 10 mg of the catalytic membrane materials, specifically Co_9S_8/HG and Co_9S_8/G. The glass vials were left undisturbed in a glove box for 8 hours. Afterwards, the supernatant was extracted for UV-vis spectroscopy analysis. The absorbance at a wavelength of 350 nm was used as a reference point in the UV-vis results for comparative analysis. Lower UV-vis peak values indicate a reduced concentration of Li_2S_6 molecules in the solution, implying that more Li_2S_6 molecules could rapidly reach the catalyst surface and get captured by the catalyst within a given time frame (e.g., Co_9S_8/HG in Figure S13).

(7) Electrochemical measurements

Li|Li symmetric cells were prepared with two lithium metal electrodes, the modified sandwiched between two layers of PP separators to avoid reactions between the functional membrane materials and lithium anode, the electrolyte is 1M LiTFSI. Then tested at the C-rate of 0.02 C to 1 C, derived from the current density of a sulfur cathode with a mass loading of 6 mg cm^{-2} and a diameter of 15 mm.

Symmetric cells for electrocatalysis measurement were assembled with two identical

electrodes (Co_9S_8/HG, Co_9S_8/G, or rGO, ~0.5 mg cm^{-2}), added with 40 μL 0.2M Li_2S_6 catholyte. CV tests were performed within a potential window of -1V to 1V at a scan rate of 3 mV s^{-1}.

Tafel plot: Li–S cells were assembled by mixing Co_9S_8/HG-S, (Co_9S_8/G-S, or G-S), SuperP and PVDF, with a mass proportion of 80:15:5 to form the cathode slurry, which was coated onto Al foil (identical mass loading ~ 0.6 mg cm^{-2}) and further punched into disks with a diameter of 15 mm and vacuum dry for overnight. Standard CR2032 coin cells were assembled with the prepared Co_9S_8/HG-S, (Co_9S_8/G-S, or G-S)) as the cathode, lithium foil as the anode, Celgard 2400 membrane as the blank LiTFSI as electrolyte. CV measurements were conducted at the scan rate of 0.04 mV s^{-1} for Tafel plot analysis.

Electrochemical performance: Mixing S/Ketjen Black, super P and PVDF with a mass ratio of 70:20:10 to prepare the cathode slurry. Coating the prepared slurry onto Al foil and followed with vacuum dry overnight noted as sulfur-based electrodes. Punch the electrodes to get disks with a diameter of 15 mm. Assembly the CR2032 coin cells with S based disks as cathode, lithium metal as the anode, the Co_9S_8/HG/PP or Co_9S_8/G/PP as separators and 54μL 1M LiTFSI electrolyte. The charging/discharging, rate performances and long-term cycling were recorded on a Land CT2001 battery testing system.

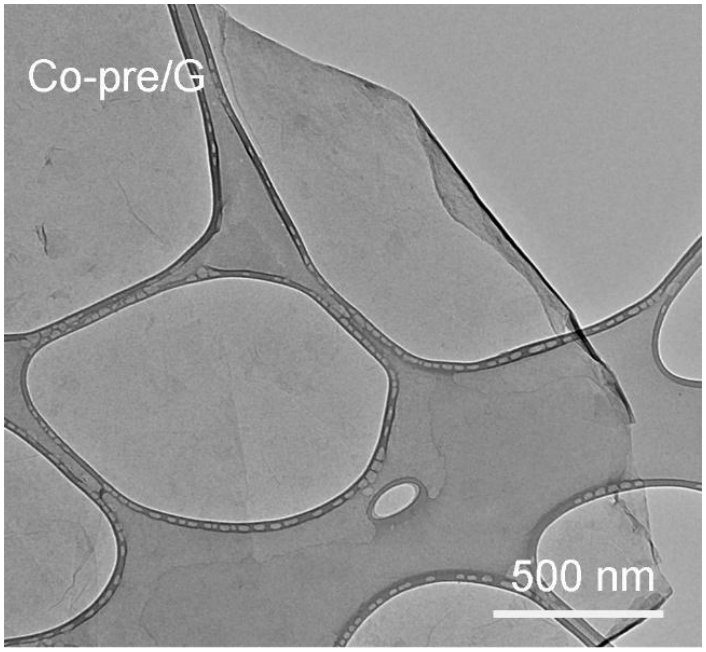

Figure S1. TEM image of Co-pre/G nanosheet, with a smooth surface and no visible signs of material growth.

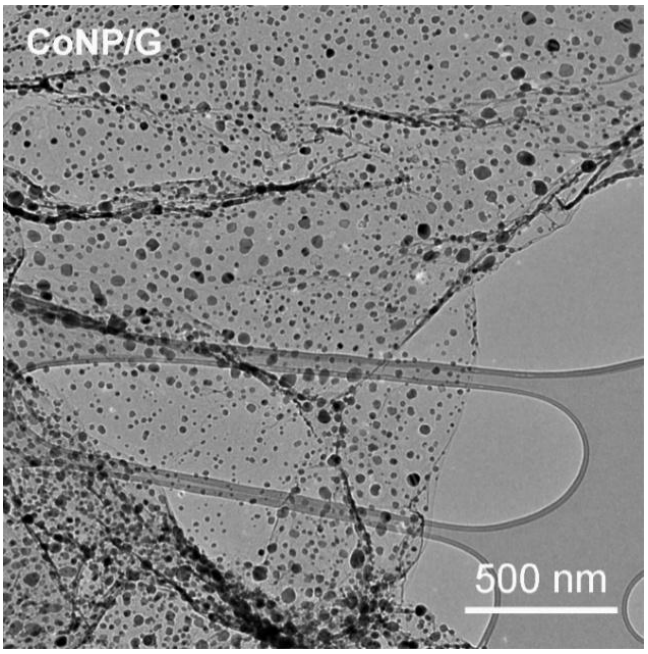

Figure S2. TEM image of CoNP/G nanosheets after annealed at 800°C in N_2, CoNPs distribute evenly on the substrate of rGO.

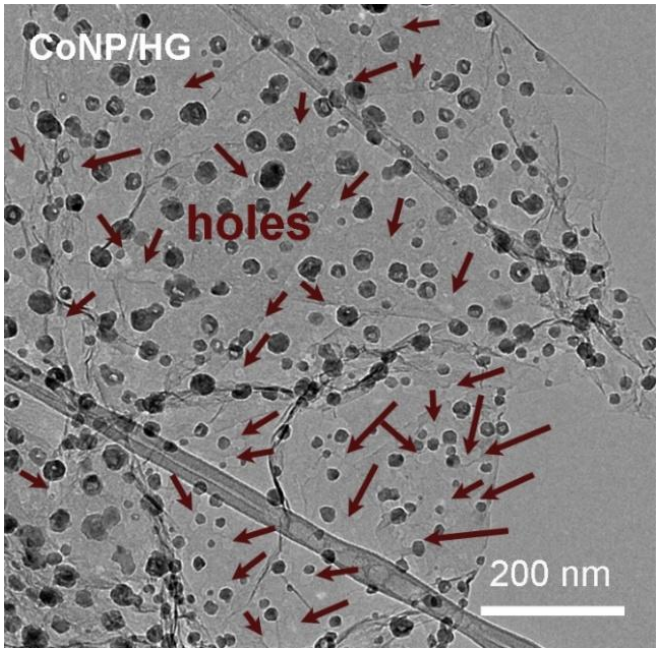

Figure S3. TEM image of CoNP/HG nanosheets after further annealing of the partially oxidized Co_3O_4-CoNP/G nanosheets at 800°C in N_2. The holes on graphene nanosheet were revealed underneath the nanoparticles (some of particles sonicated away when preparing TEM samples). This confirms that the holes are created by in-situ oxidation of graphene by the partially oxidized intermediate product Co_3O_4-Co nanoparticles, while the Co_3O_4 domains are carbothermal reduced to metallic Co at the same time.

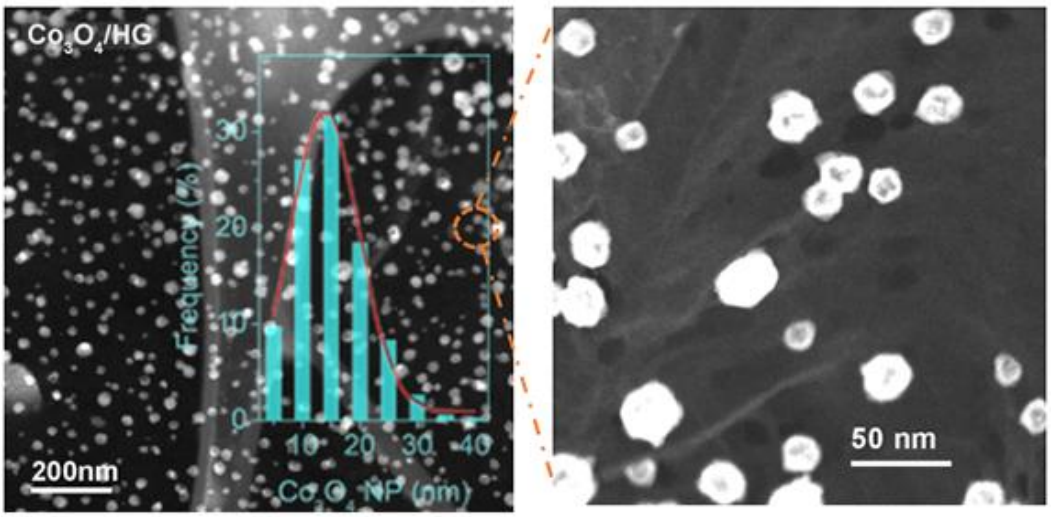

Figure S4. SEM image of Co_3O_4/HG nanosheets that were produced by further heating CoNP/HG in air at 200°C. The Co_3O_4 nanoparticle size on HG nanosheet is around 15 nm with a nanoparticle population density of approximately 366 NPs μm^{-2}. The inset is the STEM image of Co_3O_4/HG nanosheet.

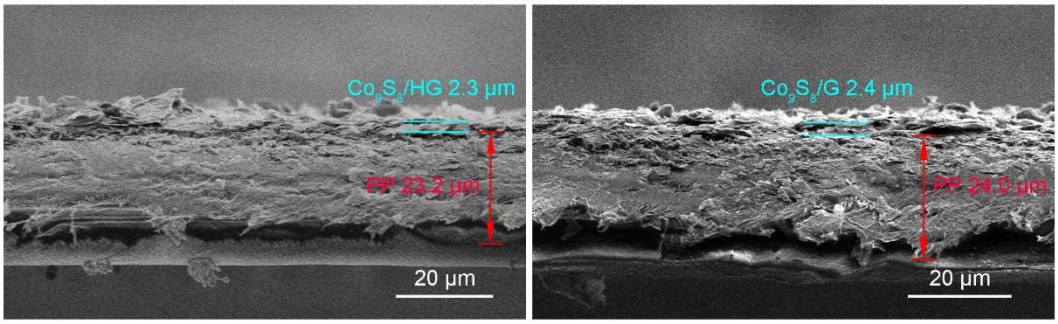

Figure S5. Cross-section SEM images of Co_9S_8/HG/PP, and Co_9S_8/G/PP membranes. Due to the blunt of the cutting knife, the substrate of PP layer is not clearly showed. The thicknesses of the two membranes are comparable with a similar material loading.

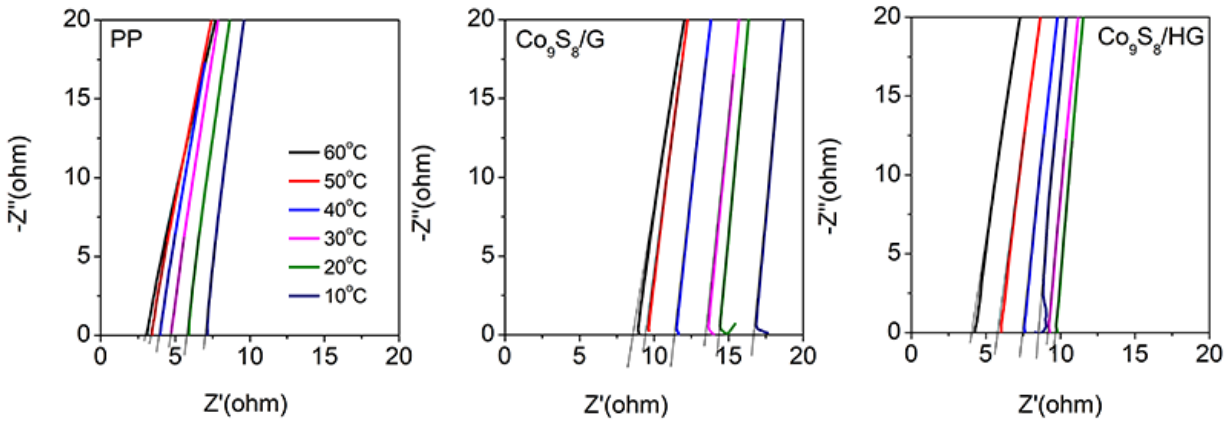

Figure S6. EIS measurements performed at different temperatures with different membranes.

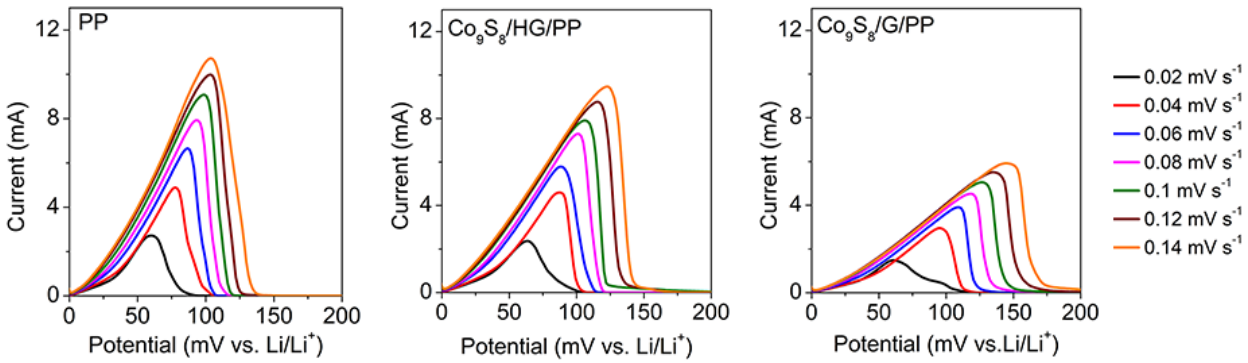

Figure S7. LSV measurements performed at different sweeping rates for various membranes.

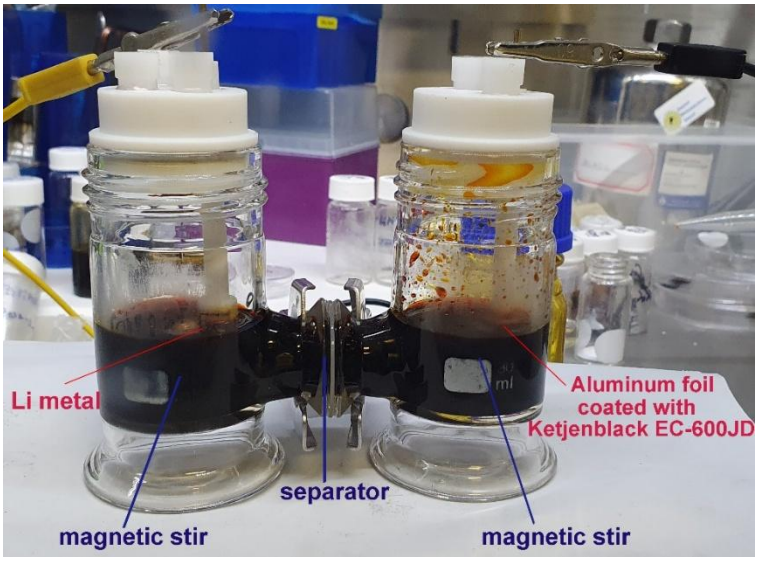

Figure S8. H-cell setup for SRR overpotential measurements.

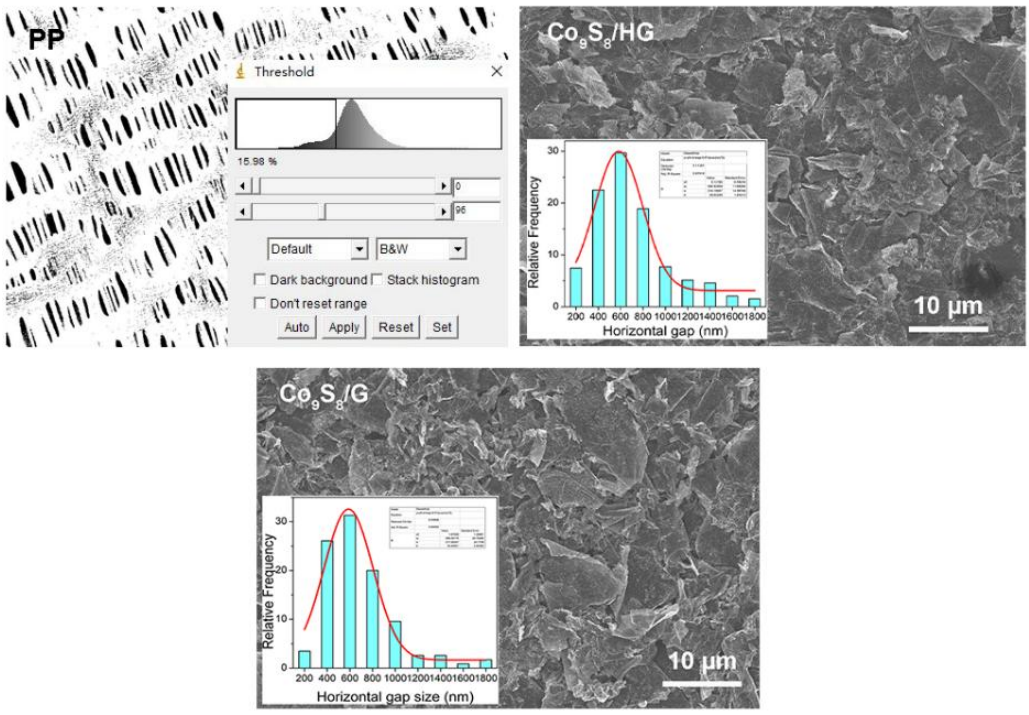

Figure S9. Statistical analysis of the pore area percentage of commercial PP membranes and gap number and size between graphene nanosheets in the Co_9S_8/HG/PP, and Co_9S_8/G/PP modified membranes.

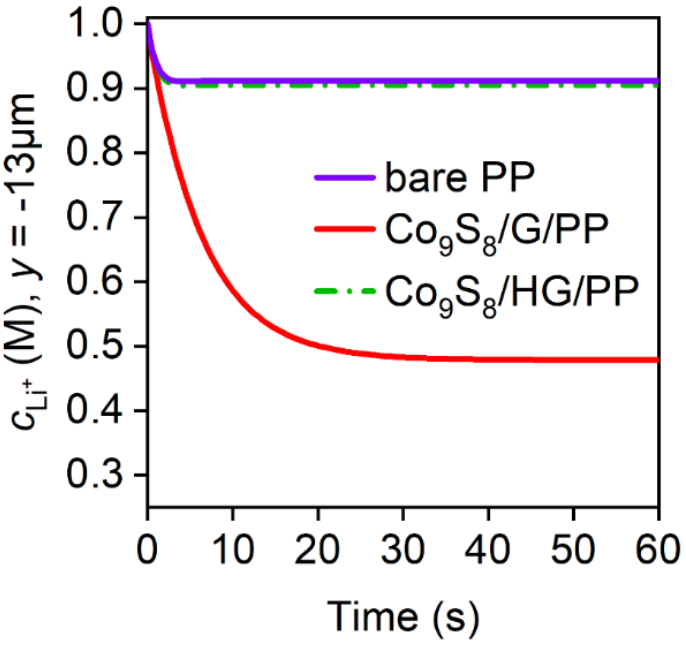

Figure S10. Instant evolution of C_{Li^+} examined at 0.5 μm right below the PP membrane.

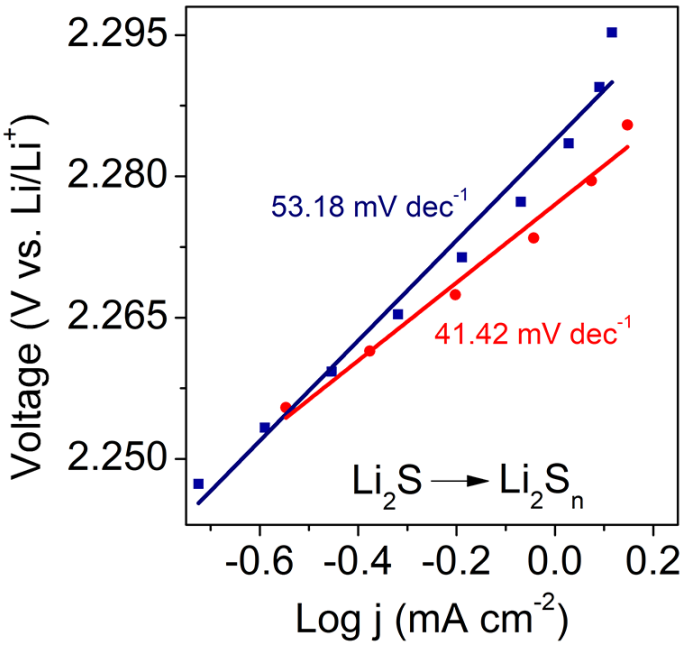

Figure S11. Tafel plots of solid Li_2S convert (A1 in Figure 6b) to soluble long-chain Li_2S_n ($4 \leq n \leq 8$).

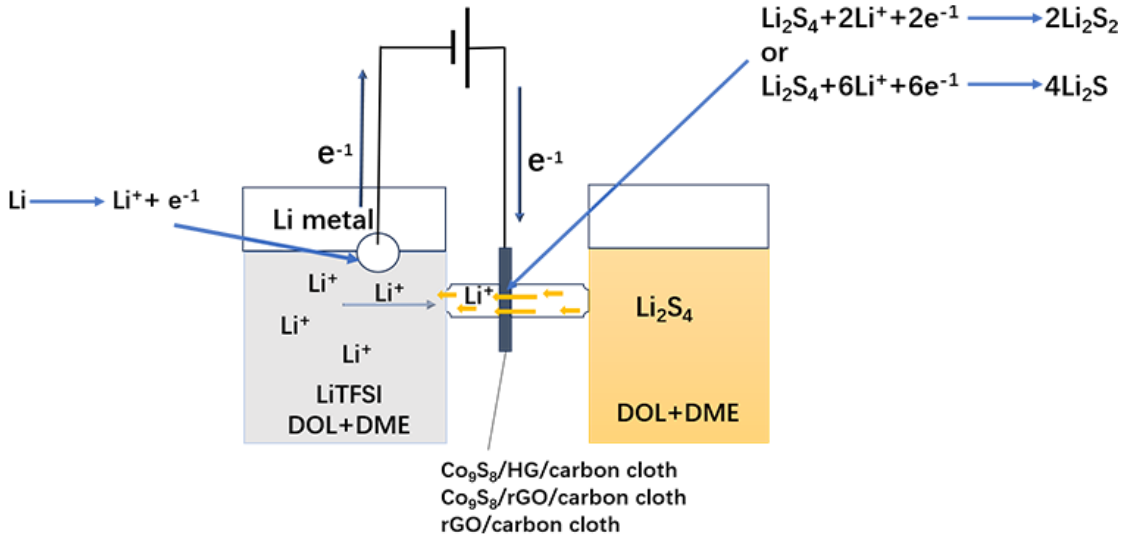

Figure S12. H-cell setup for Li_2S_2/Li_2S potentiostatic precipitation (Experiment method).

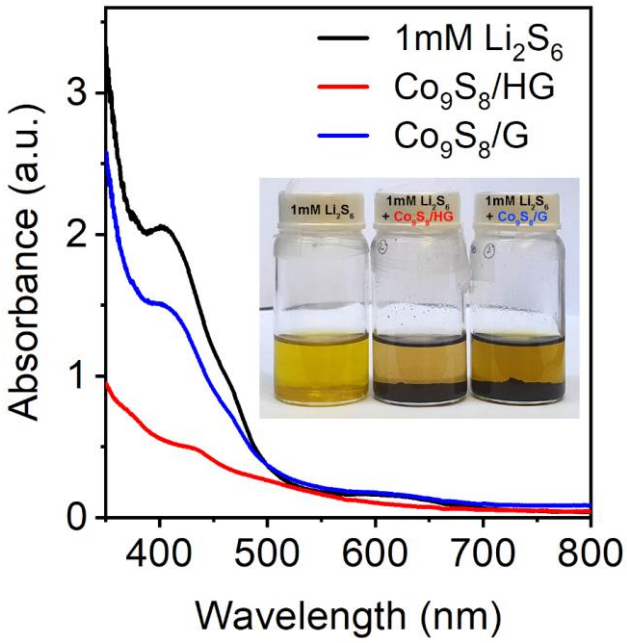

Figure S13. Li_2S_6 adsorption measurement for Co_9S_8/HG and Co_9S_8/G membranes. (Tested after for 1 h adsorption)

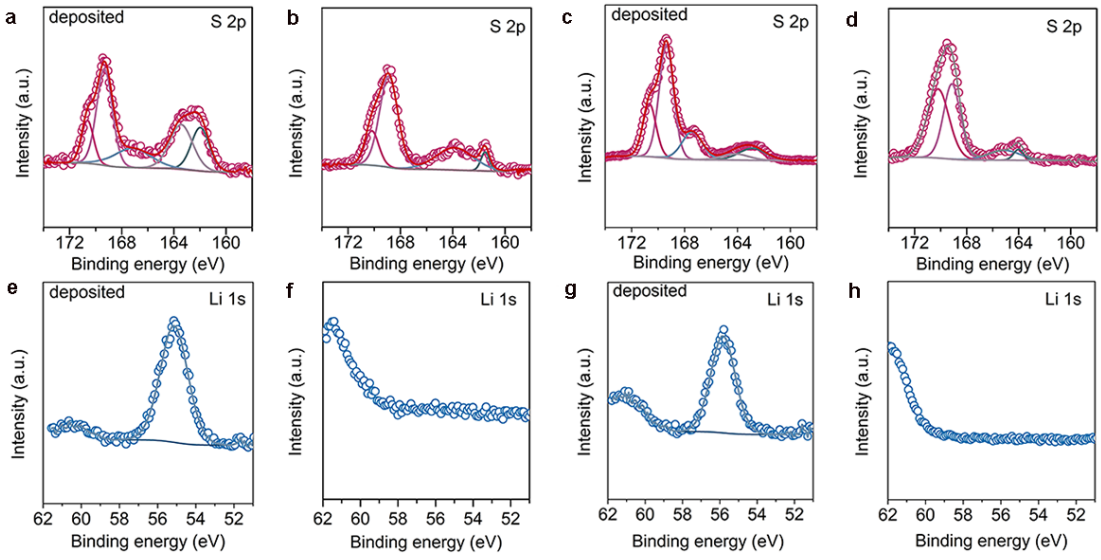

Figure S14. S 2p and Li 1s XP spectrum of a) Co_9S_8/HG after deposited, b) fresh Co_9S_8/HG, c) Co_9S_8/G after deposited, e) fresh Co_9S_8/G. Li 1s XP spectrum of e) Co_9S_8/HG after deposited, f) fresh Co_9S_8/HG, g) Co_9S_8/G after deposited, h) fresh Co_9S_8/G.

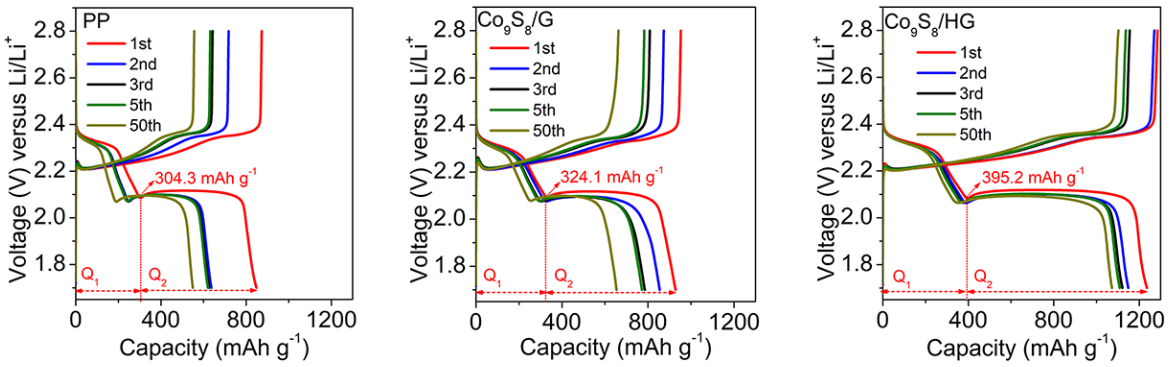

Figure S15. Charge/discharging voltage profile of Li–S cells with bare PP, Co_9S_8/G/PP, and Co_9S_8/HG/PP separators.

3.8 SI References

1. Liu, B.; Torres, J. F.; Taheri, M.; Xiong, P.; Lu, T.; Zhu, J.; Liu, Y.; Yu, G.; Tricoli, A., Dual-Ion Flux Management for Stable High Areal Capacity Lithium–Sulfur Batteries. *Advanced Energy Materials* **2022,** *12* (10), 2103444.

2. Zhou, G.; Tian, H.; Jin, Y.; Tao, X.; Liu, B.; Zhang, R.; Seh, Z. W.; Zhuo, D.; Liu, Y.; Sun, J., Catalytic oxidation of Li2S on the surface of metal sulfides for Li− S batteries. *Proceedings of the National Academy of Sciences* **2017,** *114* (5), 840-845.

3. Liu, B.; Taheri, M.; Torres, J. F.; Fusco, Z.; Lu, T.; Liu, Y.; Tsuzuki, T.; Yu, G.; Tricoli, A., Janus conductive/insulating microporous ion-sieving membranes for stable Li–S batteries. *ACS nano* **2020,** *14* (10), 13852-13864.

4. Logan, E. R.; Gering, K. L.; Ma, X.; Dahn, J., Electrolyte Development for High-Performance Li-Ion Cells: Additives, Solvents, and Agreement with a Generalized Molecular Model. *The Electrochemical Society Interface* **2019,** *28* (2), 49.

5. Valøen, L. O.; Reimers, J. N., Transport Properties of LiPF6-Based Li-Ion Battery Electrolytes. *Journal of The Electrochemical Society* **2005,** *152* (5), A882.

6. Nishida, T.; Nishikawa, K.; Fukunaka, Y., Diffusivity Measurement of LiPF6, LiTFSI, LiBF4 in PC. *ECS Transactions* **2008,** *6* (18), 1.

Chapter 4 Optimizing localized Li-ion diffusivity for Enhanced Sulfur Redox kinetics and Controlled Li_2S Deposition in High-Rate Li–S Batteries

4.1 Prologue

In this project, we synthesized a porous Co_3S_4 catalyst as a model sulfur host and demonstrated that enhancing localized Li^+ diffusivity is crucial for accelerating SRR kinetics and regulating Li_2S deposition.

I designed this project, conducted the experiments, performed the material characterization, collected, analyzed and interpreted the data. Qi Wang from University of Sydney performed the XPS characterization, Raman and SEM characterization. I drafted the manuscript, Dr. Borui, Qi Wang, Prof. Antonio Tricoli and Prof. Zongyou reviewed my manuscript.

4.2 Abstract

The sluggish conversion rate of liquid lithium polysulfides (LiPSs) to solid Li_2S is the rate-determining step in the discharging process of lithium sulfur (Li–S) battery. Incorporating functional catalysts as sulfur host is a widely adopted strategy to enhance the electrochemical kinetics of sulfur redox reaction (SRR). While extensive efforts have been dedicated to enhancing LiPSs reaction kinetics, the role of sulfur host structures in facilitating Li^+ transport and their subsequent impact on SRR kinetics remain underexplored. Herein, porous Co_3S_4 with distinct nanostructures is

synthesized and employed as model electrocatalyst to elucidate the significance of Li^+ diffusion in promoting SRR kinetics and regulating Li_2S precipitation. Experiment results reveal that Co_3S_4-T400 (average particle size: 20.7 nm, average pore diameter: 3.3 nm, and the porosity 13.6%) exhibits lower resistance to Li^+ transport and provides abundant active sites, as indicated by its larger electrochemically active surface area (ECSA). These characteristics contribute to enhanced electrocatalytic kinetics for LiPSs conversion and improved Li_2S precipitation. The Li–S batteries with S/Co_3S_4-T400/C composite electrodes demonstrate superior rate performance and long-term cycling stability at 0.2 C, retaining a specific capacity of 657 mAh g^{-1} with a low-capacity decay rate of 0.051% per cycle over 1000 cycles. This work underscores the critical role of porous structural design in sulfur cathode catalysts for accelerating SRR kinetics and regulating Li_2S deposition by enhancing localized Li^+ diffusion.

4.3 Introduction

In Li–S battery, the sulfur cathode undergoes a 16-electron redox reaction,[1-3] transforming sulfur molecular into a series of LiPSs with varying chain lengths. The conversion from soluble Li_2S_4 to solid Li_2S_2/Li_2S accounts for three-quarters of the theoretical specific capacity of 1675mAh g^{-1} (Figure 4-1a) and serves as the rate-limiting step in the sulfur cathode's electrochemical reactions.[4-6] In this process, issues such as the LiPSs shuttle movements,[7-9] sluggish SRR kinetics[5, 10, 11], the electronically insulating nature of Li_2S, and the inefficiency deposition and decomposition of Li_2S lead to rapid capacity fading,[12-15] and poor cyclability, thereby hindering the

commercialization of Li–S batteries.[16] To address these challenges in the cathode side, many groups have conducted extensive research on catalytic sulfur hosts[17] to accelerate the kinetics of SRR to effectively reduce LiPSs accumulation.[18-20]

To date, multiple approaches have been employed to enhance catalytic effects of sulfur intermediates, primarily focus on strengthening chemical binding[21-25] between electrocatalyst and LiPSs, increasing the conductivity of electrode composites, and engineering the energy band structure.[26-29] These strategies aim to stabilize LiPSs intermediates,[30-32] increase charge transfer pathways,[33-35] and lower activation energy for the conversion reactions of sulfur species,[10, 36-40] ultimately contributing to improved cycling stability and higher sulfur utilization. Cui and co-workers[41] demonstrated that, for nonconductive metal oxides to effectively facilitate lithium polysulfide conversion, LiPSs must diffuse efficiently from the oxide surface to a conductive matrix. They highlighted the importance of balancing LiPSs adsorption and diffusion on polar surfaces. Among the oxides investigated, Al_2O_3 exhibited the strongest adsorption toward Li_2S with an adsorption energy of -7.12 eV, compared to La_2O_3 (-5.85 eV), MgO (-5.71 eV), and CeO_2 (-6.33 eV). Although Al_2O_3's strong binding favors adsorption, it restricts the surface diffusion of LiPSs. These binding energies illustrate the diverse capabilities of each oxide in adsorbing and retaining lithium polysulfides, which is crucial for optimizing Li–S battery performance. The study further represented that the oxides like MgO, CeO_2, and La_2O achieve a balance between strong adsorption and adequate diffusion, promoting efficient sulfur utilization and minimize capacity decay. To address the kinetic barrier to surface diffusion, facilitating electron transfer to the

adsorbed lithium polysulfides is essential.[42] Nazar et al. synthesized Ti_4O_7 nanocrystals[43] (electrical conductivity, ~ 2 x 10^3 S cm^{-1} at room temperature) to composite with S, achieving a low-capacity decay of 0.08% per cycle at 0.5C after 250 cycles. This performance was attributed to the metallic conductivity of Ti_4O_7 and strong chemical interaction of Ti^{3+} with Li_2S_4, leading to a faster reduction kinetics and decreased shuttle effect.

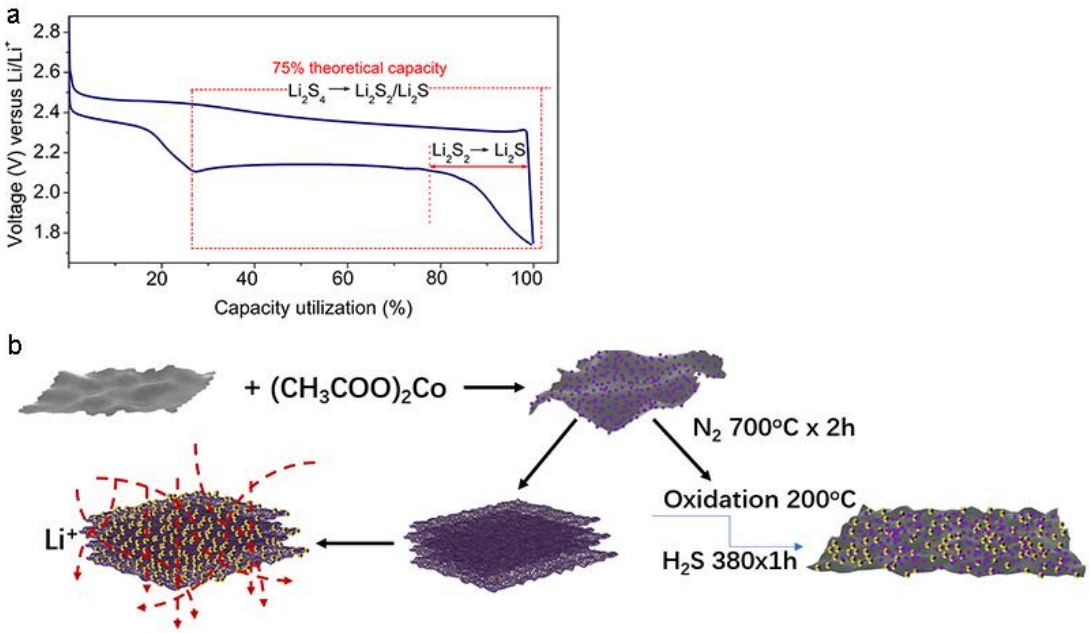

Figure 4-1. Schematic illustration of Co_3S_4 nanosheets synthesis with template method

Although significant progress has been made in investigating catalytic effects,[44-46] few studies have addressed the adverse impact of catalyst incorporation on SRR kinetics, particularly due to its effect on Li^+ diffusivity. This issue arises because traditional electrode fabrication methods often result in densely packed cathode composites, which increase ion diffusion distances and consequently degrade electrochemical performance.[39, 47] Therefore, efficient Li^+ transport not only involves the extensive

movement within the porous structure of the cathode but also emphasizes the localized mobility of lithium ions on the catalyst surface. Enhanced Li^+ conductivity enables lithium ions to rapidly access active sites on the catalyst, promoting swift engagement in LiPSs redox reactions. Furthermore, the Li_2S_2/Li_2S precipitation process is primarily governed by charge transfer rates on the surface of cathode hosts.[48] Enhancing Li^+ transport by creating continuous ion pathways contributes to efficient deposition, prevents localized aggregation.[49, 50] In this work, we developed holey-structured Co_3S_4-T400 as a model electrocatalyst, investigating the influence of its holey structure in enhancing SRR kinetics, Li_2S precipitation through facilitating Li^+ transport in cathode. Transmission electron microscope (TEM) characterization and statistical analysis confirmed that the porosity of Co_3S_4-T400 nanosheet is 13.6% with a uniformly distribution of pours, indicating that the catalyst of Co_3S_4-T400 impose less residence towards Li^+ transport compared with that of non-holey Co3S4-T200. ECSA measurements showed that the electrochemical active surface area of Co_3S_4-T400 is four times larger than that of Co_3S_4-T200, providing abundant active sites in Co_3S_4-T400 to better encapsule and catalyze LiPSs. Cells with Co_3S_4-T400 catalyst host demonstrate smaller Tafel slope, higher Li^+ diffusion coefficient (D_{Li^+}), and more uniformly Li_2S deposition, suggesting that the holey structured Co_3S_4-T400 effectively facilitate Li^+ transport for enhanced SRR kinetics and controlled Li_2S precipitation. As a proof of concept, the Li-S batteries with S/Co_3S_4-T400/C exhibited outstanding long-term cycling performance, maintaining a specific capacity of 657 mAh g^{-1} with a low-capacity decay rate of 0.051% per cycle and a high average coulombic efficiency of

98.5% over 1000 cycles. These results suggest that facilitating localized Li^+ diffusion through a porous structured catalyst is an effective strategy to accelerate SRR kinetics and regulate Li_2S precipitation, thereby improving the overall performance of Li–S battery.

4.4 Results and discussion

4.4.1 Structure and composition characterization

Figure 4-1b (SI: Experimental Method) illustrates the synthesis procedure of holey-structured Co_3S_4 nanosheet, denoted as Co_3S_4-T400. In detail, graphene oxide (GO) and cobalt acetate were dispersed in ethylene glycol (EG) and underwent a hydrothermal reflux reaction at 190° C, resulting in the reduction of GO to reduced graphene oxide (rGO) while homogenously grafting Co^{2+} onto rGO nanosheets, forming Co-pre/G composite (Figure S1). The Co-pre/G composite were further oxidized in air at 400° C for 3 hours to remove graphene, resulting in a holey nanosheet Co_3O_4-T400 (Figure S2). Subsequently, Co_3O_4-T400 reacted with hydrogen disulfide (H_2S) at 380° C for 45 minutes to produce Co_3S_4-T400, consisting of bridged Co_3S_4 nanoparticles (Figure S3). For comparative analysis, Co_3S_4-550T (Figure S4, S5) was also synthesized by oxidized the precursor at 550° C and followed with the similarly sulfidation reaction. Co_3S_4-200T (Figure S6, S7) was synthesized through a different pathway followed by our previous work. Specifically, the Co-pre/G was first annealed at 700° C for 1 hour, then oxidized in air at 200° C for 3 hours and subjected to sulfidation at 380° C for 45 minutes.

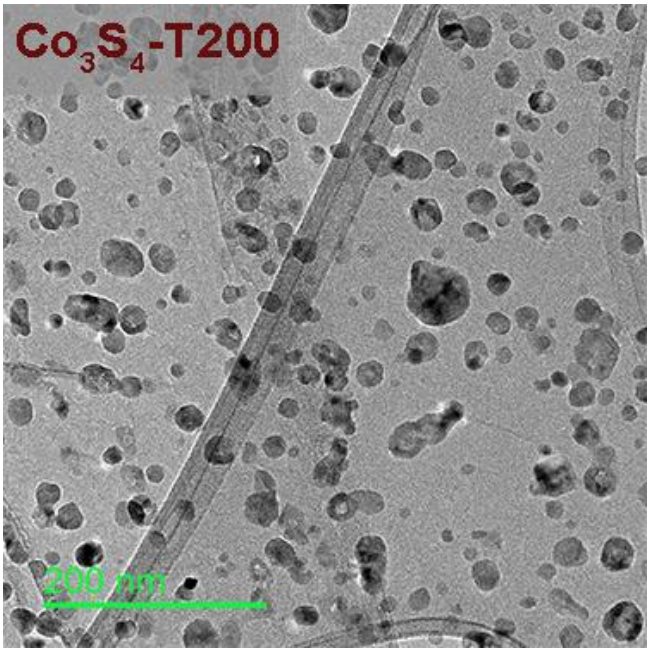

Figure 4-2. TEM image of Co3S4-200T nanosheet

The morphology of the as-prepared Co_3S_4-T200, Co_3S_4-T400 and Co_3S_4-T550 were characterized by transmission and scanning electron microscopy (TEM and SEM). Figure 4-2 presents the Co_3S_4-T200 nanosheet, indicating that Co_3S_4 nanoparticles uniformly distributed on smooth but slightly wrinkled surface of rGO, no holes visible on graphene laminar (Figure S10).

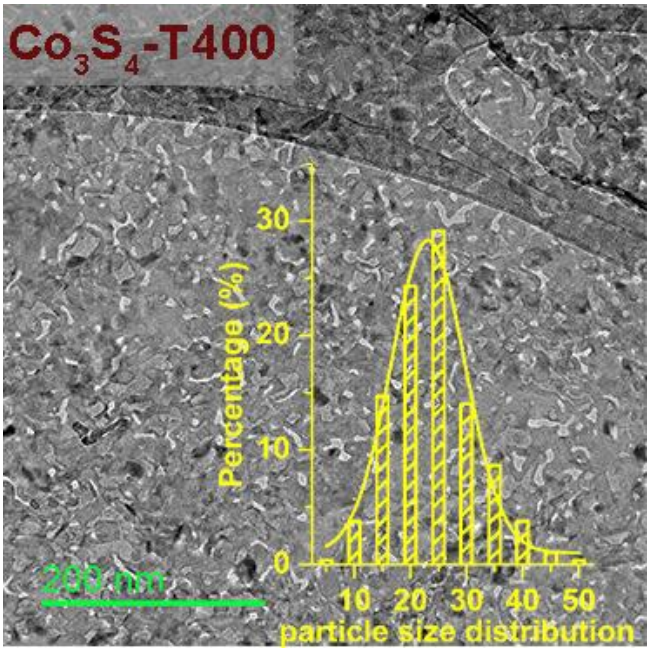

Figure 4-3. TEM image and particle size distribution of Co_3S_4-T400 nanosheet

In comparison, the graphene substrates were burned off in the high-temperature oxidation process for the Co_3S_4-T400 (Figure 4-3) and Co_3S_4-T550 (Figure 4-4) samples, leaving Co_3S_4 nanoparticles bridged together with varying particle diameters and pore size distribution (Figure S11 and S12). For Co_3S_4-T400 sample, the porous area account is 13.6%, the average particle size is 20.7 nm (Figure 4-3), and the average pore size is 3.3 nm (Figure S8).

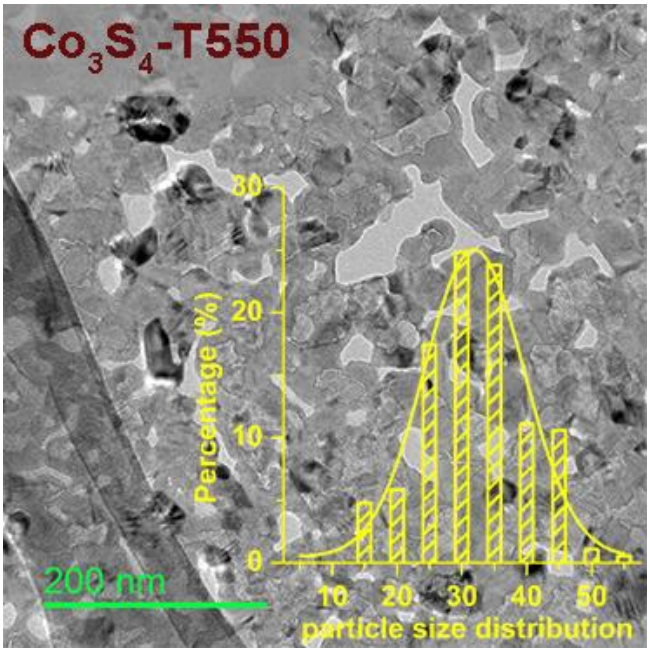

Figure 4-4. TEM image and particle size distribution of Co_3S_4-T550 nanosheet.

Figure 4 illustrates the statistical particle size distribution of Co_3S_4-T550. The porosity is 21.5%, the average particles size value is 31.1 nm (Figure 4-4), while the average pore sizes is 9.3 nm (Figure S9), presenting a trend of particles aggregation as the oxidation temperature increases.

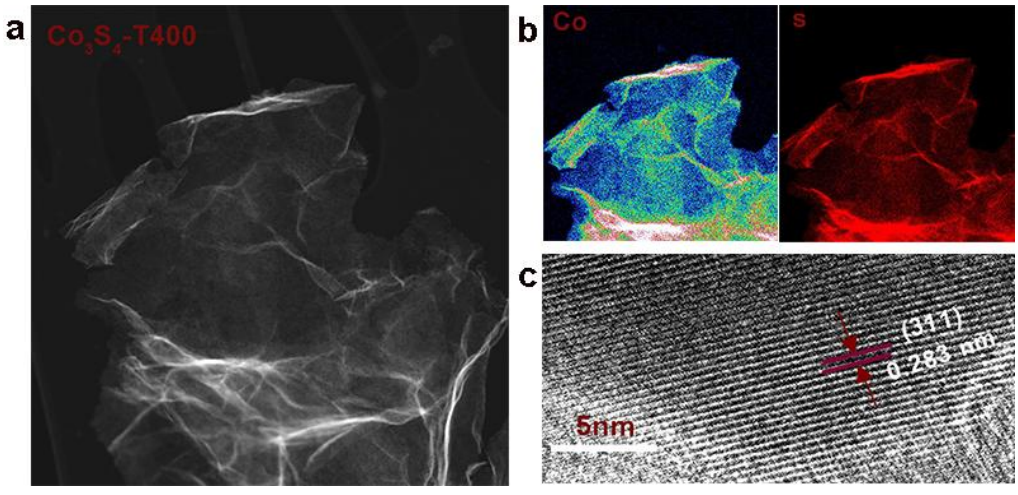

Figure 4-5. Composition analysis**.** Composition analysis. (a) STEM image of Co_3S_4-T400 nanosheet. (b) EDS mapping of Co_3S_4-T400 nanosheet, indicating elemental compositions of Co and S. (c) HRTEM of Co_3S_4-T400 showing the crystal lattice.

Energy-Dispersive spectroscopy (EDS) mapping show uniform distribution of Co and S in all the as-prepared samples, providing first evidence of Co_3S_4 formation (Figure 4-5). High-resolution TEM (HRTEM) analysis (Figure 5c) reveals the lattice fringe of 0.283 nm which is in agreement with the (311) plane spacing of Co_3S_4.

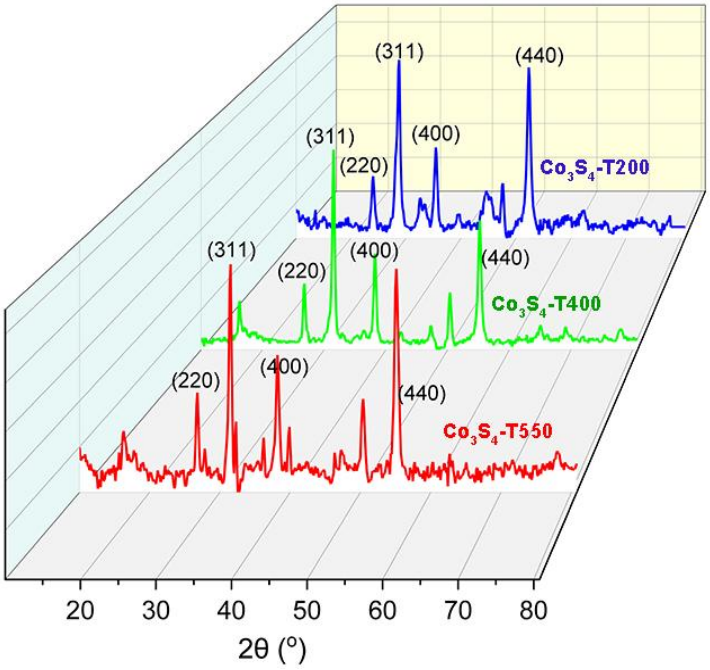

Figure 4-6. XRD patterns analysis of Co_3S_4-T200, Co_3S_4-T400, and Co_3S_4-T550.

The phase structure and purity of the as-synthesized sulfides were investigated through powder X-ray diffractometer. As indicated in Figure 4-6, the diffraction peaks at 26.7°, 31.4°, 38°, and 55° are corresponding to the (220), (311), (400), and (440) planes of cubic Co_3S_4 (PDF 42-1448). the Co_3S_4 were successfully synthesized at the temperatures of 200°C, 400°C and 550°C by oxidized in air for three hours. Specially, for Co_3S_4-T200, weak characteristic peaks of cobalt monoxide (CoS) were detected in the XRD pattern, indicating a small amount of impurity of CoO may be introduced, which is attributed to the Co element adsorbed within the closely stacked graphene

nanosheets cannot be completely oxidized at the relatively low oxidation temperature of 200°C, resulting in the formation of minor amount of CoS during the subsequent sulfidation reaction.

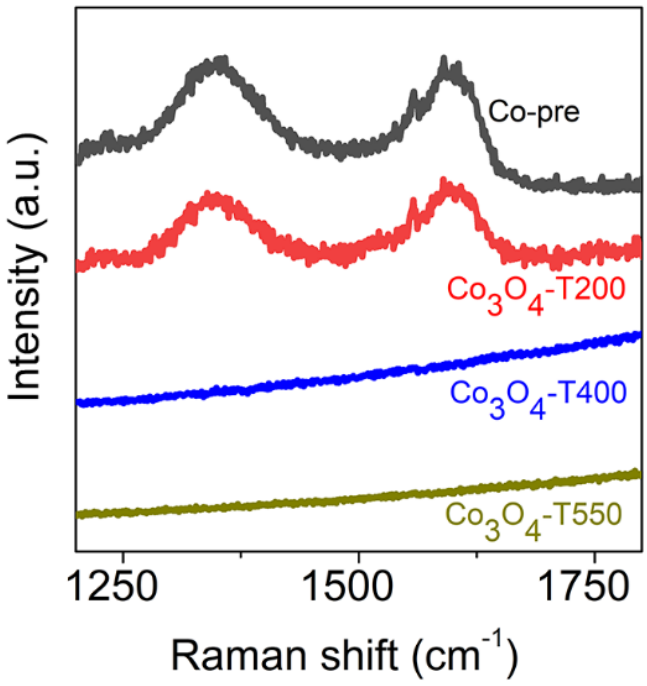

Figure 4-7. Raman spectra of synthesized materials**:** Co-pre/G, Co_3O_4-200T, Co_3O_4-T400 and Co_3O_4-T550.

Raman spectra of Co-pre/G, Co_3O_4-200T, Co_3O_4-T400 and Co_3O_4-T550 were conducted, as shown in Figure 4-7. Co-pre and Co_3O_4-T200 Raman spectrum show two strong bands at 1347 cm^{-1} and 1598 cm^{-1}, correspond to the vibrations of sp^3 graphite carbon atoms and the E_{2g} phonon of sp^2-bonded carbon atoms, indicating the existing of graphene nanosheet, while for Co_3O_4-T400 and Co_3O_4-T550, no Raman signals corresponding to graphene are observed, suggesting that the graphene nanosheets were likely decomposed or transformed at higher calcination temperatures.

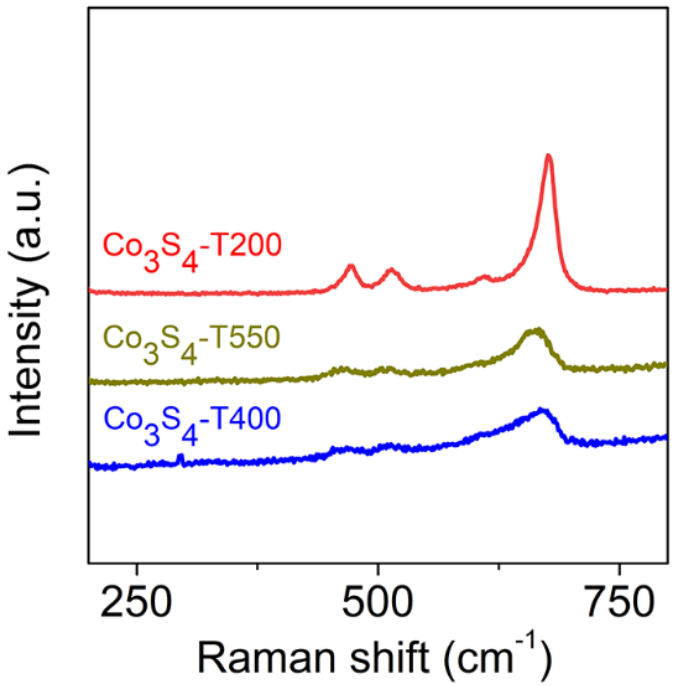

Figure 4-8. Raman spectra of sulfides: Co_3S_4-200T, Co_3S_4-T400 and Co_3S_4-T550.

Raman spectra of Co_3S_4 samples obtained at different temperatures are presented in Figure 4-8. In all Raman spectra, the corresponding Raman peaks at 191, 348, 470, 515 and 679 cm^{-1} could be indexed to A_g, E_g, F_{2g} and A_{1g} modes[51] for the spinel Co_3S_4. Their Raman modes reveal obvious broadening and weakening compared with that of Co_3S_4 synthesized at lower temperature.

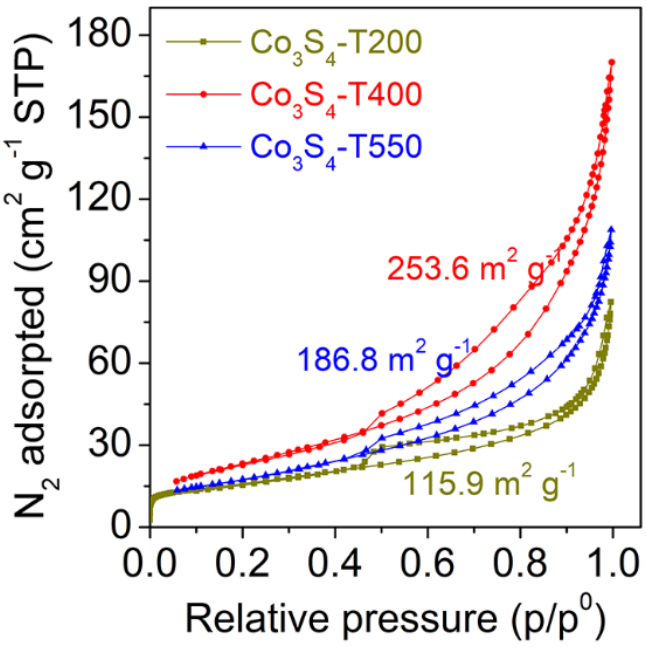

Figure 4-9. BET surface area analysis

The specific surface areas (SSA) (Figure 4-9) measured by the BET method for the Co_3S_4-T400 is 253.6 m^2 g^{-1}, 1.2 times higher than that of its non-hole counterpart Co_3S_4-T200, while Co_3S_4-T550 exhibits medium SSA among the prepared samples. The large SSA exposes a greater number of Co_3S_4 nanoparticles, enhancing the adsorption of LiPSs, accelerating their conversion, and promoting the deposition of Li_2S.

4.4.2 Polarization comparison

To examine the impact of catalyst particle size and porous morphology on Li^+ diffusion resistance, Co_3S_4-T200, Co_3S_4-T400 and Co_3S_4-T550 were individually coated (mass loading: 0.18 mg cm^{-2}) onto polypropylene (Celgard 2400) separators, forming Co_3S_4-T200/PP, Co_3S_4-T400/PP and Co_3S_4-T550/PP. These modified separators were employed in symmetric Li|Li cells to evaluate the resistance to Li^+ diffusion at different

C-rates. (SI: Experimental Method).

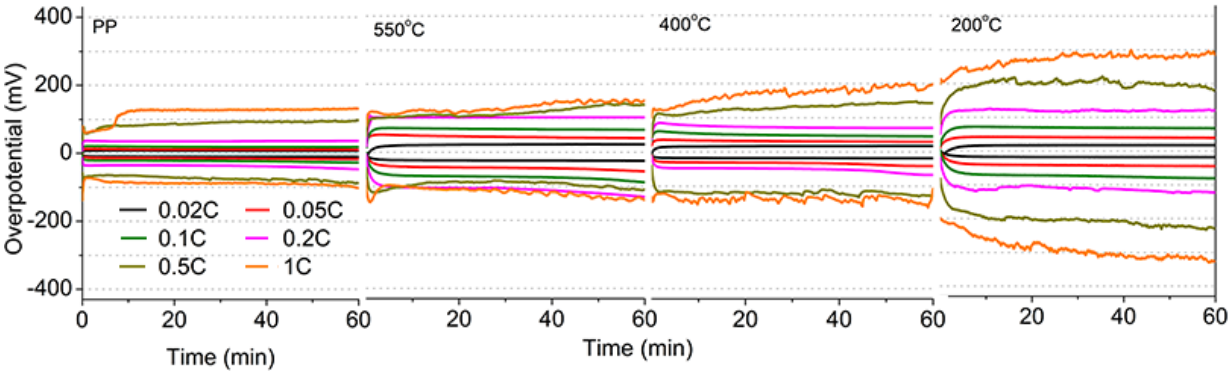

Figure 4-10. Polarization measurements**.**

Galvanostatic charging/discharging assessments were conducted at nominal C-rates, calculated based on a sulfur loading of 6 mg cm^{-2} in Li–S cells. The overpotentials were analyzed to determine the blocking effects on Li^+ diffusivity. As shown in Figure 4-10, the overpotentials for Co_3S_4-T200, Co_3S_4-T400 and Co_3S_4-T550 membranes are compared with that of the PP separator across current rates from 0.02 C to 1 C. Results reveal that the coating layers increased diffusion impedance for Li^+ transport, especially at higher C-rates. the Co_3S_4-T400 and Co_3S_4-T550 membranes exhibited a similarity of lower overpotential (reduced by 31.8% and 32.8% at 0.5 C and 1 C, respectively) compared to that of Co_3S_4-T200 (detailed decreasing ratio). This improvement can be attributed to the porous structure of the Co_3S_4-T400 and Co_3S_4-T550 materials. The former exhibits a pore area fraction of 13.6%, slightly lower than the 15.5% observed in commercial PP separators, whereas the latter reaches a significantly higher fraction of 21.5%. This perforation on the nanosheets enhances localized mobility of lithium ions on the catalyst surface, thereby facilitating improved ion transport. In contrast, the non-hole Co_3S_4-T200 separator exhibits a high

overpotential of approximately 290 mV at 1 C, reflecting a significant inhibitory effect on Li^+ transport. The findings reveal that introducing localized pathways on the catalyst surface promotes efficient Li^+ diffusivity, effectively mitigating the overpotential associated with non-porous structures and enhances Li^+ transport dynamics.

4.4.3 Electrochemical performance measurements

The electrochemical performances of Co_3S_4-T200, Co_3S_4-T400 and Co_3S_4-T550 hosts were investigated to highlight the crucial role of efficient localized Li^+ diffusion in enhancing SRR catalytic efficiency.

(1) ECSA measurement.

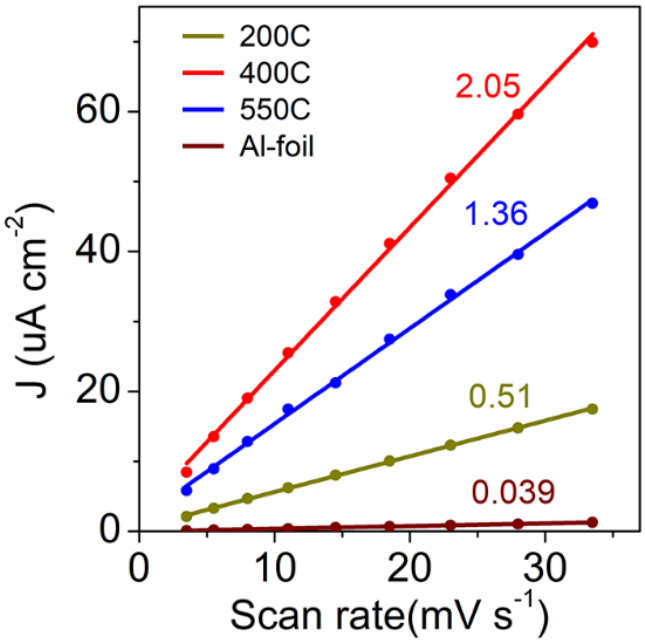

Figure 4-11. Evaluation of electrochemical active surface area (ECSA), electrochemical double-layer capacitance (C_{dl}) compared with aluminum foil. Li^+ diffusion properties of the electrodes at various scanning rates (identical active material loading ~0.5 mg cm^{-2}).

Electrochemical active surface area (ECSA) is a critical factor for electrocatalysis, the increase of surface area is often primarily responsible for enhanced catalytic activity. The cyclic voltammetry (CV) measurements for ECSA measurement (SI: Experimental Methode) were performed in the non-Faradaic current region (Figure S14). The electrochemical double-layer capacitance (C_{dl}) values, which are linearly proportional to ECSA, were derived and shown in Figure 4-11. It is found that the capacitances of Co_3S_4-T400 and Co_3S_4-T550 samples are 2.05 μF cm^{-2}, and 1.36μF cm^{-2}, respectively, which are approximately 4 times and 2.6 times larger than that of Co_3S_4-T200 (0.51 μF cm^{-2}). The aluminum foil substrate exhibits a capacitance of only 0.039 μF cm^{-2}, indicating that the contribution of the substrate on the overall capacitance of these materials is negligible. Given the well-established linear relationship between ECSA and C_{dl}, a larger C_{dl} value implies the higher the ECSA. These findings suggest that more exposed active sites in Co_3S_4-T400, leading to enhanced SRR catalytic performance.

(2) Li^+ diffusion coefficient (D_{Li^+}) comparison

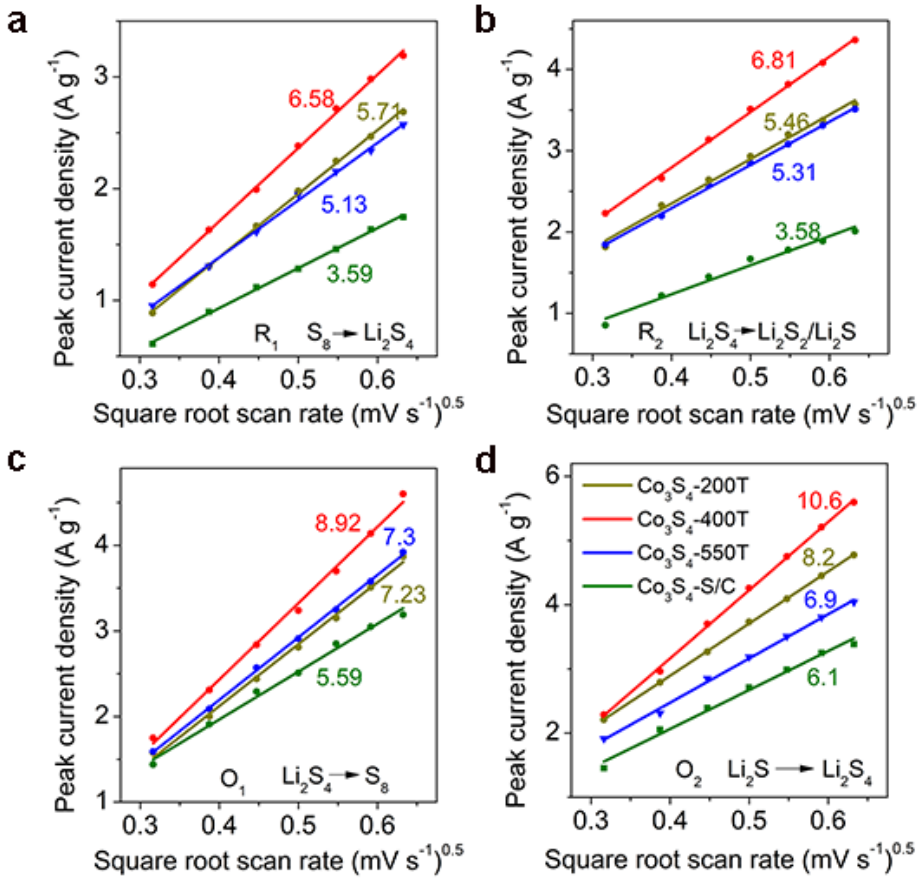

Figure 4-12. Li^+ diffusion coefficient comparison. Plot of CV peak currents of (a) the cathodic reaction R_1 (S_8 to Li_2S_4), (b) the cathodic reaction R_2 (Li_2S_4 to Li_2S_2/Li_2S), (c) the anodic reaction O_1 (Li_2S_4 to S_8) and (d) the anodic reaction O_2 (Li_2S to Li_2S_4).

The Li^+ diffusion coefficient (D_{Li^+}) is a key parameter for evaluating a catalyst's ability to enhance the kinetics of polysulfide redox reactions. Efficient Li^+ diffusion is essential for facilitating the sulfur transformation chemistry at the catalyst surface. CV measurements were performed at different scanning rate from 0.05 to 0.35 mV s^{-1} to investigate electrode kinetics with respect to the lithium-ion diffusion coefficient.[52] As shown in Figure S15, at all scan rates, there are two cathodic peaks at around 2.30 V (R_1) and 1.95 V (R_2), corresponding to the reduction of elemental sulfur (S_8) to Li_2S_4 and the subsequent formation of short-chain Li_2S_2/Li_2S. Two distinctive anodic peaks were clearly observed at around 2.5 V (O_1) and 2.4 V (O_2) for all the electrodes due to

the enhanced conversion kinetics. The reduction (R_1 and R_2) and oxidation (O_1 and O_2) peak currents show linear relationships with the square root of scanning rates, indicative of the diffusion-limited process. Li^+ diffusion coefficients were calculated according to the Randles-Sevcik equation (1):

$$I_p = 2.69 \times 10^5 \, n^{3/2} \, A \, D_{Li^+}{}^{1/2} \, C_{Li^+} v^{1/2} \quad (1)$$

where I_P is the peak current, n is the charge-transfer number during the reaction, A is the electrode area, D_{Li^+} is the lithium-ion diffusion coefficient, C_{Li^+} is the concentration of lithium ions in the electrolyte, and v is the potential scan rate. The slope of the curve ($I_P/v^{1/2}$) are positively correlated to the corresponding Li^+ diffusion rate as n, A, and C_{Li^+} are constant in Li–S coin cells. In Figure 4-12, it can be clearly seen that the S@Co_3S_4-T400 electrode exhibits much faster Li^+ diffusivity compared with the S@Co_3S_4-T200 and S@Co_3S_4-T550 electrodes. This can be attributed to the porous morphology of the Co_3S_4 nanosheets, which facilitates the localized Li^+ diffusion by formation of abundant charge transfer pathways on Co_3S_4 nanosheets, indicating decreased Li^+ diffusion barriers on the surface of Co_3S_4-T400 catalyst. Additionally, its larger ECSA provides more active sites for the adsorption and conversion of lithium polysulfides, thereby can promote the LiPSs conversion reactions. It is worth noting that Co_3S_4-T550 and Co_3S_4-T200 exhibit very similar facilitation toward lithium-ion transport. Although Co_3S_4-T550 has an average pore size of 9.3 nm which can greatly lower the Li^+ diffusion barrier, the presence of graphene in Co_3S_4-T200 (51 wt.%) enhances its electrical conductivity, partially compensating for resistance to lithium-ion transport caused by its less favorable morphology. This synergy between the graphene's conductivity and the

intrinsic properties of Co_3S_4-T200 offsets its morphological limitations, resulting in comparable performance to Co_3S_4-T550 in terms of lithium-ion diffusion.

(3) electrocatalysis ability characterization.

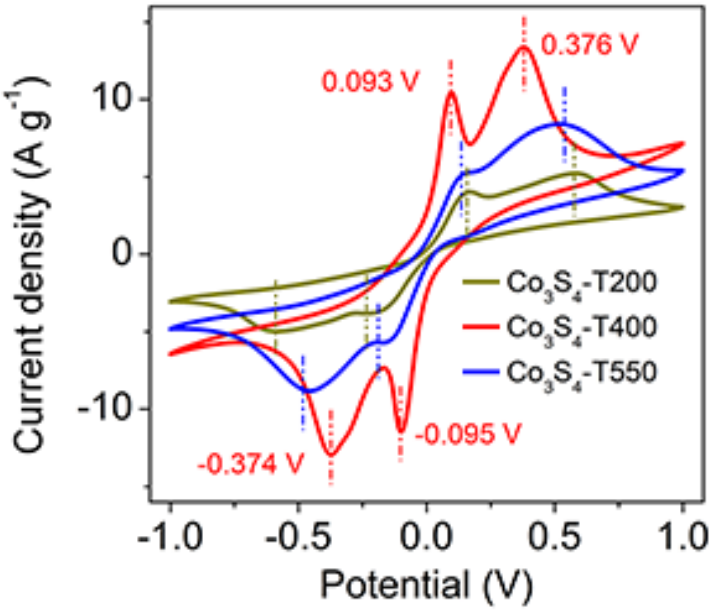

Figure 4-13. Cyclic voltammetry (CV) curves of Li_2S_6 symmetric cells at a scanning rate of 3 mV s^{-1}.

The catalytic effect was first evaluated by CV measurements in symmetric cells with identical working and counter electrodes immersed in a 0.5 M Li_2S_6 catholyte (SI: Experimental Methode). As illustrated in Figure 4-13, the voltammogram of the Co_3S_4-T400 electrodes exhibited high reversibility with four distinct peaks at -0.095 V, -0.374 V, 0.093 V and 0.0376 V under a scan rate of 3 mV s^{-1}. In contrast, the Co_3S_4-T550 and Co_3S_4-T200 electrode displayed broader redox peaks features, with the Co_3S_4-T200 electrode presenting the lowest redox current responses (Figure S16), highlighting its comparatively inferior catalytic performance.

The enhanced reaction kinetics and electrocatalytic activity toward SRR were further examined using Tafel plots. The cathodes, composed of sulfur and as-prepared catalyst hosts (10 wt.%), were designated as S@ Co_3S_4-T200, S@ Co_3S_4-T400 and S@ Co_3S_4-T550. CV tests were performed at a scan rate of 0.04mV s^{-1} to derive the Tafel slopes (SI: Experimental Methode), providing insights into the charge transfer kinetics and catalytic efficiency of the electrodes.

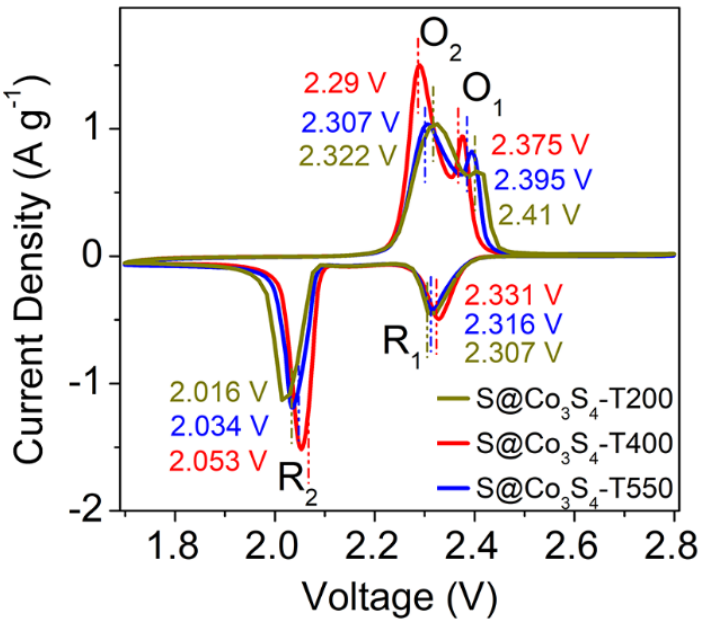

Figure 4-14. Polarization analysis with cyclic voltammetry profile

In Figure 4-14, two pairs of redox peaks were observed in cells S@Co_3S_4-T200, S@Co_3S_4-T400 and S@Co_3S_4-T550. Peak R_1 (S@Co_3S_4-T400: 2.331 V, S@Co_3S_4-T550: 2.316 V, S@ Co_3S_4-T200: 2.307 V) represents the reduction of S_8 into long-chain soluble Li_2S_n ($4 \leq n < 8$), while the peak R_2 (S@Co_3S_4-T400: 2.053 V, S@Co_3S_4-T550: 2.034 V, S@Co_3S_4-T200: 2.016 V) depicts further reduction of long-chain polysulfides to short-chain Li_2S_2/Li_2S. The S@Co_3S_4-T400 cathode exhibited a forward

shift in reduction peak voltage, while a backward shift in oxidation peak voltage, indicating reduced overpotential and voltage polarization.

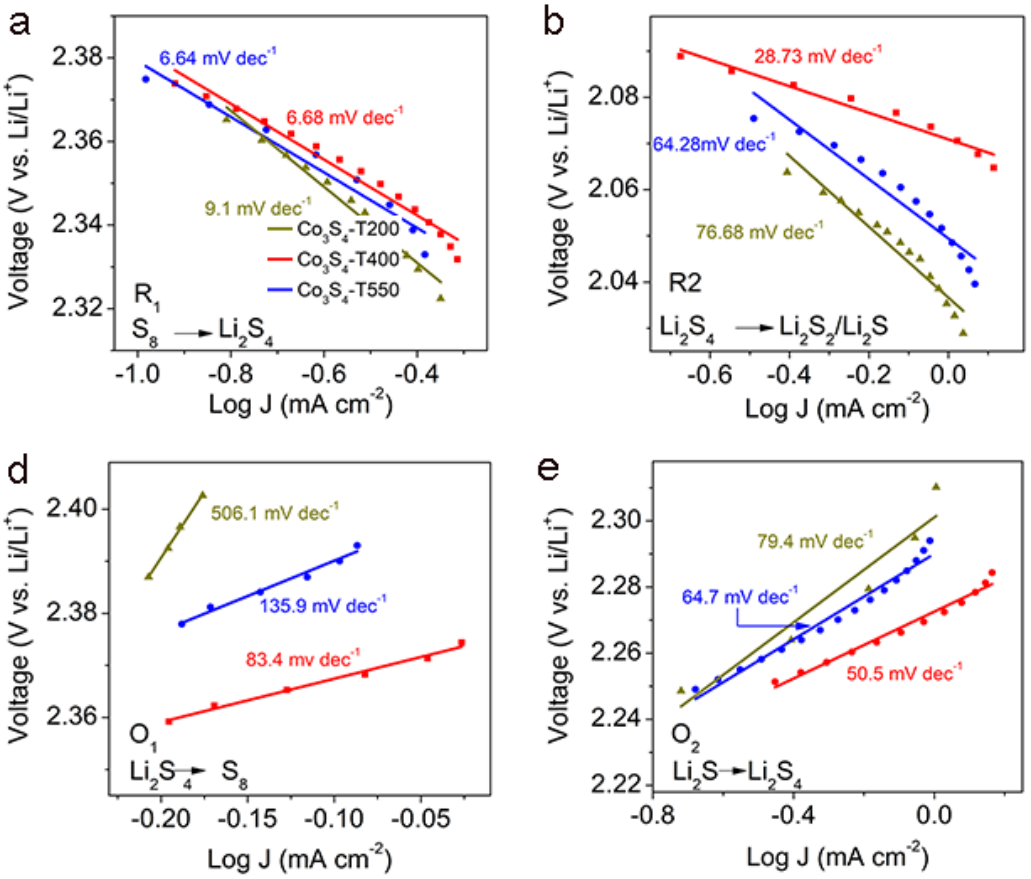

Figure 4-15. Tafel slope analysis: (a) Reduction peak R_1, S_8 convert to Li_2S_4; (b) Reduction peak R_2, Li_2S_4 convert to Li_2S_2/Li_2S. (c) Oxidation Peak O_1: Li_2S_4 convert to S_8. (d) Oxidation peak O_2: Li_2S convert to Li_2S_4.

Figure 4-15 shows Tafel plot results. It can be seen that the holey-structured Co_3S_4-T400 host exhibits a significantly smaller Tafel slope for the rate-determining conversion of Li_2S_4 to Li_2S_2/Li_2S Figure 4-15b, with a value of 28.73 mV dec^{-1}, compared to 64.28 mV dec^{-1} (Co_3S_4-T550) and 76.68 mV dec^{-1} (Co_3S_4-T200). This result highlights a pronounced improvement in catalytic activity of Co_3S_4-T400 host. Furthermore, the Co_3S_4-T400 host also exhibits enhanced catalytic kinetics for the oxidation of Li_2S back to Li_2S_4 (Figure 4-15d), showing a lower Tafel slop of 50.5 mV

dec^{-1} compared with Co_3S_4-T550 host (64.7 mV dec^{-1}) and Co_3S_4-T200 (79.4 mV dec^{-1}). Given the insulating nature of Li_2S and the crucial importance of its oxidation for achieving reversible capacity, facilitating charge transfer is essential for ensuring long cycling life. This enhanced catalytic kinetics can be attributed to the optimized porous structure of Co_3S_4-T400 host, which provides abundant charge transfer pathways and active sites for the adsorption and conversion of LiPSs. This structure promotes Li^+ transport, decreased electron transfer resistance, and enables rapid interaction with encapsulated LiPSs. As a result, the Co_3S_4-T400 host substantially boosts the catalytic efficiency of LiPSs redox conversions, supporting improved overall electrochemical performance.

(4) Li_2S potentiostatic deposition test.

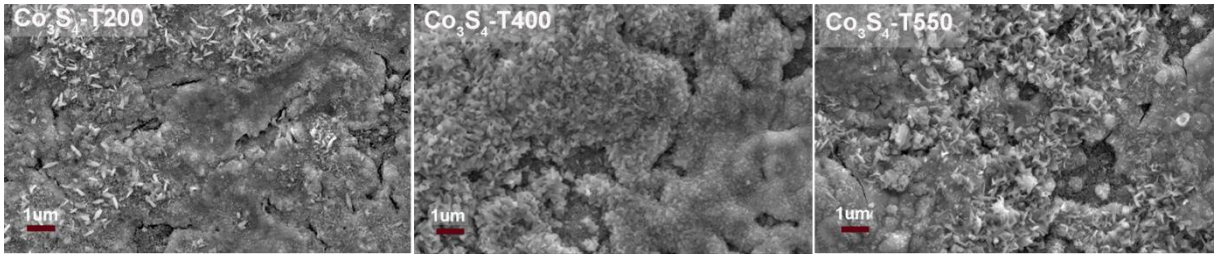

Figure 4-16. SEM characterization after Li_2S_2/Li_2S potentiostatic deposition

In order to further demonstrate the enhancement of holey-structured Co_3S_4-T200 on regulating Li_2S deposition, the potentiostatic discharge experiments were performed in coin cell batteries with Co_3S_4-T200, Co_3S_4-T400, and Co_3S_4-T550 as cathodes, paired with lithium foil anodes. The higher peak current of Co_3S_4-T200 electrode indicates that the deposition process of Li_2S can be improved by comparison to those of Co_3S_4-T400, and Co_3S_4-T550. The corresponding values for Co_3S_4-T200, Co_3S_4-T400, and Co_3S_4-

T550 are 1.29 mA, 0.092 mA, and 0.093 mA, respectively (Figure S17-S19). The surface morphology of the samples undergone potentiostatic discharging were characterized by SEM. In Figure 4-16 shows that the Co_3S_4-T400 electrode exhibits more uniform Li_2S deposition compared to the Co_3S_4-T200, Co_3S_4-T550 electrodes. This indicates that the holey-structured Co_3S_4-T400 maximizes the pathways for Li^+ diffusion while retaining a large number of active sites to facilitate the conversion of liquid Li_2S_4 to solid Li_2S. These findings suggested that optimizing the localized Li^+ diffusivity is an effective way to promote Li_2S nucleation and deposition, which plays a crucial role in accelerating the rate-degerming step of the Li–S discharging process.

(5) Battery performance tests.

The coin cells were assembled to compare the enhancement of sulfur hosts (mass ratio 10%) i.e., Co_3S_4-T200, Co_3S_4-T400, or Co_3S_4-T550, in promoting battery performance.

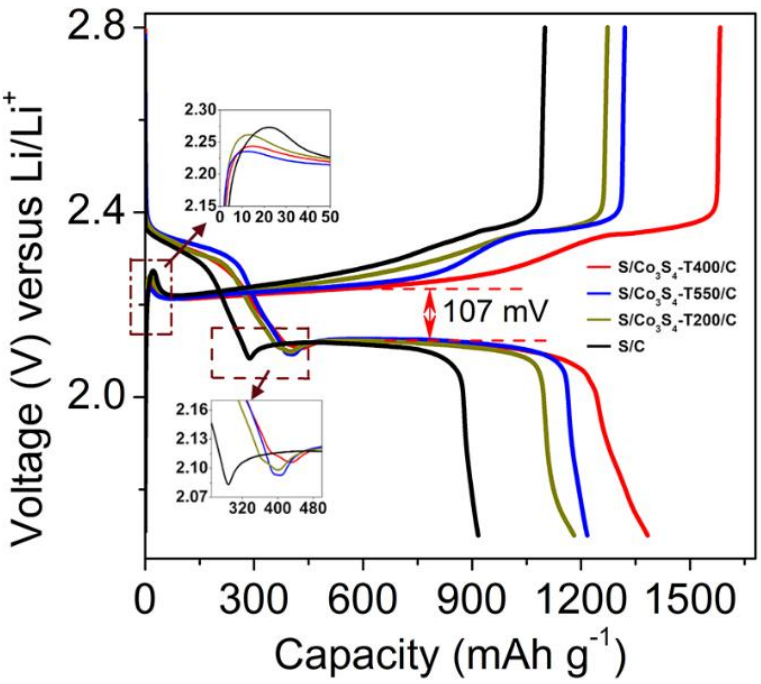

Figure 4-17. Galvanostatic charge/ discharge profiles at 0.1 C (sulfur loading ~2.1 mg cm^{-2}).

Figure 4-17 presents the galvanostatic charging-discharging profiles at 0.1 C with a sulfur loading of ~2.9 mg cm^{-2}. The battery incorporated with holey-structured Co_3S_4-T400 host exhibits a lower polarization of 107 mV, compared to 168 mV for Co_3S_4-T200 and 133 mV for Co_3S_4-T550 (Figure S20). This difference in electrochemical performance can be attributed to the morphological variations among the synthesized sulfur hosts, particularly their porosities. The porosities of Co_3S_4-T400, and Co_3S_4-T550 are 13.6% and 21.5%, respectively, whereas Co_3S_4-T200 features a smooth graphene surface with uniformly distributed Co_3S_4 nanoparticles and no visible pores. Despite its higher porosity, Co_3S_4-T550 exhibits moderate resistance to Li^+ transport, which can be ascribed to its smaller ECSA. The reduced ECSA limits its electrocatalytic capability for LiPSs conversion, thereby increasing the overall overpotential.

Figure 4-17 insets present the analysis of the voltage difference between the discharge or charge plateaus. At the onset dip of the 2.1 V plateau, the cell with Co_3S_4-T400 retains a higher potential of 2.106 V (2.092 V and 2.098 V for cells with Co_3S_4-T550 and Co_3S_4-T200 hosts), suggesting an improved catalytic activity for the conversion from long-chain Li_2S_4 to Li_2S_2/Li_2S. Similarly, the lower initial charging voltage (Co_3S_4-T200: 2.262 V; Co_3S_4-T400: 2.243 V; Co_3S_4-T550: 2.237 V;) indicates improved oxidation kinetics for Li_2S_2/Li_2S to soluble polysulfides. Figure S21 shows the capacity ratio (Q_1/Q_2) as a measure of the catalytic activity of the synthesized sulfur host samples. Q_1 corresponds to the capacity contribution from the conversion of S_8 to soluble Li_2S_4, while Q_2 represents the subsequent transformation of long-chain Li_2S_4 into solid Li_2S. For cells with Co_3S_4-T400 host, the ratio is 2.25, exceeding the theoretical value of 2.0, suggesting a nearly complete reduction of high-order polysulfides. In contrast, the lower Q_1/Q_2 ratios observed for Co_3S_4-T200 (1.98) and Co_3S_4-T200 (2.01) indicate incomplete LiPSs reduction, attributed to more severe shuttle effect. Furthermore, the battery incorporating sulfur host of Co_3S_4-T400 achieves a higher Q_1 value (425.9 mAh g^{-1}) compared to Co_3S_4-T200 (406 mAh g^{-1}) and pristine Co_3S_4-T550 (395.9 mAh g^{-1}), demonstrating that the holey-structured Co_9S_8/HG effectively enhances sulfur utilization by facilitating localized Li^+ supply.

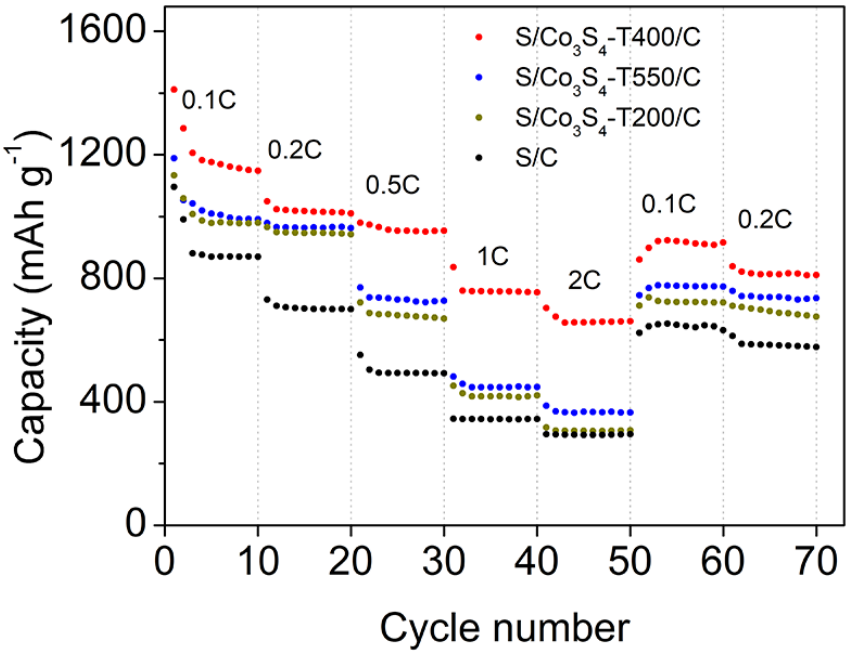

Figure 4-18. Rate performance tests of Li–S batteries with sulfur host of Co_3S_4-T200, Co_3S_4-T400, Co_3S_4-T550, or pristine S/C cathodes (sulfur loading ~1.83 mg cm^{-2}).

In addition to reducing polarization and enhancing sulfur utilization, the sulfur host Co_3S_4-T200 also demonstrates outstanding rate performance. The rate performance was compared with S/Co_3S_4-T200/C, S/Co_3S_4-T400/C, and S/Co_3S_4-T550/C cathode with a sulfur loading of ~1.83 mg cm^{-2}. The measured capacity with different cathodes generally declines with the increase of C-rates. The Li–S cells with the S/Co_3S_4-T400/C cathodes deliver higher specific capacities at various current densities from 0.1 C to 2 C (Figure 4-18), which are 1149.3, 1010.8, 951.5, 755.8, and 658.7 mAh g^{-1}, respectively. By contrast, the S/Co_3S_4-T200/C, S/Co_3S_4-T550/C, and S/C cathodes could only retain a capacity of 363.8, 312.7, and 292.9 mAh g^{-1} at 2 C. These results suggest the good rate capability of S/Co_3S_4-T400/C cathodes. Specifically, when the C-rates returns to 0.2 C, the S/Co_3S_4-T400/C cathodes are able to recover much higher deliverable capacities than other cathodes samples. The large capacity gaps are observed at all testing C-rates between the S/Co_3S_4-T400/C composite cathodes and

S/Co_3S_4-T200/C cathodes, indicating more severe irreversible processes inside the S/Co_3S_4-T200/C cathodes than S/Co_3S_4-T400/C cathodes. The irreversible processes will degrade long-term cycling stability of the sulfur composite cathodes that lack localized Li^+ diffusion pathways, hindering their ability to effectively engaged in the sulfur species conversion reactions.

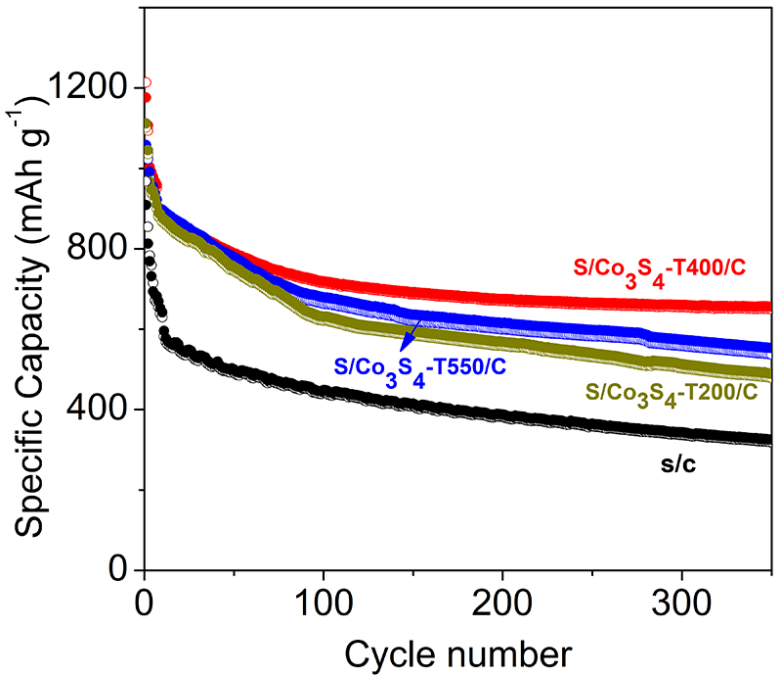

Figure 4-19. Cycling stability measurements at 0.5 C (sulfur loading ~1.83 mg cm^{-2}).

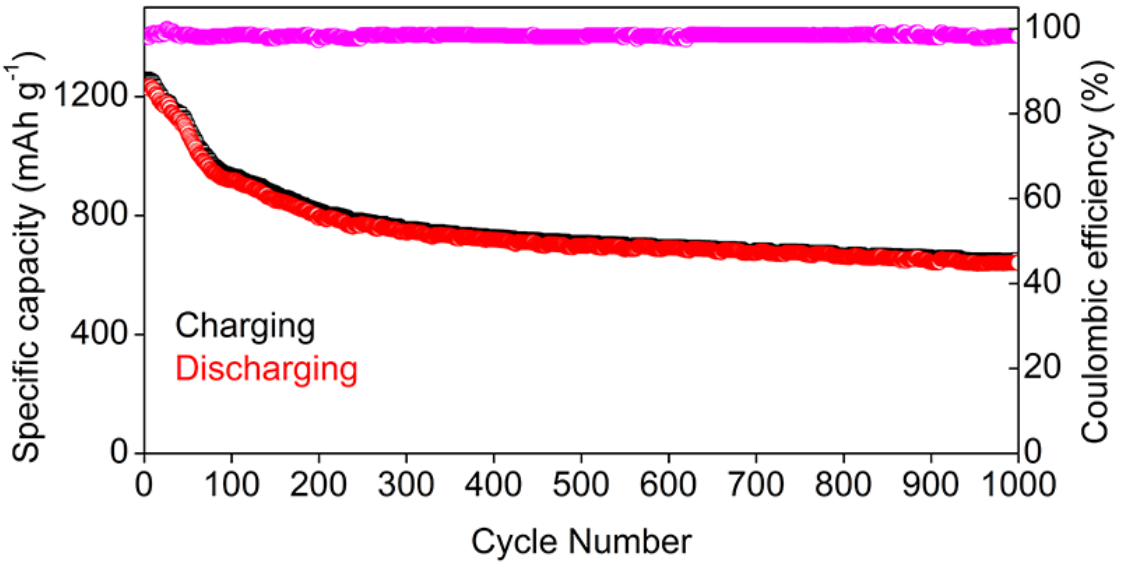

Figure 4-20. Long-term cycling test of cells with S/Co_3S_4-T400/C electrodes at 0.2 C (sulfur loading ~1.83 mg cm^{-2})

Galvanostatic cycling measurements were performed at 0.2 C and 0.5 C (Figure 4-19, 4-20) to assess the durability of Co_3S_4-T200, Co_3S_4-T400, and Co_3S_4-T550 in catalyzing the LiPSs conversion kinetics. At 0.5 C, S/ Co_3S_4-T400/C electrodes exhibit higher initial capacities and lower capacity decay within the first 20 cycles, as shown in Figure 4-19. After 40 cycles, the S/Co_3S_4-T400/C composite cathodes demonstrate greater capacity retention and more stable cycling performance compared to S/Co_3S_4-T200/C and S/Co_3S_4-T550/C, whereas the S/C cathode undergoes more severe capacity decay. Furthermore, long-term cycling tests at 0.2 C reveal that S/Co_3S_4-T400/C composite electrodes maintain a specific capacity of 657 mAh g^{-1} with a low-capacity decay rate of 0.051% per cycle and a high average coulombic efficiency of 98.1% over 1000 cycles (Figure 4-20). The enhanced cyclability can be attributed to the holey-structured Co_3S_4-T400 sulfur host, which offers abundant active sites and localized Li^+ transport pathways, facilitating rapid charge transfer and promoting sulfur

species conversion kinetics. This strategy of designing a porous sulfur host to catalyze the SRR on the cathode side, while integrating localized charge transfer pathways and abundant active sites, presents promising opportunities for further advancing high-performance Li–S batteries.

4.5 Conclusions

In summary, Co_3S_4-T200, Co_3S_4-T400, and Co_3S_4-T550 with varying porosity and ECSA were employed as model electrocatalyst to elucidate the impact of Li^+ diffusivity on promoting SRR kinetics and regulating Li_2S precipitation. TEM imaging and statistical analysis revealed that Co_3S_4-T400 possesses an average particle size of 20.7 nm, an average pore diameter of 3.3 nm, and a porosity of 13.6%. These structural characteristics endow Co_3S_4-T400 with enhanced electrochemical performance, reduced polarization and larger ECSA. Tafel plots analysis and Li^+ diffusion coefficient measurements further confirmed the superior electrocatalysis capability of Co_3S_4-T400 compared to Co_3S_4-T200 and Co_3S_4-T550. Consequently, the Li–S batteries incorporating S/Co_3S_4-T400/C composite electrodes demonstrate excellent rate performance, delivering specific capacity of 755.8 mAh g^{-1} at 1 C and 658.7 mAh g^{-1} at 2 C, while retaining a high capacity of 815.1 mAh g^{-1} when reverted to 0.2 C. Long-term cycling test at 0.2 C, showed that the S/Co_3S_4-T400/C composite electrodes retaining a specific capacity of 657 mAh g^{-1} with a low-capacity decay rate of 0.051% per cycle over 1000 cycles. Overall, this work highlights the critical role of porous-structured catalyst hosts with enhanced localized Li^+ diffusivity in accelerating

SRR kinetics and regulating Li_2S precipitation in Li–S batteries, while also providing fundamental insights into the structure-activity relationship to inform the rational design of high-performance catalysts.

4.6 References

1. Peng, L.; Wei, Z.; Wan, C.; Li, J.; Chen, Z.; Zhu, D.; Baumann, D.; Liu, H.; Allen, C. S.; Xu, X., A fundamental look at electrocatalytic sulfur reduction reaction. *Nature Catalysis* **2020,** *3* (9), 762-770.

2. Zhou, S.; Shi, J.; Liu, S.; Li, G.; Pei, F.; Chen, Y.; Deng, J.; Zheng, Q.; Li, J.; Zhao, C., Visualizing interfacial collective reaction behaviour of Li–S batteries. *Nature* **2023,** *621* (7977), 75-81.

3. Shi, Z.; Li, M.; Sun, J.; Chen, Z., Defect engineering for expediting Li–S chemistry: strategies, mechanisms, and perspectives. *Advanced Energy Materials* **2021,** *11* (23), 2100332.

4. Li, C.; Zhang, Q.; Sheng, J.; Chen, B.; Gao, R.; Piao, Z.; Zhong, X.; Han, Z.; Zhu, Y.; Wang, J., A quasi-intercalation reaction for fast sulfur redox kinetics in solid-state lithium–sulfur batteries. *Energy & environmental science* **2022,** *15* (10), 4289-4300.

5. Wang, H.; Yuan, H.; Wang, W.; Wang, X.; Sun, J.; Yang, J.; Liu, X.; Zhao, Q.; Wang, T.; Wen, N., Accelerating Sulfur Redox Kinetics by Electronic Modulation and Drifting Effects of Pre-Lithiation Electrocatalysts. *Advanced Materials* **2024,** *36* (8), 2307741.

6. Gao, T.; Ji, X.; Hou, S.; Fan, X.; Li, X.; Yang, C.; Han, F.; Wang, F.; Jiang, J.; Xu, K., Thermodynamics and kinetics of sulfur cathode during discharge in MgTFSI2–DME electrolyte. *Advanced Materials* **2018,** *30* (3), 1704313.

7. Liang, Q.; Wang, S.; Yao, Y.; Dong, P.; Song, H., Transition metal compounds family for Li–S batteries: the DFT-guide for suppressing polysulfides shuttle. *Advanced Functional Materials* **2023,** *33* (32), 2300825.

8. Ng, S. F.; Lau, M. Y. L.; Ong, W. J., Lithium–sulfur battery cathode design: tailoring metal-based nanostructures for robust polysulfide adsorption and catalytic conversion. *Advanced Materials* **2021,** *33* (50), 2008654.

9. Wang, X.; Zhang, X.; Zhao, Y.; Luo, D.; Shui, L.; Li, Y.; Ma, G.; Zhu, Y.; Zhang,

Y.; Zhou, G., Accelerated Multi-step Sulfur Redox Reactions in Lithium-Sulfur Batteries Enabled by Dual Defects in Metal-Organic Framework-based Catalysts. *Angewandte Chemie* **2023,** *135* (42), e202306901.

10. Wang, P.; Xi, B.; Huang, M.; Chen, W.; Feng, J.; Xiong, S., Emerging catalysts to promote kinetics of lithium–sulfur batteries. *Advanced Energy Materials* **2021,** *11* (7), 2002893.

11. Ren, X.; Wang, Q.; Pu, Y.; Sun, Q.; Sun, W.; Lu, L., Synergizing spatial confinement and dual-metal catalysis to boost sulfur kinetics in lithium–sulfur batteries. *Advanced Materials* **2023,** *35* (44), 2304120.

12. Su, D.; Zhou, D.; Wang, C.; Wang, G., Toward high performance lithium–sulfur batteries based on Li2S cathodes and beyond: status, challenges, and perspectives. *Advanced Functional Materials* **2018,** *28* (38), 1800154.

13. Nanda, S.; Manthiram, A., Lithium degradation in lithium–sulfur batteries: Insights into inventory depletion and interphasial evolution with cycling. *Energy & Environmental Science* **2020,** *13* (8), 2501-2514.

14. Jin, Z.; Lin, T.; Jia, H.; Liu, B.; Zhang, Q.; Li, L.; Zhang, L.; Su, Z.-m.; Wang, C., Expediting the conversion of Li2S2 to Li2S enables high-performance Li–S batteries. *ACS nano* **2021,** *15* (4), 7318-7327.

15. Ye, H.; Li, M.; Liu, T.; Li, Y.; Lu, J., Activating Li2S as the lithium-containing cathode in lithium–sulfur batteries. *ACS Energy Letters* **2020,** *5* (7), 2234-2245.

16. Li, G.; Wang, S.; Zhang, Y.; Li, M.; Chen, Z.; Lu, J., Revisiting the role of polysulfides in lithium–sulfur batteries. *Advanced Materials* **2018,** *30* (22), 1705590.

17. Liu, D.; Zhang, C.; Zhou, G.; Lv, W.; Ling, G.; Zhi, L.; Yang, Q. H., Catalytic effects in lithium–sulfur batteries: promoted sulfur transformation and reduced shuttle effect. *Advanced science* **2018,** *5* (1), 1700270.

18. Xu, H.; Jiang, Q.; Zhang, B.; Chen, C.; Lin, Z., Integrating conductivity, immobility, and catalytic ability into high-N carbon/graphene sheets as an effective sulfur host. *Advanced Materials* **2020,** *32* (7), 1906357.

19. Huang, C.; Yu, J.; Li, C.; Cui, Z.; Zhang, C.; Zhang, C.; Nan, B.; Li, J.; Arbiol,

J.; Cabot, A., Combined defect and heterojunction engineering in ZnTe/CoTe2@ NC sulfur hosts toward robust lithium–sulfur batteries. *Advanced Functional Materials* **2023,** *33* (46), 2305624.

20. Hu, A.; Zhou, M.; Lei, T.; Hu, Y.; Du, X.; Gong, C.; Shu, C.; Long, J.; Zhu, J.; Chen, W., Optimizing redox reactions in aprotic lithium–sulfur batteries. *Advanced Energy Materials* **2020,** *10* (42), 2002180.

21. Song, Y.; Cai, W.; Kong, L.; Cai, J.; Zhang, Q.; Sun, J., Rationalizing electrocatalysis of Li–S chemistry by mediator design: progress and prospects. *Advanced Energy Materials* **2020,** *10* (11), 1901075.

22. Pang, Q.; Kundu, D.; Cuisinier, M.; Nazar, L., Surface-enhanced redox chemistry of polysulphides on a metallic and polar host for lithium-sulphur batteries. *Nature communications* **2014,** *5* (1), 4759.

23. Zubair, U.; Amici, J.; Francia, C.; McNulty, D.; Bodoardo, S.; O'Dwyer, C., Polysulfide Binding to Several Nanoscale Magnéli Phases Synthesized in Carbon for Long-Life Lithium–Sulfur Battery Cathodes. *ChemSusChem* **2018,** *11* (11), 1838-1848.

24. Kong, L.; Chen, X.; Li, B. Q.; Peng, H. J.; Huang, J. Q.; Xie, J.; Zhang, Q., A bifunctional perovskite promoter for polysulfide regulation toward stable lithium–sulfur batteries. *Advanced Materials* **2018,** *30* (2), 1705219.

25. Zhou, T.; Lv, W.; Li, J.; Zhou, G.; Zhao, Y.; Fan, S.; Liu, B.; Li, B.; Kang, F.; Yang, Q.-H., Twinborn TiO 2–TiN heterostructures enabling smooth trapping–diffusion–conversion of polysulfides towards ultralong life lithium–sulfur batteries. *Energy & Environmental Science* **2017,** *10* (7), 1694-1703.

26. Zhou, F.; Gong, Z.; Wang, R.; Guo, M.; Zeng, R.; Li, Y.; Xiao, Z.; Qie, L.; Liu, J., Band Structure and Spin-State-Induced Electronic Configuration Regulation for Efficient Sulfur Redox Reaction. *Advanced Functional Materials* **2024**, 2417730.

27. Lao, Z.; Han, Z.; Ma, J.; Zhang, M.; Wu, X.; Jia, Y.; Gao, R.; Zhu, Y.; Xiao, X.; Yu, K., Band structure engineering and orbital orientation control constructing dual active sites for efficient sulfur redox reaction. *Advanced Materials* **2024,** *36* (2), 2309024.

28. Wang, L.; Hu, Z.; Wan, X.; Hua, W.; Li, H.; Yang, Q. H.; Wang, W., Li2S4 anchoring governs the catalytic sulfur reduction on defective SmMn2O5 in lithium–sulfur battery. *Advanced Energy Materials* **2022,** *12* (20), 2200340.

29. Wang, L.; Hua, W.; Wan, X.; Feng, Z.; Hu, Z.; Li, H.; Niu, J.; Wang, L.; Wang, A.; Liu, J., Design rules of a sulfur redox electrocatalyst for lithium–sulfur batteries. *Advanced Materials* **2022,** *34* (14), 2110279.

30. Hou, L.-P.; Li, X.-Y.; Bi, C.-X.; Chen, Z.-X.; Li, Z.; Su, L.-L.; Shi, P.; Jin, C.-B.; Li, B.-Q.; Huang, J.-Q., Constructing lithium oxysulfide-rich solid electrolyte interphase to shield polysulfides in practical lithium–sulfur batteries. *Journal of Power Sources* **2022,** *550*, 232144.

31. Xu, Z.-L.; Lin, S.; Onofrio, N.; Zhou, L.; Shi, F.; Lu, W.; Kang, K.; Zhang, Q.; Lau, S. P., Exceptional catalytic effects of black phosphorus quantum dots in shuttling-free lithium sulfur batteries. *Nature Communications* **2018,** *9* (1), 4164.

32. Gao, K.; Xia, D.; Ji, H.; Chen, Y.; Zhang, L.; Wang, Y.; Yi, S.; Zhou, Y.; Zhang, Z.; Chen, D., Linear-PEI-derived hierarchical porous carbon nanonet flakes decorated with MoS2 as efficient polysulfides stabilization interlayers for lithium–sulfur battery. *Energy & Fuels* **2021,** *35* (12), 10303-10314.

33. Zhang, M.; Zhu, L.; Zhou, G.; Hao, T.; Qiu, C.; Zhao, Z.; Hu, Q.; Larson, B. W.; Zhu, H.; Ma, Z., Single-layered organic photovoltaics with double cascading charge transport pathways: 18% efficiencies. *Nature communications* **2021,** *12* (1), 309.

34. Zhang, W.; Seo, D.-H.; Chen, T.; Wu, L.; Topsakal, M.; Zhu, Y.; Lu, D.; Ceder, G.; Wang, F., Kinetic pathways of ionic transport in fast-charging lithium titanate. *Science* **2020,** *367* (6481), 1030-1034.

35. Park, J.; Kim, E. T.; Kim, C.; Pyun, J.; Jang, H. S.; Shin, J.; Choi, J. W.; Char, K.; Sung, Y. E., The importance of confined sulfur nanodomains and adjoining electron conductive pathways in subreaction regimes of Li-S batteries. *Advanced Energy Materials* **2017,** *7* (19), 1700074.

36. Zhou, L.; Danilov, D. L.; Qiao, F.; Wang, J.; Li, H.; Eichel, R. A.; Notten, P. H., Sulfur reduction reaction in lithium–sulfur batteries: mechanisms, catalysts, and

characterization. *Advanced energy materials* **2022,** *12* (44), 2202094.

37. Shen, Z.; Zhang, Z.; Li, M.; Yuan, Y.; Zhao, Y.; Zhang, S.; Zhong, C.; Zhu, J.; Lu, J.; Zhang, H., Rational design of a Ni3N0. 85 electrocatalyst to accelerate polysulfide conversion in lithium–sulfur batteries. *Acs Nano* **2020,** *14* (6), 6673-6682.

38. Tao, X.; Wang, J.; Liu, C.; Wang, H.; Yao, H.; Zheng, G.; Seh, Z. W.; Cai, Q.; Li, W.; Zhou, G., Balancing surface adsorption and diffusion of lithium-polysulfides on nonconductive oxides for lithium–sulfur battery design. *Nature communications* **2016,** *7* (1), 11203.

39. Zhou, G.; Tian, H.; Jin, Y.; Tao, X.; Liu, B.; Zhang, R.; Seh, Z. W.; Zhuo, D.; Liu, Y.; Sun, J., Catalytic oxidation of Li2S on the surface of metal sulfides for Li− S batteries. *Proceedings of the National Academy of Sciences* **2017,** *114* (5), 840-845.

40. Shi, F.; Yu, J.; Chen, C.; Lau, S. P.; Lv, W.; Xu, Z.-L., Advances in understanding and regulation of sulfur conversion processes in metal–sulfur batteries. *Journal of Materials Chemistry A* **2022,** *10* (37), 19412-19443.

41. Lukatskaya, M. R.; Dunn, B.; Gogotsi, Y., Multidimensional materials and device architectures for future hybrid energy storage. *Nature communications* **2016,** *7* (1), 12647.

42. Cheng, M.; Yan, R.; Yang, Z.; Tao, X.; Ma, T.; Cao, S.; Ran, F.; Li, S.; Yang, W.; Cheng, C., Polysulfide catalytic materials for fast-kinetic metal–sulfur batteries: principles and active centers. *Advanced Science* **2022,** *9* (2), 2102217.

43. Raccichini, R.; Varzi, A.; Passerini, S.; Scrosati, B., The role of graphene for electrochemical energy storage. *Nature materials* **2015,** *14* (3), 271-279.

44. Zhang, J.; You, C.; Lin, H.; Wang, J., Electrochemical kinetic modulators in lithium–sulfur batteries: from defect-rich catalysts to single atomic catalysts. *Energy & Environmental Materials* **2022,** *5* (3), 731-750.

45. Zhou, C.; Hong, M.; Hu, N.; Yang, J.; Zhu, W.; Kong, L.; Li, M., Bi-Metallic coupling-induced electronic-state modulation of metal phosphides for kinetics-enhanced and dendrite-free Li–S batteries. *Advanced Functional Materials* **2023,** *33* (14), 2213310.

46. Hu, S.; Wang, T.; Lu, B.; Wu, D.; Wang, H.; Liu, X.; Zhang, J., Ionic-liquid-Assisted synthesis of FeSe–MnSe heterointerfaces with abundant Se vacancies embedded in N, B Co-doped hollow carbon microspheres for accelerating the sulfur reduction reaction. *Advanced Materials* **2022,** *34* (41), 2204147.

47. Liu, Y.; Xiao, C.; Lyu, M.; Lin, Y.; Cai, W.; Huang, P.; Tong, W.; Zou, Y.; Xie, Y., Ultrathin Co3S4 nanosheets that synergistically engineer spin states and exposed polyhedra that promote water oxidation under neutral conditions. *Angewandte Chemie International Edition* **2015,** *54* (38), 11231-11235.

48. Fan, F. Y.; Carter, W. C.; Chiang, Y.-M., Mechanism and Kinetics of Li2S Precipitation in Lithium-Sulfur Batteries. *Advanced Materials (Deerfield Beach, Fla.)* **2015,** *27* (35), 5203-5209.

49. Quilty, C. D.; Wu, D.; Li, W.; Bock, D. C.; Wang, L.; Housel, L. M.; Abraham, A.; Takeuchi, K. J.; Marschilok, A. C.; Takeuchi, E. S., Electron and ion transport in lithium and lithium-ion battery negative and positive composite electrodes. *Chemical Reviews* **2023,** *123* (4), 1327-1363.

50. Zhao, Z.; Pan, Y.; Yi, S.; Su, Z.; Chen, H.; Huang, Y.; Niu, B.; Long, D.; Zhang, Y., Enhanced electron delocalization within coherent nano-heterocrystal ensembles for optimizing polysulfide conversion in high-energy-density Li-S batteries. *Advanced Materials* **2024,** *36* (13), 2310052.

51. Liu, B.; Gu, H.; Torres, J. F.; Yin, Z.; Tricoli, A., Balancing polysulfide containment and energy loss in lithium–sulfur batteries. *Energy & Environmental Science* **2024,** *17* (3), 1073-1082.

52. Park, M.-S.; Yu, J.-S.; Kim, K. J.; Jeong, G.; Kim, J.-H.; Jo, Y.-N.; Hwang, U.; Kang, S.; Woo, T.; Kim, Y.-J., One-step synthesis of a sulfur-impregnated graphene cathode for lithium–sulfur batteries. *Physical Chemistry Chemical Physics* **2012,** *14* (19), 6796-6804.

4.7 Supporting Information

4.7.1 Material synthesis

(1) Preparation of GO, rGO and Co-pre/G

Graphene oxide (GO) was synthesized from natural graphite using a modified Hummers' method.[1] To prepare the precursor suspension, 30 mg of GO was dispersed in 60 mL of anhydrous ethylene glycol (EG, ≥99%, Merck Australia) and ultrasonicated for one hour. Separately, 40 mmol of cobalt acetate (≥98.0%, Merck Australia) was dissolved in 20 mL of EG and gradually added to the GO suspension under magnetic stirring for one hour. The resulting mixture was then heated to 185°C at a rate of 2°C per minute and maintained at this temperature for two hours before being allowed to cool naturally to room temperature. The product was purified using ethanol and deionized (DI) water, followed by lyophilization for 24 hours to obtain the cobalt precursor (Co-pre/rGO, Figure S1). The same procedure was followed for the preparation of reduced graphene oxide (rGO), without adding cobalt acetate.

(2) Preparation of Co_3S_4-T200, Co_3S_4-T400, and Co_3S_4-T550

Synthesis of Co_3S_4-T400, and Co_3S_4-T550 nanosheets: The Co-pre/G was oxidized in air for 3 hours at 400°C or 500°C, the graphene substrate completely oxidized with Co_3O_4 nanoparticles bridged together, forming Co_3O_4-T400 (Figure S2), and Co_3O_4-T550 (Figure S4) nanosheet. The Co_3O_4-T400, and Co_3O_4-T550 were further reacted with H_2S at 380°C for 45 mins to get Co_3S_4-T400 (Figure S3), and Co_3S_4-T550 (Figure S5) nanosheets.

Synthesis of Co_3S_4-T200 nanosheets: In contrast, the Co-pre/G was annealed in argon atmosphere for 1 hour at 700°C, then oxidized in air for 3 hours at 200°C to get Co_3O_4-T200 (Figure S6), maintaining graphene substrate. The Co_3O_4-T200 was further reacted with H_2S at 380°C for 45 mins to get Co_3S_4-T200 (Figure S3), and Co_3S_4-T200 (Figure S7) nanosheets.

(3) Preparation of electrolyte and Li_2S_4 catholyte

First, Li2S6 solutions were prepared by dissolving stoichiometric amounts of Li2S and sulfur (1:5) in a mixed solvent of DME/DOL (1:1 by volume) containing 1 M lithium bis(trifluoromethanesulfonyl)imide (LiTFSI) and 1 wt.% LiNO3.

(4) Fabrication Co_3S_4-T200/PP, Co_3S_4-T400/PP, and Co_3S_4-T550/PP membranes for overpotential measurements

The membranes were fabricated through a filtration method using a commercial polypropylene (PP) membrane (Celgard 2400, 25 μm thickness) as a substrate. 10 mg each of Co_3S_4-T200, Co_3S_4-T400, and Co_3S_4-T550 were dispersed in 50 mL of anhydrous 1-Methyl-2-pyrrolidone (NMP, 99.5%, Merck Australia) through 0.5 hour of ultrasonication. These dispersions were then gradually filtrated to get the resultant coatings (loading mass 0.18 mg cm^{-2}), Co_3S_4-T200/PP, Co_3S_4-T400/PP, and Co_3S_4-T550/PP, were dried at 50°C for overnight.

4.7.2 Material characterizations

The SEM characterization was performed using a Zeiss UltraPlus analytical FESEM at 3 kV. TEM characterization and EDX mapping were conducted on a JEOL 2100F

FEGTEM (200 kV). XRD measurements were conducted using a Bruker system (D2 Phaser) equipped with Cu Kα radiation, with an average wavelength of 1.54059 Å. N_2-adsorption isotherms measurements were conducted using a TristarII BET analyzer (Micromeritics, USA). Thermogravimetric (TG) analysis was conducted on a NETZSCH STA 449 F3 Jupiter analyzer. Raman spectra were obtained by a LabRAM HR evolution Raman spectrophotometer equipped with a charge-coupled-device (CCD) Si array detector using a solid-state excitation laser with a wavelength of 532 nm at room temperature, and a grating of 1800 (500 nm).

4.7.3 Assembly and Electrochemistry Testing of the Symmetric Cell

Both working and counter electrodes were prepared by mixing the Co_3S_4-T200, Co_3S_4-T400, or Co_3S_4-T550, Super P, and polyvinylidene fluoride binder (in a weight ratio of 75:15:1) in NMP solvent and then coated onto the carbon coated Al foil. After drying at 60 °C for 12 h, the electrodes were punched into disks with a diameter of 15 mm. The active material loading was controlled ~1.5 mg cm^{-2}. The identical working and counter electrodes of Co_3S_4-T200, Co_3S_4-T400, or Co_3S_4-T550 were assembled into the symmetric cells with 32 μL Li_2S_6 electrolyte for the catalytic effect analysis. The CV measurement of symmetric cells was conducted between -1.0 and 1.0 V (Figure S16).

For electrochemical active surface area (ECSA) measurement (Figure S14),[2] the working and counter electrodes were prepared the same methods. The LiTFSI is used as electrolytes when assembly coin cells. The CV measurements of ECSA were

conducted in the non-Faradic area between -0.15 and 0.15 V. The scan rates are: 3.5, 5.5, 8, 11, 14.5, 18.5, 23, 28, and 33.5 mV s^{-1}. ECSA is proportion to double layer capacitance (C_{dl}).

4.7.4 Nucleation Measurement of Li_2S

Nucleation of Li_2S were studied in standard 2032-coin cells. Equal quality of Co_3S_4-T200, Co_3S_4-T400, or Co_3S_4-T550 and Super P were dispersed in ethanol and then titrated on the carbon fiber cloth, working as the cathodes after drying at 60 ºC for 12 h. Lithium disk with a diameter of 16 mm was employed as the counter electrode. The electrolyte was 20 μL of 0.2 mM Li_2S_6 with 1.0 M LiTFSI in dioxolane (DOL) and 1,2-dimethoxyethane (DME) solvents. Coin cells were discharged galvanostatically at 0.112 mA to 2.06 V, followed by potentiostatic discharging at 2.05 V for Li_2S nucleation and growth. The potentiostatic discharge was terminated until the current decreased to 0.01mA.

4.7.5 Electrochemical Measurements

Standard 2032-coin cells were assembled in an argon-filled glovebox with moisture and oxygen contents below 0.1 ppm. Li metal was used as the anode (diameter: 16 mm, thickness: ~0.4 mm). Working electrodes were S/Co_3S_4-T200/C, S/Co_3S_4-T400/C, or S/Co_3S_4-T550/C composites. The electrolyte was 1 M LiTFSI in DOL/DME (1:1, vol) solvents with 1% LiNO3. The electrolyte/sulfur ratio is ~15 μL mg^{-1} for the Li-S coin cell with sulfur loading from 1mg cm^{-1} to 3 mg cm^{-1}. The galvanostatic charge/discharge tests were conducted from 1.7 to 2.8 V using a Land CT2001A Battery Testing System.

The cyclic voltammetry (CV) was conducted with BioLogic VMP-3e potentiostat, scan rate is 3 mV s^{-1}, to calculate the Tafel Slope.

Li^+ diffusion coefficient D_{Li}^+(Figure S15): the CV measurements were performed with seven sweeping rates, i.e., 0.05, 0.1, 0.15, 0.2, 0.10, 0.25, 0.3, and 0.35 mV s^{-1}, as shown in Figure S15. The D_{Li}^+ was derived using the Randles–Sevcik equation as described below according to literature[3]:

$$I_P = 2.69 \times 10^5 \text{ C mol}^{-1} \text{ V}^{-1/2} \cdot n^{3/2} \cdot A \cdot D_{Li}^{1/2} \cdot v^{1/2} \cdot C_{Li}$$

where I_p indicates the peak current (A), n is the number of electrons in the reaction (n=1 for Li electroplating/stripping processes), A is the electrode area (cm^2), v is the scanning rate (V s^{-1}), and C_{Li} is the Li^+ concentration in the electrolyte (0.001 mol cm^{-3}). Note that the constant with a value of 2.69×10^5 has units of C mol^{-1} $V^{-1/2}$. D_{Li}^+ is proportional to $I_p/v^{1/2}$, the linear relationship between the I_p and the square root of v can be derived from CV measurements.

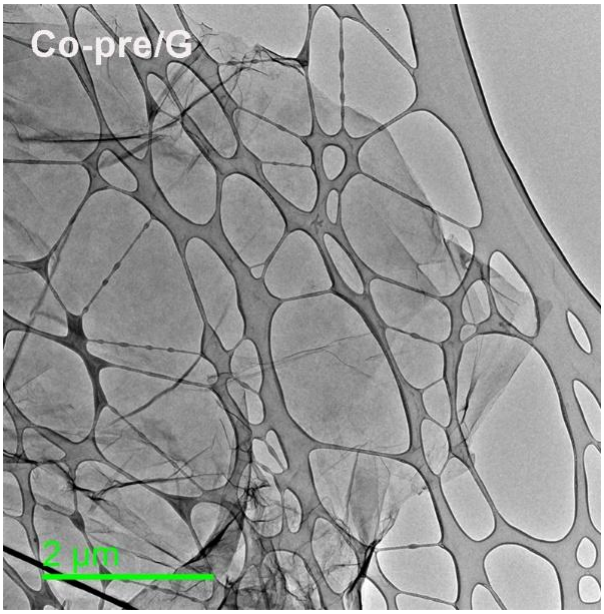

Figure S1 TEM image of Co-pre/G nanosheet

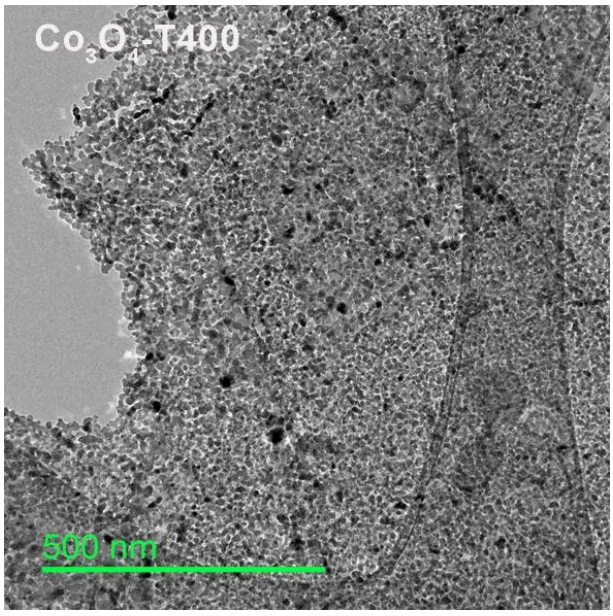

Figure S2 TEM image of Co_3O_4-T400 nanosheet.

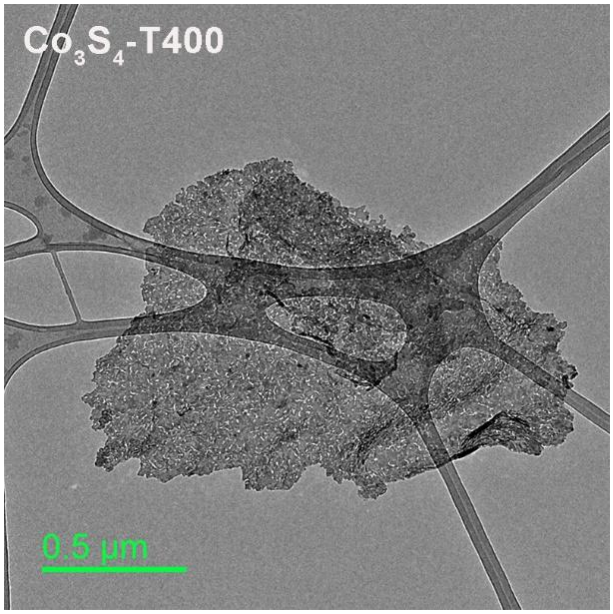

Figure S3 TEM image of Co_3S_4-T400 nanosheet.

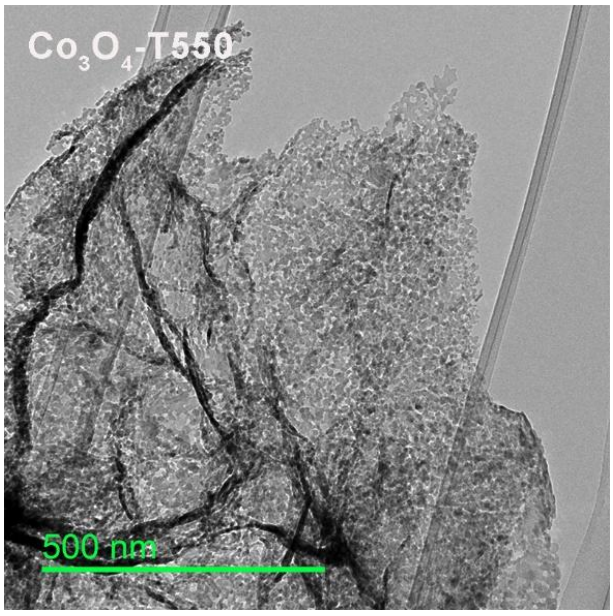

Figure S4 TEM image of Co_3O_4-T550 nanosheet.

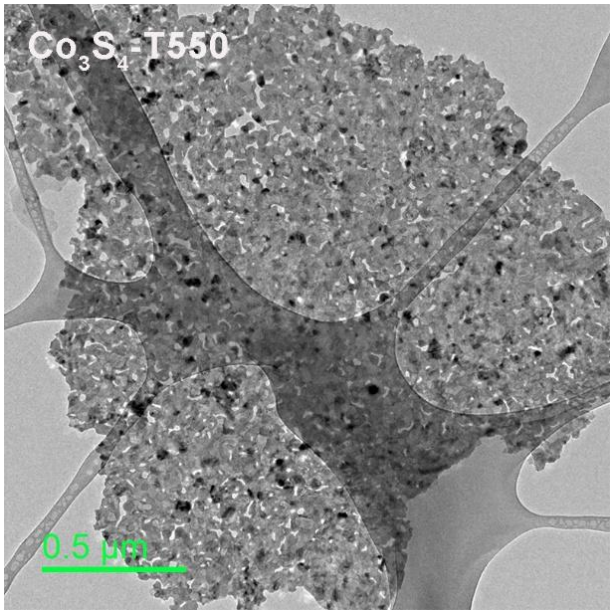

Figure S5 TEM image of Co_3S_4-T550 nanosheet.

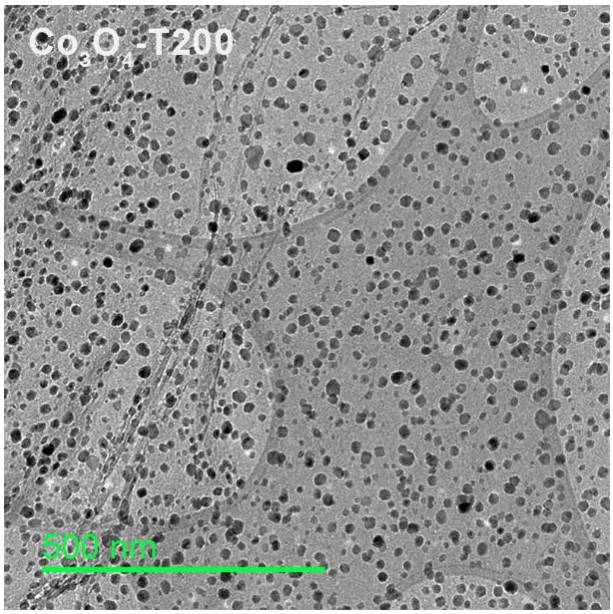

Figure S6 TEM image of Co_3O4-T200 nanosheet.

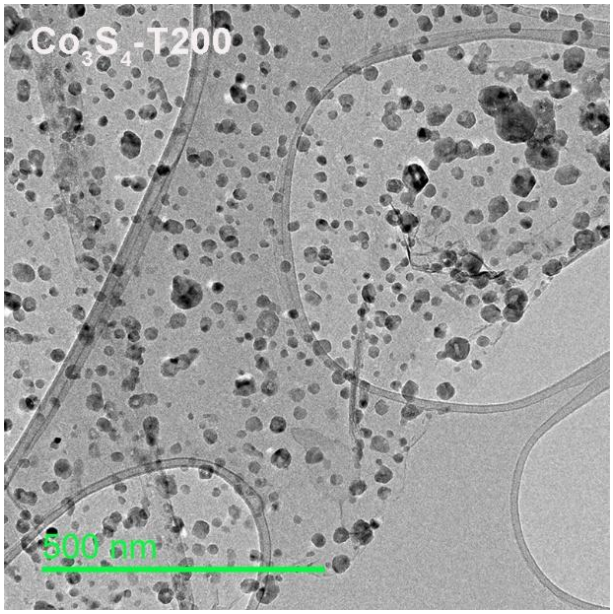

Figure S7 TEM image of Co_3S_4-T200 nanosheet.

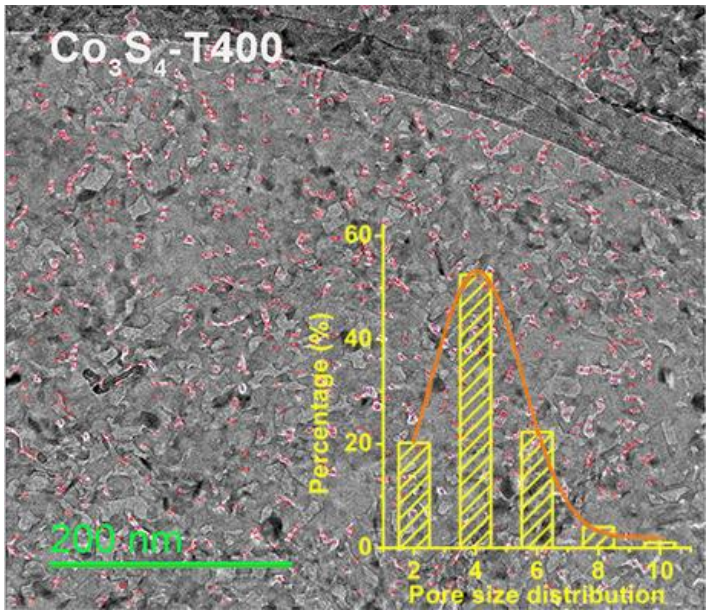

Figure S8 Statistic analysis of pore size distribution of Co_3O4-T400 nanosheet.

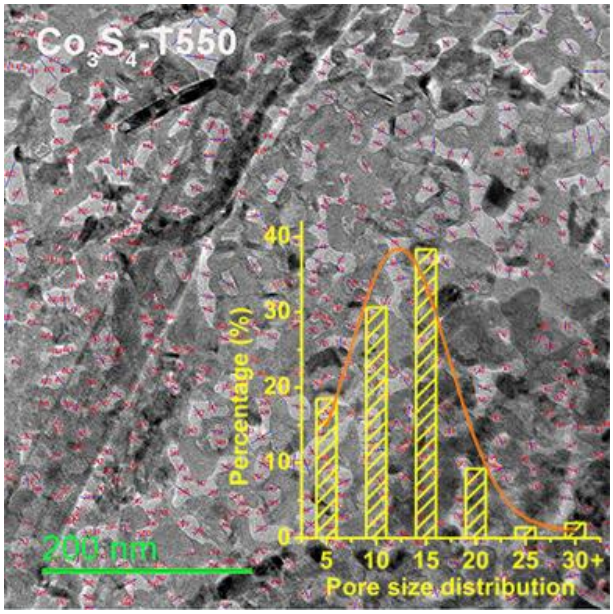

Figure S9 Statistic analysis of pore size distribution of Co_3S_4-T550 nanosheet.

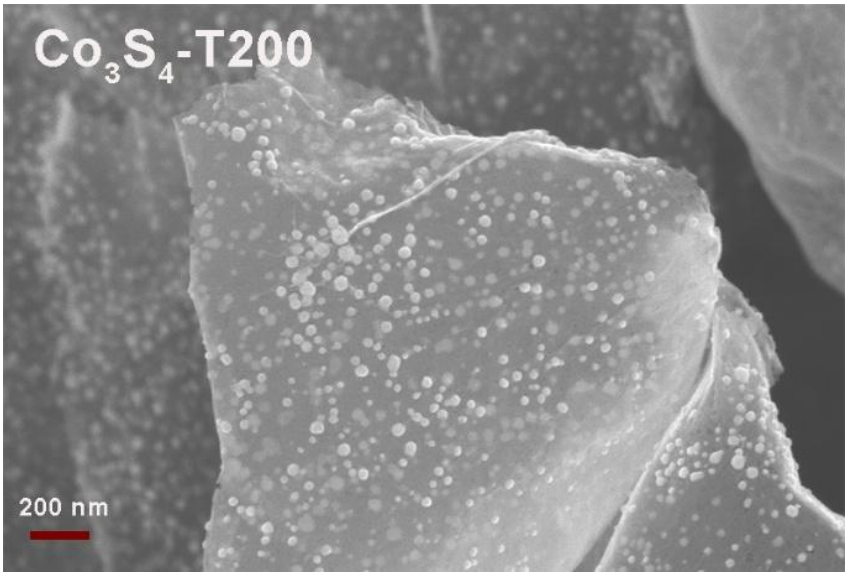

Figure S10 SEM image of Co_3S_4-T200 nanosheet.

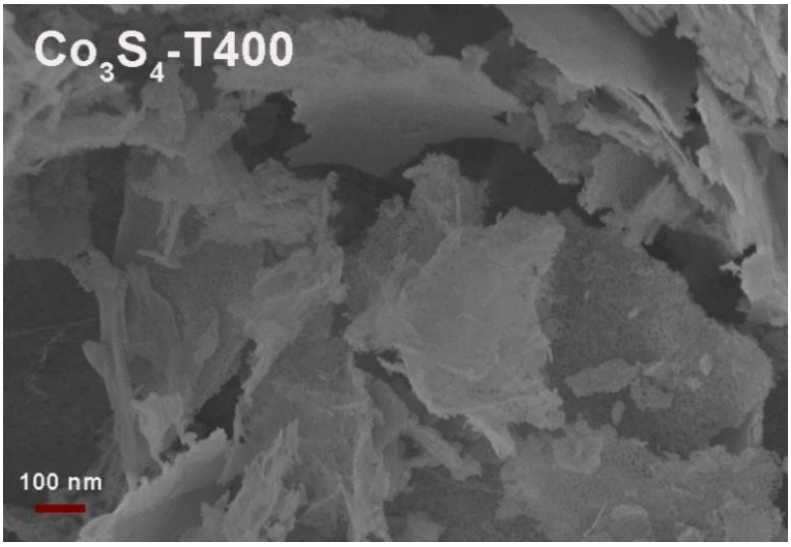

Figure S11 SEM image of Co_3S_4-T400 nanosheet.

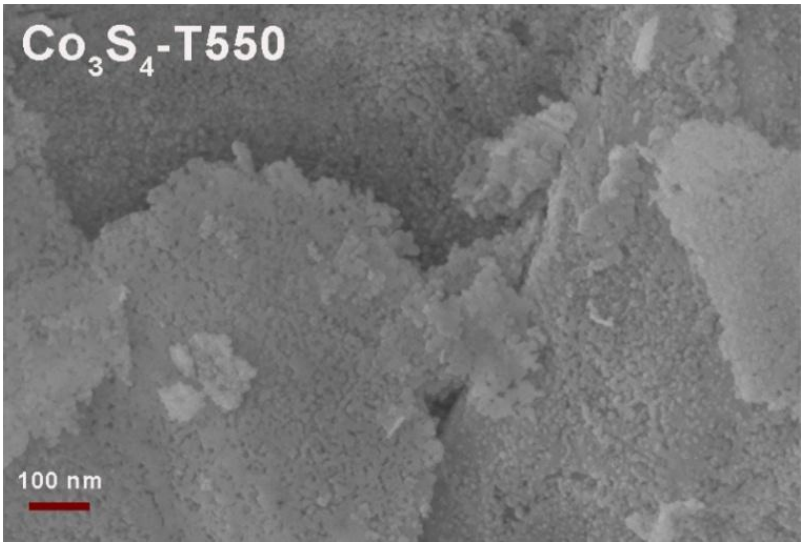

Figure S12 SEM image of Co_3S_4-T550 nanosheet.

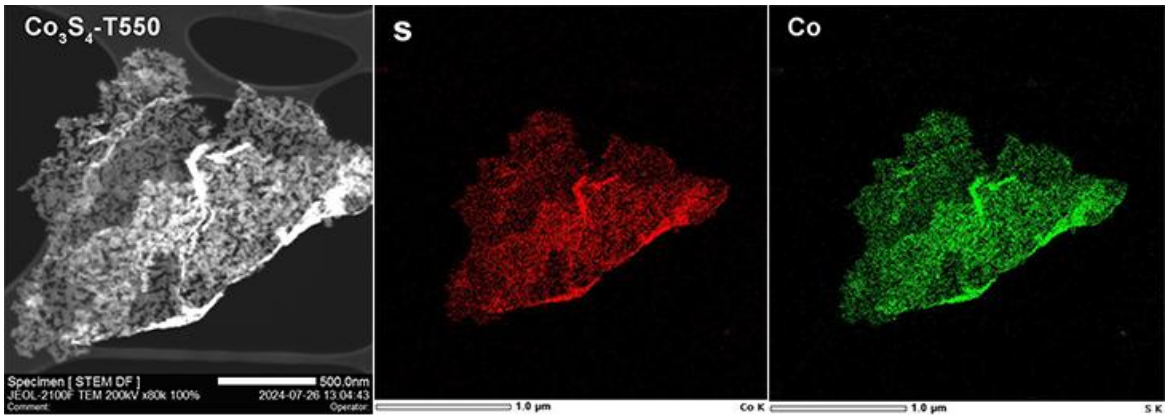

Figure S13 EDS mapping of Co_3S_4-T400 nanosheet.

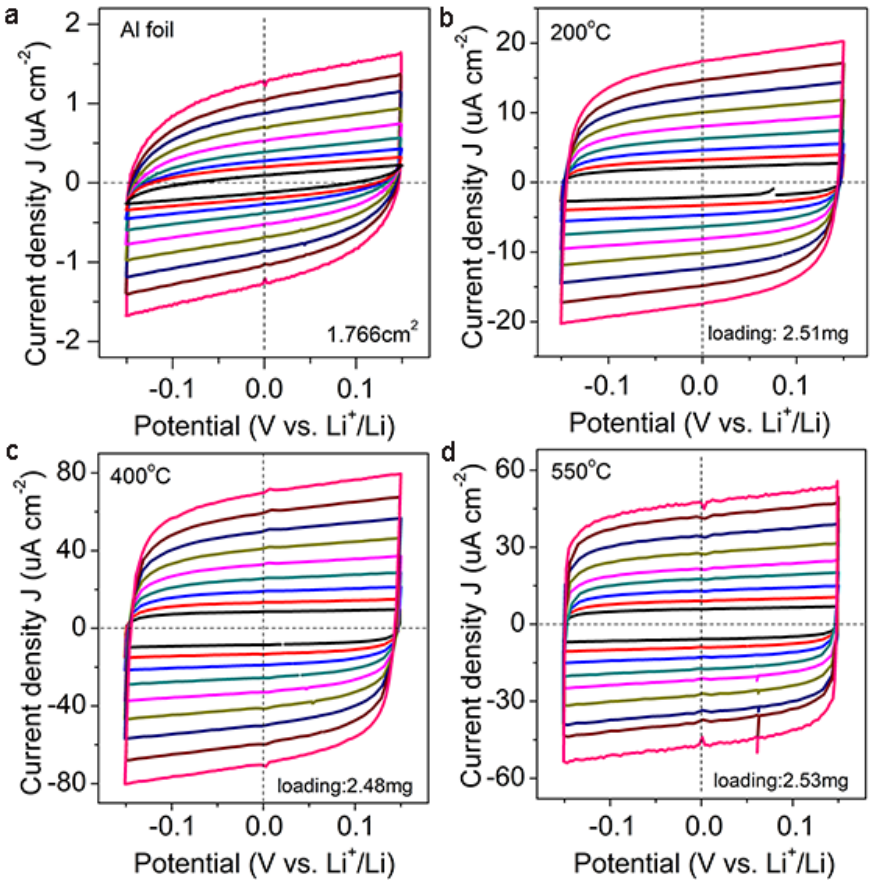

Figure S14 Electrochemical specific surface area (ECSA) measurements of the catalyst. Cyclic voltammetry (CV) curves of (a) aluminium foil, (b) Co_3S_4-200T; (c) Co_3S_4-400T; (d) Co_3S_4-550T.

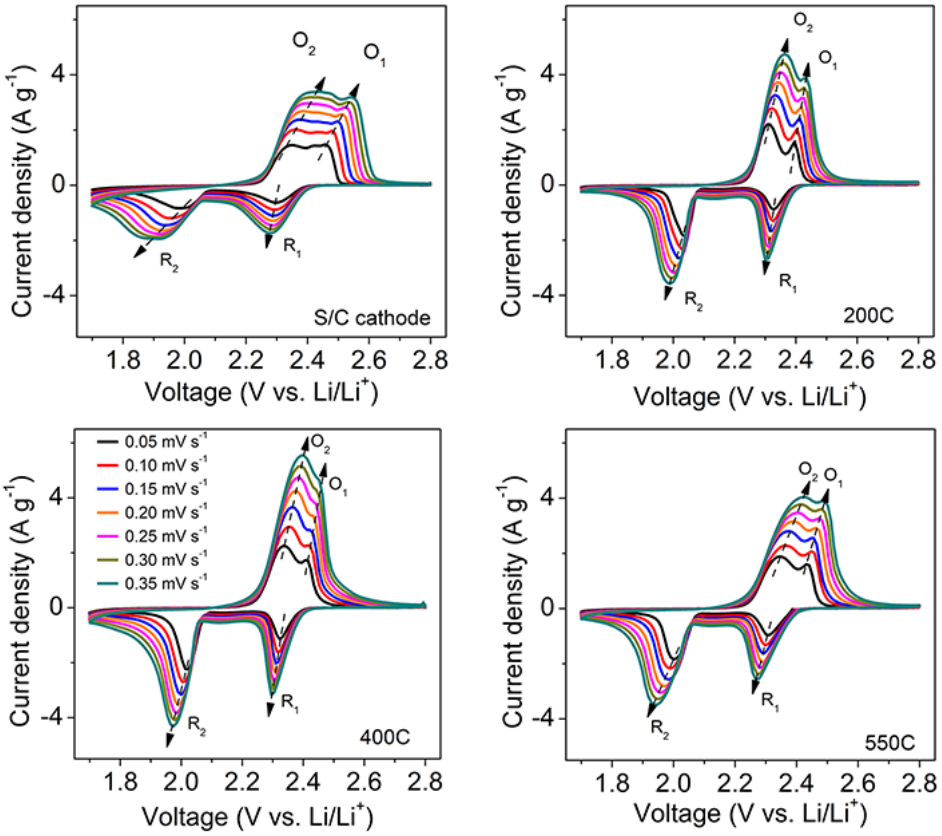

Figure S15 Lithium-ion diffusion properties on the surface of as-synthesized electrocatalyst. CV curves of (a) pure S-C cathode, (b) Co_3S_4-200T-S, (c) Co_3S_4-400T-S, (d) Co_3S_4-550T-S

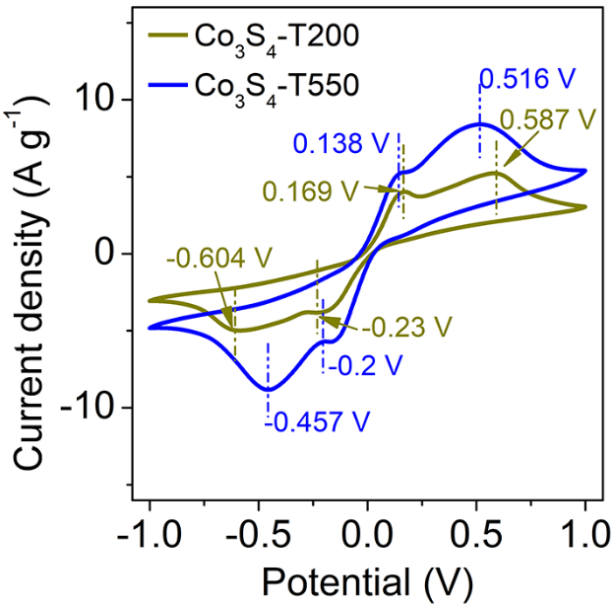

Figure S16 Cyclic voltammetry (CV) curves of Li_2S_6 symmetric cells with Co_3S_4-T200, and Co_3S_4-T550 electrodes at a scanning rate of 3 mV s^{-1}.

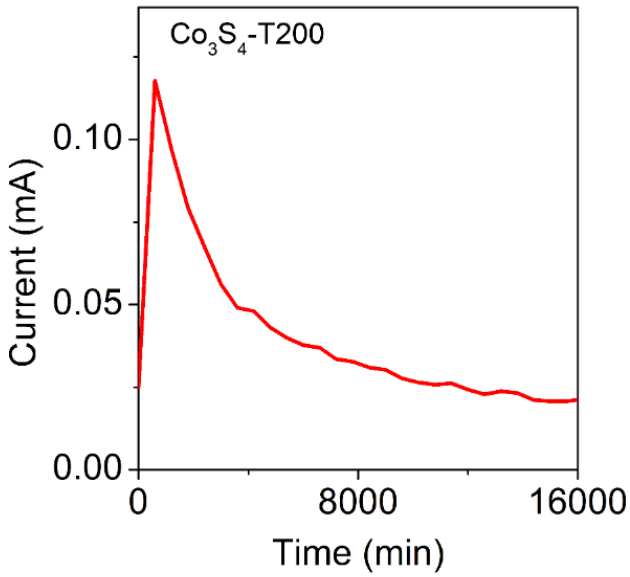

Figure S17 Potentiostatic discharging (2.05 V) current of Co_3S_4-T200.

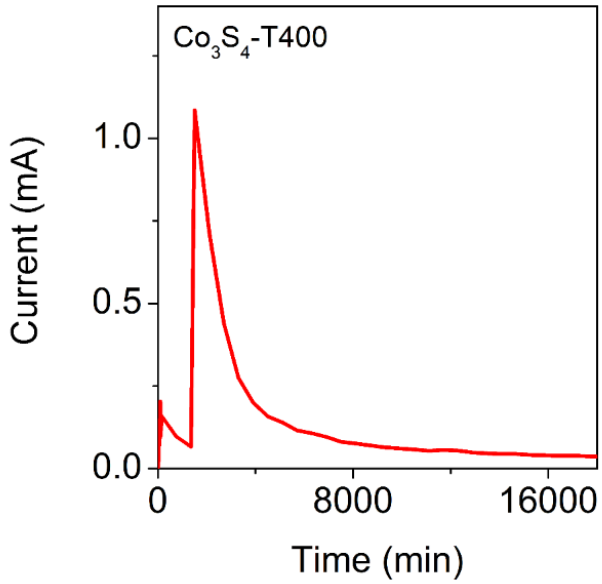

Figure S18 Potentiostatic discharging (2.05 V) current of Co_3S_4-T400.

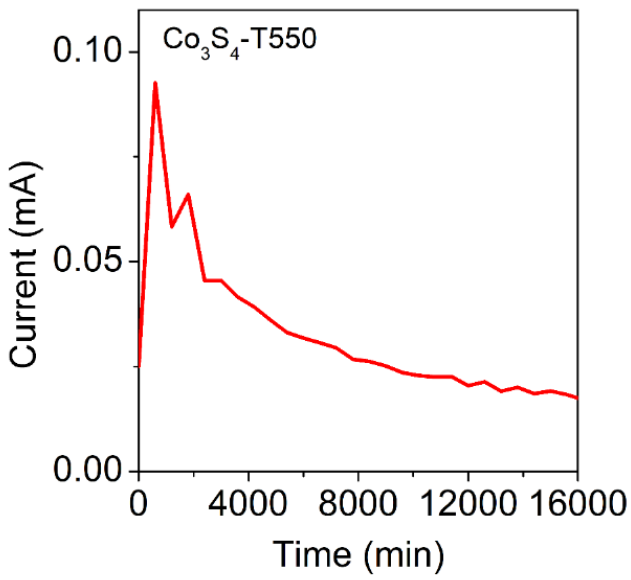

Figure S19 Potentiostatic discharging (2.05 V) current of Co_3S_4-T550.

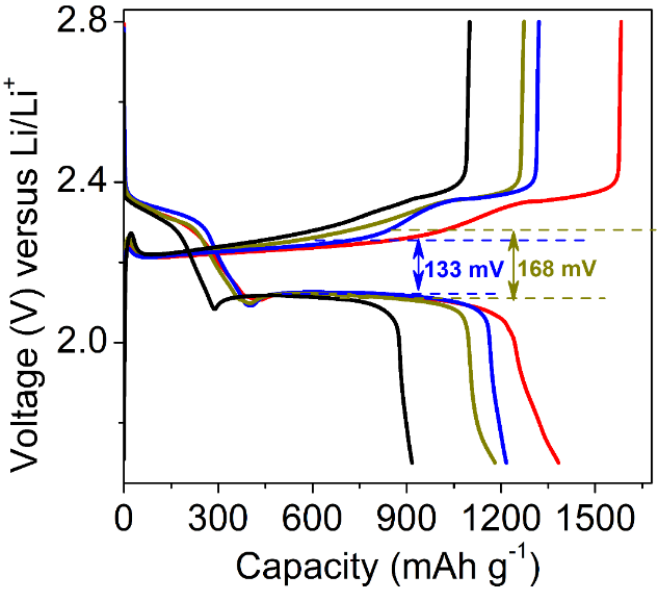

Figure S20 Overpotential measured with Galvanostatic charge-discharge profile at 0.1 C in Li–S batteries with sulfur host of Co_3S_4-T400, or Co_3S_4-T550.

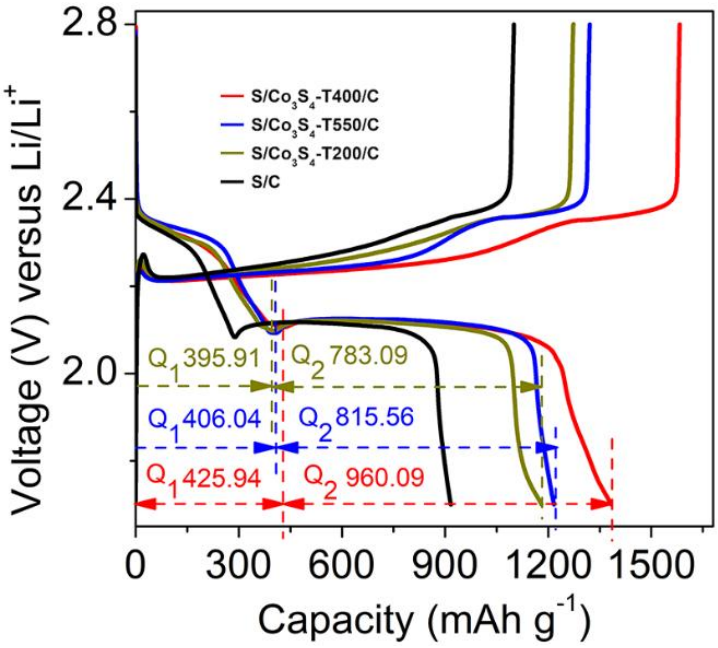

Figure S21 Charge/discharging capacity profile of Li–S cells with sulfur host of Co_3S_4-T400, or Co_3S_4-T550. C-rate: 0.1 C

4.8 SI References

1. Liu, B.; Torres, J. F.; Taheri, M.; Xiong, P.; Lu, T.; Zhu, J.; Liu, Y.; Yu, G.; Tricoli, A., Dual-Ion Flux Management for Stable High Areal Capacity Lithium–Sulfur Batteries. *Advanced Energy Materials* **2022,** *12* (10), 2103444.

2. Trasatti, S.; Petrii, O., Real surface area measurements in electrochemistry. *Pure and applied chemistry* **1991,** *63* (5), 711-734.

3. Zhou, G.; Tian, H.; Jin, Y.; Tao, X.; Liu, B.; Zhang, R.; Seh, Z. W.; Zhuo, D.; Liu, Y.; Sun, J., Catalytic oxidation of Li2S on the surface of metal sulfides for Li− S batteries. *Proceedings of the National Academy of Sciences* **2017,** *114* (5), 840-845.

Chapter 5 Summary and Future Perspective

5.1 Preamble

Energy density is a crucial metric for assessing the portability and efficiency of battery technologies. Lithium–sulfur (Li–S) batteries, known for their high theoretical energy density, are strong candidates for next-generation energy storage. Among the factors affecting their performance, lithium-ion (Li^+) diffusivity plays a key role by influencing reaction kinetics, charge/discharge rates, and active material utilization.

This dissertation investigates how Li^+ transport impacts the electrochemical performance of Li–S batteries through three interrelated research projects. In Chapter 3, two main strategies are explored: 1) the use of functionalized interlayers or modified separators to suppress the shuttle effect and regulate LiPSs diffusion, and 2) the incorporation of conductive, catalytically active sulfur host materials to enhance redox kinetics.

Chapter 2 and Chapter 4 examine the trade-offs between potential energy density loss from added interlayer materials and the performance gains from improved Li^+ transport and catalytic activity. These approaches collectively improve LiPSs conversion, accelerate ion transport, and enhance the cycling stability, rate capability, and long-term durability of Li–S batteries.

While these strategies have proven effective in improving LiPSs conversion and overall

electrochemical performance, the fundamental mechanisms underlying the catalytic transformation of polysulfides are still not fully understood and remain a topic of active research. Although the studies in chapters 3 and 4 have shown that electrocatalysts can promote the conversion of soluble long-chain polysulfides into insoluble Li_2S/Li_2S_2, these final products are electronically insulating and tend to accumulate on the catalyst surface, forming a passivating layer that hinders further charge transfer. This surface passivation significantly undermines the long-term catalytic activity and electrochemical stability of the system.

To address this issue, future research should focus on rational catalyst design strategies aimed at regulating Li_2S/Li_2S_2 nucleation and growth, minimizing catalyst deactivation, and improving the electronic connectivity within the cathode composite. Structural engineering approaches, such as constructing three-dimensional conductive frameworks, introducing hierarchical porosity, or incorporating multifunctional interfaces, may offer promising pathways to mitigate passivation and enhance the durability and efficiency of polysulfide conversion efficiency. Overcoming these challenges will be critical for advancing Li–S battery technologies toward practical high-energy-density applications.

A summary of the key contents and conclusions is provided below.

5.2 Main Research Methods

5.2.1 Modified membrane materials cause energy density loss by increasing Li^+ transport resistance

For Li–S batteries, Microporous membranes have been widely investigated as a potential solution strategy to 'polysulfide shuttle effect'. However, an often-overseen consequence of this strategy is the unintended hindrance to lithium-ion mobility, which compromises the battery energy density. In this thesis, we investigated the energy losses associated with the use of seven commonly reported membrane materials in the literature. Our experimental findings indicate that Li–S batteries employing a commercial polypropylene (PP) separator experience a minimum energy density reduction of 20% when the overpotential exceeds 250 mV. The addition of a microporous membrane as a polysulfide barrier on the PP separator significantly exacerbates energy loss. Li|Li symmetric cell tests reveal that certain membrane types, including graphene oxide (GO), molybdenum disulfide (MoS_2), and reduced graphene oxide (rGO), exhibit overpotentials exceeding 350 mV at a 1C rate. This issue becomes even more pronounced when these membranes are tested in H-cells, which means that take the sluggish sulfur redox reaction into account. Holey graphene with different porosity were synthesized to quantify the blockage effect of modified membrane towards Li^+ transport (e.g., 050HG: porousity:18.2%; 030HG: porosity:11.1%), along with modeling studies, confirm that the observed overpotentials arise from the physical obstruction of Li^+ transport. This highlights the necessity of balancing soluble polysulfide suppression and energy loss. For the construction of efficient Li–S batteries,

the optimal effective hole area percentage should be comparable to that of commercial PP separators (~15.5%), ensuring a trade-off where it is small enough to mitigate the polysulfide shuttle effect and prevent internal short-circuiting while being large enough to minimize excessive overpotential. Specifically, holey graphene membranes with 18.2% and 11.1% surface porosity can reduce polysulfide diffusion by 62.5% and 113%, respectively, while increasing the overpotential for Li^+ transport by only 33.3% and 60%. These findings provide a design framework for multi-scale porous membranes to achieve a balance between LiPS confinement and energy density retention.

5.2.2 Li^+ mobility impact the electrocatalytic ability

Li^+ diffusivity is critical for enhancing SRR kinetics in Li–S batteries for both functional modified membrane/interlayer in separator, or catalytic sulfur host materials in cathodes.

In the second project, Co_9S_8-grafted holey graphene (Co_9S_8/HG) was introduced as a modified membrane in Li–S battery, highlighting the critical role of charge transfer in optimizing the redox reaction kinetics of trapped LiPSs. TEM and statistical analysis reveal that Co_9S_8/HG exhibits a porosity of ~16.2%, slightly higher than commercial PP separators (15.5%), ensuring minimal resistance to Li^+ migration. BET analysis indicates that Co_9S_8/HG possesses a 67% SSA than its non-holey counterpart (Co_9S_8/G), providing more active sites for catalyzing LiPSs conversion. Electrochemical performance measurements, supported by computational simulations,

confirm that the porous structure of Co_9S_8/HG accelerates SRR kinetics by facilitating rapid charge transfer and promoting Li_2S deposition. Battery tests further validate its superior rate capability and long-term cycling stability. At a 0.2 C rate, Li–S cells with Co_9S_8/HG maintain a capacity of 671 mAh g^{-1} after 900 cycles, with a low-capacity decay rate of 0.044% per cycle. The enhanced performance is attributed to the porous architecture, which enables efficient Li^+ diffusion, ensuring rapid engagement in SRR kinetics.

In Chapter 4, Co_3S_4-T400, with an average particle size of 20.7 nm, an average pore diameter of 3.3 nm, and a porosity of 13.6%, was synthesized via a template method to investigate the influence of Li^+ diffusivity on SRR kinetics and Li_2S precipitation. These structural features enable Co_3S_4-T400 to exhibit enhanced electrochemical performance, lower resistance to Li^+ diffusion, and a larger ECSA. Tafel plot analysis, Li^+ diffusion coefficient measurements, and Li_2S potentiostatic precipitation tests further confirm the superior electrocatalytic capability of Co_3S_4-T400 compared to Co_3S_4-T200 and Co_3S_4-T550. As a result, Li–S batteries incorporating S/Co_3S_4-T400/C composite electrodes achieve excellent rate performance, delivering specific capacities of 755.8 mAh g^{-1} at 1C and 658.7 mAh g^{-1} at 2 C, while recovering a high capacity of 815.1 mAh g^{-1} upon reverting to 0.2 C. Long-term cycling tests at 0.2 C show that the S/ Co_3S_4-T400/C electrodes maintain a specific capacity of 657 mAh g^{-1} with an ultra-low capacity decay rate of 0.051% per cycle over 1000 cycles.

5.3 Challenges and Prospects

Despite significant advancements in capacity retention and cycling stability through catalytic modification of separators and sulfur/host composites, the practical implementation of lithium–sulfur (Li–S) batteries remains constrained by several persistent challenges. The key reasons are:

- the gradual passivation of catalysts due to insulating Li_2S deposition;[1-3]
- the need to significantly increase sulfur loading to meet practical energy output comparable to Li-ion batteries;[4, 5] and
- the continued vulnerability of the lithium metal anode[6, 7].

In the future, research on Li–S battery may include: (i) Mechanical understanding of catalysis. Investigating the catalytic mechanism between the catalyst and sulfur species is crucial for identifying key intermediate products that govern the acceleration of sulfur species conversion kinetics.[8] Understanding this mechanism is fundamentally significant for developing strategies to enhance the long-term stability of catalysts. (ii) Rational catalyst design. Engineering 3D catalysts to address passivation issues caused by insulating Li_2S deposition is essential.[9, 10] The solid-state, electron-insulating Li_2S accumulates on the catalyst surface, gradually isolating it from electron transport and rendering it catalytically inactive. Therefore, designing tailored sulfur catalyst to regulate Li_2S precipitation is crucial for enhancing electrocatalytic kinetics of SRR. (iii) Development of solid-state Li–S batteries (SS Li–S). Transitioning to SS Li–S batteries offer a promising route to fundamentally eliminate the polysulfide shuttle

effect. While strategies such as physical confinement, chemical adsorption, and catalytic conversion have shown promise, a complete solution has yet to be realized.

In parallel, the flammability and leakage risks associated with liquid electrolytes—exacerbated by lithium dendrite growth—pose significant safety concerns. Solid-state electrolytes (SSEs) have thus garnered increasing interest due to their potential to suppress dendrites and enhance overall cell safety.[11, 12]

Solid-state electrolytes (SSEs) used in solid-state lithium–sulfur batteries (LSBs) are primarily classified into two categories:

- Solid polymer electrolytes (SPEs) and inorganic SSEs. SPEs provide a solvation environment similar to that of liquid electrolytes; however, lithium-ion (Li^+) transport is hindered by the limited mobility of polymer chains.[13, 14] Consequently, SPEs typically exhibit low ionic conductivity (<10^{-6} S cm^{-1}) at room temperature (RT), thereby requiring elevated operating temperatures above 60 °C to achieve acceptable performance.[15, 16] Moreover, the poor mechanical strength of SPEs ineffective in suppressing lithium dendrite growth.
- Inorganic solid-state electrolytes (SSEs) enable Li^+ transport via a hopping mechanism between lattice sites.[17, 18] Among oxide-based SSEs, widely studied systems include NASICON-type $Li_{1+x}AlxGe_{2-x}(PO4)_3$ (LAGP) and ($Li_{1+x}Al_xTi_{2-x}(PO_4)_3$ (LATP),[19, 20] perovskite-type $Li_{3x}La_{(2/3)-x}TiO_3$ (LLTO),[21] and garnet-type $Li_7La_3Zr_2O_{12}$ (LLZO),[22, 23] all of which exhibit ionic conductivities exceeding 10^{-}

^{4}S cm^{-1} at room temperature and good chemical stability, but the rigidity leads to high interfacial resistance.[24-26]

Sulfide-based SSEs, on the other hand, offer ionic conductivities exceeding 10^{-2} S cm^{-1}, comparable to liquid electrolytes—and exist in various forms (glassy, glass–ceramic, crystalline)[27-30]. Despite their excellent conductivity, their extreme sensitivity to air/moisture and narrow electrochemical stability window limit practical application, particularly at the reactive interfaces with sulfur cathodes and lithium metal anodes.

Recent progress has deepened our understanding of solid-state Li–S electrochemistry, enabling targeted strategies to improve interfacial contact and reaction kinetics. Current research is increasingly focused on engineering key performance parameters to bridge the gap between theoretical and practical performance, including high areal sulfur loading, optimized electrolyte-to-sulfur ratios, and balanced N/P ratios.[31]

Nonetheless, achieving commercially viable Li–S batteries still require breakthroughs in materials design, interfacial engineering, and system integration. Addressing these challenges will be critical to unlocking the full potential of Li–S chemistry for next-generation high-energy, safe, and sustainable energy storage systems.

5.5 Reference

1. Sun, J.; Liu, Y.; Liu, L.; Bi, J.; Wang, S.; Du, Z.; Du, H.; Wang, K.; Ai, W.; Huang, W., Interface engineering toward expedited Li2S deposition in lithium–sulfur batteries: a critical review. *Advanced Materials* **2023,** *35* (29), 2211168.

2. Cai, D.-Q.; Yang, J.-L.; Liu, T.; Zhao, S.-X.; Cao, G., Interfaces-dominated Li2S nucleation behavior enabled by heterostructure catalyst for fast kinetics Li-S batteries. *Nano Energy* **2021,** *89*, 106452.

3. Jiang, Q.; Xu, H.; Hui, K. S.; Ye, Z.; Zha, C.; Lin, Z.; Zheng, M.; Lu, J.; Hui, K. N., Breaking the Passivation Effect for MnO2 Catalysts in Li− S Batteries by Anion-Cation Doping. *Angewandte Chemie* **2024,** *136* (46), e202408474.

4. Peng, H. J.; Huang, J. Q.; Cheng, X. B.; Zhang, Q., Review on high-loading and high-energy lithium–sulfur batteries. *Advanced Energy Materials* **2017,** *7* (24), 1700260.

5. Wang, M.; Bai, Z.; Yang, T.; Nie, C.; Xu, X.; Wang, Y.; Yang, J.; Dou, S.; Wang, N., Advances in high sulfur loading cathodes for practical lithium-sulfur batteries. *Advanced Energy Materials* **2022,** *12* (39), 2201585.

6. Wang, Q.; Liu, B.; Shen, Y.; Wu, J.; Zhao, Z.; Zhong, C.; Hu, W., Confronting the challenges in lithium anodes for lithium metal batteries. *Advanced Science* **2021,** *8* (17), 2101111.

7. Lin, D.; Liu, Y.; Cui, Y., Reviving the lithium metal anode for high-energy batteries. *Nature nanotechnology* **2017,** *12* (3), 194-206.

8. Cheng, M.; Yan, R.; Yang, Z.; Tao, X.; Ma, T.; Cao, S.; Ran, F.; Li, S.; Yang, W.; Cheng, C., Polysulfide catalytic materials for fast-kinetic metal–sulfur batteries: principles and active centers. *Advanced science* **2022,** *9* (2), 2102217.

9. Qin, J.; Wang, R.; Xiao, P.; Wang, D., Engineering cooperative catalysis in Li–S batteries. *Advanced Energy Materials* **2023,** *13* (26), 2300611.

10. Song, Y.; Cai, W.; Kong, L.; Cai, J.; Zhang, Q.; Sun, J., Rationalizing electrocatalysis of Li–S chemistry by mediator design: progress and prospects.

Advanced Energy Materials **2020,** *10* (11), 1901075.

11. Ge, S.; Sasaki, T.; Gupta, N.; Qin, K.; Longchamps, R. S.; Aotani, K.; Aihara, Y.; Wang, C.-Y., Quantification of lithium battery fires in internal short circuit. *ACS Energy Letters* **2024,** *9* (12), 5747-5755.

12. Wang, Y.; Feng, X.; Peng, Y.; Zhang, F.; Ren, D.; Liu, X.; Lu, L.; Nitta, Y.; Wang, L.; Ouyang, M., Reductive gas manipulation at early self-heating stage enables controllable battery thermal failure. *Joule* **2022,** *6* (12), 2810-2820.

13. Stephan, A. M., Review on gel polymer electrolytes for lithium batteries. *European polymer journal* **2006,** *42* (1), 21-42.

14. Fergus, J. W., Ceramic and polymeric solid electrolytes for lithium-ion batteries. *Journal of Power Sources* **2010,** *195* (15), 4554-4569.

15. An, Y.; Han, X.; Liu, Y.; Azhar, A.; Na, J.; Nanjundan, A. K.; Wang, S.; Yu, J.; Yamauchi, Y., Progress in solid polymer electrolytes for lithium-ion batteries and beyond. *Small* **2022,** *18* (3), 2103617.

16. Li, S.; Chen, Y.-M.; Liang, W.; Shao, Y.; Liu, K.; Nikolov, Z.; Zhu, Y., A superionic conductive, electrochemically stable dual-salt polymer electrolyte. *Joule* **2018,** *2* (9), 1838-1856.

17. Famprikis, T.; Canepa, P.; Dawson, J. A.; Islam, M. S.; Masquelier, C., Fundamentals of inorganic solid-state electrolytes for batteries. *Nature materials* **2019,** *18* (12), 1278-1291.

18. Liang, J.; Li, X.; Adair, K. R.; Sun, X., Metal halide superionic conductors for all-solid-state batteries. *Accounts of Chemical Research* **2021,** *54* (4), 1023-1033.

19. Morimoto, H.; Awano, H.; Terashima, J.; Shindo, Y.; Nakanishi, S.; Ito, N.; Ishikawa, K.; Tobishima, S.-i., Preparation of lithium ion conducting solid electrolyte of NASICON-type Li1+ xAlxTi2− x (PO4) 3 (x= 0.3) obtained by using the mechanochemical method and its application as surface modification materials of LiCoO2 cathode for lithium cell. *Journal of Power Sources* **2013,** *240*, 636-643.

20. Safanama, D.; Sharma, N.; Rao, R. P.; Brand, H. E.; Adams, S., Structural evolution of NASICON-type Li 1+ x Al x Ge 2− x (PO 4) 3 using in situ synchrotron X-

ray powder diffraction. *Journal of Materials Chemistry A* **2016,** *4* (20), 7718-7726.

21. Kwon, W. J.; Kim, H.; Jung, K.-N.; Cho, W.; Kim, S. H.; Lee, J.-W.; Park, M.-S., Enhanced Li+ conduction in perovskite Li 3x La 2/3− x□ 1/3− 2x TiO 3 solid-electrolytes via microstructural engineering. *Journal of materials chemistry A* **2017,** *5* (13), 6257-6262.

22. Murugan, R.; Thangadurai, V.; Weppner, W., Fast lithium ion conduction in garnet-type Li7La3Zr2O12. *Angewandte Chemie-International Edition in English-* **2007,** *46* (41), 7778.

23. Rettenwander, D.; Geiger, C.; Tribus, M.; Tropper, P.; Wagner, R.; Tippelt, G.; Lottermoser, W.; Amthauer, G., The solubility and site preference of Fe3+ in Li7−3xFexLa3Zr2O12 garnets. *Journal of solid state chemistry* **2015,** *230*, 266-271.

24. Feng, W.; Zhao, Y.; Xia, Y., Solid interfaces for the garnet electrolytes. *Advanced Materials* **2024,** *36* (15), 2306111.

25. Zhang, J.; Wang, C.; Fu, J.; Ye, M.; Zhai, H.; Li, J.; Tan, G.; Tang, X.; Sun, X., Reducing Surface Roughness to Achieve Li2CO3-Existent Lithiophilic Interface in Garnet-Type Solid-State Batteries. *Advanced Functional Materials* **2025,** *35* (9), 2416229.

26. Dixit, M. B.; Vishugopi, B. S.; Zaman, W.; Kenesei, P.; Park, J.-S.; Almer, J.; Mukherjee, P. P.; Hatzell, K. B., Polymorphism of garnet solid electrolytes and its implications for grain-level chemo-mechanics. *Nature Materials* **2022,** *21* (11), 1298-1305.

27. Kondo, S.; Takada, K.; Yamamura, Y., New lithium ion conductors based on Li2S-SiS2 system. *Solid State Ionics* **1992,** *53*, 1183-1186.

28. Seino, Y.; Ota, T.; Takada, K.; Hayashi, A.; Tatsumisago, M., A sulphide lithium super ion conductor is superior to liquid ion conductors for use in rechargeable batteries. *Energy & Environmental Science* **2014,** *7* (2), 627-631.

29. Kamaya, N.; Homma, K.; Yamakawa, Y.; Hirayama, M.; Kanno, R.; Yonemura, M.; Kamiyama, T.; Kato, Y.; Hama, S.; Kawamoto, K., A lithium superionic conductor. *Nature materials* **2011,** *10* (9), 682-686.

30. Kato, Y.; Hori, S.; Saito, T.; Suzuki, K.; Hirayama, M.; Mitsui, A.; Yonemura, M.; Iba, H.; Kanno, R., High-power all-solid-state batteries using sulfide superionic conductors. *Nature energy* **2016,** *1* (4), 1-7.

31. Lee, J.; Zhao, C.; Wang, C.; Chen, A.; Sun, X.; Amine, K.; Xu, G.-L., Bridging the gap between academic research and industrial development in advanced all-solid-state lithium–sulfur batteries. *Chemical Society Reviews* **2024,** *53* (10), 5264-5290.

List of publications

Articles:

1. Liu, B.; **Gu, H.**; Torres, J. F.; Yin, Z.; Tricoli, A. J. E.; Science, E., Balancing polysulfide containment and energy loss in lithium–sulfur batteries. *Energy Environ. Sci.*, 22024, 17 (3), 1073-1082.

2. Mei, J.; Wang, J.; **Gu, H.**; Du, Y.; Wang, H.; Yamauchi, Y.; Liao, T.; Sun, Z.; Yin, Z. J. A. M., Nano polymorphism–enabled redox electrodes for rechargeable batteries. Adv. Mater. 2021, 33 (8), 2004920.

3. Ding, J.; Zhang, D.; Riaz, A.; **Gu, H.**; Zheyan Soo, J.; Reddy Narangari, P.; Jagadish, C.; Hoe Tan, H.; Karuturi, S. Scalable Amorphous $NiFe(OH)_x$/Fe/Graphene Bifunctional Electrocatalyst via Solution-Corrosion for Water Splitting. *CCS Chem.* **2024**, *6* (11), 2692– 2703,

4. Yin, H.; Sun, Z.; Liu, K.; Li, Z.; Wibowo, A. A.; Chen, **J.; Gu,** H.; Jing, X.; Chen, Y.; MacDonald, D. J. J. o. M. C. A., Solar-Driven Dehydrogenation and Dehydration of Formate to Syngas with Near-Zero CO2 Emission. Journal of Material Chemistry A, **2025**.

Conference:

2024 International Symposium on Advanced Materials & Sustainable Technology